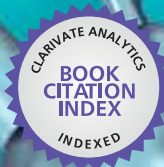




IntechOpen

Functionalized Nanomaterials

Edited by Muhammad Akhyar Farrukh



WEB OF SCIENCE™

FUNCTIONALIZED NANOMATERIALS

Edited by **Muhammad Akhyar Farrukh**

Functionalized Nanomaterials

<http://dx.doi.org/10.5772/63186>

Edited by Muhammad Akhyar Farrukh

Contributors

Abdulaziz S. Alaboodi, Subbarayan Sivasankaran, Sandra Paszkiewicz, Rabin Bissessur, Muhammad Waseem, Adnan Younis, Cecilia Sánchez Jiménez, Alexandra Viruete, Jenny Arratia-Quijada, Gregorio Arizaga, Surjakanta Rana, AK Mitra

© The Editor(s) and the Author(s) 2016

The moral rights of the and the author(s) have been asserted.

All rights to the book as a whole are reserved by INTECH. The book as a whole (compilation) cannot be reproduced, distributed or used for commercial or non-commercial purposes without INTECH's written permission.

Enquiries concerning the use of the book should be directed to INTECH rights and permissions department (permissions@intechopen.com).

Violations are liable to prosecution under the governing Copyright Law.



Individual chapters of this publication are distributed under the terms of the Creative Commons Attribution 3.0 Unported License which permits commercial use, distribution and reproduction of the individual chapters, provided the original author(s) and source publication are appropriately acknowledged. If so indicated, certain images may not be included under the Creative Commons license. In such cases users will need to obtain permission from the license holder to reproduce the material. More details and guidelines concerning content reuse and adaptation can be found at <http://www.intechopen.com/copyright-policy.html>.

Notice

Statements and opinions expressed in the chapters are those of the individual contributors and not necessarily those of the editors or publisher. No responsibility is accepted for the accuracy of information contained in the published chapters. The publisher assumes no responsibility for any damage or injury to persons or property arising out of the use of any materials, instructions, methods or ideas contained in the book.

First published in Croatia, 2016 by INTECH d.o.o.

eBook (PDF) Published by IN TECH d.o.o.

Place and year of publication of eBook (PDF): Rijeka, 2019.

IntechOpen is the global imprint of IN TECH d.o.o.

Printed in Croatia

Legal deposit, Croatia: National and University Library in Zagreb

Additional hard and PDF copies can be obtained from orders@intechopen.com

Functionalized Nanomaterials

Edited by Muhammad Akhyar Farrukh

p. cm.

Print ISBN 978-953-51-2855-7

Online ISBN 978-953-51-2856-4

eBook (PDF) ISBN 978-953-51-4128-0

We are IntechOpen, the first native scientific publisher of Open Access books

3,350+

Open access books available

108,000+

International authors and editors

114M+

Downloads

151

Countries delivered to

Our authors are among the
Top 1%

most cited scientists

12.2%

Contributors from top 500 universities



WEB OF SCIENCE™

Selection of our books indexed in the Book Citation Index
in Web of Science™ Core Collection (BKCI)

Interested in publishing with us?
Contact book.department@intechopen.com

Numbers displayed above are based on latest data collected.
For more information visit www.intechopen.com



Meet the editor



Dr. Muhammad Akhyar Farrukh is an associate professor and founding director of Nano-Chemistry Lab. at GC University Lahore, Pakistan. He was selected by UNESCO and participated as a “Representative of Pakistan” in founding WAYS in Morocco. He was awarded “Young Chemist Award” by IUPAC in Italy in 2007 and selected as “Young Scientist” by TWAS in Egypt and IAP in Germany in 2010. He was selected as “Young Scientist” by IAP/World Economic Forum in China in 2010. He was selected as “Young Researcher” in 2013 by the Council for Lindau Nobel Laureate Meetings. He was awarded IUPAC-2015 *Award for Chemists* as an outstanding chemist from developing countries. He has *published* over 90 *papers* in international/national reputed journals, published/edited 20 *books*, issued/filed 07 *US patents*, presented 44 *papers* in international/national conferences, and given 24 *plenary/invited lectures* in 24 *countries up to 2016*.

Contents

Preface XI

Section 1 Non-Carbon Compounds 1

- Chapter 1 **Structural Characterization and Mechanical Behavior of Al 6061 Nanostructured Matrix Reinforced with TiO₂ Nanoparticles for Automotive Applications 3**
S. Sivasankaran and Abdulaziz S. Alaboodi

- Chapter 2 **Fungal-Derived Nanoparticles as Novel Antimicrobial and Anticancer Agents 37**
Muhammad Waseem and Muhammad Atif Nisar

- Chapter 3 **Cerium Oxide Nanostructures and their Applications 53**
Adnan Younis, Dewei Chu and Sean Li

- Chapter 4 **Functionalization of Surfaces in Layered Double Hydroxides and Hydroxide Salt Nanoparticles 69**
Gregorio Guadalupe Carbajal Arizaga, Cecilia Sánchez Jiménez, Alexandra Viruete and Jenny Arratia-Quijada

Section 2 Carbon Compounds 89

- Chapter 5 **Intercalation of C₆₀-Fullerol into Graphite Oxide 91**
Raymond Arsenault and Rabin Bissessur

- Chapter 6 **Covalently Functionalized Nano-Graphene Oxide for Fine Chemical Synthesis 105**
Surjyakanta Rana and Sreekantha B. Jonnalagadda

- Chapter 7 **Multifunctional Polymer Nanocomposites Based on Thermoplastic Polyesters 123**
Sandra Paszkiewicz

Chapter 8	Nanocomposites of Carbon Nanotubes and Semiconductor Nanocrystals as Advanced Functional Material with Novel Optoelectronic Properties	145
	Rima Paul and Apurba Krishna Mitra	

Preface

Nano means “small,” it is equal to one billionth of a meter, and generally the nanometer scale runs from 1 to 100 nm while discussing the applications of nanomaterials. Nanomaterials have very high potency and emerge with large applications piercing through all the discipline of knowledge, leading to industrial and technological growth. Nanotechnology is expected to have an impact on nearly every industry including food, medical devices, chemical coatings, personal health, catalysis, sensors, water purification, computer games, solar cells, water splitting, etc.

Nanotechnology is a multidisciplinary science that has its roots in fields such as colloidal science, device physics, and biomedical and supramolecular chemistry. The scope of the topic is quite large; however, the objective of this book is to cover maximum main areas focusing on synthesis techniques, characterization of nanomaterials with various techniques like thermogravimetric analysis (TGA), scanning electron microscopy (SEM), X-ray powder diffraction (XRD), transmission electron microscopy (TEM), energy-dispersive X-ray (EDX), nuclear magnetic resonance (NMR) spectroscopy, and Fourier transform infrared spectroscopy (FTIR), etc., and their multiple applications.

This book is divided into two sections with “Non-carbon Compounds” and “Carbon Compounds.” The synthesis, characterization, and applications of metal, metal oxides, and metal hydroxide nanoparticles and composites are covered in the section “Noncarbon Compounds,” while the section “Carbon Compounds” focuses on the carbon nanotubes, graphite oxide, graphene oxide, etc.

I would like to thank the Publishing Process Manager Ms. Andrea Koric for her cooperation throughout the process of publication of this book.

Dr. Muhammad Akhyar Farrukh
Nano-Chemistry Laboratory
GC University Lahore
Pakistan

Non-Carbon Compounds

Structural Characterization and Mechanical Behavior of Al 6061 Nanostructured Matrix Reinforced with TiO₂ Nanoparticles for Automotive Applications

S. Sivasankaran and Abdulaziz S. Alaboodi

Additional information is available at the end of the chapter

<http://dx.doi.org/10.5772/65947>

Abstract

The main aims of the present chapter are to: learn synthesis procedure of AA 6061-x wt.% TiO₂ nanocomposites (x = 0, 2, 4, 6, 8, 10 and 12 wt.%) by mechanical alloying (MA); investigate structural characterization of manufactured nanocomposite powders using X-ray line profile analysis, scanning electron microscope (SEM) and transmission electron microscope (TEM); examine consolidation method and mechanical behavior in terms of sintered density, Vickers hardness and compressive stress-strain behavior; study the improvement of ductility in nanocomposites; and simulate the mechanical behavior using ANSYS. Here, the synthesized nanocomposites via MA were consolidated using conventional uniaxial die compaction; then, the green compacts were sintered at different temperatures. TEM microstructures of as-milled powder samples showed the matrix crystallite sizes ranging from 45 to 75 nm, which depended on the amount of reinforcement. A remarkable decrease in matrix powder particles size with the function of reinforcement was observed due to the ceramic nano TiO₂ particles acted as milling agent. The sintered nanocomposites yielded maximum strength of 1.126 GPa. The study of tri-modeled composite and its mechanical behavior revealed the possibility of achieving improvements in ductility and toughness for nanocomposites. The simulated mechanical behavior results using finite element method were good agreement with experimental results.

Keywords: mechanical alloying, nanocrystallite matrix, nanoparticles, characterization, mechanical behavior

1. Introduction

Production of suitable materials to make our lives as comfortable, scientific development is playing a major role nowadays. Materials science and engineering is establishing the appropriate relationship between atomic structure and physical properties of materials which would design a novel material to attain improved properties [1]. The best performances of most of the components can be achieved in the present scenario by nanocomposites. The combined properties of metallic and ceramic materials compared with monolithic alloys can be achieved by metal matrix composites (MMCs) as it possesses high tensile strength, fatigue resistance, wear resistance and high elastic modulus. Several methods, namely, powder metallurgy (P/M), stir casting, pressure infiltration etc., have been developed for manufacturing of MMCs. In aerospace, space, automotive and structural parts, particulate lightweight aluminum-based nanocrystallite matrix reinforced with nanoparticles have outstanding properties [2] as it has an excellent combination of mechanical and physical properties [3]. Amid all Al alloys, Al 6061 possesses outstanding formability besides its high strength and excellent corrosion resistance [4, 5]. The superior performance of nanocomposites can be obtained by uniform, homogeneous and embedding of nanoparticles over the nanocrystallite matrix [6]. Agglomeration/clustering of very fine/nanoreinforcement particles over metal matrix would deteriorates the mechanical properties [7]. However, it can be avoided by mechanical alloying (MA) which is one of the solid-state powder metallurgy (P/M) process [2]. Further, uniform distribution and embedding of nanoreinforcement over the matrix can be achieved which would improve the mechanical performances of materials. The mechanical alloying is one of the severe plastic deformation (SPD) technique. During mechanical alloying (MA), high strain is given on the material and the structural refinement such as crystallite size reduction, lattice strain increment, changes in dislocation density, lattice parameter variation etc., would occur by shear and fracture of powder phase mixtures. By this process, nanostructured/nanocrystallite materials can be manufactured [2]. Conventional cold uniaxial die compaction process is one of simple and economic one of consolidation of powder materials into bulk-shaped products followed by sintering under controlled atmosphere. Various authors have worked on P/M aluminum-based metal matrix composites reinforced by ceramic particles such as graphite, silicon carbide particulate (SiCp), aluminum oxide (Al_2O_3), titanium carbide (TiC), vanadium carbide (VC), aluminum nitride (AlN), boron carbide (B_4C), silicon nitride (Si_3N_4), titanium boride (TiB_2), aluminum boride (AlB_2), zirconium carbide (ZrC) and magnesium boride (MgB_2) which have been successfully dispersed and investigated via mechanical alloying/mechanical milling. There is no detailed study concerning TiO_2 powders used as a reinforcement in Al-based MMCs. Titania (TiO_2) has outstanding properties, namely, good wear and corrosion resistance, low coefficient of thermal expansion, high thermal shock resistance, excellent catalytic performance and thermal stability at high temperatures [8, 9]. The material selected as AA 6061- TiO_2 particulate MMCs is mainly proposed for automotive and aircraft parts. For instance, it can be suitable for automotive engine pistons and connecting rod, bicycle hub, bike frames, valves and valve parts, brake pistons, hydraulic pistons, marine fittings, electrical fittings, contactors, aircraft fittings and couplings.

2. Synthesis and consolidation procedure of nanocomposites

2.1. Nanocomposite powders preparation

In the present investigation, the AA 6061 Al alloy reinforced with different weight percentage of TiO₂ particulate nanocomposite powders was prepared by MA (high-energy ball milling) method. The AA 6061 Al alloy matrix composition and powder size of each elemental powder used in this study are given in **Table 1**. **Figure 1(a)** and **(c)** shows the morphologies of as-received Al and TiO₂ powder particles, respectively, using secondary electron image (SEI) of scanning electron micrograph (SE-SEM). From **Figure 1(a)** and **(c)**, it can be observed that the Al matrix powder particles were in irregular flake-like shape and TiO₂ particles were in clustered tetragonal shape. **Figure 1(b)** and **(d)** shows the X-ray diffraction patterns of as-received Al and TiO₂ particles, respectively, which indicated the well-crystalline nature of the powders. The as-received TiO₂ particles are in anatase formed and tetragonal structure with average clustered particles size of <1 µm which was measured by laser scattering system technique. The prepared nanocomposites contained 0, 2, 4, 6, 8, 10 and 12 wt.% of TiO₂ powder particles were completely embedded in the soft alloy matrix using the planetary type high-energy ball mill (Insmart systems Ltd., Hyderabad, India) (**Figure 2a**). Nine highly hardened stainless steel balls of 20 mm diameter (33.5 g mass of each ball, totally, 301.5 g) together with 30 g mass of AA 6061_{100-x}–x wt.% TiO₂ (x=0–12 with a step of 2 wt.%) powder mixture under toluene medium as a process control agent (PCA) were poured in a hardened stainless steel vial. The ball-to-powder ratio (BPR) was set approximately 10:1. The plate (i.e., sun wheel) speed of mill was set to 100 rpm (bowl/vial speed, 280 rpm). The milling was carried out in wet medium using toluene (C₆H₅CH₃) of sulfur free (Ranbaxy, India) to prevent undue oxidation, agglomeration of powders, balls and vial with the powder [10]. The composite powders containing the different wt.% of TiO₂ were milled up to 40 h. The milling was carried out up to 20 min and then alternated with 20 min of cooling to avoid significant temperature rise. The

Name of the element(s)	Purity, %	Elements concentration (gravimetric, wt.%)	Powder size, µm (mesh size)
Silicon, Si	99.3	0.600	-45 (<325)
Iron, Fe	99.7	0.700	-75 to +45 (<200 to >325)
Copper, Cu	99.4	0.275	-45 (<325)
Manganese, Mn	99	0.150	-75 to +45 (<200 to >325)
Magnesium, Mg	99.7	1.000	-75 to +45 (<200 to >325)
Chromium, Cr	99.8	0.195	-45 (<325)
Zinc, Zn	99.4	0.250	-45 (<325)
Titanium, Ti	99.3	0.150	-45 (<325)
Aluminum, Al	99.7	Bal	-45 (<325)

Table 1. Chemical composition and powder size used to make AA 6061 Al alloy matrix.

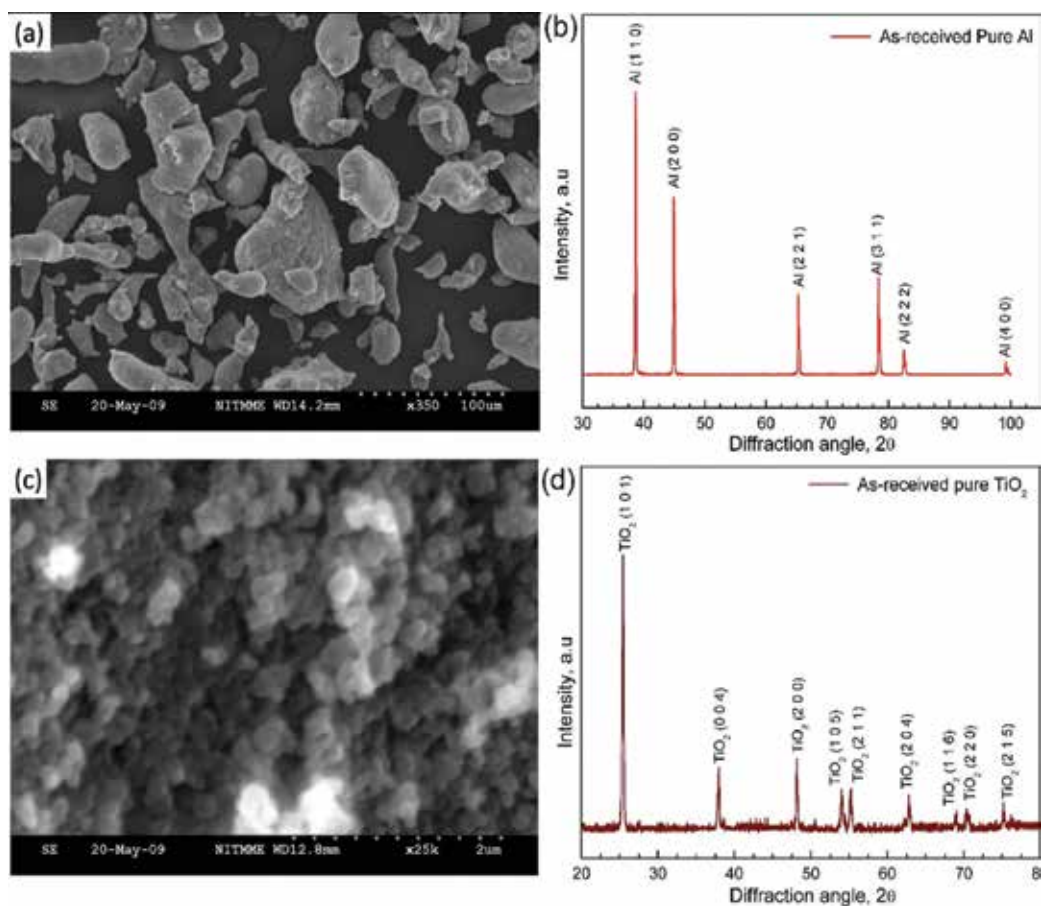


Figure 1. The morphology of as-received powders: (a) Al and (c) TiO₂, XRD patterns of as-received powders: (b) Al and (d) TiO₂.

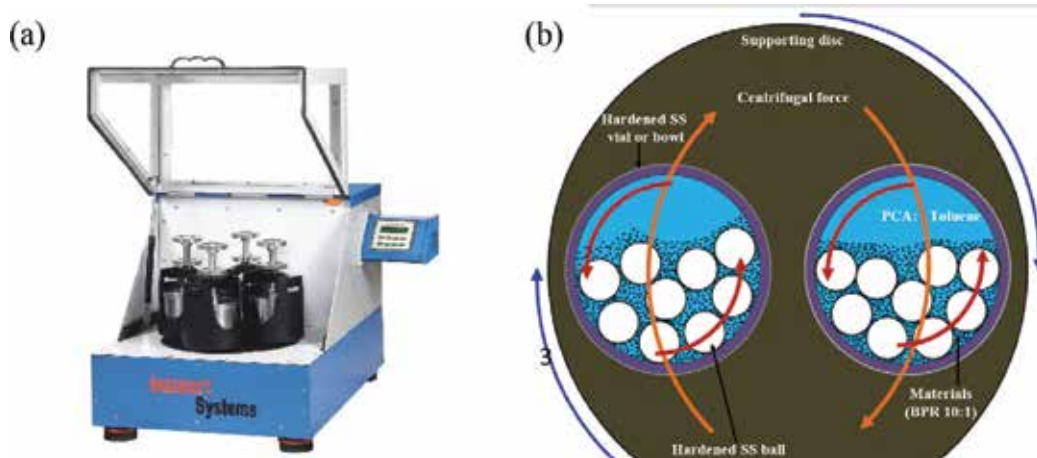


Figure 2. (a) High-energy planetary ball mill and (b) schematic diagram showing the synthesis of nanocomposite powders.

schematic diagram of synthesizing the nanocomposite by high-energy ball milling method is also shown in **Figure 2b**.

2.2. Synthesis of trimodeled composite powders

In order to evaluate the improvement of ductility while maintaining high strength and toughness for nanostructured AA 6061-TiO₂ composite materials, trimodeled AA 6061-TiO₂ nanocomposite powders (three phases consisting of nanocrystallite matrix, nano ceramic and coarse crystallite matrix) were synthesized by the same planetary high-energy ball milling. For instance, first, the nanostructured composite powder of AA 6061-12 wt.% TiO₂ was synthesized by 40 h of MA using the same ball milling parameters mentioned in Section 2.1 (consists of nanocrystallite matrix and nano-TiO₂ ceramic). Then, these nanocomposite powders were mechanically blended with 0, 5, 10, 15, 20, 25 and 30 wt.% coarse grains (CG) elemental powders corresponding to AA 6061 alloy matrix composition in the same planetary ball mill. Here, the BPR of 1:1 at 120 rpm for 2 h was carried out.

2.3. Consolidation of composite powders

A hydraulic press (**Figure 3a**) capacity of 40 tons made by Insmart systems, Hyderabad, India, was used to do uniaxial compaction. The cold uniaxial compaction is an important process in P/M to attain near net shape fabrication of engineering components prior to sintering [11, 12]. First, the precursor powders obtained from high-energy ball milling were cold compacted using conventional cold uniaxial pressing in a rigid double end compaction type with compaction pressure of 500 MPa [13, 14]. The obtained dimensions of compacted samples called green pellets were 10 mm in diameter and 6–7 mm thickness [15]. The die was made of high-carbon high-chromium hardened and tempered steel (inner and outer diameters of 10 and 60 mm), and the two punches (10 mm diameter) were made of the same material as die to consolidate the powders from top to bottom simultaneously. Zinc stearate [Zn (C₁₈H₃₅O₂)₂] was used as lubricant to minimize the friction between powder particles and die wall during compaction process. **Figure 3b** shows the schematic design of the double end compaction die.

For investigating the sintering behavior, the consolidated nanocomposites of AA 6061_{100-x}-x wt.% TiO₂ (x=0, 4, 8 and 12 wt.%) of the green pellets compacted at 500 MPa were degassed first at 350°C for 60 min [16]. Then, the degassed samples were sintered for 120 min in the temperature range of 400, 475, 550 and 625°C under reducing atmosphere [17] in a mechanical pusher furnace as applicable to P/M industries. The schematic diagram of mechanical pusher furnace is shown in **Figure 4**.

2.4. Consolidation of trimodeled composite powders

The synthesized trimodeled AA 6061-12 TiO₂ nanocomposite consisting of 0, 5, 10, 15, 20, 25 and 30 wt.% CG 6061 alloy (obtained from elemental powders by mixing) matrix powders was first dried and stress recovered at 343 K under N₂ atmosphere (mass flow rate of 63/h and dew point temperature of <-40°C) [17]. The stress recovering of trimodeled composite powders was carried out to avoid the unwanted oxide phase at elevated temperature during sintering. These stress recovered powders were then consolidated by cold uniaxial compaction at 500 MPa. The post-compacts were degassed and then sintered at 823 K for 6 h under N₂ atmosphere [17].

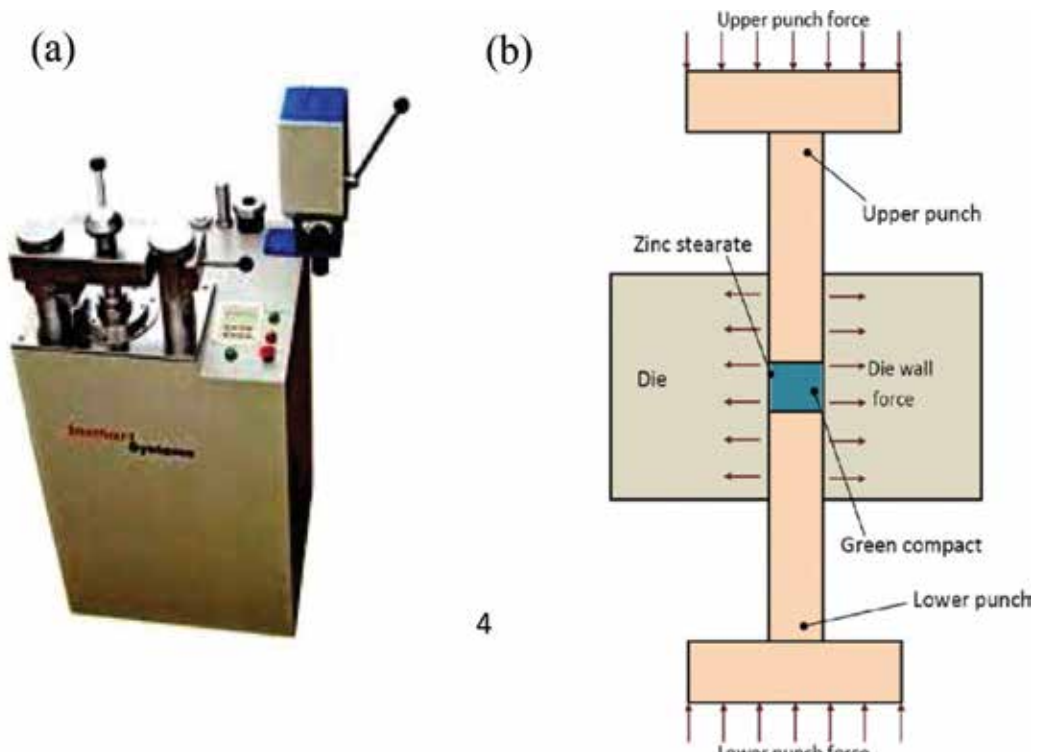


Figure 3. (a) Hydraulic press and (b) schematic diagram of conventional cold uniaxial compaction die process (double end compaction type).

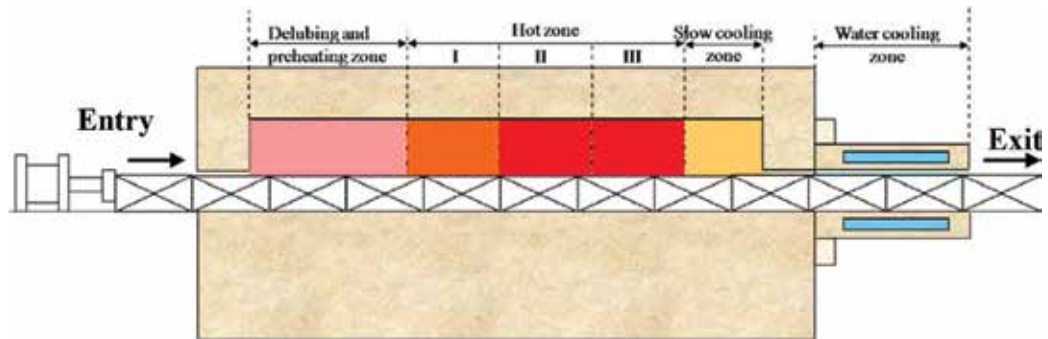


Figure 4. Schematic diagram of mechanical pusher furnace.

3. Structural characterization methods

3.1. Geometric characterization techniques

The transmission electron microscope (TEM) and X-ray diffraction (XRD) can be effectively used for investigating the structural characterization of fine powders, polycrystalline materials, amorphous materials and thin films. These two techniques are the commanding

qualitative characterization techniques used in various areas of materials science [18, 19]. The structural characterization in terms of crystallites size, lattice strain, crystal structure, crystallinity, composition and strain variance can be determined/investigated using these instruments [20]. However, the morphology of powders such as powder shape, size etc., and detailed microstructure of compacted and sintered samples can be studied qualitatively using scanning electron microscope (SEM).

3.2. X-ray diffraction (XRD)

The XRD patterns are used to identify the structure and the different phases present in the materials. The phase constitution of milled powders, post-compacts, post-sintered and post-deformed preforms are evaluated by XRD using CuK α radiation. The used XRD equipment is made by D/MAX ULTIMA III, Rigaku Corporation, Japan, operating at 30 mA and 40 kV. The set 2°/min scanning speed and 20–100° scanning range were used here. It is well known that the average crystallite size and lattice strain or microstrain or lattice distortions owing to the presence of lattice defects which commonly occurred in MA products can be easily measured by XRD peaks of line profile analysis [20]. During MA with respect to milling time and percentage of reinforcements in the matrix, XRD peak broadening occurs which depends upon crystallite size and strain present in the nanocomposites/nanomaterials. Therefore, nanostructured materials/nanocomposites have a large volume of grain boundaries when compared to bulk materials [21]. If a material is not having any strain mean, Scherer's formula can be used to calculate crystallite size (Simplest method) [22]. Williamson–Hall (W–H) [23] and Warren–Averbach (W–A) [24] analyses are other two analytical methods which are generally used to measure the strain and the crystallite size of nanomaterials/nanocomposites. The W–A method is based on Fourier analysis of peak intensities in which Fourier coefficients are used to separate the crystallite size and strain contribution from XRD peak profiles. However, this approach needs peak intensities at high diffraction angles. But, it is difficult to use this method when higher angle reflections are weak [25]. On the other hand, the W–H method is used to investigate the same information at lower diffraction angle. Also, it is easy and suitable for lattice strain and crystallite size calculation of cubic crystals. Therefore, reduction in crystallite size and rise in microstrain can be found out using W–H analysis of Eq. (1).

$$\beta_{hkl} \cos \theta_{hkl} = \left(\frac{K\lambda}{t} \right) + 4\epsilon \sin \theta_{hkl} \quad (1)$$

Here, K is the shape factor of 0.9, λ is the X-ray wavelength of 1.5406 Å, θ_{hkl} is the Bragg angle in degree and t is the effective crystallite size in nm and ϵ is the lattice strain. The X-ray line profile breadth, β_{hkl} , after corrected instrumental broadening as a full width at half-maximum (FWHM), was calculated on each reflection of 2 θ . For constructing a linear plot of $\beta_{hkl} \cos \theta$ against $4 \sin \theta_{hkl}$ for determining crystallite size and lattice strain, X-ray diffraction of first five reflections (1 1 1), (2 0 0), (3 1 1), (2 2 2) and (4 0 0) was used. Then, crystallite size (t) was obtained from the intercept c (i.e., $c = K\lambda/t$) and the strain (ϵ) from the slope (i.e., $m = \epsilon$).

3.3. Scanning electron microscope (SEM)

The milled powder samples were analyzed for powder morphological evaluation by scanning electron microscopy (SEM) using HITACHI S 3000 H operating at 8.5 mA and 20 kV.

Before examining the powder samples in SEM, sputtering was done on the surface of the powders to conduct charge away from the surface. The microstructure of sintered preforms (after polishing and etching) was examined by F E I Quanta FEG 200—high-resolution scanning electron microscope (HR-SEM) with EDAX operating at 30–50 kV. In order to identify and confirm the elements shown in the SEM micrographs, energy dispersion spectrometer (EDS) was used. During analysis, both secondary electron image (SEI) mode and back-scattered electron image (BSEI) mode were operated.

3.4. Transmission electron microscope (TEM)

To measure the matrix crystallite size exactly, and identifying the embedding and distribution of nano level reinforcement in the matrix grain, both dark and bright field image of transmission electron microscope (TEM) can be used. Selected area of diffraction (SAD) patterns is also used to confirm the NC nature of the samples. Here, PHILIPS CM 12 TEM was used with spot EDAX facility. For powder samples, first the ball-milled powder particles were under suspension in ethanol (volatile liquid) and then a drop of this suspension was allowed to dry on a thin carbon foil supported by a conventional microscope grid leaving the powder particles ready for the observation. For sintered solid samples, manual polishing and mechanical grinding were performed until the sample thickness $<100 \text{ }\mu\text{m}$ was achieved. Following mechanical grinding, the samples were then dimpled to sample thickness of approximately $50 \text{ }\mu\text{m}$. Finally, ion milling was carried out on the dimpled samples using an ion miller of Edwards Model E306A.

4. Mechanical testing methods

4.1. Density measurement

The density of the post-compacts and sintered preforms was estimated precisely by Archimedes principle [26] using electronic density balance. This principle is based on first measuring weight of sample in air column and then weighed in water column. Then, the ratio of weight of sample in air column and apparent loss of weight (difference between weight of air column and water column) give the specific gravity (SG) of post-compacts/sintered preforms. Lastly, the density of post-compact/sintered density can be determined by multiplying the SG and density of water. Here, paraffin treatment was performed over the samples to avoid infiltration of water into the sample [27]. The calculated error in the density treatment was conformed within 1%. Three independent experimental readings were used and averaged for investigation. In addition, theoretical density of sintered composites with different percentage of reinforcements was determined using the rule of mixture.

4.2. Hardness measurement

Mechanical properties in terms of strength can be analyzed using hardness measurements. The hardness of sintered preforms was measured using PC-based Ratnakar Vickers tester. Here, the hardness was tested at a load of 1 kg. At least 15 measurements were taken

in various places of polished samples for each sample. Then the average was taken for investigation.

4.3. Simple compression test

The uniaxial simple compression test [28] was done using servo-controlled universal testing machine with strain rate of 10^{-3} s^{-1} at room temperature to determine the maximum compressive strength. For compression test, the sample size of 5 mm×5 mm×10 mm was used as per ASTM standard [29]. The samples were cut from sintered one by wire-cut electrical discharge machine; then polished by abrasive sheet of SiC paper to 1200 grit; further graphite lubricant was applied at the top and bottom surface of samples to minimize friction effect. Here, three samples were used in each composition, and the average was used for the interpretation.

5. Results and discussion

5.1. Morphology of nanocomposite powders as function reinforcement

The main purpose of studying the powder surface morphological examination is to investigate the powder particle shape changes while manufacturing of AA 6061_{100-x}-x wt.% TiO₂, x=0, 2, 4, 6, 8, 10 and 12 wt.% particulate nanocomposite powders produced by MA. The homogeneous distribution of reinforcement particles over the nanocrystallite matrix, embedding of reinforcement particles inside the nanocrystallite matrix, presence of any agglomeration or clustering of reinforcement particles with the nanocrystallite matrix, powder particles shape and particle size can be investigated through the ball-milled powder particles as it influences the mechanical properties. The powder morphology can be evaluated qualitatively by secondary electron image (SEI) of SEM and back-scattered electron image (BSEI) of SEM. **Figure 5** shows the influence of reinforcement addition in the nanocrystallite matrix powders after 40-h MA. It can be clearly seen from **Figure 5** that the size of the particle/agglomerate decreased with the function of reinforcement considerably. However, almost spherical-shaped and equiaxed particles were obtained in all the system with the same milling condition (40 h). These results implied the attainment of equilibrium state [30–32] after 40-h MA. The morphological results showed that the addition of TiO₂ particles in the matrix produced the powder morphology size reduction of matrix steadily. This was attributed to TiO₂ ceramic particles also acted as milling agent. Further, it was observed here that the embedding and dispersing of nano-sized TiO₂ particles of around 119 nm with the soft Al alloy matrix powder for AA 6061-12 wt.% TiO₂ nanocomposite (**Figure 5h**). The morphological results showed that the addition of TiO₂ particles favors to refining of matrix particles during MA. On the other hand, despite the ductile nature of the Al matrix, the formation of large agglomerate size (**Figure 5a**) was diminished with the presence of TiO₂ particles. This is due to the fact that the increasing percentage of TiO₂ particles in the soft matrix decreases the ductility so as to increase the amount fracture in the matrix particles before impacts of matrix particles that cause lamination. These results inferred here that more amount of work hardening occurred in higher amount of reinforcement. The decreasing of particle/agglomerate size of the matrix with carrying reinforcement was also observed by several

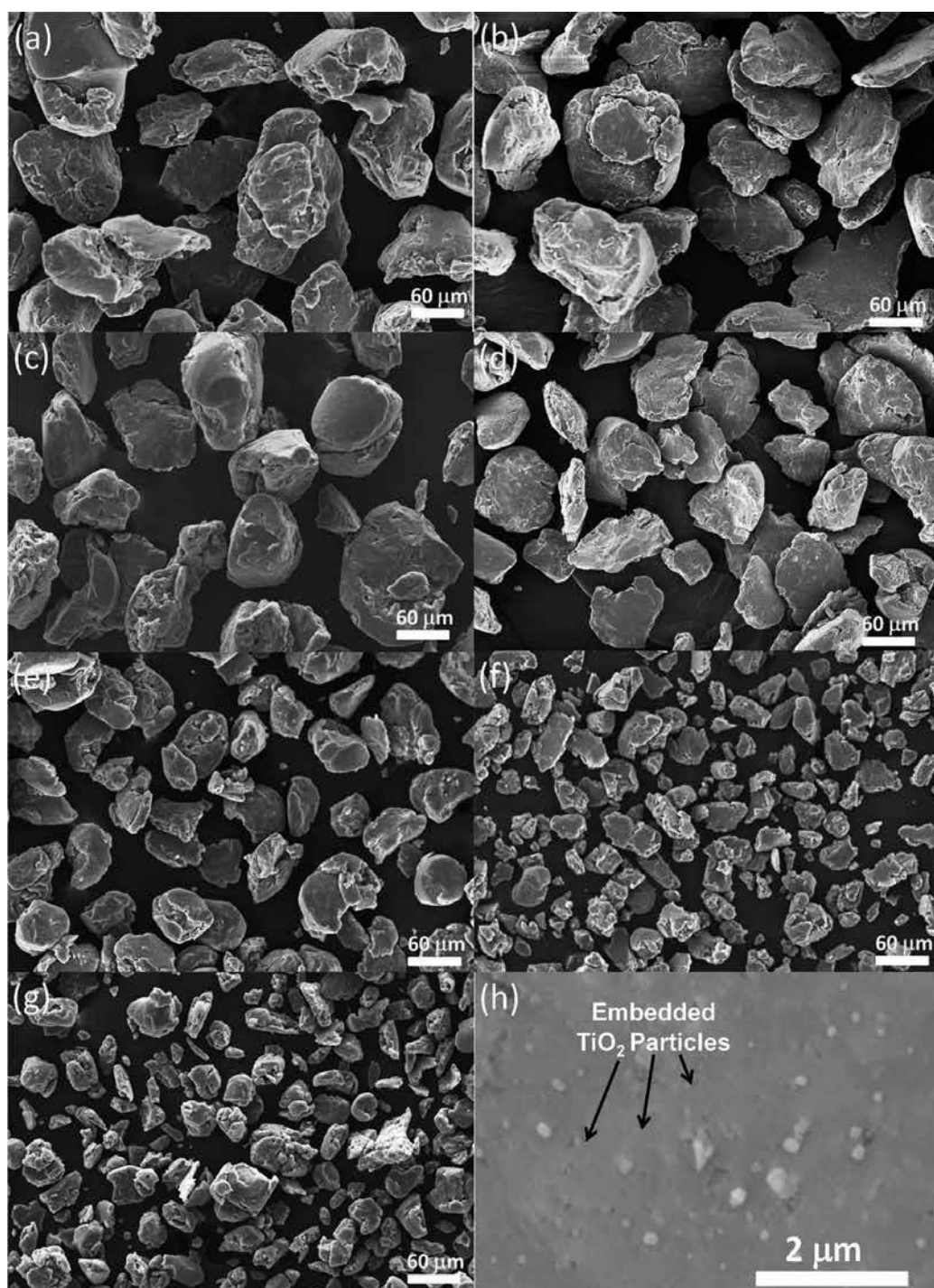


Figure 5. The morphology of AA 6061_{100-x}-x wt.% TiO₂ nanocrystallite/nanocomposite powder after 40-h MA: (a) 0%, (b) 2%, (c) 4%, (d) 6%, (e) 8%, (f) 10%, (g) 12% and (h) BSEI of magnified view of (g) shows the embedding of TiO₂ particles on the matrix.

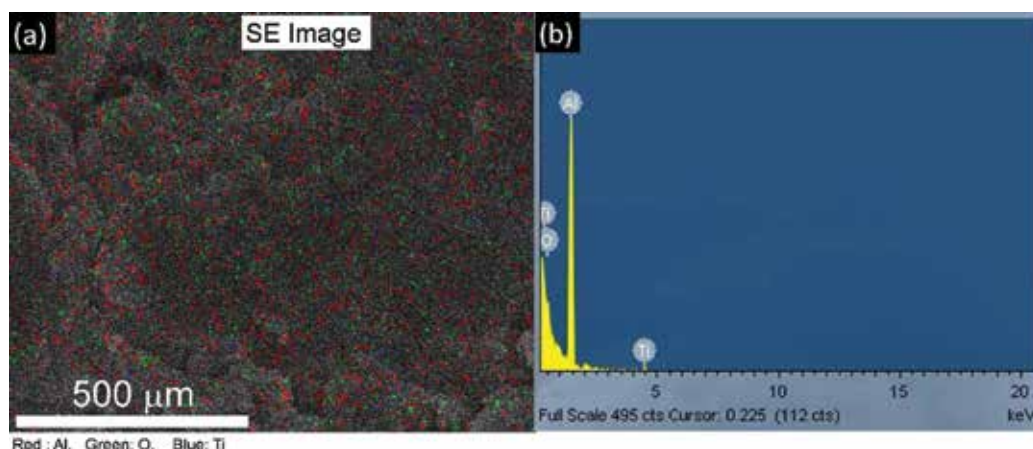


Figure 6. (a) EDAX mapping of AA 6061-10 wt.% TiO₂ nanocomposite powder after 40-h MA, red, green and blue indicates Al, O and Ti elements, respectively and (b) the corresponding EDAX spectrum.

researchers related to Al-based MMCs processed via MA/MM [33–36]. **Figure 6** shows the X-ray mapping of 40-h powders which confirms the uniform TiO₂ particles within the Al matrix (Red: Al, Green: O and Blue: Ti).

5.2. Effect of percentage of reinforcement on powder morphology of nanocomposite powders

Figure 7 shows the influences of the addition of TiO₂ ceramic particles on nanocrystallite AA 6061 matrix particles size. It was observed here that the intensity of fracture mechanism increased and dominated the soft ductile matrix particle-particle cold welding as the percentage of TiO₂ ceramic particles increased in the soft Al alloy matrix. These resulted the formation of very fine particles/agglomerates in the case of 12 wt.% TiO₂-reinforced nanocomposites (**Figures 5g** and **7**) when compared to unreinforced nanocrystallite alloy powder (**Figures 5a** and **7**) during the same milling condition (40 h). The increasing of hard ceramic particles would accelerate the fracturing process which was also reported elsewhere [37]. It was attributed to importing more collisions on matrix powders which meant high-velocity energy acted over the matrix powders. Thus, it was clear here that the tendency for fracturing was higher than the cold welding for longer milling time of 40 h. In general, after reaching the steady state of longer milling (40 h here) under wet milling, particle-particle cold welding on soft ductile alloy matrix would occur. Consequently, the particle/agglomerate size would start to increase (**Figure 5a**) when compared to un-milled matrix powder (**Figure 1a**). This was attributed to higher cold welding tendency overcoming the fracture process [38]. However, almost equiaxed with spherical-shaped and refined microstructure were obtained. Further, the rate of soft alloy matrix particle-particle getting cold-welded started to decrease as the percentage of TiO₂ ceramic particles increased. This was attributed to more domination of fracturing tendency of TiO₂ particles. Therefore, the powder/agglomerate size started to decrease in the case of higher reinforced nanocomposites (AA 6061-12 wt.% TiO₂, **Figures 5g** and **7**). Similar kind of results was observed by Fogagnolo et al. 2003 [39] during ball milling

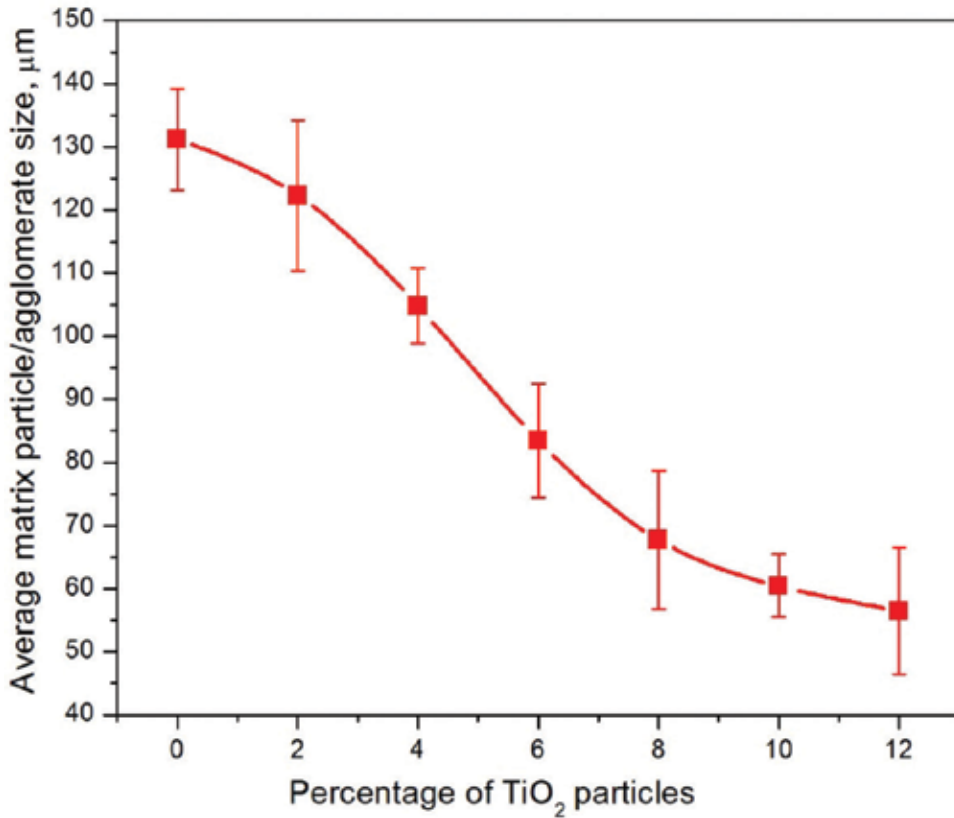


Figure 7. Influences of TiO₂ ceramic particles on nanocrystallite AA 6061 matrix particles/agglomerate size after 40-h MA.

of Al-AlN system. Also, it can be explained in another way that the strength increased as the percentage of reinforcement particles increased according to Orowan strengthening mechanism.

The particle size of reinforcement phase decreased in which the clustered average particle size of TiO₂ of around 1 μm (**Figure 1c**) was reduced to individual TiO₂ particles of 119 nm (**Figure 5h**). The TiO₂ particle size after 40-h MA of AA 6061-12 wt.% TiO₂ nanocomposite powders was checked using bright and dark field image of transmission electron microscope (TEM) (**Figure 8**). Using several bright and dark field images of TEM, the average TiO₂ particle size of around 120 nm was obtained (50 particles were counted), which coherent with the results obtained from back-scattered electron image of SEM morphology. The pink color arrow head indicates the TiO₂ particles. Hence, the result of the higher percentage of TiO₂ phase in the soft matrix produced smaller particle/agglomerate size of the nanocomposite powders (40-h milling) (**Figure 5g**) [39–41]. The addition of TiO₂ powder particles had great influence on the morphological characteristics of the fabricated nanocomposite powders via MA.

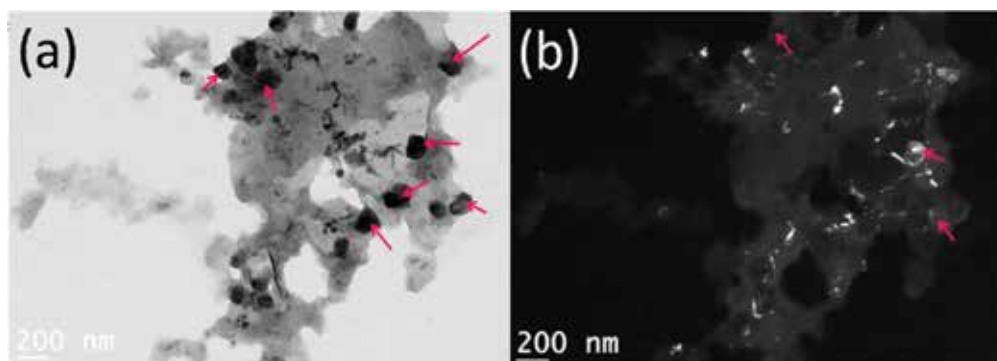


Figure 8. TEM image of AA 6061-12 wt.% TiO₂ nanocomposite powder: (a) bright field image and (b) dark field image.

5.3. Structural evaluation of mechanically alloyed nanocomposite powders

The process of manufacturing of MMCs powders through MA causes morphological and structural changes. Severe plastic deformation of the powder particles during MA can lead to grain refining, variation in the crystallite size, accumulation of internal stress, density of dislocation and variation of the lattice parameter [42]. The objective of this study is to report the structural characteristics of MAed powders (40 h) as the function of reinforcement (0, 2, 4, 6, 8, 10 and 12 wt.% TiO₂) using XRD, TEM and EDS.

5.3.1. XRD analysis

Figure 9 shows the XRD patterns of Al 6061- x wt.% TiO₂, ($x=0, 2, 4, 6, 8, 10$ and 12 wt.%) nanocomposites powders after 40-h MA. This figure clearly shows that the Al peak width, for example, at (1 1 1) plane, increased with the percentage of reinforcement. This was due to which TiO₂ particles were also acting as a milling agent which accelerated the milling process. The inset of **Figure 9** shows that the case of 12 wt.% TiO₂ nanocomposite powders more broadened Al peak at (1 1 1) plane occurred than unreinforced nanocrystallite powders. It indicates that more spatial coherent length confinement occurred in higher reinforced nanocomposite [43]. Also, it can be noted from the inset of **Figure 9** that shifting of Bragg's angle occurred in the case of 12 wt.% TiO₂ particulate nanocomposite powders. These results show that more distortion occurred in higher reinforced nanocomposite powder than unreinforced nanocrystallite powder during the same milling time. Further, the shifting of Bragg's angle indicates the changes in the lattice parameter value with respect to percentage of reinforcement during 40-h MA. The increasing of peak broadening of matrix phase by the addition of reinforcement ceramic phase can be clearly seen from **Figure 10**. The structural characteristics such as crystallite size, lattice microstrain, dislocation density, lattice parameter and the unit cell volume of Al as the function of reinforcement after 40-h milling are reported in **Table 2**. Owing to the characteristics of high-energy ball milling, large amount of structural defects in terms of dislocations would occur due to severe plastic deformation [44]. Severe plastic deformation (SPD) of high-energy milling brings about a deformed lattice with high dislocation density during early stage of milling. These indicate the amount of dislocations pile up near the GBs

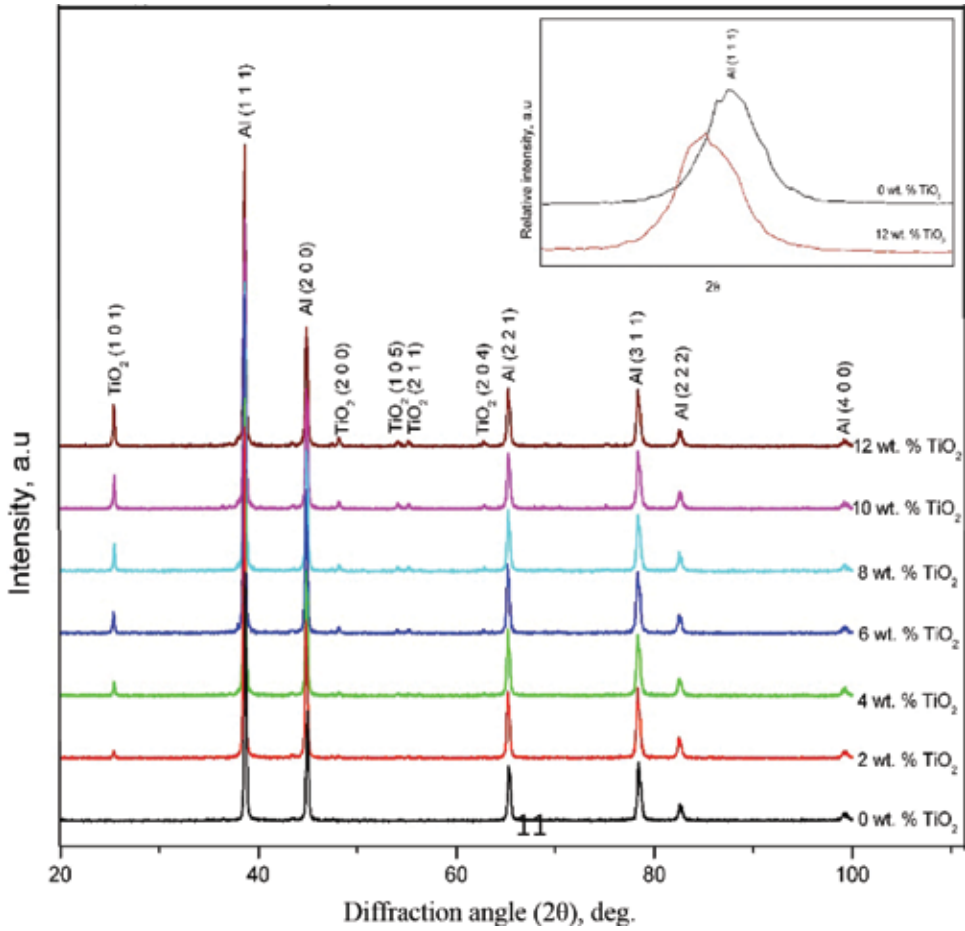


Figure 9. XRD patterns of AA 6061_{100-x}-x wt.% TiO₂ (x=0, 2, 4, 6, 8, 10 and 12%) nanocrystallite/nanocomposite powder after 40 h of high-energy ball milling. Inset shows shift in Bragg's angle.

will be increased. When prolonged milling, sometimes the GBs might have turned to be soft or relaxed. On this time, the amount of dislocations pileup near the GBs will be decreased. Hence, for MAed powders, dislocations are the main defects of which dislocation density (ρ_D) can be determined as [45]:

$$\rho_D = 2\sqrt{3} \frac{\langle \varepsilon_{r.m.s} \rangle}{tb}, \quad (2)$$

where $\langle \varepsilon_{r.m.s} \rangle$ is RMS lattice strain which is determined as:

$$\langle \varepsilon_{r.m.s} \rangle = \left(\frac{2}{\pi} \right)^{1/2} \left(\frac{\Delta d}{d_{0(hkl)}} \right), \quad (3)$$

$\Delta d = d_{(hkl)} - d_{0(hkl)}$, where $d_{(hkl)}$ and $d_{0(hkl)}$ are the calculated and observed interplanar spacing, t is the crystallite size in m and b is the burgers vector of dislocation in m which is equal to $a/\sqrt{2}$ for the FCC structure, a is the lattice parameter in m . The actual lattice parameter was

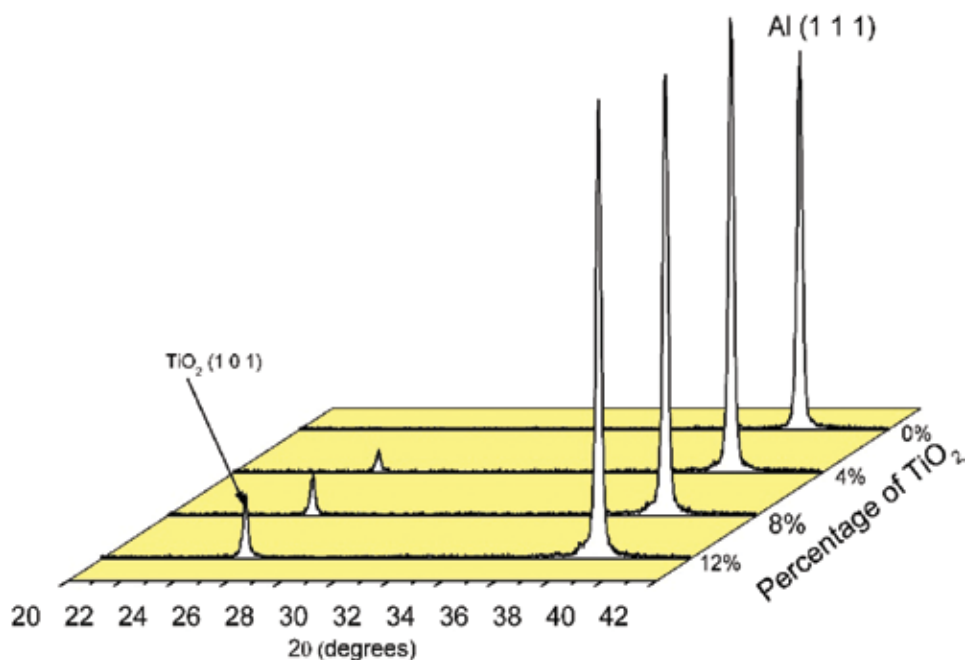


Figure 10. XRD patterns of AA 6061_{100-x}–x wt.% TiO₂, x=0, 4, 8, and 12%, composite powder after 40 h of high-energy ball milling.

Composition	Grain size (<i>t</i>), nm	Lattice strain (<i>e</i>), %	r.m.s. strain ($\times 10^{-3}$)	Dislocation density (ρ) $\times 10^{14}$, m ⁻²	Lattice parameter (<i>a</i>), Å	Unit cell volume (<i>V</i>), Å ³	Volume fraction of TiO ₂
6061 AA	65±2.50	0.3254±0.0031	2.5961	4.8476±0.0025	4.0473±0.00020	66.297±0.0098	0
6061 AA+2% TiO ₂	60.5±1.85	0.1640±0.0018	1.3082	2.6150±0.0015	4.0471±0.00015	66.287±0.0042	0.01793
6061 AA+4% TiO ₂	58±5.00	0.1906±0.0024	1.5214	3.1988±0.0078	4.0471±0.00015	66.287±0.0074	0.03588
6061 AA+6% TiO ₂	53±3.2	0.1490±0.0020	1.1893	2.5629±0.0032	4.0470±0.00018	66.2973±0.0035	0.04937
6061 AA+8% TiO ₂	50±4.60	0.2231±0.0017	1.7805	4.3651±0.0034	4.0469±0.00020	66.286±0.0045	0.06587
6061 AA+10% TiO ₂	48.7±2.5	0.2165±0.0016	1.7276	4.2637±0.0021	4.0469±0.00024	66.286±0.0022	0.07896
6061 AA+12% TiO ₂	46±2.00	0.1993±0.0023	1.5903	3.9407±0.0019	4.0468±0.00015	66.272±0.0031	0.09862

Table 2. Structural characterization of AA 6061_{100-x}–x wt.% TiO₂ composite powder after 40-h milling, x = 0, 2, 4, 6, 8, 10 and 12%.

obtained as described by Cullity [22], by constructing the linear plot between the calculated lattice parameter for each Bragg's angle and the corresponding value of $\cos^2\theta/\sin\theta$.

5.3.2. TEM analysis

The TEM micrographs of AA 6061_{100-x}–x wt.% TiO₂ (x=0, 4, 8 and 12 wt.%) nanocomposite powder is shown in **Figure 11a–l**. The matrix crystallite size was calculated based on several bright and dark field images (**Figure 11**), and minimum of more than 200 grains was counted

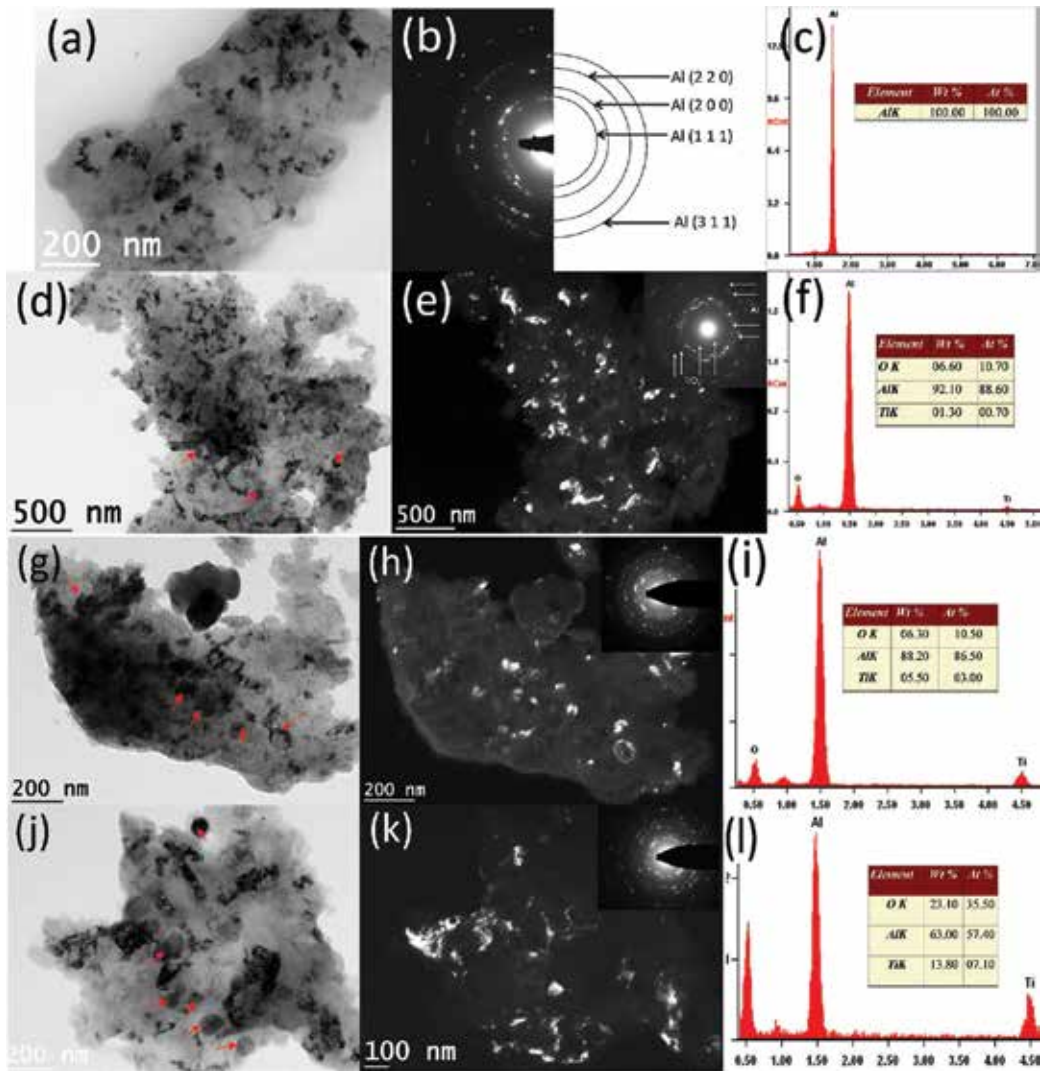


Figure 11. TEM micrographs of as-milled nanocomposite powders: (a) bright field image (BFI) of 0% TiO₂, (b) SAD pattern of 0% TiO₂, (c) EDAX analysis of 0% TiO₂, (d) BFI of 4% TiO₂, (e) dark field image (DFI) of 4% TiO₂ (inset shows the SAD), (f) EDAX analysis of 4% TiO₂, (g) BFI of 8% TiO₂, (h) DFI of 8% TiO₂ (inset shows the SAD), (i) EDAX analysis of 8% TiO₂, (j) BFI of 12% TiO₂, (k) DFI of 12% TiO₂ (inset shows the SAD) and (l) EDAX analysis of 12% TiO₂. Note: single arrow represents TiO₂ particle.

for each composition to get the average grain size. The calculated matrix crystallite size for 0, 4, 8 and 12 wt.% TiO₂ nanocomposite powders were to be around 69, 63, 54 and 49 nm, respectively. From the selected area of diffraction (SAD), the continuous sharp ring pattern was observed in all the system which confirmed the nanocrystalline nature of the Al matrix in as-milled (MA, 40 h) condition [34]. Single arrow in the bright field images of **Figure 11** indicates the TiO₂ particle embedded in the matrix. Further, the corresponding EDAX analysis was also performed and tabulated in the respective figures. The presence and embedding

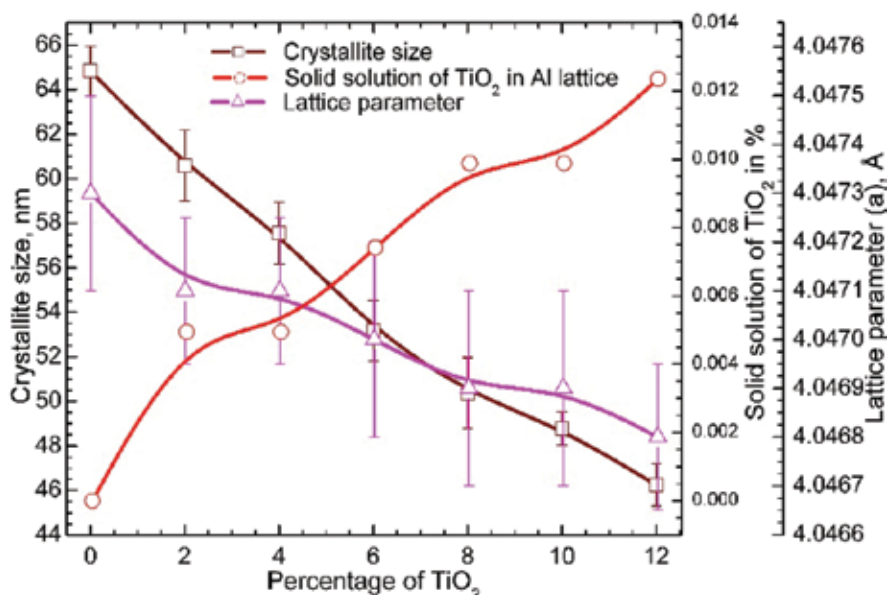


Figure 12. Variation in crystallite size, lattice parameter and solid solution of TiO₂ for AA 6061_{100-x}-x wt.% TiO₂ (x=0, 2, 4, 6, 8, 10 and 12 wt.%) nanocomposite powder as a function of reinforcement.

of TiO₂ particles in the matrix were confirmed by EDAX spectrum in which the TiO₂ spectrum was observed to increase with percentage of reinforcement.

5.3.3. Effect of percentage of reinforcement on structural changes

The XRD results from **Figure 10** corroborate that an increase in the amount of TiO₂ in the soft matrix results in a finer crystallite size. The crystallite size variation with percentage of reinforcement is shown in **Figure 12**. The crystallite size of soft matrix was around 65, 60, 57, 53, 50, 48 and 46 nm for 0, 2, 4, 6, 8, 10 and 12 wt.% of TiO₂ particulate composite powder, respectively, after 40-h MA. As the weight percentage of hard TiO₂ content increased, the ductility of the alloy matrix particles decreased, resulting in the dominance of fragmentation which led to a finer grain size in the case of higher TiO₂ content. The estimated lattice parameter (**Table 2** and **Figure 12**) of Al matrix for all reinforced nanocomposite powder was a lower value than the lattice parameter of pure FCC-Al at room temperature (4.0496 Å). This indicates that distortions occurred in the Al lattice and decreasing of lattice parameter with percentage of reinforcement meaning that ceramic phase addition influenced the lattice parameter considerably [46]. The decreased lattice parameter with percentage of reinforcement was due to the balancing between the dissolution of Ti and O atoms in which O atoms dissolution dominated at the higher reinforcement particulate composite powders. Because, the atomic radius of O atom is lower than the atomic radius of Al atom and the atomic radius of Ti atom is higher than Al. Therefore, the O atom can easily dissolve in the Al lattice which decreased the lattice parameter. However, numerically, the deviation of lattice parameter value with percentage of reinforcement was very little. This can be checked by calculating

the percentage of solid solution of TiO_2 particles from XRD results. The percentage of solid solution of TiO_2 increased with the percentage of reinforcement. Numerically, this value is equivalent to zero.

5.4. Sintering behavior of nanocomposites

The excellent mechanical properties can be expected from P/M processed composites when the second phase particles (here TiO_2 ceramic particles) is homogeneously distributed in the matrix. Generally, in conventional metal matrix composites (MMCs), matrix-to-reinforcement particle size ratio would affect the mechanical performances of MMCs. If matrix-to-particle size ratio is greater than unity mean, clustering/agglomeration of reinforcement particles over the matrix would occur which decrease the mechanical properties. This is owing to the fact that reinforcement clusters/agglomerates cannot transfer tensile and shear stresses as it form interparticulate boundaries that act cracks [46]. Therefore, the main objectives of the present section are to investigate whether there is any effect on matrix-to-reinforcement particle size ratio (here, all the samples are greater than unity) as here the reinforcement particles size is around 119 nm, percentage of reinforcement and grain refinement on hardness and densification behavior of nanocomposites.

5.4.1. Influence of reinforcement content on sintering of nanocomposites

Figure 13a shows the densification in terms of percentage of theoretical density of nanocomposite sintered over the temperature range 400–625°C with a step size of 75°C. The percentage of theoretical density sintered nanocomposite at 400°C was 80.25, 81.50, 83.00 and 84.50% for 0, 4, 8 and 12 wt.% TiO_2 particles, respectively, which varied from 80 to 84%. It is interesting to note that the percentage of theoretical density was increased from 80% (unreinforced NC/UFG alloy) to 84% (12 wt.% reinforced nanocomposite) with the function of reinforcement. The increasing percentage of theoretical density with the function of reinforcement was attributed to abrupt changes in the powders morphology size reduction. The observed rate of increased percentage theoretical density was marginally greater up to 4% TiO_2 and then, it increased considerably up to 12 wt.% TiO_2 . This was attributed to a powder matrix particle size reduction, uniform distribution and complete embedded/dispersed TiO_2 particles on the soft alloy matrix. The sintering response with function of reinforcement and function of temperature can be evaluated by a contour graph which is shown in **Figure 13b**. From **Figure 13b**, the percentage of theoretical density curves increased steadily first over both the percentage of reinforcement and sintering temperature up to 500°C. Beyond the sintering temperature of 550°C, irrespective of the reinforcement, the percentage of theoretical density increased slightly. One can notice that the percentage of theoretical density increased with the function of reinforcement. The highest percentage of theoretical density can be achieved when the percentage of reinforcement is >10 wt.% between the temperature range from 500 to 550°C. The highest percentage of theoretical density achieved on this region was attributed to powder morphology size reduction and homogeneous with embedded nano-sized Titania particles in the matrix [47]. Further, at the lower value of percentage of reinforcement (<2 wt.%), the percentage of theoretical density can be achieved only around 80%. This worsened sintering

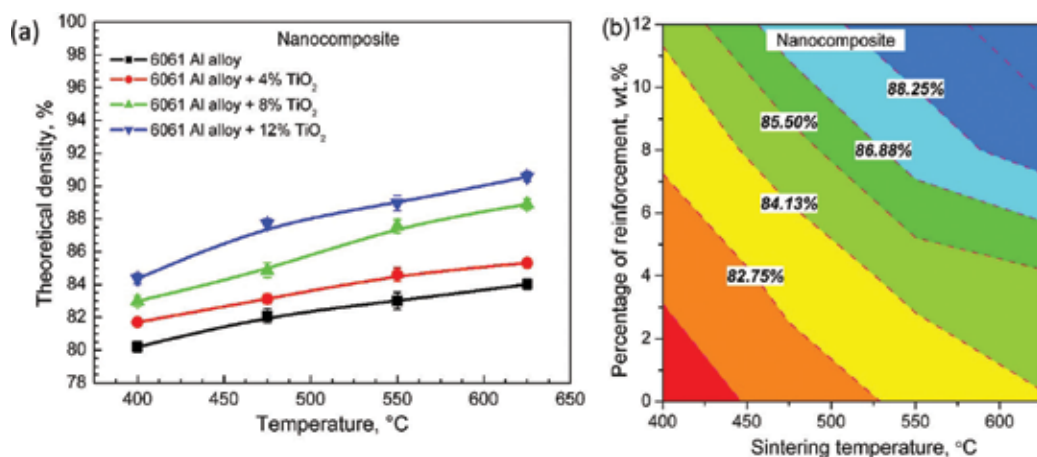


Figure 13. (a) Densification of AA 6061_{100-x}-x wt.% of TiO₂, x=0, 4, 8 and 12 wt.% nanocomposites, (b) contour graph of sintering behavior in terms of % theoretical density.

behavior was attributed to very large agglomerate size with almost spherical morphology of the matrix after 40-h milling (**Figure 5a**).

5.4.2. Structural evolution of sintered nanocomposites

The XRD patterns of 0, 4, 8 and 12 wt.% reinforced particulate nanocomposite sintered at 550°C for 2 h are shown in **Figure 14**. The observed phases are mainly α -Al and TiO₂. The crystallite size of α -Al phase for these sintered nanocomposites was calculated by standard Williamson Hall analysis. The calculated crystallite size after sintering at 550°C is 308, 265, 238 and 205 nm for 0, 4, 8 and 12 wt.% reinforced nanocomposite, respectively. The measured crystallite sizes were in ultrafine level. To confirm the crystallite size in ultrafine level, AA 6061–12 wt.% TiO₂ sintered at 550°C sample was examined using TEM analysis. **Figure 15a** shows the bright field image of 12 wt.% reinforced nanocomposite. From **Figure 15a**, the observed crystallite size of α -Al matrix was almost equiaxed. Further, nanometer-sized Titania particles were uniformly distributed and embedded in the α -Al matrix. **Figure 15b** shows the corresponding selected area of diffraction (SAD) patterns which produced a ring pattern. These results confirmed that the individual grains of α -Al matrix were separated by high-angle grain boundaries and have a random orientation with neighboring grains. Also, the SAD ring pattern reveals that α -Al grains are in ultra-fine level. Further, the average grain size of the α -Al matrix is found to be around 225±15 nm based on 250 grains counted from the bright field images of TEM microstructure.

Figure 16a shows the crystallite size of AA 6061_{100-x}-x wt.% TiO₂ (x=0, 4, 8 and 12%) nanocomposites in as-milled and as-sintered at 550°C. Metal matrix composites are all immiscible systems in which the diffusion (migration of atoms) of one kind into the other is usually restricted because crystallite growth would occur based on diffusion. Therefore, MMCs, in such immiscible systems very small crystal growth is expected on heating [48]. This is

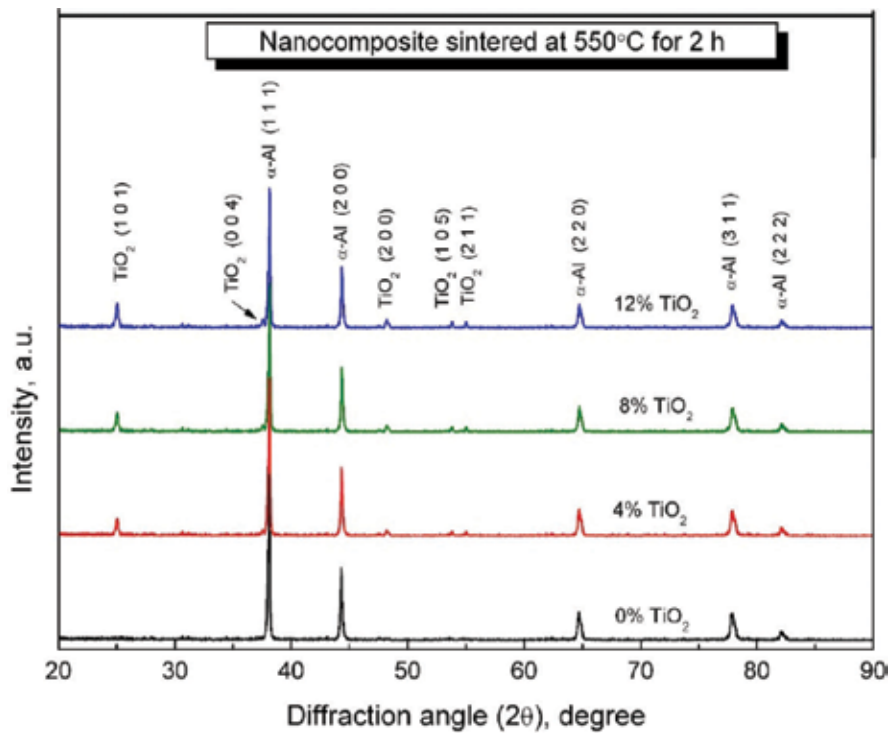


Figure 14. XRD patterns of AA 6061_{100x-x} wt.% TiO₂, x=0, 4, 8 and 12 wt.% nanocomposite sintered at 550 °C for 2 h.

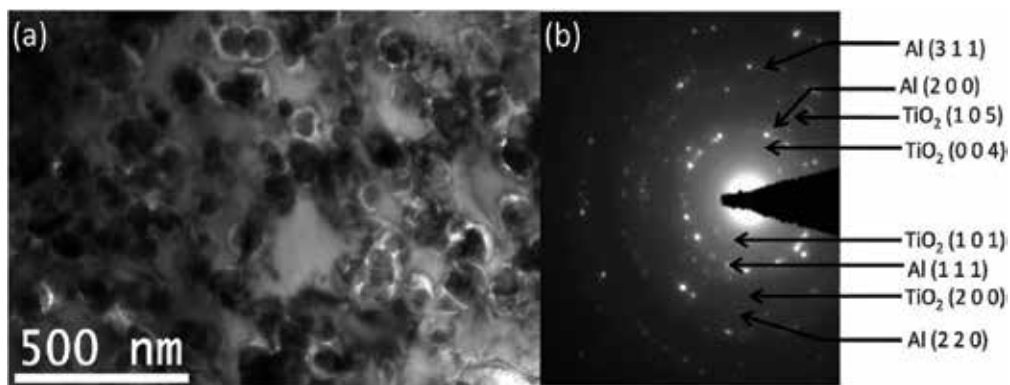


Figure 15. (a) TEM bright field image of AA 6061-12 wt.% TiO₂ nanocomposite sintered at 550°C; (b) the corresponding SAD ring pattern indicating *UFG* nature of matrix.

clearly evident from **Figure 16a**, wherein the growth of crystallite size of α -Al was restricted significantly after sintering at 550°C for higher percentage of reinforcement. It is to be noted here that an increase in the TiO₂ content of the nanocomposites, the nano-sized Titania (~119 nm) particles pinned the matrix grain boundary and prevented the grain growth dur-

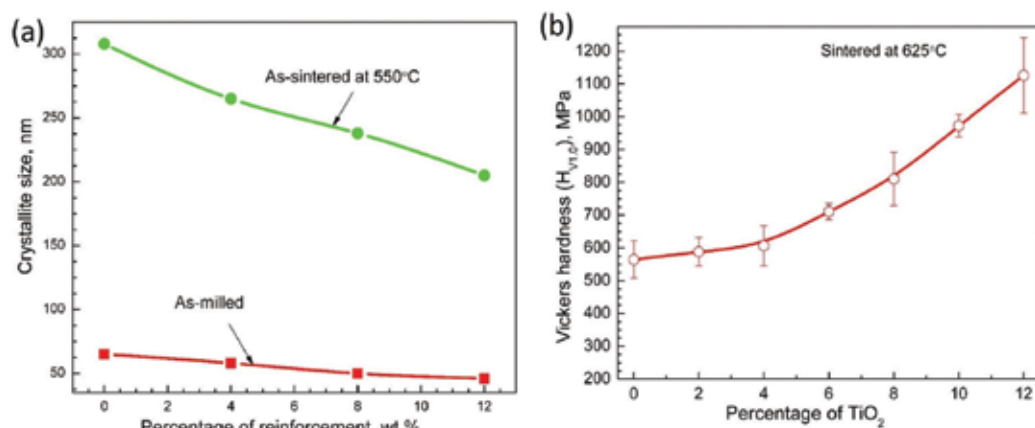


Figure 16. (a) Crystallite size as function of reinforcement in as-milled and as-sintered at 550°C condition and (b) effect of composition on Vickers hardness of AA 6061_{100-x} wt.% TiO₂ (x=0, 2, 4, 6, 8, 10 and 12) bulk micro and nanocomposites (sintered at 625°C).

ing sintering. An increase in the TiO₂ content reduced the probability of Al-Al contacts and increased the probability of Al-TiO₂ interfaces and hence reduced their tendency for crystallite growth due to the immiscible nature of the soft Al alloy matrix with hard TiO₂ particles [49].

5.4.3. Influence of reinforcement content on hardness of sintered nanocomposites

The measured Vickers hardness values as function of sintering temperature is given in **Table 3**. From **Table 3**, it was observed that the Vickers hardness values increased steadily first up to 4% TiO₂ and then increased abruptly as the percentage of reinforcement increased after 40-h milling. The highest value of hardness for AA 6061-12 wt.% TiO₂ nanocomposites was obtained after sintering at 625°C. This was attributed to crystallite refinement occurred in the structure, very fine particle size of matrix and embedding of larger quantity of TiO₂ particles in the matrix [46]. **Figure 16b** shows the variation in hardness of the nanocomposites sintered at 625°C as a function of percentage of TiO₂ particles. The hardness varied from 564 to 1126 MPa to the corresponding increase of TiO₂ content. This higher value was attributed to their finer grain size and the presence of nano-sized TiO₂ particles as dispersoid in the matrix and embedded in the soft matrix. Very high hardness value was obtained at higher reinforcement [46], which was due to very fine particle size distribution, crystallite refinement, highly embedded TiO₂ ceramic particles in the matrix and improved dislocation density at the grain boundary. The hardness of AA 6061-12 wt.% TiO₂ nanocomposites was 1.41–2.11 times higher than that of unreinforced AA 6061 unreinforced alloy. For instance, the observed size of the hardness indentation for 0, 4, 8 and 12 wt.% TiO₂ nanocomposite sintered at 550°C was around 0.185, 0.179, 0.161 and 0.146 μ m, respectively. The matrix crystallite sizes based on peak profile analyses were 308, 265, 238 and 205 nm (**Figure 14**) for 0, 4, 8 and 12 wt.% TiO₂ nanocomposite, respec-

Composition	Vickers hardness, $H_{V1.0}$ (MPa) (function of sintering temperature)			
	400°C	475°C	550°C	625°C
6061 Al alloy	488.14±35.6	497.91±50.5	540.78±54.8	564.60±57.2
6061 Al alloy+2% TiO ₂	506.24±42.3	525.82±32.8	561.18±24.9	588.36±43.7
6061 Al alloy+4% TiO ₂	533.22±53.9	548.77±54.7	576.93±57.9	606.35±60.8
6061 Al alloy+6% TiO ₂	570.15±52.4	602.48±37.2	645.31±46.7	710.80±24.6
6061 Al alloy+8% TiO ₂	608.73±62.4	648.66±65	712.54±72.0	810.47±81.5
6061 Al alloy+10% TiO ₂	621.35±42.8	724.89±27.5	790.35±53.7	972.64±34.3
6061 Al alloy+12% TiO ₂	628.90±63.9	793.10±81	866.09±86.9	1126.12±115

Table 3. Vickers hardness as a function of sintering temperature.

tively. These results indicated that as the crystallite size decreases, the hardness impression was also decreases steadily due to more refinement occurs in the structure with the reinforcement content in the same milling condition. It can be concluded here that there was no possibility of clusters/agglomerates formation in these nanocomposites; the matrix-to-reinforcement particle size ratio was insignificant in Vickers hardness. To conform this one, the back-scattered electron images (BSEI) of 2, 6 and 8 wt.% TiO₂-reinforced particulate sintered nanocomposite at 550°C is shown in **Figure 17a–f**. In this, left side of **Figure 17a, c and e** shows the microstructure of sintered preform at low-magnification (400 ×) value. The corresponding magnified view is shown on right side of **Figure 17b, d and f** for 2, 6 and 8 wt.% reinforced composite, respectively. Even at high magnification itself in all preforms, there was no clustering observed in the present manufactured nanocomposite. In **Figure 17**, double arrow represents the distribution of reinforcement particles on the matrix. Hence, better mechanical properties can be expected in the case of nanocomposite which meant the effect of matrix-to-reinforcement particle size ratio on the present nanocomposites was almost nil.

5.5. Mechanical behavior of nanocomposites

5.5.1. Compressive stress-strain curves of nanocomposites

The mechanical behavior in terms of simple uniaxial compressive stress-strain curves at room temperature (303 K) of AA 6061-*x* wt.% TiO₂ (*x*=0, 4, 8 and 12 wt.%) nanocomposites is shown in **Figure 18**. From **Figure 18**, it was observed that the compressive stress flow curve was started to increase drastically when the amount of reinforcement of TiO₂ ceramic particles increases in the nanocrystallite matrix. Maximum ultimate compressive strength of 442 MPa was obtained in AA 6061-12 wt.% TiO₂ nanocomposite which was 1.6 times higher than AA 6061 nanocrystallite alloy. The observed ultimate compressive strengths were 275, 295, 365 and 442 MPa for 0, 4, 8 and 12 wt.% TiO₂-reinforced nanocomposites, respectively. The corresponding decreased compressive strains were 0.076, 0.065, 0.052 and 0.039 for 0, 4, 8 and 12 wt.% TiO₂-reinforced nanocomposites, respectively. The increase in value of compressive strength and decrease in strain with the function of nano-TiO₂ particles were attributed to

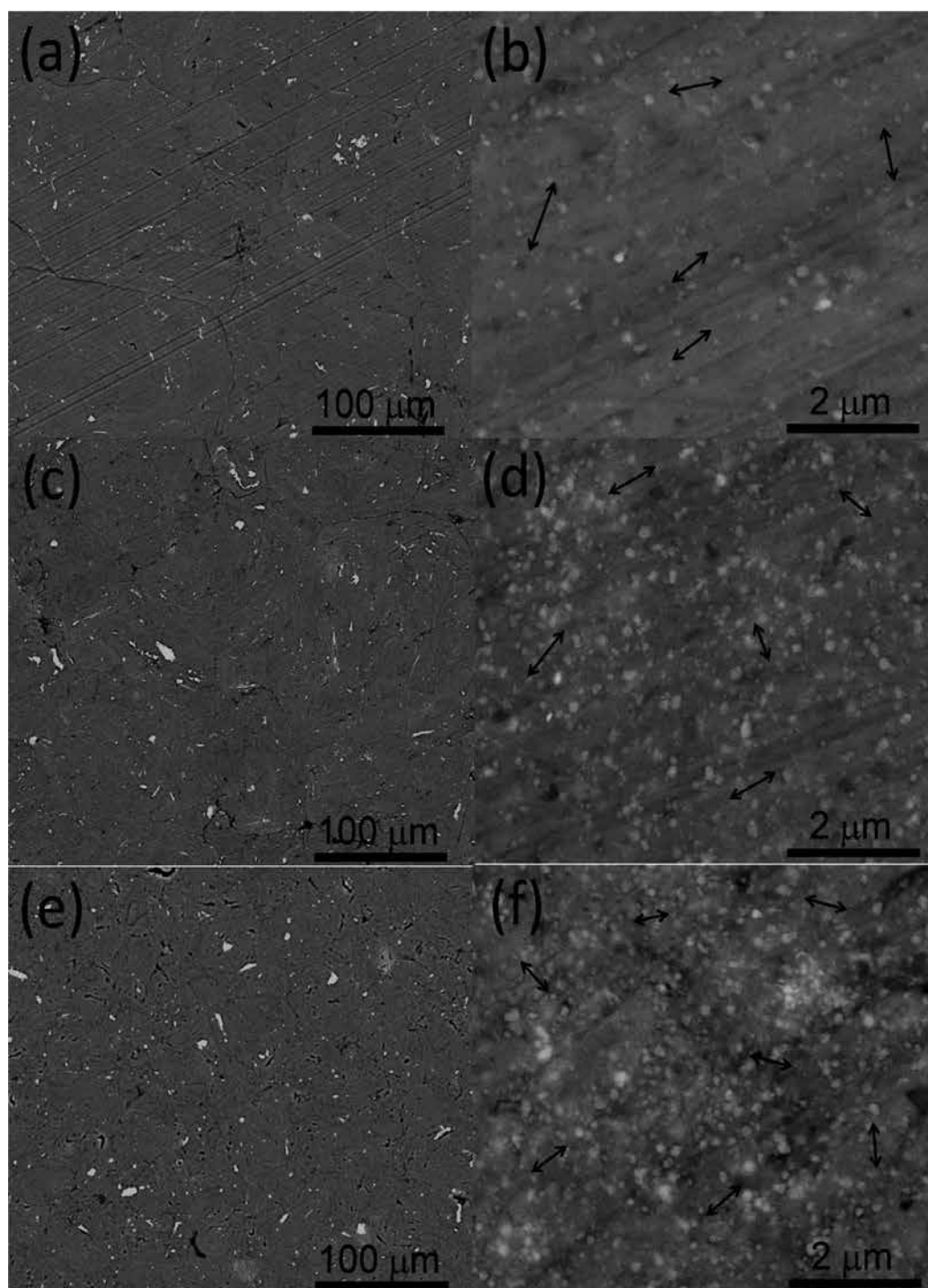


Figure 17. SEM/BSEI of sintered nanocomposite AA 6061_{100-x}-x wt.% TiO₂ at 550°C. Left side of (a), (c) and (e) shows 2, 6 and 12 wt.% TiO₂ nanocomposite. Right side of (b), (d) and (f) shows magnified view of corresponding sintered preforms. Note: double arrow represents the distribution of TiO₂ particles.

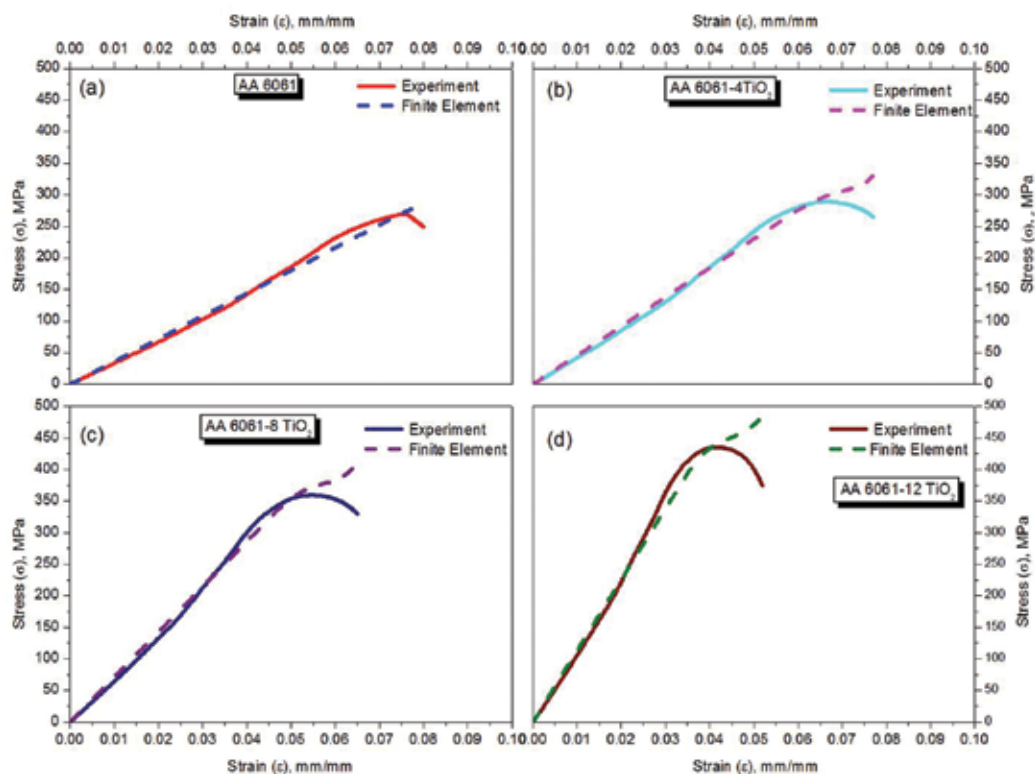


Figure 18. Compressive stress-strain curves of experimental and finite element analysis of: (a) AA 6061 alloy, (b) AA 6061-4TiO₂, (c) AA 6061-8TiO₂, (d) AA 6061-12TiO₂ nanocomposites.

crystallite refinement in the matrix, uniform distribution and embedding of reinforcements over the matrix. Due to this, effective load transfer between matrix and reinforcement had occurred.

5.5.2. Finite element simulation of compressive stress-strain curves of nanocomposites

Finite element simulations were also carried out using simple uniaxial compressive stress-strain data. In the simulation, 3D solid model of 5 mm×5 mm×10 mm as per ASTM standard specimen was used; one end of model was set as fixed support, and the other end was used to give compressive load. Before simulations, the material properties such as density, Young's modulus value, Poisson's ratio and ultimate compressive strength were given as input in ANSYS workbench software. **Figure 18** in dashed line shows the finite element results. Excellent agreement between experimental results and finite element results was observed. **Figure 19a** and **b** shows the stress distribution at ultimate compressive strength of AA 6061 and AA 6061-12 wt.% TiO₂ nanocomposites, respectively. It can be observed from **Figure 19** that the stress concentration at the bottom of developed/simulated model was more in AA 6061-12 wt.% TiO₂ nanocomposite when compared to AA 6061 nanocrystallite alloy. This was attributed to more crystallite refinement, uniform distribution of nano TiO₂ particle and more amount of embedding of TiO₂ ceramic particles over the matrix.

5.5.3. Compressive stress-strain curves of trimodeled nanocomposites

It was observed from **Figure 18** that the manufactured nanocomposites exhibited highest compressive strength. However, it showed poor in toughness and ductility. Therefore, in order to improve toughness and ductility by sacrificing the strength slightly, trimodel-based nanocomposites were successfully fabricated. These trimodel nanocomposites were consisting of nanocrystallite matrix (after 40-h MA), nano TiO₂ particles (~119 nm) and coarse crystallite matrix. It was expected that the addition of coarse crystallite matrix in the nanostructured materials would enhance the toughness and ductility. As an example, AA 6061-12 wt.% TiO₂ nanocomposites (after 40-h MA) were taken here for investigation. **Figure 20** shows the compressive stress-strain curves of AA 6061-12 wt.% TiO₂- y wt.% CG nanocomposites (y=0, 5, 10, 15, 20, 25 and 30) of both experiment (**Figure 20a**) and finite element (**Figure 20b**). Inspection of AA 6061-12 wt.% TiO₂ nanocomposite curves showed that there was a poor strain (poor in ductility) of around 0.039 mm/mm only; however, it exhibited an ultimate compressive strength of 442 MPa. The poor value of strain (ductility) for nanostructured alloy/composites via MA was attributed to MA processing which causes residual moisture during cold consolidation led to pores after sintering [50], segregation of impurities created by milling media (i.e., balls and vial material) [51] and the dispersoid-matrix interface de-cohesion [52]. The measured ultimate compressive strength for 0, 5, 10, 15, 20, 25 and 30% CG nanocomposites were 442, 449, 454, 474, 461, 438 and 427 MPa, respectively. These results revealed that the ultimate compressive strength was started to increase up to 15 wt.% CG matrix in AA 6061-12 wt.% TiO₂ nanocomposites, and then, it started to decrease from 20 to 30 wt.% CG matrix in the nanocomposites. Indeed, as the CG matrix increases in the nanocomposites, it tries to accommodate the dislocation mobility. Further, the CG tries to arrest the crack propagation that usually occurs in nanocomposites as it is subjected either tensile force or compressive force. Around 7% of increased ultimate compressive strength was observed in AA 6061-12 wt.% TiO₂-15 wt.% CG nanocomposites when compared to AA 6061-12 wt.% TiO₂ nanocomposite. The corresponding compressive strain was 0.039, 0.050, 0.057 and 0.071 mm/mm for 0, 5, 10 and 15 CG nanocomposites, respectively. This was attributed to enhanced densification by increasing soft phase and uniform distribution of CG matrix in nanocomposite structures. However, the observed ultimate compressive strength started to decrease when the CG matrix addition was beyond 15%. This was expected to the domination of softer CG matrix and coalescences of CG particles which might have decreased the effective load transfer rate. In contrast, the ductility was improved in a better manner as the large number of CG matrix phase in the nanocomposites might have effectively delayed the crack initiation in nanocomposites during deformation. The compressive ductility for 30% CG trimodel nanocomposite was around 520>0% CG nanocomposites. To conform the uniform distribution and coalescence of CG matrix in nanocomposite, the microstructures of AA 6061-12 TiO₂- y wt.% CG (y=0, 10, 20 and 30) nanocomposites were taken and the same is shown in **Figure 20a-d**. From the microstructures, two different regions, namely, gray regions and white regions were seen. The gray region characterizes ultra-fine grain (UFG) matrix phase embedded with nano-TiO₂ ceramic particles, whereas the white region characterizes CG matrix phase. From **Figure 21b-d**, it was very clear that a good homogeneous distribution of CG matrix phase was observed in UFG matrix. Further, it can be observed that as the percentage of CG matrix phase increases, the size of CG domain also increases. Due to this, the dislocations move a significant distance without crystallite boundary interruption when trimodel material is deformed [53, 54]. Therefore, it was expected to

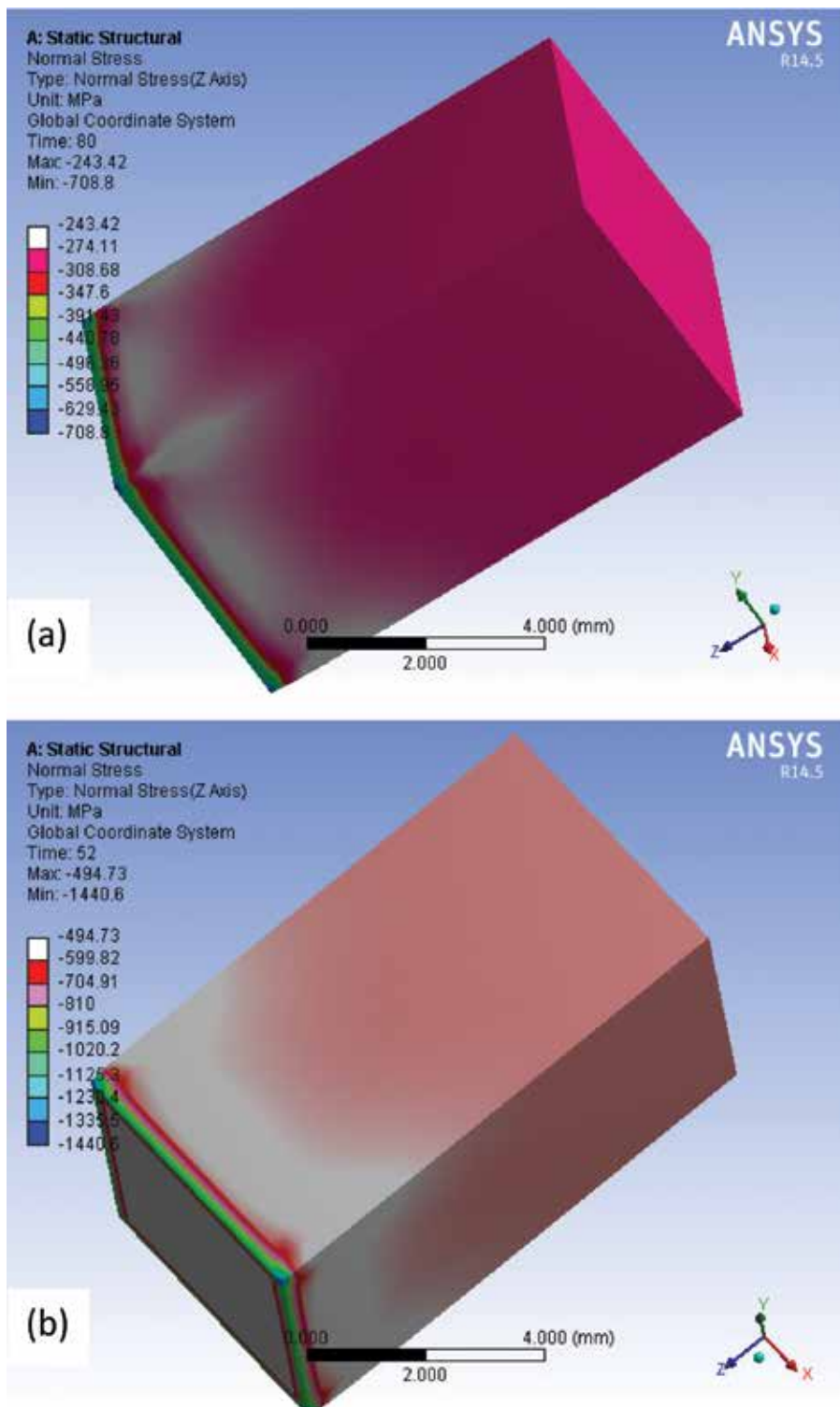


Figure 19. Stress distribution at ultimate compressive strength of simulated model of: (a) AA 6061 nanocrystalline alloy, (b) AA 6061-12 wt.% TiO₂ nanocomposite.

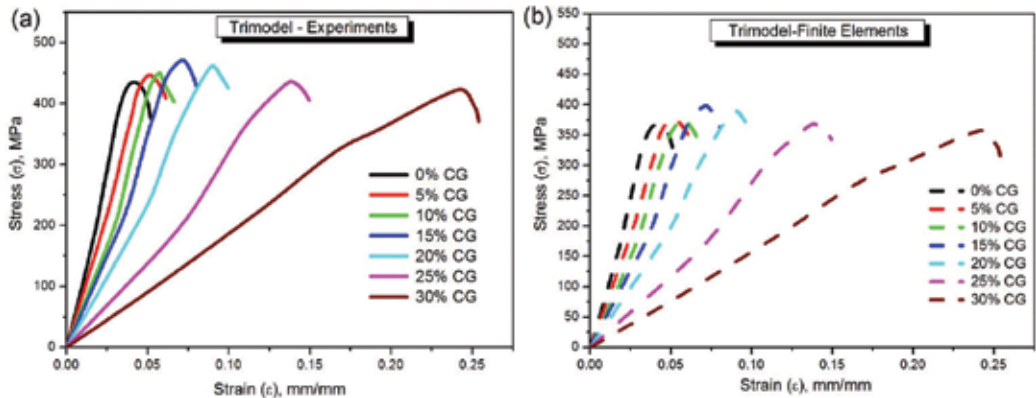


Figure 20. Compressive stress-strain curves of AA 6061-12 wt.% TiO_2 - y wt.% CG nanocomposites (y=0, 5, 10, 15, 20, 25 and 30): (a) experimental results and (b) finite element results.

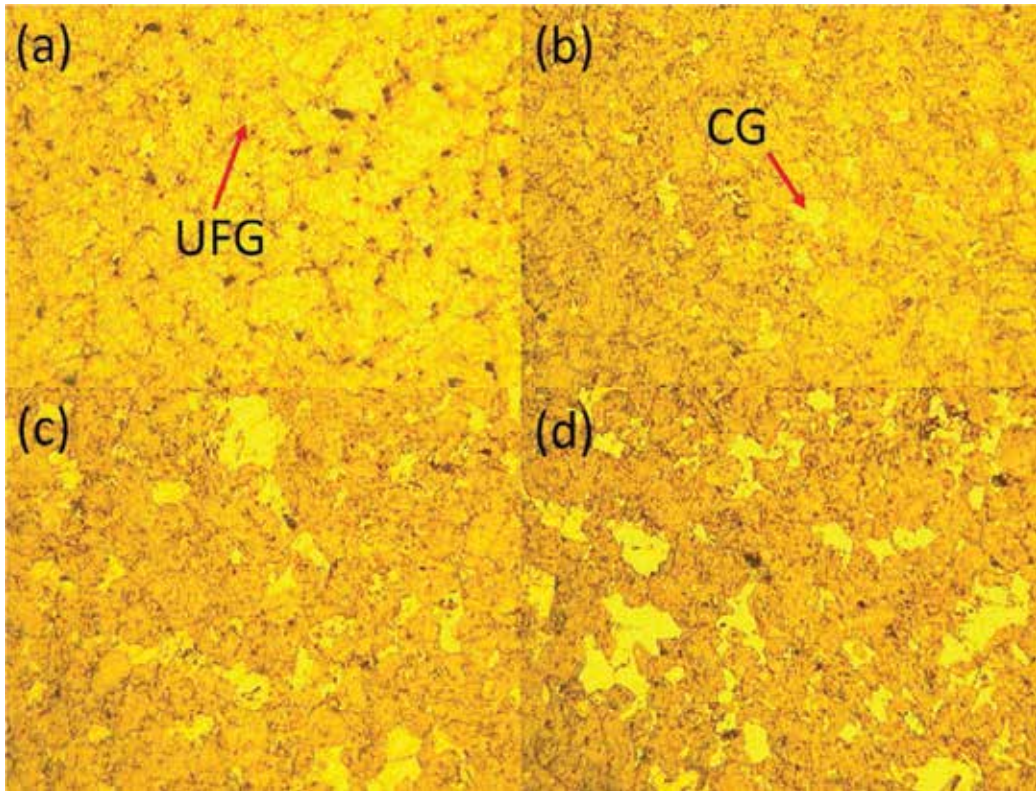


Figure 21. Trimodel microstructures of as-sintered AA 6061-12 wt.% TiO_2 composites containing x wt.% CG matrix: (a) x=0%, (b) x=10%, (c) x=20% and (d) x=30%. The gray regions represent UFG matrix reinforced with nano Titania, the bright regions represent CG matrix.

have improvement in ductility of nanocomposite material by incorporating CG matrix. The size of CG matrix phase was not increased up to 15% CG-blended nanocomposites. The measured average CG size was less than 45 μm up to 15% CG-blended composites due to non-coalescence of individual CG matrix particles. Conversely, the average size of CG matrix phase started to increase when CG matrix content increases beyond 15% (**Figure 21c and d**). From **Figure 20d**, AA 6061-12 wt. TiO_2 -30% CG nanocomposite is clearly showing a very large size of CG matrix phases due to coalescence of individual CG matrix particles. Witkin et al. [55] have also observed the same behavior while studying the bimodal crystallite size of Al-Mg alloy (0, 15 and 30% CG matrix phase) prepared by cryomilling and blending. Due to this, a good ductility was observed by slight decrement of compressive strength.

6. Summary and conclusions

A new nanocomposite of AA 6061 Al alloy reinforced with different weight percentage of titania particles was developed and was successfully synthesized and investigated for its mechanical behavior. It was found that the matrix powder particle size, shape and its morphology, reinforcement particle size and its distribution on the matrix, amount of reinforcement, crystallite size of the matrix and type of microstructures (bimodal and/or trimodal) were reflected and influenced the performance of the fabricated light weight-based nanocomposite which is suitable for automotive and structural applications.

6.1. Powder surface morphology

The powder morphology of nanocomposite powders with the function of reinforcement was investigated. It was experimentally found that the incorporation of hard ceramic reinforcements in the nanocomposite powders exhibited drastic changes on the morphological characteristics of MMCs. The produced nanocomposite powders morphology showed that all powder particles regardless of the reinforcement were almost in spherical-shaped and equiaxed particles which indicated the attainment of steady-state condition during 40-h MA. On the other hand, the irregular flake-like morphology of as-received soft matrix powder particles was eliminated after 40-h MA and changed to a shape near the equiaxed. Further, nano-sized TiO_2 particles are completely embedded in soft matrix of nanocomposite powder after 40 MA. There is no way of forming of reinforcement clustering in nanocomposite powder via MA during the time taken (40 h) for the present investigation.

6.2. Structural evaluation

The structural characteristics of ball-milled mechanically alloyed powders were investigated and reported. These results confirmed the occurrence of structural refinement in nanocomposites with the function of reinforcement through mechanical alloying, and hence, decreased crystallite size was observed. The MA time selected for this study produced the crystallite size of around 46 and 65 nm for 12 wt.% reinforced particulate nanocomposite and unreinforced nanocrystallite powders, respectively. The nanocrystalline nature of the matrix powder particle and aggregation of nanocomposite powder particle was confirmed by TEM analysis.

6.3. Mechanical strength and sintering behavior

Nanostructured AA 6061 Al alloy reinforced with different weight percentage of TiO₂ particles processed via MA followed by cold consolidation and sintering yielded maximum strength (hardness) of around 1.126 GPa of matrix grain size of 200–300 nm (*UFG*) embedded with nano-sized Titania (~119 nm). This was attributed to structural refinement contributed from various strengthening mechanisms such as grain size, dislocation, solid solution and dispersion strengthening. Here, the matrix to reinforcement particle size ratio of nanocomposite was greater than unity and even very higher value. However, excellent behavior in terms of densification, sinterability and Vickers hardness was obtained. These results indicated that the effect of matrix to reinforcement particle size ratio was insignificant in the case of nanocomposite because there was no possibility of reinforcement clusters while manufacturing of MMCs via MA.

6.4. Compressive stress-strain behavior

The compressive stress-strain curves of nanocomposites were started to increase drastically with the function of reinforcement which indicated the enhancement of compressive strength while it exhibited the decreased value of ductility with the function of reinforcement. These results were attributed to more crystallite refinement and complete embedding of titania ceramic particles in the matrix. A trimodel grain size distribution for enhancing the ductility and toughness of high strength AA 6061–TiO₂ nanocomposites was fabricated successfully and the uniaxial compressive deformation behavior through simple compression test at room temperature was studied, analyzed and reported. These results explained that the addition of coarse crystallite powder particles in the nanostructured materials would enhance the ductility, delay the plastic instability and enhance toughness. In other words, the addition of CG matrix phase decelerates the micro-crack nucleation cum proliferation in nanostructured phase during deformation. Therefore, the ductility in nanocomposite materials can be improved which would be suitable for manufacturing of automotive and structural components. Here, the 30% CG-incorporated nanocomposite exhibited improved ductility of around 500% more than that of 0% CG incorporated nanocomposite.

Author details

S. Sivasankaran* and Abdulaziz S. Alaboodi

*Address all correspondence to: sivasankarangs1979@gmail.com

Department of Mechanical Engineering, College of Engineering, Qassim University, Kingdom of Saudi Arabia

References

- [1] Callister, Jr. W.D. Fundamental of material science and Engineering, 2nd edition, John Wiley & Sons, Hoboken, NJ, New York City, United States 2007.

- [2] Suryanarayana, C. (2001) Mechanical alloying and milling, *Prog. Mater. Sci.*, **46**, 1–184.
- [3] Smagorinski, M.E., P.G. Tsantrizos, S. Grenier, A. Cavasin, T. Brzezinski and G. Kim. (1998) The properties and microstructure of Al-based composites reinforced with ceramic particles, *Mater. Sci. Eng. A.*, **244(1)**, 86–90.
- [4] Ramesh, C.S., A.R. Anwar Khan, N. Ravikumar and P. Savanprabhu. (2005) Prediction of wear coefficient of Al 6061–TiO₂ composites, *Wear.*, **259**, 602–608.
- [5] Troeger, L.P. and E.A. Starke. (2000) Microstructural and mechanical characterization of a superplastic 6xxx aluminium alloy, *Mater. Sci. Eng. A.*, **277**, 102–113.
- [6] Boselli, J., P.D. Pitcher, P.J. Gregson and I. Sinclair. (2001) Numerical modeling of particle distribution effects on fatigue in Al–SiC_p composites, *Mater. Sci. Eng. A.*, **300**, 113–124.
- [7] Ganguly, P. and W.J. Poole. (2002) Effect of reinforcement distribution on failure mechanism in aluminum based metal matrix composites, *Mater. Sci. Forum.*, **396–402**, 1139–1144.
- [8] Ramesh, C.S., R. N. Ahmed, M.A. Mujeebu and M.Z. Abdullah. (2009) Fabrication and study on tribological characteristics of cast copper–TiO₂–boric acid hybrid composites, *Mater. Des.*, **30**, 1632–1637.
- [9] Fan, L., J. Dongmei and M. Xueming. (2009) The effect of milling atmospheres on photocatalytic property of Fe-doped TiO₂ synthesized by mechanical alloying, *J. Alloys Compd.*, **470**, 375–378.
- [10] Sivasankaran, S., K. Sivaprasad, R. Narayanasamy, Vijay KumarIyer. (2010) An investigation on flowability and compressibility of AA 6061_{100-x}–x wt.% TiO₂ microand nanocomposite powder prepared by blending and mechanical alloying, *Powder Technol.*, **201**, 70–82.
- [11] Martin, L.P., A.M. Hodge and G.H. Campbell. (2007) Compaction behavior of uniaxially cold-pressed Bi-Ta composites, *Scr. Mater.*, **57**, 229–232.
- [12] Panelli, R. and F.A. Filho. (2001) A study of a new phenomenological compacting equation, *Powder Technol.*, **114**, 255–261.
- [13] Bouvard, D. (2000) Densification behaviour of mixtures of hard and soft powders under pressure, *Powder Technol.*, **111**, 231–239.
- [14] Çomoğlu, T. (2007) An overview of compaction equations, *J. Fac. Pharm, Ankara.*, **36(2)**, 123–133.
- [15] Baoju, B., X. Youjun, Z. Shiqiong and Y. Qianlian. (2000) Influence of ultrafine fly ash composite on the fluidity and compressive strength of concrete, *Cem. Concr. Res.*, **30**, 1489–1493.
- [16] Showaiter, N. and M. Youseffi. (2008) Compaction, sintering and mechanical properties of elemental 6061 Al powder with and without sintering aids, *Mater. Des.*, **29**, 752–762.
- [17] Nayar, H.S. Sintering atmosphere, powder metal technologies and applications, Volume 7 of ASM Handbook, Materials Park, OH, Russell Township, Geauga County, Ohio, United States 1998.

- [18] Löffler, J. and J. Weissmüller. (1995) Grain-boundary atomic structure in nanocrystalline palladium from X-ray atomic distribution functions, *Phys. Rev. B: Condens. Matter*, **52**(10), 7076–7093.
- [19] Zhong, Y., D. Ping, X. Song and F. Yin. (2009) Determination of grain size by XRD profile analysis and TEM counting in nano-structured Cu, *J. Alloys Compd.*, **476**, 113–117.
- [20] Scardi, P., M. Leoni and R. Delhez. (2004) Line broadening analysis using integral breadth methods: a critical review, *J. Appl. Cryst.*, **37**, 381–390.
- [21] Hall, B.D., D. Zanchet and D. Ugarte. (2000) Estimating nanoparticle size from diffraction measurements, *J. Appl. Cryst.*, **33**, 1335–1341.
- [22] Cullity, B.D. (1978) Elements of X-ray diffraction, second ed. Addison Wesley, London, UK, 1978.
- [23] Williamson, G.K. and W.H. Hall. (1953) X-ray line broadening from filed aluminium and wolfram, *Acta Metal.*, **1**, 22–31.
- [24] Warren, B.E. and B.L. Averbach. (1952) The separation of cold-work distortion and particle size broadening in X-ray patterns, *J. Appl. Phys.*, **23**, 497.
- [25] Biju, V., N. Sugathan, V. Vrinda and S.L. Salini. (2008) Estimation of lattice strain in nanocrystalline silver from X-ray diffraction line broadening, *J. Mater. Sci.*, **43**, 1175–1179.
- [26] Abdullah, E.C. and D. Geldart. (1999) The use of bulk density measurements as flowability indicators, *Powder Technol.*, **102**, 151–165.
- [27] Heckel, R.W. (1961) Density-pressure relationships in powder compaction, *Metall. Soc. AIME.*, **221**, 671–675.
- [28] Jia, D., K.T. Ramesh and E. Ma. (2000) Failure mode and dynamic behavior of nanophase iron under compression, *Scr. Mater.*, **42**, 73–78.
- [29] Jiang, J. and B. Dodd. (1995) Workability of aluminium-based metal-matrix composites in cold compression. *Composites*, **26**, 62–66.
- [30] Rodriguez, A., J.M. Gallardo and E.J. Herrera. (1997) Structure and properties of attrition-milled aluminum powder, *J. Mater. Sci.*, **32**, 3535–3539.
- [31] Sivasankaran, S., K. Sivaprasad, R. Narayanasamy, Vijay Kumar Iyer. (2010) Synthesis, structure and sinterability of 6061 AA_{100-x}-x wt.% TiO₂ composites prepared by high-energy ball milling, *J. Alloys Compd.*, **491**, 712–721.
- [32] Gan, K. and M. Gu. (2008) The compressibility of Cu/SiC powder prepared by high-energy ball milling, *J. Mater. Process. Technol.*, **199**, 173–177.
- [33] Alizadeh, M. and M.M. Aliabadi. (2011) Synthesis behavior of nanocrystalline Al–Al₂O₃ composite during low time mechanical milling process, *J. Alloys Compd.*, **509**, 4978–4986.

- [34] Sivasankaran, S., K. Sivaprasad, R. Narayanasamy and P.V. Satyanarayana. (2011) X-ray peak broadening analysis of AA 6061_{100-x}-x wt.% Al₂O₃ nanocomposite prepared by mechanical alloying, *Mater. Charact.*, **62**, 661–672.
- [35] Razavi-Tousi, S.S., R. Yazdani-Rad and S.A. Manafi. (2011) Effect of volume fraction and particle size of alumina reinforcement on compaction and densification behavior of Al–Al₂O₃ nanocomposites, *Mater. Sci. Eng. A.*, **528**, 1105–1110.
- [36] Khadem, S.A., S. Nategh and H. Yoozbashizadeh. (2011) Structural and morphological evaluation of Al–5 vol.%SiC nanocomposite powder produced by mechanical milling, *J. Alloys Compd.*, **509**, 2221–2226.
- [37] Hesabi, Z.R., H.R. Hafizpour and A. Simchi. (2007) An investigation on the compressibility of aluminium/nano-alumina composite powder prepared by blending and mechanical milling, *Mater. Sci. Eng. A.*, **454–455**, 89–98.
- [38] Razavi, S.S., R. Yazdani Rad, E. Salahi, I. Mobasherpour and M. Razavi. (2009) Production of Al-20 wt.% Al₂O₃ composite powder using high energy milling, *Powder Technol.*, **192**, 346–351.
- [39] Fogagnolo, J.B., E.M. Ruiz-Navas, M.H. Robert and J.M. Torralba. (2003) Effect of mechanical alloying on the morphology, microstructure and properties of aluminium matrix composite powders, *Mater. Sci. Eng. A.*, **342**, 131–143.
- [40] El-Eskandarany, M.S. Mechanical alloying for fabrication of advanced engineering materials, William Andrew Publishing, New York, 2000.
- [41] Witkin, D.B. and E.J. Lavernia. (2006) Synthesis and mechanical behavior of nanostructured materials via cryomilling, *Prog. Mater. Sci.*, **51 (1)**, 1–60.
- [42] Kumaran, S., T. Sasikumar, R. Arockiakumar and T. Srinivasa Rao. (2008) Nanostructured titanium aluminides prepared by mechanical alloying and subsequent thermal treatment, *Powder Technol.*, **185(2)**, 124–130.
- [43] Venugopal, T., K. Prasad Rao and B.S. Murty. (2007) Mechanical and electrical properties of Cu-Ta nanocomposites prepared by high energy ball milling, *Acta Mater.*, **55(13)**, 4439–4445.
- [44] Schilling, P.J., J.H. He, J. Cheng and E. Ma. (1996) Extended X-ray absorption fine structure of metastable bcc and fcc phases in mechanically alloyed Fe-Cu, *Appl. Phys. Lett.*, **68(6)**, 767–769.
- [45] Zhao, Y.H., H.W. Shang and K. Lu. (2001) Microstructure evolution and thermal properties in nanocrystalline Fe during mechanical attrition, *Acta Mater.*, **49**, 365–375.
- [46] Fogagnolo, J.B., M.H. Robert and J.M. Torralba. (2006) Mechanically alloyed AlN particle-reinforced Al-6061 matrix composites: Powder processing, consolidation and mechanical strength and hardness of the as-extruded materials, *Mater. Sci. Eng. A.*, **426(1–2)**, 85–94.

- [47] Evirgen, A. and M.L. Övecoglu. (2010) Characterization investigations of a mechanically alloyed and sintered Al-2 wt%Cu alloy reinforced with WC particles, *J. Alloys Compd.*, **496**, 212–217.
- [48] Shanmugasundaram, T., M. Heilmaier, B.S. Murty and V. Subramanya Sarma. (2009) Microstructure and mechanical properties of nanostructured Al-4Cu alloy produced by mechanical alloying and vacuum hot pressing, *Metall. Mater. Trans. A.*, **40(12A)**, 2798–2801.
- [49] S. Sivasankaran, K. Sivaprasad, R. Narayanasamy and M. Saravanan. (2015) Effect of coarse grain matrix content on the mechanical behavior of trimodaled AA 6061-TiO₂ nanocomposite prepared by mechanical alloying, *International Journal of Advanced Manufacturing Technology* **78(1–4)**, 385–394”.
- [50] Srivatsan, T.S., E.J. Lavernia and F.A. Mohamed. (1990) Influence of oxides on the properties of PM Al-Li-Cu alloys, *Int. J. Powder Metall.*, **26(4)**, 321–334.
- [51] Benjamin, J.S. and R.D. Schelleng. (1981) Dispersion strengthened aluminum-4 Pct magnesium alloy made by mechanical alloying, *Metall. Mater. Trans. A.*, **12A**, 1827–1832.
- [52] Riedel, H. Fracture at high temperature, Springer-Verlag, Berlin, 1987.
- [53] Ye, J., B.Q. Han, Z. Lee, B. Ahn, S.R. Nutt and J.M. Schoenung. (2005) A tri-modal aluminium based composite with super-high strength, *Scr. Mater.*, **53**, 481–486.
- [54] Sivasankaran, S., K. Sivaprasad, R. Narayanasamy. (2011) Microstructure, cold workability and strain hardening behavior of trimodaled AA6061-TiO₂ nanocomposite prepared by mechanical alloying, *Mater. Sci. Eng. A.*, **528**, 6776–6787.
- [55] Witkin, D., Z. Lee, R. Rodriguez, S. Nutt and E.J. Lavernia. (2003) Al-Mg alloy engineered with bimodal grain size for high strength and increased ductility, *Scr. Mater.*, **49**, 297–302.

Fungal-Derived Nanoparticles as Novel Antimicrobial and Anticancer Agents

Muhammad Waseem and Muhammad Atif Nisar

Additional information is available at the end of the chapter

<http://dx.doi.org/10.5772/66922>

Abstract

In order to control microbial resistance against commonly used antibiotics, it is indispensable to develop novel and efficient antimicrobial agents. For this purpose, metallic nanoparticles (mainly inorganic) with their antimicrobial activities represent an effective solution for this global problem. However, synthesis of nanoparticles involves the use of expensive, poisonous and dangerous chemicals responsible for different biological and environmental hazards. This fact increases the necessity of developing environment-friendly procedure by means of green synthesis (using plants) and extra-biological methods (using microbes such as bacteria and fungi). More recently, metallic nanoparticles, derived from fungal sources, have demonstrated their potential not only as a new-generation antimicrobial agents but also as anticancer agents. Therefore, this chapter is aimed to explore the various nanoparticles producing fungi with ultimate objective of elucidating the possible (i) mechanism of biosynthesis of metallic NPs by various fungi and (ii) mode of action of these mycosynthesized NPs on bacterial cell. This chapter would certainly increase our knowledge about interaction of nanoparticles with bacterial cell for their use in health biotechnology.

Keywords: nanoparticles, silver, myconanosynthesis, fungi, cancer, antibacterial activities

1. Introduction

In the field of nanotechnology and nanomaterial, more specifically, nanoparticles are extremely important because of their unique optical, physicochemical, and biological facets. Though their biological synthesis is still at early stages and many material scientists around the globe are working on the production of nanoparticles from different sources including plants, animals, microbes, and metallic compounds like gold, silver, platinum, etc. Various studies on biosyn-

thesis of nanoparticles have been carried out using a wide array of microorganisms such as algae, bacteria, actinomycetes, fungi, yeasts, and viruses [1, 2]. Among the many possible bio-resources, biologically active products from fungi and yeast represent excellent scaffolds for this purpose. Since fungi and yeast are very effective secretors of extracellular enzymes and number of species grow fast and therefore culturing and keeping them in the laboratory is very simple [3]. They are able to produce metal nanoparticles and nanostructure via reducing enzyme extracellularly [3, 4]. Not only the harvesting of extracellularly synthesized nanoparticles from fungi is easy and inexpensive [2, 5], they can also be manipulated by controlling the pH, temperature, substrate concentration (metal ions), and reaction time [6, 7]. Therefore, the biosynthesis could be ideally used for large-scale production of nanoparticles for several industrial applications [3]. Importantly, fungi have also secreted fairly large amount of proteins and secondary metabolites extracellularly, and hence, the fungal biomass could reduce the metal ions more easily leading to the rapid formation of nanoparticles [8]. Because of these advances, the myco-based extracellular synthesis method is often considered as a better resource for higher productivity of nanoparticles [4].

On the other hand, increasing incidence of microbial resistance to clinically approved classes of antibiotics has emerged in recent years and is a major health problem, requiring to develop novel and effective antimicrobial agents [4, 9–11]. Owing to their antibacterial activities, metallic nanoparticles (mainly silver and gold) represent a novel and an effective solution for overcoming bacterial resistance. In general, nanoparticles are divided into two groups, i.e., organic and inorganic, where the later one being significant biomedical agents [12]. These silver and gold nanoparticles, derived from microbial sources, have demonstrated their potential not only as a new generation antimicrobial [13] agents against a broad spectrum of Gram-positive and Gram-negative bacteria including multidrug-resistant human pathogens, but also as anti-cancer agents [3]. They have also significantly enhanced the bactericidal activity when used in combination with standard antibiotics [14]. However, synthesis of nanoparticles involves the use of expensive, poisonous, and dangerous chemicals responsible for different biological and environmental hazards. This fact increases the necessity of developing environment-friendly procedure by means of green synthesis (using plants) and extra biological methods (using microbes such as bacteria and fungi) [15]. Therefore, as a part of our continuing search to identify microorganisms with the potential to synthesize nanoparticles with amazing biological properties, interest has spurred on microbes [11], especially fungi. Indeed a few fungal species around the globe have been reported to secrete nanoparticles. Therefore, the present chapter is aimed to provide an overview of nanoparticles producing fungi, with the ultimate objective of producing effective antimicrobial agents.

2. Biosynthesis of nanoparticles by fungi

In the last decade, biomineralization has been developed as an emerging and attractive technique for the synthesis of metallic nanoparticles. In which microbial cells are preferably being used for the synthesis of nanosized material involving the oxidation/reduction of metallic ions (like silver, gold, platinum, etc.) giving rise to nanostructures and nanoparticles [16].

This green synthesis of metallic nanoparticles undergo three necessary steps (**Figure 1**) that are (i) choice of appropriate solvent medium, (ii) choice of appropriate reducing agent (environment friendly), and (iii) stabilizing agents or substances for silver nanoparticles stability [17]. Generally, this reduction is carried out by means of microbial enzymes (**Figure 1**), present in microbes, and considered to be responsible for synthesis of nanoparticles by those organisms [18, 19].

For this purpose, various fungi have been used as novel and assuring resources for manufacturing of nanoparticles extracellularly as well as intracellularly, such as *Aspergillus*, *Pencillium*, *Fusarium*, and *Verticillium*. Though synthesis of metallic nanoparticles (NPs) having defined size, shape, and composition by fungi are major challenges in this field [20, 21]. In general, fungal enzymes with reducing capabilities are mostly responsible for reduction of metal ions (**Figure 1**) to their corresponding nanoparticle(s) as described earlier [22]. We will discuss biosynthesis of NPs from various fungi one by one.

2.1. Biosynthesis of nanoparticles by *Fusarium*

Several fungal strains belonging to genera *Fusarium* have been studied for the production of metallic nanoparticles. Dias and coworkers [23] have screened different *Fusarium* species to be used as potential candidate(s) for biosynthesis of silver NPs. They have obtained the tiniest size silver-nanoparticles (Ag-NPs) by *Fusarium oxysporum* through extracellular reduction of Ag^+ ions in aqueous medium [24–26]. Generally, two methods were used to evaluate the synthesis of silver nanoparticles by *Fusarium* species involving (i) silver reduction method that involve the fungus biomass in conical flask containing AgNO_3 solution and distilled water. In other method, fungal filtrate were obtained by keeping fungal biomass in distilled water for 72 h at 28°C that was further challenged with AgNO_3 solution (10^{-3} M). In this study, several strains of *Fusarium oxysporum* were exposed to AgNO_3 solution (10^{-3} M) leading to the reduction of silver ions and thereby formation of silver hydrosol. The silver nanoparticles produced

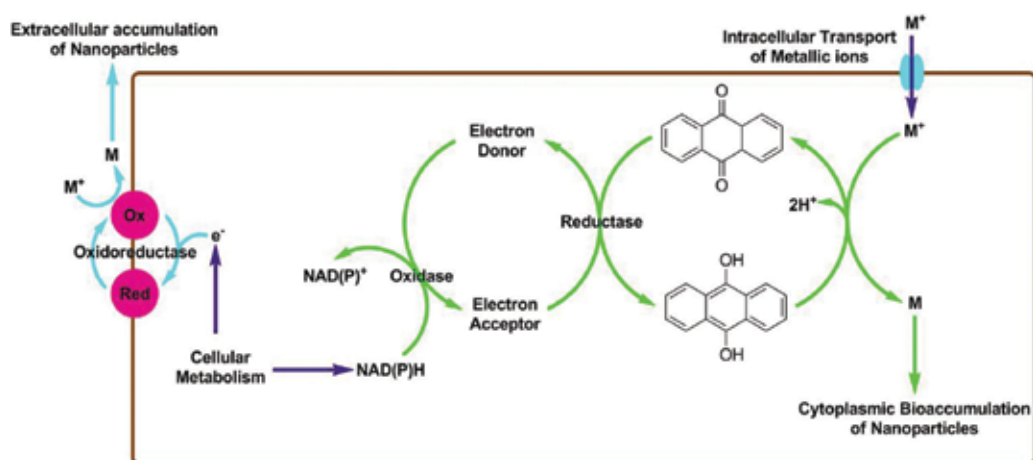


Figure 1. Intracellular and extracellular biosynthesis of metallic nanoparticles (NPs) by fungi.

were in range of 20–50 nm in diameter as a result of nitrate-dependent reductase and shuttle quinone extracellular activities [27]. Similar study was also performed using similar fungal species, i.e., *Fusarium oxysporum* by Mohammadian et al. [28] who observed that synthesis of silver nanoparticles was extremely rapid even at ambient conditions that can compete with chemical synthesis, highly stable even for months in darkness (without light). To date, various *Fusarium* species have been reported to produce metallic nanoparticles for silver [13, 29–33], zirconia [34, 35], platinum NPs intra- and extracellularly [13, 32].

2.2. Biosynthesis of nanoparticles by *Penicillium*

Certain filamentous fungi such as *Penicillium* were also investigated for the synthesis of metallic nanoparticles. For this purpose, various studies have been carried out using different species of *Penicillium* including (but not limited to) *P. brevicompactum* [36], *P. fellutanum* [37], *Penicillium* sp. [38], *P. citrinum* [39], *P. fellutanum* [36], and *P. purpurogenum* [40]. Nanoparticles produced by *Penicillium* spp. are relatively more stable at neutral pH (>8.0) due to repulsion as they possess zeta potential (negative) [41]. In another study, where *P. fellutanum* was challenged with silver ions, it could reduce metallic ions in 10 min, when it came in contact with fungus filtrate [37]. Presence of single protein having molecular weight of about 70 kDa was observed in gel electrophoreses. The authors supposed that nitrate reductase enzymes could possibly be responsible for the reduction of silver ions (**Figure 1**). In addition, the whole reduction process could be manipulated by controlling concentration and exposure time to Ag^+ ions, pH, and temperature [37, 42]. Although exact mechanism commanding the Ag^+ ions reduction is not yet comprehended, however, authors have assumed that reducing agents are secreted by fungi as a response to stress posed by metal ions [40, 42]. Moreover, these silver NPs were uniformly distributed over fungal mycelium (*Penicillium* sp.) suggesting that silver NPs were bound with cells of fungal surface. This was further confirmed by FTIR spectroscopy. In which it was described that both carbonyl groups from amino acid residues and peptides of protein(s) had strong affinities for binding with Ag^+ ions in order to form protective covering around silver NPs to avoid their clustering [36].

2.3. Biosynthesis of nanoparticles by *Aspergillus*

Biosynthesis of NPs from species belonging to genera *Aspergillus* is more desirable and economically important due to its occurrence in natural habitat along with easy culturing on growth media [43]. In the same study, five species belonging to genus *Aspergillus*, i.e., *A. nidulans*, *A. flavus*, *A. terreus*, *A. fumigatus*, and *A. niger*, were synthesized, in which *A. terreus* was proved to be more potent NPs producer among all and was further investigated. It was observed that silver NPs were highly stable even after 4 months due to the presence of stabilizing agents mostly “protein” that would allow functionalizing the NPs with other biological molecules [44]. Their proper functionalizing is an important factor for appropriate antimicrobial activities of these metallic nanoparticles (NPs). In addition, FTIR analyses revealed amide linkages between amino acid residues and NPs. Most active functional groups involved in the reduction of silver ions being the hydroxyl, carboxyl, and carbonyl groups [10, 43, 45–48]. Depending on the biological system used, different sizes and shapes of NPs had been reported ranging from 5 to 45 nm [49] with spherical NPs being the dominant [43].

In another study, AgNP were synthesized using aqueous supernatant of *A. niger*. Synthesized silver NPs were mainly round shape ranging in size from 1 to 20 nm [50]. Various studies have shown the mycosynthesis of silver nanoparticles extracellularly through the reduction of Ag⁺ ions using different species belonging to genus *Aspergillus*, such as *A. niger* [51], *A. flavus* [52], *A. terreus* [53], *A. clavatus* [54, 55], *A. fumigatus* [56], and *A. tamari* [57]. Majority of these NPs were in the range of 1–20 nm with spherical shape.

2.4. Biosynthesis of nanoparticles by other fungi

Various other fungal genera were also exploited for the synthesis of silver nanoparticles. Metallic NPs can be synthesized using fungal biomass and cell-free supernatant. Among eukaryotes, yeast was repeatedly explored for the formation of metallic nanoparticles. Since then, many studies were carried out in order to evaluate the fungal potential as potent producer of silver nanoparticles. For example, cadmium nanoparticles (CdS) were synthesized intracellularly by *Schizosaccharomyces pombe* and *Candida glabrata* when challenged with Cd⁺² ions [42, 58–60]. The authors proposed that these NPs were covered with phytochelatin [42]. Similarly, other studies have also reported the biosynthesis of metallic nanoparticles using fungi such as *Toluopsis* sp. for Pb nanocrystals [60] and for Cu NPs using *Humicola* sp. [61]. Formation of gold nanoparticles was described in yeast *Yarrowia lipolytica* NCIM 3589 that were highly stable [62, 63]. As described earlier, shape and size of NPs mainly rely on the reaction conditions like temperature, pH, metal concentrations, and reaction time [16].

However, first example of intracellular mycosynthesis of silver and gold NPs was demonstrated using *Verticillium* sp. biomass, challenged with aqueous silver ions [64, 65]. Although the mechanism of biosynthesis was not clearly understood, however, it was assumed that metal ions (silver or gold) either (i) adsorbed on cell surface or enter into cytoplasm via diffusion. In both cases, these metallic ions were reduced by enzymes present on the cellular membrane and/or cytoplasm [64, 65]. Similarly, different species belonging to genus *Trichoderma* and *Phoma* were also screened for the synthesis of metallic NPs with dimensions ranging from 8 to 60 nm [66, 67] for the selection of potential species as a new synthesizer of silver NPs.

3. Application of mycosynthesized nanoparticles in biomedics

Mycosynthesized nanoparticles are of extreme importance because of their unique optical, physicochemical and biological facets. These nanosized particles are continuously being used in different fields including electronics [68], catalytic processes [69], optical devices [12], sensor technology [70], biological labeling [71], and may suppress the expression of proteins associated with adenosine triphosphate production [72], agriculture, pharmacology, and environmental monitoring [73]. More recently they are being used as novel antimicrobial and anticancer agents [61, 74–82]. Antimicrobial mediators can be either synthetic and/or partially modified natural compounds [82, 83]. Type of antimicrobials agent(s) may vary according to targeted pathogens, e.g., antibacterial (for bacteria), antifungal (for fungi), and antiviral (for virus). Similarly, their mechanism of action on microbial cell varies according to the nature of the antimicrobial agents and pathogens. Main targets for antimicrobial compounds could be

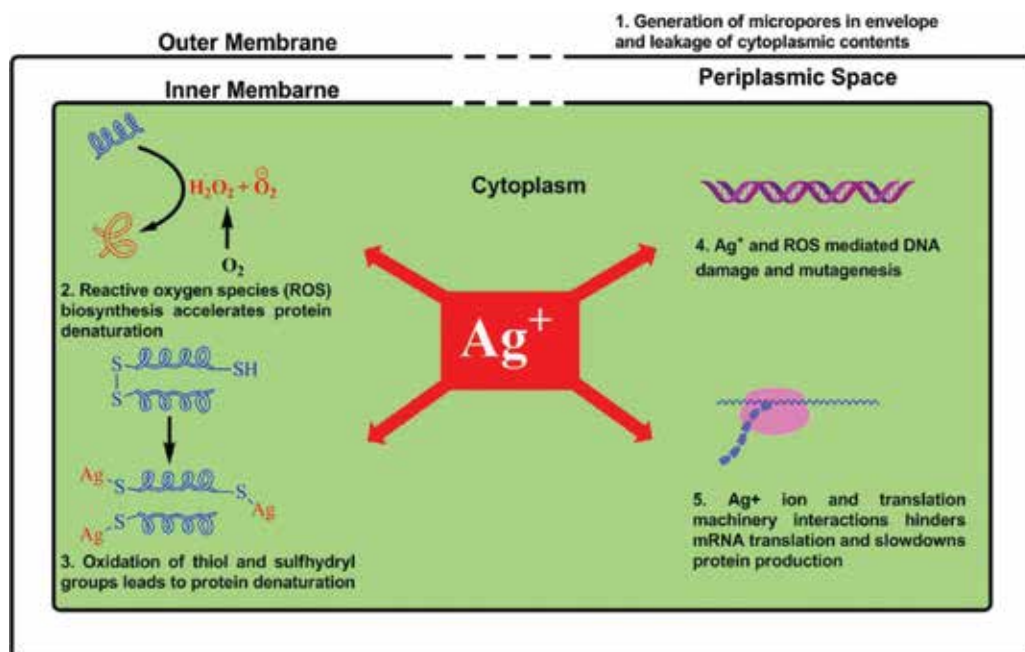


Figure 2. Possible mechanism of action of silver NPs on bacterial cell.

cell wall (cephalosporins, bacitracin, penicillins, etc.) and protein synthesis, DNA replication (tetracyclines, chloramphenicol, lincosamides, etc.) and metabolism (intermediary) processes (valinomycin, Gramicidin A, etc.), and DNA-synthesis (rifampicin, sulfonamides, quinolones, etc.) as described in **Figure 2** [82]. However, abusive use of antimicrobials against various pathogens has evolved into the development of highly adapted and resistant microbes. In addition, these resistant microbes are now being spread globally, challenging the treatment to common infections, and posing significant health threat around the globe. Multidrug-resistant bacteria, such as methicillin-resistant *Staphylococcus aureus* (MRSA) and vancomycin-resistant enterococci, have emerged as a symbol of global health hazard during the last decade.

4. Antibacterial activity of mycosynthesized nanoparticles

Uses of nanoparticles in medicine, particularly in the treatment of bacterial infections, have proved them as effective and novel healing tools against microorganisms. Though for centuries, natural silver has already been considered as one of the most safe and nontoxic inorganic antimicrobial agents [84]. Even silver nanoparticles have also exhibited broad-spectrum antimicrobial properties due to its unique physiochemical and biological characteristics [85]. Recently, silver NPs have shown excellent antimicrobial efficacy against certain bacterial pathogens such as *Bacillus subtilis*, *Staphylococcus aureus*, *Escherichia coli*, *Staphylococcus epidermis*, *Leuconostoc mesenteroides*, *Klebsiella pneumonia*, and *K. mobilis* [84]. Reason for their higher antimicrobial efficacy lies with higher surface area-to-volume ratio of AgNPs that enables

them to bring large portion of Ag atoms in contact with the environment (i.e., microbial cell). However, mechanism of antibacterial activity of silver NPs has not been completely understood [84–88].

Silver nanoparticles have shown inhibitory effect on growth in both Gram-positive and Gram-negative bacteria. As described earlier, larger surface area of silver nanoparticles are believed to be key player in interaction with bacterial cell wall and would have resulted in more antibacterial activity. Although mechanism of action of silver NPs on bacterial cell is debatable; however, assumed mechanism include (i) adherence of AgNPs with bacterial cell wall causing membrane lysis, ultimately releasing cellular contents leading to destruction of cell structure and death [89–91], (ii) interaction of Ag ions with free thiol groups (–SH) and disulfide bridges (–S–S–) of cellular enzymes and membrane of bacteria to downregulate or inactivate the cellular protein synthesis by interfering the translation [72, 91, 92], (iii) blocking DNA replication [93], and (iv) inhibition of signal transduction by dephosphorylation of peptide substrates on tyrosine residues (**Figure 2**) [91]. Furthermore, inhibitory effect of AgNPs varied for different bacterium, e.g., Gram-positive bacteria were more susceptible to silver nanoparticles as compared to Gram-negative one [84]. The authors have found larger inhibition zone (diameter) in case of *S. aureus* than that of *E. coli* suggesting that variation in inhibitory response could be attributed to difference in cell wall and capsular composition, S-layer thickness, cellular metabolism and its byproducts, or a combination of these [84].

5. Anticancer potential of mycosynthesized nanoparticles

About 10 million people are being diagnosed with cancer annually, with higher mortality rate around the globe [94]. It is generally developed due to disturbance in various physiological processes like cell signaling and apoptosis [94]. In this disease, continuous growth of cancer cell due to resistance to wide range of anticancer agents has become the major challenge to pharmacist while treating the disease [95, 96]. Certain factors such as insufficient drug concentrations approaching tumor cells, intolerable cytotoxicity, nonspecific distribution of anticancer agents, and poor monitoring of drug responses particularly in developing countries has made cancer incurable [97, 98].

Recently, the emerging field of nano-biomedicine has highlighted the possibility of metallic NPs to be used for disease diagnosis and cancer treatment in humans [94]. Among various metallic NPs, silver nanoparticles are considered as novel and promising nanoproducts that can be exploited in the field of nanomedicine due to their unique and distinctive properties. Although antibacterial activity of Ag nanoparticles is well established, however, their anticancer activities have recently been reported against various cancerous cell lines [94, 99], and mechanism of action of AgNPs are still under evaluation and there are many ambiguities that should be addressed in future research.

It is well established that silver nanoparticles when interacting with various biomolecules, such as DNA, proteins, and carbohydrates, may cause cell death due to apoptosis or cytotoxicity

probably through reactive oxygen species (ROS) [32, 94]. Various factors influencing cytotoxicity of silver nanoparticles include dosage, contact time, and size of particles. For example, in case of human epidermoid larynx (Hep-2) cell line, cellular damage was dose dependent, causing cell death through ROS [96, 100, 101]. In another study, silver nanoparticles have shown cytotoxic effect through loss of mitochondrial integrity and activation of caspase-cascade exhibiting the apoptotic effect leading to cell death. In a recent study, AgNPs from plant extract, inhibited proliferation of human colon cancer cell line HCT15 while suppressing its cellular growth, inhibiting the G_0/G_1 -phase, interfering DNA synthesis, and ultimately causing cell death through apoptosis [102]. Another important criterion for efficient anticancer drug is its ability to induce apoptosis cancer cell since they generally escape from programmed cell death [103]. In recent studies it has been shown that silver nanoparticles possess this property [104]. The authors have treated the tumor-bearing mice (*in vivo*) with AgNPs that have reduced the tumor weight and increased its life span. The hematologic studies revealed reduced white blood cell (WBC) and platelet count in diseased mice as compared to control (disease free) suggesting that silver NPs were relatively nontoxic and did not produce any change in hematologic parameters and controlled the WBC that were important constituent of immune system of body. The authors further proposed that silver NPs could be used as potent therapeutic agents in order to delay the tumor progression in DLA cell lines through growth suppression and cytotoxic effects that increased vascular permeability leading to tumor cell death that could be linked to caspase enzyme activation. However, mode of action of silver NPs due to which they inhibit cell proliferation and viability causing tumor cell death has not been clearly understood.

6. Conclusion

The use of nanoparticles in the field of medicine is proving to be a novel and promising technique in order to treat various infections. Among various NPs, silver NPs have proved to possess therapeutic alternative that can be exploited in diagnostic and treatment of certain bacterial infections and cancer. To date, various fungi have been reported to biosynthesize the silver nanoparticles. A few among them have been evaluated for the treatment of infection(s) caused by bacterial pathogens providing evidence for their potential role as a new generation antimicrobial agents against a broad spectrum of Gram-positive and Gram-negative bacteria including multidrug-resistant human pathogens. In addition, monodispersed silver NPs can be synthesized by controlling various parameters (such as pH, temperature, etc.) to avoid toxic effects on human cells. Furthermore, biosynthesized silver NPs have successfully exhibited the anticancer activities against different cancer cell lines through inhibiting cell progression (cell proliferation), ROS formation, blockage of DNA synthesis, and apoptosis. However, further research work is required to understand possible mechanism of action of antibacterial and anticancer activities of silver NPs on microbial cell. Various factors (physiochemical and biological) affecting bioavailability, biocompatibility, and cellular toxicity of silver NPs at molecular level should also be addressed in future research that will open new insight for their application alone or in combination with other bioactive agents to control and treat the microbial infections and cancer.

Author details

Muhammad Waseem* and Muhammad Atif Nisar

*Address all correspondence to: muhammad.waseem@gcuf.edu.pk

Department of Microbiology, Government College University, Faisalabad, Pakistan

References

- [1] Narayanan, K.B. and N. Sakthivel, Biological synthesis of metal nanoparticles by microbes. *Advances in Colloid and Interface Science*, 2010. 156(1–2): 1–13.
- [2] Thakkar, K.N., S.S. Mhatre, and R.Y. Parikh, Biological synthesis of metallic nanoparticles. *Nanomedicine: Nanotechnology, Biology and Medicine*, 2010. 6(2): 257–262.
- [3] Mishra, A., et al., Microbial synthesis of gold nanoparticles using the fungus *Penicillium brevicompactum* and their cytotoxic effects against mouse mayo blast cancer C2C12 cells. *Applied Microbiology and Biotechnology*, 2011. 92(3): 617–630.
- [4] Muhsin, T.M. and A.K. Hachim, Mycosynthesis and characterization of silver nanoparticles and their activity against some human pathogenic bacteria. *World Journal of Microbiology and Biotechnology*, 2014. 30(7): 2081–2090.
- [5] Fayaz, A.M., et al., Biogenic synthesis of silver nanoparticles and their synergistic effect with antibiotics: a study against gram-positive and gram-negative bacteria. *Nanomedicine: Nanotechnology, Biology and Medicine*, 2010. 6(1): 103–109.
- [6] Sathishkumar, M., K. Sneha, and Y.S. Yun, Immobilization of silver nanoparticles synthesized using *Curcuma longa* tuber powder and extract on cotton cloth for bactericidal activity. *Bioresource Technology*, 2010. 101(20): 7958–7965.
- [7] Krishnaraj, C., et al., Synthesis of silver nanoparticles using *Acalypha indica* leaf extracts and its antibacterial activity against water borne pathogens. *Colloids and Surfaces B: Biointerfaces*, 2010. 76(1): 50–56.
- [8] Gade, A.K., et al., Exploitation of *Aspergillus niger* for synthesis of silver nanoparticles. *Journal of Biobased Materials and Bioenergy*, 2008. 2(3): 243–247.
- [9] Goffeau, A., Drug resistance: The fight against fungi. *Nature*, 2008. 452(7187): 541–542.
- [10] Jain, N., et al., Extracellular biosynthesis and characterization of silver nanoparticles using *Aspergillus flavus* NJP08: A mechanism perspective. *Nanoscale*, 2011. 3(2): 635–641.
- [11] Elbeshehy, E.K.F., A.M. Elazzazy, and G. Aggelis, Silver nanoparticles synthesis mediated by new isolates of *Bacillus s*, nanoparticle characterization and their activity against Bean Yellow Mosaic Virus and human pathogens. *Frontiers in Microbiology*, 2015. 6: 453.

- [12] Jain, J., et al., Silver nanoparticles in therapeutics: Development of an Antimicrobial gel formulation for topical use. *Molecular Pharmaceutics*, 2009. 6(5): 1388–1401.
- [13] Ingle, A., et al., Mycosynthesis of silver nanoparticles using the fungus *fusarium acuminatum* and its activity against some human pathogenic bacteria. *Current Nanoscience*, 2008. 4(2): 141–144.
- [14] Dar, M.A., A. Ingle, and M. Rai, Enhanced antimicrobial activity of silver nanoparticles synthesized by *Cryphonectria* sp. evaluated singly and in combination with antibiotics. *Nanomedicine: Nanotechnology, Biology and Medicine*, 2013. 9(1): 105–110.
- [15] Balakumaran, M.D., et al., Mycosynthesis of silver and gold nanoparticles: Optimization, characterization and antimicrobial activity against human pathogens. *Microbiological Research*, 2016. 182: 8–20.
- [16] Gericke, M. and A. Pinches, Biological synthesis of metal nanoparticles. *Hydrometallurgy*, 2006. 83(1–4): 132–140.
- [17] Raveendran, P., J. Fu, and S.L. Wallen, Completely “green” synthesis and stabilization of metal nanoparticles. *Journal of the American Chemical Society*, 2003. 125(46): 13940–13941.
- [18] Kalimuthu, K., et al., Biosynthesis of silver nanocrystals by *Bacillus licheniformis*. *Colloids and Surfaces B: Biointerfaces*, 2008. 65(1): 150–153.
- [19] Kalishwaralal, K., et al., Extracellular biosynthesis of silver nanoparticles by the culture supernatant of *Bacillus licheniformis*. *Materials Letters*, 2008. 62(29): 4411–4413.
- [20] Mukherjee, P., et al., Green synthesis of highly stabilized nanocrystalline silver particles by a non-pathogenic and agriculturally important fungus *T. asperellum*. *Nanotechnology*, 2008. 19(7): p. 075103.
- [21] Gaikwad, S.C., et al., Screening of different *Fusarium* species to select potential species for the synthesis of silver nanoparticles. *Journal of the Brazilian Chemical Society*, 2013. 24: 1974–1982.
- [22] Boroumand Moghaddam, A., et al., Nanoparticles biosynthesized by fungi and yeast: A review of their preparation, properties, and medical applications. *Molecules*, 2015. 20(9): 16540–16565.
- [23] Dias, M.A., et al., Removal of heavy metals by an *Aspergillus terreus* strain immobilized in a polyurethane matrix. *Letters in Applied Microbiology*, 2002. 34(1): 46–50.
- [24] Ahmad, A., et al., Extracellular biosynthesis of silver nanoparticles using the fungus *Fusarium oxysporum*. *Colloids and Surfaces B: Biointerfaces*, 2003. 28(4): 313–318.
- [25] Bansal, V., et al., Biosynthesis of zirconia nanoparticles using the fungus *Fusarium oxysporum*. *Journal of Materials Chemistry*, 2004. 14(22): 3303–3305.
- [26] Birla, S.S., et al., Rapid synthesis of silver nanoparticles from *Fusarium oxysporum* by optimizing physiocultural conditions. *The Scientific World Journal*, 2013. 2013: p. 12.

- [27] Durán, N., et al., Mechanistic aspects of biosynthesis of silver nanoparticles by several *Fusarium oxysporum* strains. *Journal of Nanobiotechnology*, 2005. 3(1): p. 8.
- [28] Mohammadian, A., S. Shojaosadati, and M. Habibi Rezaee, *Fusarium oxysporum* mediates photogeneration of silver nanoparticles. *Scientia Iranica*, 2007. 14(4): 323–326.
- [29] Sadowski, Z., et al., Synthesis of silver nanoparticles using microorganisms. *Materials Science-Poland*, 2008. 26(2): 419–424.
- [30] Khosravi, A. and S.A. Shojaosadati, Evaluation of silver nanoparticles produced by fungus *Fusarium oxysporum*. *International Journal of Nanotechnology*, 2009. 6(10–11): 973–983.
- [31] Bawaskar, M., et al., A new report on mycosynthesis of silver nanoparticles by *Fusarium culmorum*. *Current Nanoscience*, 2010. 6(4): 376–380.
- [32] Durán, N., et al., Potential use of silver nanoparticles on pathogenic bacteria, their toxicity and possible mechanisms of action. *Journal of the Brazilian Chemical Society*, 2010. 21: 949–959.
- [33] Deepa, K. and T. Panda, Synthesis of gold nanoparticles from different cellular fractions of *Fusarium oxysporum*. *Journal of Nanoscience and Nanotechnology*, 2014. 14(5): 3455–3463.
- [34] Bharde, A., et al., Extracellular biosynthesis of magnetite using fungi. *Small*, 2006. 2(1): 135–141.
- [35] Riddin, T., M. Gericke, and C. Whiteley, Analysis of the inter-and extracellular formation of platinum nanoparticles by *Fusarium oxysporum* f. sp. *lycopersici* using response surface methodology. *Nanotechnology*, 2006. 17(14): p. 3482.
- [36] Shaligram, N.S., et al., Biosynthesis of silver nanoparticles using aqueous extract from the compactin producing fungal strain. *Process biochemistry*, 2009. 44(8): 939–943.
- [37] Kathiresan, K., et al., Studies on silver nanoparticles synthesized by a marine fungus, *Penicillium fellutanum* isolated from coastal mangrove sediment. *Colloids and surfaces B: Biointerfaces*, 2009. 71(1): 133–137.
- [38] Singh, D., et al., Optimization and characterization of silver nanoparticle by endophytic fungi *Penicillium* sp. isolated from *Curcuma longa* (turmeric) and application studies against MDR *E. coli* and *S. aureus*. *Bioinorganic Chemistry and Applications*, 2014. 2014: p. 8.
- [39] Honary, S., et al., Green synthesis of silver nanoparticles induced by the fungus *Penicillium citrinum*. *Tropical Journal of Pharmaceutical Research*, 2013. 12(1): 7–11.
- [40] Maliszewska, I., A. Juraszek, and K. Bielska, Green synthesis and characterization of silver nanoparticles using ascomycota fungi *Penicillium nalgioense* AJ12. *Journal of Cluster Science*, 2014. 25(4): 989–1004.
- [41] Zhang, X., et al., Biosynthesis of size-controlled gold nanoparticles using fungus, *Penicillium* sp. *Journal of Nanoscience and Nanotechnology*, 2009. 9(10): 5738–5744.

- [42] Maliszewska, I., *Microbial Synthesis of Metal Nanoparticles*, in *Metal Nanoparticles in Microbiology*, M. Rai and N. Duran, Editors. 2011, Springer Berlin Heidelberg: Berlin, Heidelberg, 153–175.
- [43] Khalil, N.M., Biogenic silver nanoparticles by *Aspergillus terreus* as a powerful nanoweapon against *Aspergillus fumigatus*. *African Journal of Microbiology Research*, 2013. 7(50): 5645–5651.
- [44] Hennebel, T., et al., Biogenic metals in advanced water treatment. *Trends in Biotechnology*, 2009. 27(2): 90–98.
- [45] Xie, J., et al., Silver nanoplates: From biological to biomimetic synthesis. *ACS Nano*, 2007. 1(5): 429–439.
- [46] Gajbhiye, M., et al., Fungus-mediated synthesis of silver nanoparticles and their activity against pathogenic fungi in combination with fluconazole. *Nanomedicine: Nanotechnology, Biology and Medicine*, 2009. 5(4): 382–386.
- [47] Ghaseminezhad, S.M., S. Hamed, and S.A. Shojaosadati, Green synthesis of silver nanoparticles by a novel method: Comparative study of their properties. *Carbohydrate Polymers*, 2012. 89(2): 467–472.
- [48] Priyadarshini, S., et al., Synthesis of anisotropic silver nanoparticles using novel strain, *Bacillus flexus* and its biomedical application. *Colloids and Surfaces B: Biointerfaces*, 2013. 102: 232–237.
- [49] Alani, F., M. Moo-Young, and W. Anderson, Biosynthesis of silver nanoparticles by a new strain of *Streptomyces* sp. compared with *Aspergillus fumigatus*. *World Journal of Microbiology and Biotechnology*, 2012. 28(3): 1081–1086.
- [50] Sagar, G. and B. Ashok, Green synthesis of silver nanoparticles using *Aspergillus niger* and its efficacy against human pathogens. *European Journal of Experimental Biology*, 2012. 2: 1654–1658.
- [51] Kumar, A., et al., Silver-nanoparticle-embedded antimicrobial paints based on vegetable oil. *Natural Matererial*, 2008. 7(3): 236–241.
- [52] Ranjbar Navazi, Z., M. Pazouki, and F.S. Halek, Investigation of culture conditions for biosynthesis of silver nanoparticles using *Aspergillus fumigatus*. *Iranian Journal of Biotechnology*, 2010. 8(1): 56–61.
- [53] Jaidev, L.R. and G. Narasimha, Fungal mediated biosynthesis of silver nanoparticles, characterization and antimicrobial activity. *Colloids and Surfaces B: Biointerfaces*, 2010. 81(2): 430–433.
- [54] Verma, V.C., R.N. Kharwar, and A.C. Gange, Biosynthesis of antimicrobial silver nanoparticles by the endophytic fungus *Aspergillus clavatus*. *Nanomedicine*, 2009. 5(1): 33–40.
- [55] Li, G., et al., Fungus-mediated green synthesis of silver nanoparticles using *Aspergillus terreus*. *International Journal of Molecular Sciences*, 2011. 13(1): 466–476.

- [56] Saravanan, M. and A. Nanda, Extracellular synthesis of silver bionanoparticles from *Aspergillus clavatus* and its antimicrobial activity against MRSA and MRSE. *Colloids and Surfaces B: Biointerfaces*, 2010. 77(2): 214–218.
- [57] Raliya, R. and J.C. Tarafdar, Biosynthesis and characterization of zinc, magnesium and titanium nanoparticles: An eco-friendly approach. *International Nano Letters*, 2014. 4(1): 93.
- [58] Reese, R. and D.R. Winge, Sulfide stabilization of the cadmium-gamma-glutamyl peptide complex of *Schizosaccharomyces pombe*. *Journal of Biological Chemistry*, 1988. 263(26): 12832–12835.
- [59] Dameron, C.T., et al., Biosynthesis of cadmium sulphide quantum semiconductor crystallites. *Nature*, 1989. 338(6216): 596–597.
- [60] Kowshik, M., et al., Microbial synthesis of semiconductor PbS nanocrystallites. *Advanced Materials*, 2002. 14(11): 815.
- [61] Ahmad, A., et al., Fungus-based synthesis of chemically difficult-to-synthesize multifunctional nanoparticles of CuAlO₂. *Advanced Materials*, 2007. 19(20): 3295–3299.
- [62] Agnihotri, M., et al., Biosynthesis of gold nanoparticles by the tropical marine yeast *Yarrowia lipolytica* NCIM 3589. *Materials Letters*, 2009. 63(15): 1231–1234.
- [63] Pimprikar, P.S., et al., Influence of biomass and gold salt concentration on nanoparticle synthesis by the tropical marine yeast *Yarrowia lipolytica* NCIM 3589. *Colloids and Surfaces B: Biointerfaces*, 2009. 74(1): 309–316.
- [64] Mukherjee, P., et al., Fungus-mediated synthesis of silver nanoparticles and their immobilization in the mycelial matrix: A novel biological approach to nanoparticle synthesis. *Nano Letter*, 2001. 1: 515–519.
- [65] Mukherjee, P., et al., Bioreduction of AuCl₄⁻ ions by the fungus, *Verticillium* sand surface trapping of the gold nanoparticles formed. *Angewandte Chemie International Edition*, 2001. 40(19): 3585–3588.
- [66] Devi, T.P., et al., *Biosynthesis of silver nanoparticles from Trichoderma species*. *Indian J Exp Biol*, 2013. 51(7): p. 543-7.
- [67] Gade, A., et al., Screening of different species of *Phoma* for the synthesis of silver nanoparticles. *Biotechnology and Applied Biochemistry*, 2013. 60(5): 482–493.
- [68] Zhang, W., et al., Biosynthesis and structural characteristics of selenium nanoparticles by *Pseudomonas alcaliphila*. *Colloids Surf B Biointerfaces*, 2011. 88(1): 196–201.
- [69] Rauter, H., et al., Nanotechnology for smart polymer optical devices. *Macromolecular Symposia*, 2004. 217(1): 109–134.
- [70] Schrand, A.M., et al., Can silver nanoparticles be useful as potential biological labels? *Nanotechnology*, 2008. 19(23): 235104.
- [71] Jin, R., The impacts of nanotechnology on catalysis by precious metal nanoparticles. *Nanotechnology Reviews*, 2012. 1(1): 31–56.

- [72] Yamanaka, M., K. Hara, and J. Kudo, Bactericidal actions of a silver ion solution on *Escherichia coli*, studied by energy-filtering transmission electron microscopy and proteomic analysis. *Applied and Environmental Microbiology*, 2005. 71(11): 7589–7593.
- [73] Navarro, E., et al., Toxicity of silver nanoparticles to *Chlamydomonas reinhardtii*. *Environmental Science & Technology*, 2008. 42(23): 8959–8964.
- [74] Aymonier, C., et al., Hybrids of silver nanoparticles with amphiphilic hyperbranched macromolecules exhibiting antimicrobial properties. *Chemical Communications*, 2002(24): 3018–3019.
- [75] Schabes-Retchkiman, P.S., et al., Biosynthesis and characterization of Ti/Ni bimetallic nanoparticles. *Optical Materials*, 2006. 29(1): 95–99.
- [76] Ping, G., et al., Preparation and antibacterial activity of $\text{Fe}_3\text{O}_4/\text{Ag}$ nanoparticles. *Nanotechnology*, 2007. 18(28): 285604.
- [77] Jo, Y.K., B.H. Kim, and G. Jung, Antifungal activity of silver ions and nanoparticles on phytopathogenic fungi. *Plant Disease*, 2009. 93(10): 1037–1043.
- [78] Kim, J.A., et al., Role of cell cycle on the cellular uptake and dilution of nanoparticles in a cell population. *Nature Nanotechnology*, 2012. 7(1): 62–68.
- [79] Prabhu, S. and E.K. Poullose, Silver nanoparticles: Mechanism of antimicrobial action, synthesis, medical applications, and toxicity effects. *International Nano Letters*, 2012. 2(1): 32.
- [80] Lemire, J.A., J.J. Harrison, and R.J. Turner, Antimicrobial activity of metals: Mechanisms, molecular targets and applications. *Nature Reviews Microbiology*, 2013. 11(6): 371–384.
- [81] Saharan, V., et al., Synthesis of chitosan based nanoparticles and their in vitro evaluation against phytopathogenic fungi. *International Journal of Biological Macromolecules*, 2013. 62: 677–683.
- [82] Rudramurthy, R.G., et al., Nanoparticles: Alternatives against drug-resistant pathogenic microbes. *Molecules*, 2016. 21(7): 836.
- [83] von Nussbaum, F., et al., Antibacterial natural products in medicinal chemistry—exodus or revival? *Angewandte Chemie International Edition*, 2006. 45(31): 5072–5129.
- [84] Rahimi, G., F. Alizadeh, and A. Khodavandi, Mycosynthesis of silver nanoparticles from *Candida albicans* and its antibacterial activity against *Escherichia coli* and *Staphylococcus aureus*. *Tropical Journal of Pharmaceutical Research*, 2016. 15(2): 371–375.
- [85] Waghmare, S.R., et al., Ecofriendly production of silver nanoparticles using *Candida utilis* and its mechanistic action against pathogenic microorganisms. *3 Biotechnology*, 2015. 5(1): 33–38.
- [86] Nanda, A. and M. Saravanan, Biosynthesis of silver nanoparticles from *Staphylococcus aureus* and its antimicrobial activity against MRSA and MRSE. *Nanomedicine: Nanotechnology, Biology and Medicine*, 2009. 5(4): 452–456.

- [87] Marambio-Jones, C. and E.M.V. Hoek, A review of the antibacterial effects of silver nanomaterials and potential implications for human health and the environment. *Journal of Nanoparticle Research*, 2010. 12(5): 1531–1551.
- [88] Bhati-Kushwaha, H., A. Kaur, and C. Malik, The synthesis and role of biogenic nanoparticles in overcoming chilling stress. *Indian Journal of Plant Sciences*, 2013. 2(4): 54–62.
- [89] Feng, Q., et al., A mechanistic study of the antibacterial effect of silver ions on *Escherichia coli* and *Staphylococcus aureus*. *Journal of Biomedical Materials Research*, 2000. 52(4): 662–668.
- [90] Guggenbichler, J.P., et al., A new technology of microdispersed silver in polyurethane induces antimicrobial activity in central venous catheters. *Infection*, 1999. 27(1): S16–S23.
- [91] Gopinath, P.M., et al., Multi-functional nano silver: A novel disruptive and theranostic agent for pathogenic organisms in real-time. *Scientific Reports*, 2016. 6: 34058.
- [92] Davies, R.L. and S.F. Etris, The development and functions of silver in water purification and disease control. *Catalysis Today*, 1997. 36(1): 107–114.
- [93] Fox, C.L. and S.M. Modak, Mechanism of Silver Sulfadiazine Action on Burn Wound Infections. *Antimicrobial Agents and Chemotherapy*, 1974. 5(6): 582–588.
- [94] Jeyaraj, M., et al., An investigation on the cytotoxicity and caspase-mediated apoptotic effect of biologically synthesized silver nanoparticles using *Podophyllum hexandrum* on human cervical carcinoma cells. *Colloids Surf B Biointerfaces*, 2013. 102: 708–717.
- [95] Abraham, I., et al., Current status on Marine products with reversal effect on cancer multidrug resistance. *Marine Drugs*, 2012. 10(10): 2312–2321.
- [96] Rai, M., et al., Broad-spectrum bioactivities of silver nanoparticles: The emerging trends and future prospects. *Applied Microbiology and Biotechnology*, 2014. 98(5): 1951–1961.
- [97] Misra, R., S. Acharya, and S.K. Sahoo, Cancer nanotechnology: Application of nanotechnology in cancer therapy. *Drug Discovery Today*, 2010. 15(19–20): 842–850.
- [98] Seigneuric, R., et al., From nanotechnology to nanomedicine: Applications to cancer research. *Current Molecular Medicine*, 2010. 10(7): 640–652.
- [99] Joshi, P., et al., The anticancer activity of chloroquine-gold nanoparticles against MCF-7 breast cancer cells. *Colloids and Surfaces B: Biointerfaces*, 2012. 95: 195–200.
- [100] Justin Packia Jacob, S., J.S. Finub, and A. Narayanan, Synthesis of silver nanoparticles using *Piper longum* leaf extracts and its cytotoxic activity against Hep-2 cell line. *Colloids and Surfaces B: Biointerfaces*, 2012. 91: 212–214.
- [101] Satyavani, K., et al., Toxicity study of silver nanoparticles synthesized from Suaeda Monoica on Hep-2 cell line. *Avicenna Journal of Medical Biotechnology*, 2012. 4(1): 35–39.
- [102] Prabhu, D., et al., Biologically synthesized green silver nanoparticles from leaf extract of *Vitex negundo* L. induce growth-inhibitory effect on human colon cancer cell line HCT15. *Process Biochemistry*, 2013. 48(2): 317–324.

- [103] Mendoza, F.J., et al., Anti-tumor chemotherapy utilizing peptide-based approaches- apoptotic pathways, kinases, and proteasome as targets. *Archivum Immunologiae et Therapiae Experimentalis*, 2005. 53(1): 47–60.
- [104] Sriram, M.I., et al., Antitumor activity of silver nanoparticles in Dalton's lymphoma ascites tumor model. *International Journal of Nanomedicine*, 2010. 5: 753–762.

Cerium Oxide Nanostructures and their Applications

Adnan Younis, Dewei Chu and Sean Li

Additional information is available at the end of the chapter

<http://dx.doi.org/10.5772/65937>

Abstract

Due to excellent physical and chemical properties, cerium oxide (ceria, CeO_2) has attracted much attention in recent years. This chapter aimed at providing some basic and fundamental properties of ceria, the importance of oxygen vacancies in this material, nano-size effects and various synthesis strategies to form diverse structural morphologies. Finally, some key applications of ceria-based nanostructures are reviewed. We conclude this chapter by expressing personal perspective on the probable challenges and developments of the controllable synthesis of CeO_2 nanomaterials for various applications.

Keywords: biofilm, wastewater treatment, biofilm technologies, molecular methods, biofilter media, ceria, metal oxide, nanostructure, nanocomposite, redox reactions, oxygen vacancies

1. Introduction

In nanotechnology, nanomaterials play a vital role in various fields of science, such as physics, chemistry and materials sciences. As a key component of nanomaterials, nanoparticles are single particles or species whose diameter ranges from one to few tens of nanometres. Over the past few years, considerable efforts were made to develop many nanoparticles/nanocrystals for the development of new cutting-edge applications in communications, energy storage, sensing, data storage, optics, transmission, environmental protection, cosmetics, biology and medicine. Due to their limited size and a high density of corner or edge surface sites, the

nanocrystals can exhibit unique physical and chemical properties, including optical, electrical and magnetic properties.

Due to reduced sizes, the nanoparticles possess high surface to volume ratios, which make them highly reactive with distinct characteristics. It is highly desirable to tune the properties of materials through various means such as shapes, morphologies and surface to volume ratios. Over the past few years, the researchers and scientists have made enormous efforts to develop nanoparticles with controlled morphologies, shapes and size. There are various possible synthesis routes, including liquid (chemical method), solid and gaseous media [3–15] for the synthesis of nanocrystals. However, chemical routes are considered as the most popular methods to synthesize nanoparticles, which can offer the advantages of low cost, eco-friendliness and reliability over other methods. Moreover, this method can also offer rigorous control on shape- and size-controlled synthesis of the nanoparticles.

Till now, nanoparticles of many materials, including metal oxides, ferrites, rare-earth oxides and so on, have been developed. Cerium (Ce) belong to rare-earth family and its abundance is much higher than copper and tin (66.5 and 60 ppm, respectively) [1–2]. Its high abundance made this material technologically important with wide applications in various sectors, such as auto-exhaust catalyst [3], low-temperature water-gas shift (WGS) reaction [4], oxygen sensors [5], oxygen permeation membrane systems [6], fuel cells [7, 8], glass-polishing materials [9], electrochromic thin-film application [10], as well as biotechnology, environmental chemistry and medicine [11, 12].

It is generally believed that the reduced particle sizes may originate at high interface densities and hence may lead to enhanced non-stoichiometry levels [13]. Based on this, a lot of attention was paid to explore the nanostructures' ceria interfacial redox reactions and transport properties with respect to bulk ceria.

This chapter is organised as follows. Section 2 presents cerium oxide (CeO_2) and material properties of CeO_2 . Section 3 describes imperfections/defect chemistry in CeO_2 . Section 4 describes the importance of oxygen vacancies in ceria. Section 5 presents nano-size effect. In Section 6, applications of CeO_2 in various fields are described. Finally, Section 7 presents concluding remarks and outlook.

2. Cerium oxide (CeO_2): material properties

2.1. Electronic structure

Cerium dioxide (CeO_2 /ceria) is considered the most stable oxide of the cerium. Cerium is the second member and the most reactive element in the lanthanide series. Being electropositive in nature, cerium exists in dual oxidation modes, Ce^{3+} and Ce^{4+} . The Ce^{4+} oxidation state is usually considered more stable than $3+$ due to $\text{Ce}(4+)$ electronic structure $[\text{Xe}]4f^0$ being more stable state as empty than $[\text{Xe}]4f^1$ for Ce^{3+} . Cerium usually has two types of oxides named cerium dioxide (CeO_2) and cerium sesquioxide (Ce_2O_3), but in a larger context, CeO_2 is used as cerium oxide due to higher stability over Ce_2O_3 .

2.2. Crystal structure

Cerium dioxide (CeO_2) has a fluorite structure (FCC) with space group $\text{Fm}\bar{3}\text{m}$ and it consists of a simple cubic oxygen sub-lattice with the cerium ions occupying alternate cube centres as shown in **Figure 1**. **Figure 1** illustrates the structure of the stoichiometric CeO_2 with the four coordinated oxygen (represented by solid red big balls) and the eight coordinated cerium (represented by solid blue small balls). Cerium is at the centre of tetrahedron whose corners are occupied by oxygen atoms [14].

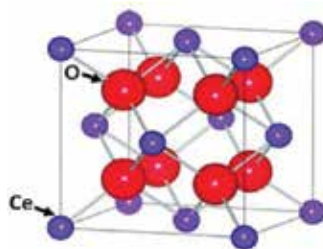


Figure 1. FCC structure for CeO_2 [14].

2.3. Microstructure

The microstructure of CeO_2 thin films can be of various shapes depending on substrate material, deposition method, deposition parameters and composition contents. Therefore, the film growth can result in epitaxial films on the one hand or polycrystalline films with varying grain sizes from few nanometres up to several hundred micrometres on the other hand. Polycrystalline films consist of a certain number of grains, which can play a key role in the electrical conduction process in thin films by forming depletion layers with low conductivity similar to Schottky barriers in metal-insulator junctions [15].

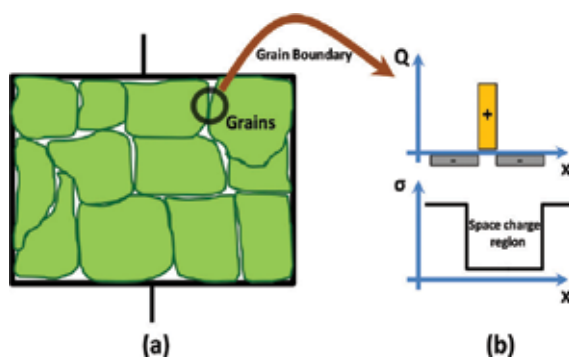


Figure 2. (a) Cross-section of a polycrystalline thin film capacitor showing grains. The crystal orientation and size of the grains depends on the preparation parameters. (b) Space charge region and the consequent change of the conductivity at the grain boundaries.

Figure 2(a) represents a schematic cross-section of a ceramic thin film capacitor with grains randomly distributed in between capacitor plates. The region between the grains in **Figure 2(b)** shows the space-charge region and the reduced conductivity due to the immovable positive charges. For thin films with smaller grain sizes, the space-charge region can exceed the grain size, leading to entirely depleted films with locally distributed conductivities far below the bulk conductivity of the material [16].

3. Imperfections/defect chemistry in bulk ceria

For an ideal crystalline solid, atoms are periodically arranged in a regular and symmetrical way. The formation of a crystal structure is based on the combination of a basis and infinite space lattice. This space lattice can be further split into unit cells and the combination of identical cells forms the entire crystalline structure. Imperfections in crystal structures are occurred by displacing atoms from their lattice positions that lead to break symmetry of the perfect periodic crystal lattice. In ceria, the intrinsic and extrinsic defects can exist. The presence of intrinsic defect may be due to thermal disorderness in crystal, which can be formed by redox reactions between the solid and surrounding atmosphere. Frenkel and Schottky defects are considered to be more plausible crystalline intrinsic defects. The extrinsic defects in crystal may be formed by introducing foreign dopant or due to impurities.

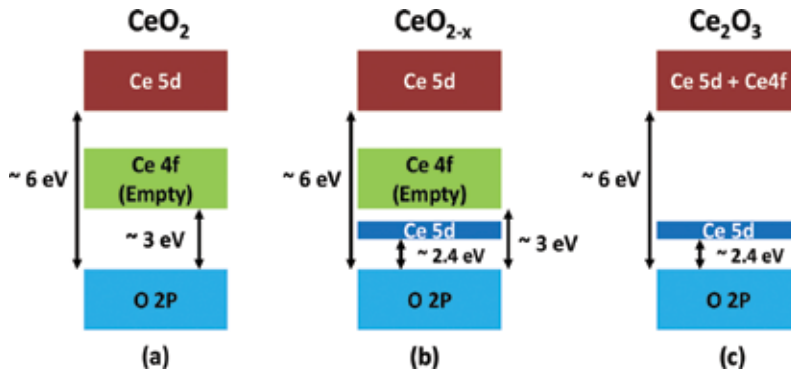


Figure 3. Schematic electronic structures of (a) stoichiometric CeO_2 , (b) partially reduced CeO_{2-x} and (c) Ce_2O_3 . Blue blocks represent filled bands, whereas green and red blocks are drawn as empty boxes.

The most dominant and stable known defects in ceria are linked to the presence of oxygen vacancies under a wide range of conditions. A reversible transition in the oxidation state of two cerium ions from Ce^{3+} to Ce^{4+} may generate neutral oxygen vacancies in ceria. The process can be shown as



Thus, a neutral species $\frac{1}{2}\text{O}_2$ (g) is formed if an oxygen ion (O^{2-}) leaves the ceria lattice. The two electrons left behind were trapped at two cerium sites, i.e. they become localized at two cerium sites. At such cerium sites, the electron prefers to occupy an empty Ce4f state that splits the Ce4f band into two sub-bands: an occupied Ce4f full band and an empty Ce4f empty band as shown in **Figure 3**.

Practically, the reduction limit of non-stoichiometric ceria is Ce_2O_3 , where all cerium ions are found in a Ce^{3+} oxidation state. The electronic band structure of Ce_2O_3 bears resemblance to that of partially reduced ceria, in which Ce4f empty and Ce5d bands have been merged together in the conduction band as shown in **Figure 3(c)**.

4. Importance of oxygen vacancies in CeO_2

Cerium oxide can accommodate high oxygen deficiency by the substitution of lower valent elements on the cation sub-lattice. Due to this property, high oxygen ion conductivities are expected, which indicate towards its potential applications as a solid electrolyte in solid oxide fuel cells (SOFCs) [17]. At the same time, CeO_2 is also well known to release significant levels of oxygen at low oxygen partial pressures (P_{O_2}) and elevated temperatures leading to a mixed ionic electronic conductivity. Due to ease in redox-based reactions, ceria can easily occupy multiple oxidation states such as $\text{Ce}(3+)$ and $\text{Ce}(4+)$; therefore, electrons in ceria can be thought to exist as small polarons. The motion of the electrons in the ceria lattice can be imagined as a thermally mediated hopping mechanism [18]. For carrier and transport properties, the concentration of vacancies that are more mobile and can contribute to oxygen-ion transport in the solid solutions should be taken into account [19].

Generally, three low-index lattice planes exist on the surface of CeO_2 nanocrystals: (100), (110) and (111). From **Figure 4**, the stability of all three planes is different and follows the sequence $(111) > (110) > (100)$, whereas the activity follows the reverse order [20–23].

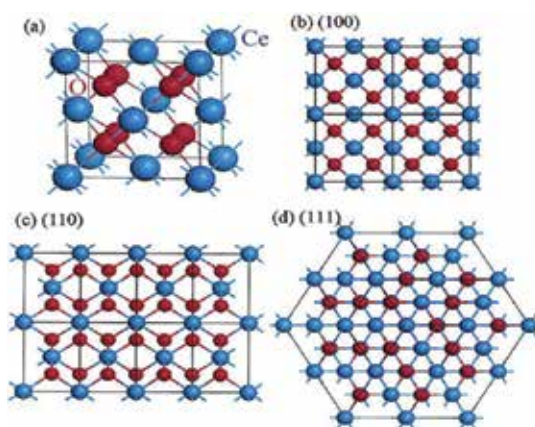


Figure 4. (a) Face-centred crystal cell of the CeO_2 structure. (b–d) The (100) [or (200)], (110) and (111) planes of the CeO_2 structure. (Reprinted with permission from reference [24] © 2003 American Chemical Society.)

The formation energy of oxygen vacancies at (111) exposed facet is higher than (110) and (100) facets; therefore, there are more oxygen vacancies on the (110) and (100) planes than (111). For example, nanoparticles usually constitute octahedral or truncated octahedral shapes and they are mainly exposed to most stable (111) facets to keep surface energy as minimum as possible. While 1D nanostructures such as nanorods and nanowires possess the (110) and (100) planes, 3D nanocubes can expose (100) planes. Therefore, nanorods and nanocubes should have more oxygen vacancies on their surfaces. Meanwhile, the concentration of oxygen vacancies in the crystal can also be influenced by many other internal or external factors, such as temperature and doping elements, etc. [25]. The existence of oxygen vacancies and their transportation in crystal are very important phenomena. Higher concentration of oxygen vacancies provides ease in the movement of oxygen atoms within crystal, which favour redox reactions on its surface for excellent catalytic activities.

5. Nano-size effects

By decreasing particle size, ceria nanoparticles demonstrate the formation of more oxygen vacancies. The large surface area to volume ratio existing in a nanoparticle enables CeO_2 to react differently resulting in unique properties. For instance, two orders of magnitude high catalytic activity for CO oxidation was observed by synthesizing 3–4 nm sized CeO_2 nanoparticles supporting Au over a regular bulk cerium oxide support medium [26, 31]. Therefore, it is feasible to tune the specific reactivity of ceria nanoparticles by controlling their size. Furthermore, nano-sized CeO_2 can have enhanced electronic conductivity, size lattice relaxation and many other effects as compared to bulk ceria.

Additionally, for determining particle reactivity, building nano-sized particle is very crucial in a way that the lattice of nanoceria expands if the particle size is reduced. The expansion of lattice would decrease its oxygen release and reabsorption capabilities. A detailed electron diffraction study on nanoceria was conducted previously [27] in which a systematic lattice expansion was observed by reducing the size of ceria particles down to nanoscale over bulk ceria. Their findings suggested that by having ultra-small-sized (1.1 nm) ceria nanoparticle, a large fraction of the cerium atoms occupy fully reduced state, even though the ceria nanoparticles retain a cubic-shaped lattice rather than hexagonal lattice [27]. In another theoretical study on ceria nanoparticles, the simulation calculations revealed that by increasing ceria particle size the formation energy of oxygen vacancies is reduced [28].

6. Applications of ceria

Being technologically important functional material, ceria has remarkable applications in many diverse fields. In this section, a brief discussion on some of the most widely known commercial and industrial applications of ceria and nanoceria is presented.

6.1. Solid oxide fuel cells

Solid oxide fuel cells (SOFCs) are considered to have great potential in providing clean and reliable electric power; therefore, research in this area attracts great attention in recent years. Many reports suggest that ceria-based ion conductors possess huge resistance to carbon deposition and have potential to allow unstoppable supply of dry hydrocarbon fuels to the anode [29, 30].

Gorte and Vohs [31] first demonstrated a direct electrochemical oxidation of hydrocarbons such as methane and toluene using SOFC at 973 and 1073 K with copper and ceria composite. The anode was designed as Cu/CeO₂/YSZ, with Cu primarily utilized as the current collector and the function of CeO₂ was to impart catalytic activity for the required oxidation reactions. These anodes were found to have inherently high redox stability, large sulphur tolerance and were operative with sulphur contents up to 400 ppm without losing its significance performance [32].

Ceria-based ceramics are well known to exhibit mixed ionic and electronic conductivity in a reducing atmosphere due to reversible redox transition between Ce³⁺ and Ce⁴⁺. Additionally, their excellent catalytic activities also correspond to ease in an oxygen-vacancy formation mechanism. Another effective method to increase the reforming reactions of hydrocarbon, i.e. to facilitate C–H bond breaking process is the addition of noble metals, such as Pt, Rh, Pd and Ru.

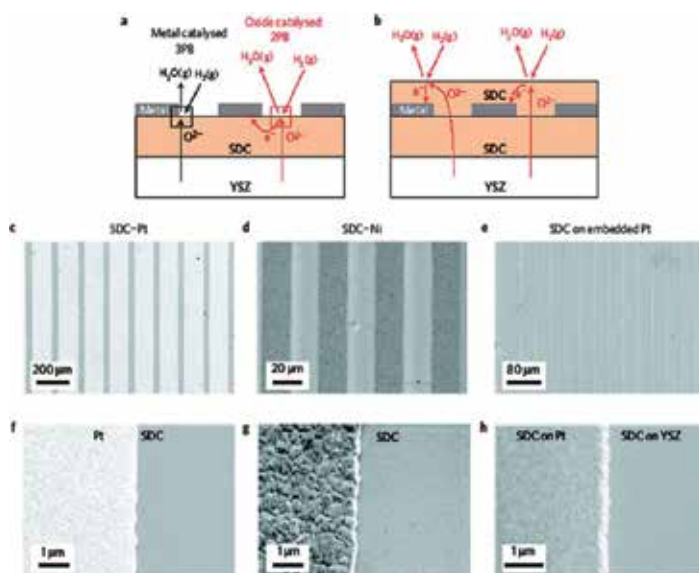


Figure 5. Metal patterning on ceria thin films. (a) Schematic figure showing the macroscopic reaction sites and the steps involved for surface reaction and bulk diffusion. (b) Patterned electrode with an embedded current collector that restricts the metallic phase contribution. (c–h) After electrochemical characterisation, the SEM images were recorded under humid atmospheres at 650°C. (SDC ¼ Sm0.2Ce0.8O1.9d, YSZ ¼ Y0.16Zr0.84O1.92). (Reprinted from reference [35] with permission from Nature Publishing Group.)

Gd-doped CeO_2 -based electrolyte films having Ru and Ni as incorporated metals were fabricated to evaluate the role of metal catalysts in anode reactions by Hibino et al. [33, 34].

The anodes were directly operated on various hydrocarbons at 600°C and the results demonstrated that the presence of Ru catalyst favours the reforming reactions of unreacted hydrocarbons by steam and carbon dioxide. This further avoids the gas-phase diffusion of fuels by restricting the interference of steam and CO_2 . The obtained power density in this case was 750 mW cm^{-2} with dry methane, which was quite analogous to the power density of 769 mW cm^{-2} achieved with wet hydrogen [33, 34].

The reduction of activation over potential for hydrogen oxidation by having ceria-based anodes for SOFC has been exemplified in many reports. Moreover, well-defined geometry and having porous or composite electrodes structure based on ceria were also described. In a report, Chueh et al. [35] demonstrated well-defined interferences occupied ceria-metal structures, in which near-equilibrium H_2 oxidation reaction pathway was subjugated by electrocatalysis at the oxide-gas interface with a minimal contribution that was observed from oxide-metal-gas triple-phase boundaries as shown in **Figure 5**. The similar phenomenon was observed even for structures with reaction site densities approaching those of commercial SOFCs [35].

By keeping the ceria-catalysed reaction site density fixed as 2PB, the density of metal-catalysed reaction site (3PB) was varied by a factor of 16; no substantial change was observed in the electrochemical activity. Later on, the addition of metals did not put much impact on the electrochemical activities, respectively. They conclude that the rational design of ceria nanostructures promote electrochemical activities and thus provide a new route to achieve high performance [35].

6.2. Catalytic applications

The tendency of oxygen uptake and release of ceria due to reversible transition between Ce^{3+} and Ce^{4+} makes this material a key ingredient for catalytic applications and reactions. Various nano-micro ceria structures have been fabricated, and their catalytic applications are extensively reported in recent years.

Carbon monoxide (CO) oxidation is the most exclusively studied reaction in this category. During CO oxidation, ceria nanomaterials can elevate the oxygen storage capability of catalysts at low temperatures. Generally, high surface area occupied nanomaterials are considered ideal for this application. The high surface area provides a greater tendency to active species to contact with reactants, and therefore an enhanced catalytic performance can be expected. There are different reports that discuss various morphologies to evaluate the CO oxidation performance. For instance, nanotubes exhibit inner and outer surfaces that unadventurously provide active sites for the reactants adsorption that leads to better catalytic performance in CO oxidation [36]. On the other hand, nano-sized particles also exhibit high surface area, but demonstrate poor catalytic performance; while nanorods, with low surface area and larger diameter, were found to be more active in CO oxidation [37–40]. This unusual behaviour of diverse morphologies is mainly attributed to the exposed planes. For example, the nanoparticles have dominant (111) exposed planes, whereas the nanorods' edges are terminated by

(110) and (100) planes. The (110) and (100) planes are considered to be more active than the (111) plane and hence are found to express significantly enhanced redox properties required for excellent catalytic activities in CO oxidation.

In a study, Kayama et al. [41] introduced a new concept of fabricating ceria particles' aggregates around central silver metal (rice-ball-like structure) which is quite different than conventional core-shell-like configuration. The catalytic activities of fabricated structure were evaluated, and it was found that below 300°C CeO₂-Ag oxidizes soot much more efficiently than pure CeO₂ and Ag-CeO₂ that oxidize soot above 300°C as shown in **Figure 6**.

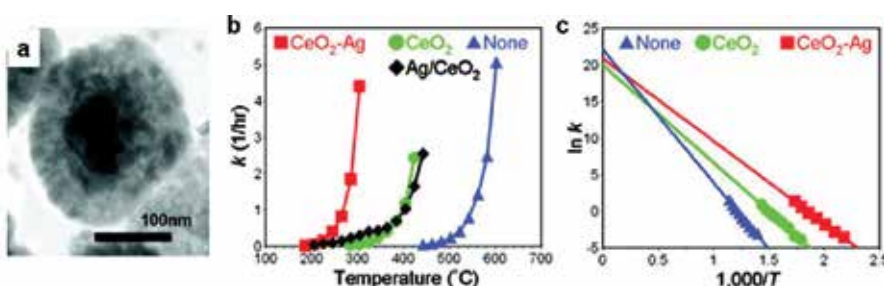


Figure 6. (a) Transmission electron microscopy image of rice-ball nanostructured CeO₂-Ag; (b and c) evaluation of properties in the presence and absence of a catalyst; (b) evaluations of carbonaceous soot oxidation; (c) Arrhenius plots. (Reprinted with permission from reference [41]. Copyright 2010 American Chemical Society.)

In the absence of rice-ball nanostructure, the oxidation by the catalyst was inefficient at low temperatures below 300°C. Therefore, it was suggested that the synthesis mechanism of the rice-ball-like structure can potentially be extended to other compositions.

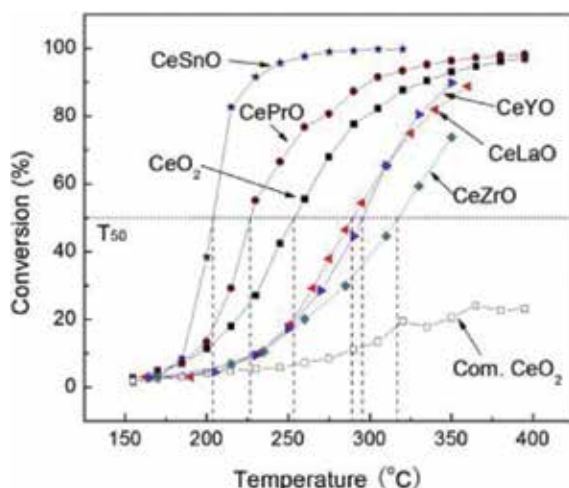


Figure 7. Conversion profile of carbon monoxide versus temperature. (Reprinted from reference [42] with permission from Elsevier Ltd.)

Doping foreign elements into ceria matrix can considerably tune the inherent physical and chemical properties of ceria. To keep this in mind, Y-, La-, Zr-, Pr- and Sn-doped ceria were reported by Xiao et al. [42]. In their work, they fabricated a flower-like structure, and the catalytic activities towards CO oxidation were recorded for all dopant elements as shown in Figure 7.

From the figure, two main observations were recorded. (i) The doping of Sn and Pr enhanced the catalytic activities of ceria-based nanoflower structure and this behaviour was attributed to the variable valence states of Pr and Sn. (ii) The doping of Y, La and Zr in CeO_2 did not express considerable catalytic activities, and this trend was explained on the basis of the stable valence states of dopants. Also, they suggested that the doping cations having stable valence state partially suppress the redox reactions, i.e. Ce^{4+} to Ce^{3+} conversion which ultimately suppress the oxygen storage capacity in ceria.

6.3. Photocatalysis

Globally, efficient visible light photocatalytic water splitting is an active area of research for renewable energy as well as water and air purification. A novel and efficient Au-supported CeO_2 nanoparticle-based photocatalysts were fabricated, and its visible light activities were reported by Primo et al. [43]. Excellent photocatalytic activity of ceria nanoparticles was observed for oxygen generation from water as shown in Figure 8.

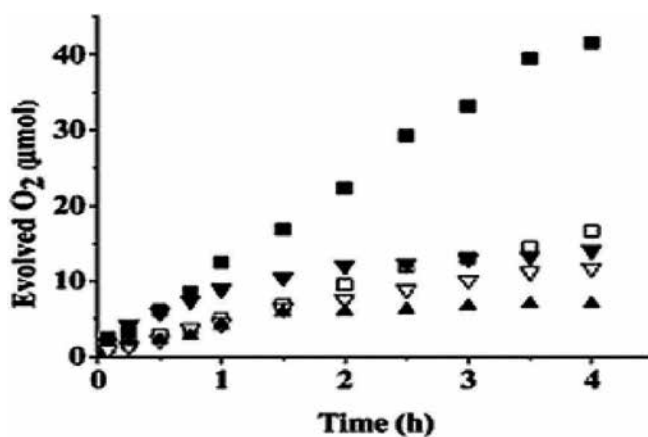


Figure 8. (a) Oxygen evolved upon visible light ($\lambda > 400$ nm) illumination of an aqueous AgNO_3 suspension containing the photocatalysts. ■ Au (1.0 wt%)/ CeO_2 (A); □ Au (1.0 wt%)/ CeO_2 (B); ▼ Au (3.0 wt%)/ CeO_2 (A); ▽ Au (3.0 wt%)/ CeO_2 (B); ▲ $\text{WO}_3\cdot\text{CeO}_2$ (A) was prepared by biopolymer template synthesis whilst CeO_2 (B) was obtained from Aldrich. (Reprinted with permission from reference [43]. Copyright 2011 American Chemical Society.)

Figure 8 shows the evolved oxygen over time for visible-light illumination for various Au loadings on CeO_2 catalysts. The sample, with 1.0 wt% loading of Au, renders a more profound photocatalyst than 3.0 wt% Au. Under UV light illumination, the ceria sample (A) prepared by the novel biopolymer template procedure having smaller particle size was found to be more efficient than the large particle-sized occupied commercial CeO_2 (B) sample. Their observations

were quite different from other reports on TiO_2 and WO_3 , in which under UV light, the photocatalytic activity was poor and reduced, while Au-supported CeO_2 delivers outclass photocatalytic response under visible light.

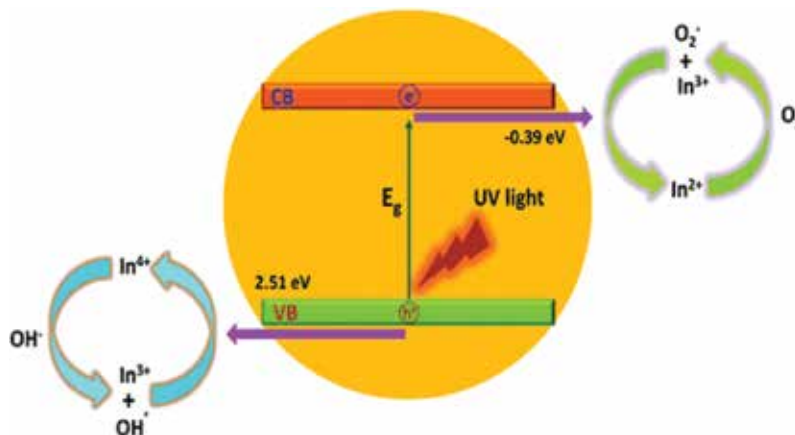


Figure 9. Schematic diagram of the degradation mechanisms for the MO dye with indium doped CeO_2 nanocrystals under ultraviolet-visible light irradiation. (Reprinted with permission from reference [44].)

Recently, our group has successfully synthesized ultra-small-sized ceria nanocubes. The effect of indium doping on oxygen vacancies' concentration and subsequently on photocatalytic response was investigated in detail [44]. Various In doping concentrations ranging from 0, 5 to 15% were fabricated and their photocatalytic responses were evaluated. By increasing Indium doping concentration, the photocatalytic activities were found to be enhanced up to a certain extent (10% In doping). After this doping concentration, the photocatalytic activities were suppressed. The possible reason may be due to the presence of In^{3+} , which may serve as an electron acceptor and electron donor simultaneously (from In^{3+} to In^{2+} and/or from In^{3+} to In^{4+}) to localize the charge carriers. This localization may further enlarge the separation of electron-hole pairs by trapping at energy levels in close proximity to the valence and conduction bands [44]. This effect is schematically described in **Figure 9**.

Ceria nanomaterials have also a potential application for environmental remediation. The photocatalytic activities of CeO_2 nanotubes and nanoparticles were investigated and compared with commercial TiO_2 (P25) as shown in **Figure 10** [45]. A well-known toxic pollutant named 'aromatic benzene' that is commonly found in urban ambient air and is of substantial concern regarding environmental health was used in photocatalytic measurements.

The results in **Figure 10** demonstrate that at the reaction time of 22 h, the CeO_2 -NT expressed excellent photocatalytic performance towards the gas-phase degradation of benzene. The amount of CO_2 over CeO_2 -NT was maintained at 29 ppm even after 10 h of reaction time. On the contrary, ceria nanoparticles and P25 nanoparticles demonstrate quite uneven photocatalytic behaviour of benzene degradation.

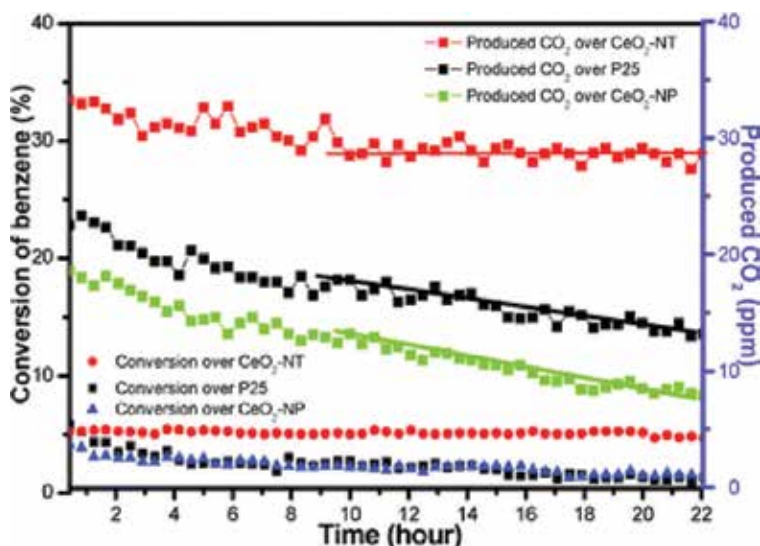


Figure 10. Time-online data for gas-phase photocatalytic degradation of benzene over the samples of commercial P25, CeO_2 nanoparticles (NPs) and the as-prepared CeO_2 nanotubes (NTs). (Reprinted from reference [45] with permission from Royal Society of Chemistry.)

7. Concluding remarks and future outlook

In this chapter, some fundamental physical and chemical properties of ceria were addressed in the beginning. In the later half, recent progress in the shape-controlled synthesis and morphology-dependant performance of ceria nano-microstructures was highlighted. Although, the microstructures, morphologies, characterization approaches and theoretical studies of ceria-based nanostructured materials are extensively investigated in recent years with the achievement of some exceptional encouraged results. However, there are still numerous contests such as cost-effective synthetic processes for morphology-dependent catalytic and biomedical applications that required more efforts to tackle the key fundamental issues.

Another important fatal issue in the preparation of ceria-based materials is 'Sintering'. Particles can easily agglomerate at high temperatures, which is a big reason for sudden drop in specific surface area of nanomaterials and reduced crystal defects. Although, the addition of rare-earth elements somehow facilitates anti-sintering phenomenon; however, this restricts the limitation of special additives in ceria-based nanomaterials. Therefore, to spread the span of nanoceria applications, this problem needs to be addressed comprehensively. Finally, vast scale production of ceria nanomaterials is also challenging. It is essentially required to develop and improve more valuable preparation of technologies for industrial and commercial applications combined with deepening comprehension of the formation mechanisms.

Author details

Adnan Younis*, Dewei Chu and Sean Li

*Address all correspondence to: a.younis@unsw.edu.au

School of Materials Science and Engineering, University of New South Wales, Sydney, Australia

References

- [1] Ahrens TJ. Global Earth Physics: Handbook of Physical Constants, American Geophysical Union, Washington DC. 1995.
- [2] Lide D. CRC Handbook of Chemistry and Physics, CRC Publishing Co., Boca Raton, FL. 88th edn. 2007.
- [3] Kaspar J, Fornasiero P, Graziani M. Use of CeO₂-based oxides in the three-way catalysis. *Catalysis Today*. 1999; 50(2): 285–298.
- [4] Fu Q, Saltsburg H, Flytzani-Stephanopoulo M. Active nonmetallic Au and Pt species on ceria-based water–gas shift catalysts. *Science*. 2003; 301(5635): 935–938.
- [5] Jasinski P, Suzuki T, Anderson HU. Nanocrystalline undoped ceria oxygen sensor. *Sensors and Actuators B Chemical*. 2003; 95(1):73–77
- [6] Yin X, Hong L, Liu ZL. Oxygen permeation through the LSCO-80/CeO₂ asymmetric tubular membrane reactor. *Journal of Membrane Science*. 2006;268(1): 2–12.
- [7] Park SD, Vohs JM, Gorte RJ. Direct oxidation of hydrocarbons in a solid oxide fuel cells. *Nature*. 2000; 404: 265–267.
- [8] Sun CW, Hui R, Roller J. Cathode materials for solid oxide fuel cells: a review. *Journal of Solid State Electrochemistry*. 2010; 14(7):1125–1144.
- [9] Feng XD, Sayle DC, Wang ZL, Paras MS, Santora B, Sutorik AC, Sayle TXT, Yang Y, Ding Y, Wang XD, Her YS. Converting ceria polyhedral nanoparticles into single-crystal nanospheres. *Science*. 2006; 312(5779):1504–1508.
- [10] Ozer N. Optical properties and electrochromic characterization of sol–gel deposited ceria films. *Solar Energy Materials and Solar Cells*. 2001; 68(3–4): 391–400.
- [11] Asati A, Santra S, Kaittanis C, Nath S, Perez JM. Oxidase-like activity of polymer-coated cerium oxide nanoparticles. *Angewandte Chemie International Edition*. 2009; 48: 2308–2312. doi:10.1002/anie.200805279.

- [12] Tarnuzzer RW, Colon J, Patil S, Seal S. Vacancy engineered ceria nanostructures for protection from radiation-induced cellular damage. *Nano Letters*. 2005; 5: 2573–2577.
- [13] Tuller HL, Ionic conduction in nanocrystalline materials. *Solid State Ionics*. 2000; 131: 143–157.
- [14] Malavasi L, Fisher CAJ, Islam MS. Oxide-ion and proton conducting electrolyte materials for clean energy applications: structural and mechanistic features. *Chemical Society Reviews*. 2010; 39(11): 4370–4387.
- [15] Neumann H, Arlt G. Maxwell-Wagner relaxation and degradation of SrTiO₃ and BaTiO₃ ceramics. *Ferroelectrics*. 1986; 69(1): 179–186.
- [16] Waser R. The role of grain boundaries in conduction and breakdown of perovskite-type titanates. *Ferroelectrics*. 1992; 133(1): 109–114.
- [17] Guo X, Waser R. Electrical properties of the grain boundaries of oxygen ion conductors: acceptor-doped zirconia and ceria. *Progress in Materials Science*. 2006; 51: 151–210.
- [18] Tuller HL, Nowick AS. Small polaron electron-transport in reduced CeO₂ single-crystals. *Journal of Physics and Chemistry of Solids*. 1977; 38: 859–867.
- [19] Kilner JA. Defects and conductivity in ceria-based oxides. *Chemical Letters*. 2008; 37: 1012–1015.
- [20] Sayle DC, Maicaneanu SA, Watson GW. Atomistic models for CeO₂(111), (110), and (100) nanoparticles, supported on yttrium-stabilized zirconia. *Journal of American Chemical Society*. 2002; 124(138): 11429–11439.
- [21] Jiang Y, Adams JB, van Schilfgaarde M. Density-functional calculation of CeO₂ surfaces and prediction of effects of oxygen partial pressure and temperature on stabilities. *Journal of Chemical Physics*. 2005; 123: 064701.
- [22] Chen Y, Hu P, Lee MH, Wang H. Au on (1 1 1) and (1 1 0) surfaces of CeO₂: a density-functional theory study. *Surface Science*. 2008; 602(10): 1736–1741.
- [23] Sayle TXT, Cantoni M, Bhatta UM, Parker SC, Hall SR, Möbus G, Molinari M, Reid D, Seal S, Sayle DC. Strain and architecture-tuned reactivity in ceria nanostructures; enhanced catalytic oxidation of CO to CO₂. *Chemistry of Materials*. 2012; 24(10): 1811–1821.
- [24] Wang ZL, Feng XD. Polyhedral shapes of CeO₂ nanoparticles. *Journal of Physical Chemistry B*. 2003; 107: 13563–13566.
- [25] Campbell CT, Peden CHF. Oxygen vacancies and catalysis on ceria surfaces. *Science*. 2005; 309: 713–714
- [26] Carrettin S, Concepcion P, Corma A, Nieto JML, Puentes VF. Nanocrystalline CeO₂ increases the activity of Au for CO oxidation by two orders of magnitude. *Angewandte Chemie International Edition*. 2004; 43: 2538–2540.

- [27] Hailstone RK, DiFrancesco AG, Leong JG, Allston TD, Reed K. J. A study of lattice expansion in CeO₂ nanoparticles by transmission electron microscopy. *Journal of Physical Chemistry C*. 2009; 113(34): 15155–15159
- [28] Migani A, Vayssilov GN, Bromley ST, Illas F, Neyman KM. Dramatic reduction of the oxygen vacancy formation energy in ceria particles: a possible key to their remarkable reactivity at the nanoscale. *Journal of Material Chemistry*. 2010; 20: 10535–10546.
- [29] Marina OA, Mogensen M. High-temperature conversion of methane on a composite gadolinia-doped ceria–gold electrode. *Applied Catalysis A*. 1999; 189: 117–126.
- [30] Gorte RJ, Vohs JM. Nanostructured anodes for solid oxide fuel cells. *Current Opinion on Colloid and Interface Science*. 2009; 14: 236–244.
- [31] Park SD, Vohs JM, Gorte RJ. Direct oxidation of hydrocarbons in a solid oxide fuel cells. *Nature*. 2000; 404: 265–267.
- [32] He HP, Gorte RJ, Vohs JM. Highly sulfur tolerant Cu–ceria anodes for SOFCs. *Electrochem. Solid-State Letters*. 2005; 8: A279–A280.
- [33] Hibino T, Hashimoto A, Yano M, Suzuki M, Sano M. Ru-catalyzed anode materials for direct hydrocarbon SOFCs. *Electrochimica Acta*. 2003; 48:2531–2537.
- [34] Hibino T, Hashimoto A, Asano K, Yano M, Suzuki M, Sano M. An intermediate-temperature solid oxide fuel cell providing higher performance with hydrocarbons than with hydrogen. *Electrochemical and Solid-State Letters*. 2002; 5:A242–A244.
- [35] Chueh WC, Hao Y, Jung W, Haile SM. High electrochemical activity of the oxide phase in model ceria–Pt and ceria–Ni composite anodes. *Nature Materials*. 2012; 11: 156–161.
- [36] Pan CS, Zhang DS, Shi LY. CTAB assisted hydrothermal synthesis, controlled conversion and CO oxidation properties of CeO₂ nanoplates, nanotubes, and nanorods. *Journal of Solid State Chemistry*. 2008; 181: 1298–1306.
- [37] Tana, Zhang M, Li J, Li H, Li Y, Shen W. Morphology-dependent redox and catalytic properties of CeO₂ nanostructures: nanowires, nanorods and nanoparticles. *Catalysis Today*. 2009; 148: 179–183,
- [38] Zhang DS, Niu FH, Yan TT, Shi LY, Du XJ, Fang JH. Ceria nanospindles: template-free solvothermal synthesis and shape-dependent catalytic activity. *Applied Surface Science*. 2011; 257: 10161–10167.
- [39] Pan CS, Zhang DS, Shi LY, Fang JH. Template-free synthesis, controlled conversion, and CO oxidation properties of CeO₂ nanorods, nanotubes, nanowires, and nanocubes. *European Journal of Inorganic Chemistry*. 2008; 2008(15): 2429–2436.
- [40] Wu Z, Li M, Overbury SH. On the structure dependence of CO oxidation over CeO₂ nanocrystals with well-defined surface planes. *Journal of Catalysis*. 2012; 285: 61–73.

- [41] Kayama T, Yamazaki K, Shinjoh H. Nanostructured ceria–silver synthesized in one-pot redox reaction catalyzes carbon oxidation. *Journal of American Chemical Society*. 2010; 132: 13154–13155.
- [42] Xiao GL, Li S, Li H, Chen LQ. Synthesis of doped ceria with mesoporous flower-like morphology and its catalytic performance for CO oxidation. *Microporous and Mesoporous Materials*. 2009; 120: 426–431.
- [43] Primo A, Marino T, Corma A, Molinari R, García H. Efficient visible-light photocatalytic water splitting by minute amounts of gold supported on nanoparticulate CeO₂ obtained by a biopolymer templating method. *Journal of American Chemical Society*. 2011; 133: 6930–6933.
- [44] Younis A, Chu D, Kaneti YV, Li S. Tuning the surface oxygen concentration of {111} surrounded ceria nanocrystals for enhanced photocatalytic activities. *Nanoscale*. 2016; 8(1): 378–387.
- [45] Tang Z, Zhang Y, Xu Y. A facile and high-yield approach to synthesize one-dimensional CeO₂ nanotubes with well-shaped hollow interior as a photocatalyst for degradation of toxic pollutants. *RSC Advances*. 2011; 1: 1772–1777.

Functionalization of Surfaces in Layered Double Hydroxides and Hydroxide Salt Nanoparticles

Gregorio Guadalupe Carbajal Arizaga,
Cecilia Sánchez Jiménez, Alexandra Viruete and
Jenny Arratia-Quijada

Additional information is available at the end of the chapter

<http://dx.doi.org/10.5772/66002>

Abstract

Layered double hydroxides (LDH) and layered hydroxide salts (LHS) are widely studied as matrices to design new materials with applications in several areas of science and technology. Both LDH and LHS are composed of molecular layered units with surfaces fully covered by hydroxyl groups and positive-charge residues within the layers; therefore, anions in the interlayer space are needed. Even though these anions are described as interlayer species without a covalent interaction with the molecular layered units, the substitution of hydroxyl groups is also possible; in other words, the functionalization of the surface could occur. This chapter reviews results previously published related to the functionalization phenomenon in LDH and LHS, which is not considered in most of the scientific reports of new materials derived from these compounds. In this text, the use of copper probes to study electron paramagnetic resonance spectra, reinforced with infrared spectroscopy to confirm functionalization, is described. The occurrence of functionalization instead of a simple anion exchange provides a change of properties in the final nanosized material.

Keywords: functionalization, layered double hydroxide, layered hydroxide salt, electron paramagnetic resonance

1. LDH

1.1. Layered double hydroxides

Layered double hydroxides (LDH) form a class of ionic lamellar inorganic materials that are positively charged. These compounds are also named as anionic clays or hydrotalcite-like compounds. The structure of these compounds is formed by metal cations octahedrally coordinated by hydroxyl groups. The resulting octahedra share their edges to form infinitely large layers where hydroxyl groups cover both surfaces of each layer. The peculiar feature in LDH is that metal cations must be a combination of divalent and trivalent cations with ionic radii close to that of Mg^{2+} [1]. The trivalent cations in the layers produce a positive charge residue in the octahedra where they are located.

The interlayer domain contains charge compensation anions and solvation molecules. The size and orientation of species intercalated inside the interlayer region influence the interlayer distance and basal space of the resulting materials [2]. The basal space of LDH observed by powder X-ray diffraction is around 7–10 Å [3]. Anions may be small, e.g., CO_3^{2-} , Cl^- , SO_4^{2-} , RCO_2^- , or large such as methotrexate, 5-fluoruracil, and ibuprofen [4–6].

The chemical composition of LDH is represented by the general formula $[\text{M}^{2+}_{1-x}\text{M}^{3+}_x(\text{OH})_2]^{x+}(\text{A}^{n-})_x/n \cdot z\text{H}_2\text{O}$, where M and A^{n-} correspond to metallic and anionic species, respectively. The most common M^{2+} are Mg^{2+} , Zn^{2+} , Ni^{2+} , Ca^{2+} , Co^{2+} , Cu^{2+} , and Mn^{2+} , whereas M^{3+} are Al^{3+} , Ga^{3+} , Fe^{3+} , and Mn^{3+} [7]. The x mole fraction of the trivalent cation is normally between 0.2 and 0.4 [8]. This fraction determines the electrostatic charge density in the layers, thus influencing the size of the interlayer space and a variety of physicochemical properties such as adhesion, reactivity, ion-exchange capacity, and rotation of chemical species into the interlayer space and on the surface [7]. More details related to the structure of LDH can be found in some published revisions [9, 10].

1.2. Reversible ion exchange

The LDH have a flexible interlayer space, which allows it to retain ions with different sizes, such as proteins, enzymes, deoxyribonucleotides, viruses, pesticides, drugs, and dyes. The intercalated species improve their solubility and biocompatibility as they are protected from degradation by external chemical and biological attack, thus extending half-life and function. The intercalation of this large variety of anions is reversible and this effect is used to design nanoparticles for controlled release. The releasing mechanism in LDH is carried out by ion-exchange reaction due to the presence of electrolytes or due to the partial dissolution of layers in slightly acidic conditions, thus the molecule intercalated or functionalized into LDH can be released in a controlled manner [11, 12].

1.3. Synthesis

A number of easy and low-cost synthetic techniques have been successfully employed in the preparation of LDH. The most commonly used is a simple coprecipitation method; the second is based on the classical ion-exchange process; the third is the reconstruction or memory effect

process [1, 13], although a recent analysis demonstrates that this “memory effect” is merely a direct synthesis [14].

The coprecipitation method with alkali is performed with a solution of inorganic salts. The most used salts are nitrates, chlorides, or carbonates. In some cases, an ageing step is required to increase crystallinity or the particle size [8].

The ion-exchange method is based on the exchange of the anions present in the interlayer region. In addition, it is strongly influenced by the electrostatic attraction between the layers and the new anion [8]. Nitrate ions are usually used as precursors for ion-exchange reactions because they are easily replaced [1].

The synthesis by calcination reconstruction has been widely reported. It is based on the capacity of layered hydroxides to be transformed in oxides by calcination and then converted reversibly to layered double hydroxides by hydration for 24 hours. This process can be realized in the presence of organic ions/molecules to intercalate them inside the interlayer galleries of LDH. However, the recent analysis of the growth process determined that the divalent metal oxides (with alkaline nature) react with the amphoteric aluminum oxide in water, thus this method is not an actual reconstruction [14].

Some other methods, such as salt hydrolysis [15, 16], sol-gel synthesis using ethanol and acetone solutions, and a fast nucleation process followed by a separate aging step at elevated temperatures, have also been reported [8].

1.4. Advanced applications

LDH have found a wide field of applications in the last two decades, which reflects the importance of studying these compounds. Advanced applications have been found in the biomedical field as nanovehicles for delivery of ibuprofen, enalaprilate [17], 5-fluoracil, methotrexate [18], DNA segments [19], cosmeceuticals [20], as well as nanoparticles for diagnoses through fluorescent or magnetic analyses [21–23].

2. Layered hydroxides salts

Layered hydroxide salts (LHS) form a family of inorganic crystalline compounds with a similar layered structure of that found in LDH and a similar anion-exchange ability [24, 25]. The particles of LHS can be synthesized in the nanometric scale and they have been used as a basis to produce novel materials with tunable properties [26, 27].

Although the first articles reporting the anion-exchange property in LHS appeared in the early 1970s [26], the use of these compounds to prepare new materials by exchanging the interlayer anion occurred after 1990 [28, 29]. In order to understand the anion-exchange process and the possibility of functionalization events in LHS, the structure and composition will be described in the next section.

2.1. Structure and composition

The structure of LHS, as well as that of LDH, is based on the layered organization of single hydroxides, such as Brucite, $\text{Mg}(\text{OH})_2$ [30], where a divalent cation occupies the octahedral position coordinated, in principle, by hydroxyl groups (**Figure 1a**). A single hydroxide, when synthesized in the presence of other anions, could retain them while conserving the coordination of the metal cations exclusively by hydroxyl groups. This is the case of α -nickel hydroxide, which is capable of allocating nitrate anions between two electrostatically neutral hydroxide layers (**Figure 1b**). However, by modifying synthesis parameters detailed in the bibliography [31], the nitrate anions can isomorphically replace some hydroxyl groups, thus producing an LHS structure: nickel hydroxide nitrate with composition $\text{Ni}_3(\text{OH})_4\text{NO}_3$. This structure is represented in **Figure 1c** and is the most common LHS containing chloride, nitrate sulfate or acetate (**Figure 1b**) [24, 32, 33]. The molecular formula to represent this type of LHS is $\text{M}(\text{OH})_{2-x}(\text{A}^{n-})_{x/n}$, where M is the divalent cation and A^{n-} is an anion with n^- charge. Regarding the metal cation, LHS have been prepared with Mg^{2+} , Ni^{2+} , Zn^{2+} , Ca^{2+} , Cd^{2+} , Co^{2+} , and Cu^{2+} , which can be combined in the same structure [28].

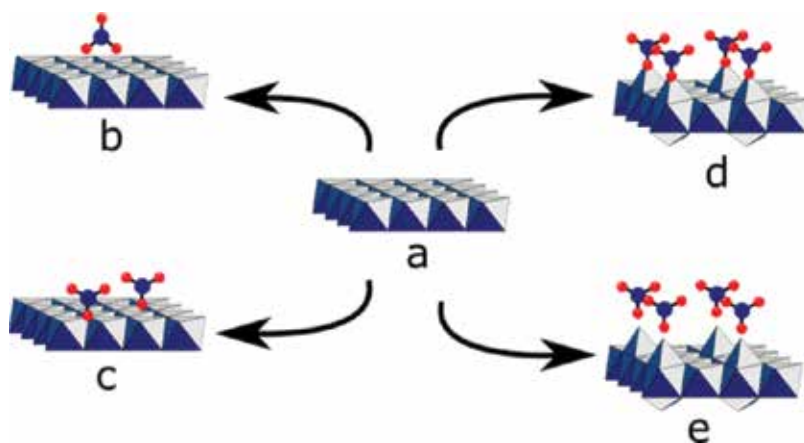


Figure 1. Single-layer representation of (a) single hydroxide, (b) single hydroxide with intercalated nitrate ions, (c) an LHS with isomorphic hydroxyl substitution by nitrate ions, (d) dentate LHS layer with functionalized tetrahedral, and (e) dentate LHS layer with loose nitrate ions.

Another structural change observed in LHS with respect to Brucite, especially those composed by zinc cations, is that 2/5 of M^{2+} is displaced from the octahedral center to the surface of the layers producing tetrahedrons and giving the aspect of dentate layers as shown in **Figure 1d** and **1e** [33]. The metal cation in the center and three hydroxyl groups in the base, shared with the octahedrons, form the tetrahedrons. The apex can be occupied either by the A^{n-} anion or by a water molecule. In the former case the A^{n-} directly coordinates the metal center (**Figure 1d**), whereas in the structure where water occupies the apex, the A^{n-} remains free in the interlayer space (**Figure 1e**) [33]. Examples of both structures are zinc hydroxychloride ($\text{Zn}_5(\text{OH})_8\text{Cl}_2 \cdot \text{H}_2\text{O}$) and zinc hydroxynitrate ($\text{Zn}_5(\text{OH})_8(\text{NO}_3)_2 \cdot (2\text{H}_2\text{O})$), respectively [34, 35].

2.2. Synthesis

Layered hydroxide salts are synthesized by the same procedures used to prepare layered double hydroxides. The precipitation of salt solutions with sodium hydroxide is the easiest and most practical method [35, 36–38]. This method is recommended when a large amount of product is desired. For example, when a copper acetate solution reacts with sodium hydroxide, the copper hydroxide acetate is obtained [39].

Another method based on the slow decomposition of urea allows to obtain different compositions by changing the synthesis parameters [40]. For example, a mixture of cobalt nitrate with urea heated inside an oven at 80, 100, 120, and 160°C produces $\text{Co}(\text{OH})_{1.7}(\text{NO}_3)_{0.3}$, $\text{Co}(\text{OH})_{1.7}(\text{NO}_3)_{0.3} \cdot 0.35\text{H}_2\text{O}$, $\text{Co}(\text{OH})_{1.75}(\text{NO}_3)_{0.25} \cdot 0.66\text{H}_2\text{O}$, and $\text{Co}(\text{OH})_2(\text{NO}_3)_{0.3} \cdot 0.66\text{H}_2\text{O}$, respectively [40].

2.3. Surface modification with organic anions

The growing interest in studying LHS is based on the ability to exchange the interlayer A^{n-} anion either by organic or inorganic anions. The wide number of possible combinations in composition results in materials with novel properties. Nonetheless, the insertion of a new anion is not always a simple task, thus the researchers have developed some strategies to obtain new LHS. According to common definitions of functionalization [41, 42], the modification of an LHS surface with new molecules or ions produces a functionalized LHS; however, in a deeper perspective, the effective functionalization of layered units is related to the substitution of hydroxyl sites. The methods to modify the LHS are presented in this section regardless of whether they produce an effective functionalization or simply substitution of A^{n-} anions.

2.3.1. Anion exchange

This is the most applied method to modify an LHS. First, an LHS must be synthesized by the precipitation or urea method as described above, and preferably the interlayer A^{n-} anion in the starting compound should be weakly attracted by the metal cation-like acetate, chloride, or nitrate. Otherwise, anions with a large negative charge density (e.g., carbonate) are strongly retained by the layers and reduce the exchange efficiency [1].

An example of an anion exchange is the reaction of copper hydroxide acetate dispersed in ethanol, mixed with benzoic acid and stirred for 36 h. The benzoate anions substitute acetate and produce the LHS copper hydroxide benzoate [39].

2.3.2. Coprecipitation

The coprecipitation method is adequate to intercalate A^{n-} anions with large volume, for example, dyes or surfactants [43]. The layered units of the hydroxide salt are formed during the synthesis in the presence of A^{n-} anions that are captured to stabilize the stacking and form the particles. This process avoids the high activation energy needed to expand the interlayer space in the anion-exchange reactions. A representative experiment to obtain a modified LHS by coprecipitation requires an aqueous solution starting with the addition of zinc nitrate to a

vessel with water and sodium dodecylbenzenesulfonate. This solution is slowly mixed with an NaOH solution. The white suspension formed contains nanoparticles of zinc hydroxide dodecylbenzenesulfonate [43].

2.3.3. Solid state

The solid-state method was developed to reduce or avoid the use of solvents. This method requires one M^{2+} salt mixed with a reagent providing the counter ion and urea. One reaction was exemplified above with the cobalt hydroxide nitrate compounds. Another example where the A^{n-} anion is organic has been found in the reaction of magnesium nitrate, urea, and benzoic acid. The heat of this mixture at 110°C produces a magnesium hydroxide benzoate compound [44].

Although the aim of this method is also to increase the selectivity of products and reduce purification steps, the reaction periods are larger and temperatures are higher [31, 40, 44].

2.4. The nanometric dimensions of LHS

Size of LHS nanoparticles depends on the synthesis method followed. Commonly, particles obtained by precipitation or coprecipitation present nanometric dimensions. The scanning electron microscope image presented in **Figure 2** corresponds to a zinc hydroxide nitrate salt prepared by precipitation of a zinc nitrate solution with sodium hydroxide. The histogram demonstrates that the particle sizes, although with large dispersion, fall in the nanometric dimensions.

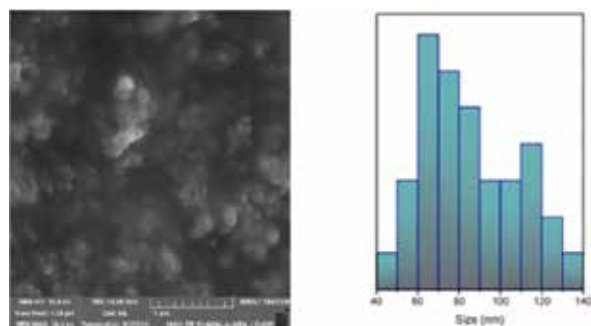


Figure 2. Scanning electron microscope image of zinc hydroxide nitrate obtained by precipitation and the histogram demonstrating that the particles presented nanometric dimensions.

3. Functionalization studies in LDH and LHS

Functionalization of materials is defined as the insertion of chemical functional groups in the surface of materials regardless of their crystalline or amorphous nature [45]. Functionalization reactions can be conducted in metals [46], ceramics [47], and synthetic or natural polymers [48,

49]. The aim of functionalization is to modify, tune, or add surface properties to a material once they play a key role in the overall performance of materials [42], especially those with nanometric sizes. For example, the functionalization of silica with sulfonic or thiol groups enables the scavenging of Cr^{3+} and Pb^{2+} cations from aqueous solution [50, 51]; gallium nitride nanoparticles become stable in aqueous suspension after functionalization with cysteine [52]; bismuth germanate ($\text{Bi}_4\text{Ge}_3\text{O}_{12}$) nanoparticles could recognize leukemia cells after functionalization with a monoclonal antibody [53]; and functionalization could also be useful to reduce toxicity of nanoparticles (like hydroxyapatite) in biomedical applications [54].

A recent review has detailed the strategies of functionalizing ceramic oxides and gave an important classification to understand them. This classification comprises three groups: physical, chemical, and biological reactions [42].

However, it is important to point out that this classification is one of the approaches to organize the description of functionalization methods. Another classification of ceramics functionalization includes surface coating and *in situ* surface modification [41].

At this point, in both classifications it is necessary to identify that the functionalization term is not limited to the insertion of a chemical functional group to a surface in a covalent manner, and the surface modification through a coating or physisorption is also contemplated [42]. In this regard, adsorbed molecules onto materials with high porosity are also named functionalized materials. Examples of typical functionalization reports are represented in **Figure 3**.

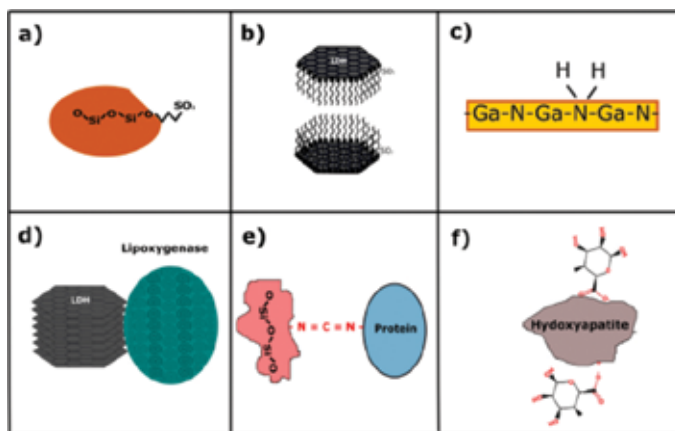


Figure 3. Representative examples of functionalization reactions. (a) Covalent functionalization of silica with propyl-sulfate [50], (b) ionic modification of an LDH with dodecylsulfate [55], (c) gallium nitride surface functionalized with amino groups [56], (d) LDH functionalized with lipoxigenase [57], (e) silica functionalized with carbodiimide and then with a protein [42], and (f) hydroxyapatite functionalized with glucuronic acid [54].

The following section strictly focuses on those functionalization reactions where the crystallographic sites of hydroxyl groups in layers of LDH and LHS are partially substituted by other anions, i.e., when the insertion of new functional groups in the surface strictly occurs.

3.1. Functionalization in layered double hydroxides and layered hydroxide salts

The covalent growth of layered units with divalent and trivalent cations involves the coordination with hydroxyl groups. Under this condition, the octahedral arrangement—where the metal cation is coordinated by six ions—satisfies the number of ligands determined by the 4th rule of Pauling [58], and the presence of additional anions to stabilize the residual positive charge located in those centers occupied by trivalent cations is strictly restricted in the first coordination sphere. Then, the anions beyond this sphere satisfy the electrostatic neutrality. The overall arrangement corresponds to layers fully covered by hydroxyl groups and A^{n-} anions loosely attached to this hydroxylated surface. Nonetheless, it is possible to find structures where anions substitute the hydroxyl sites [59].

Regarding LHS compounds, the natural functionalization—or substitution of hydroxyl groups by anions—is observed in the structures of **Figure 1c–e**. As demonstrated, these anions can be further substituted through a low-energy anion-exchange reaction [28]. Although several new materials prepared by exchange reaction have been reported, a detailed study to determine if the resulting material is functionalized or simply intercalated is not always conducted.

The following section presents a case study using Cu^{2+} cations spread in cationic sites of LDH and LHS as probes to determine if functionalization occurs by means of electron spectroscopy.

3.2. Synthesis of LDH and LHS with Cu^{2+} probes

Divalent copper cations, Cu^{2+} , are paramagnetic species with at least one unpaired electron. The magnetic coupling of this electron with a nuclear spin equal to 3/2 results in a spectrum with four signals under an isotropic environment. In solid compounds, the anisotropic effect produces more lines, in principle, one set of four signals per orientation of the electron with respect to the applied magnetic field [60].

On the other hand, LDH and LHS are composed of metal cations with a similar radius to that of Mg^{2+} , and therefore Cu^{2+} cations can be used to prepare these structures and they serve as EPR (Electron Paramagnetic Resonance) probes if they are spread along the layers [59, 61, 62] or on other solid compounds [63].

The experiment to determine the amount of copper needed to obtain a single crystal phase along with a clear EPR signal comprised the synthesis of LDH and LHS particles with different contents of Cu^{2+} cations [62].

The synthesis of an LDH group was prepared by precipitation of a solution with nitrate salts of Zn^{2+} and Al^{3+} cations mixed with three contents of Cu^{2+} : 0.2, 1.0, and 10.0 mol% with respect to Zn^{2+} . Regarding the synthesis of the LHS, the nitrate salt solution only contained zinc cations and the same atomic percent of copper. Details of this synthesis can be found in the literature [62].

The analysis by X-ray diffraction of these compounds revealed profiles of layered structures and no second phases of copper compounds were observed in the LDH modified with 0.2 mol % of Cu^{2+} , and therefore the compound was suitable for the intercalation/functionalization

study. Another important piece of information from these diffractograms is that LDH were formed, therefore cations –including Cu^{2+} – occupied octahedral positions.

In the case of the LHS, the diffraction patterns confirmed that the structure of a zinc hydroxide salt was properly formed. This structure corresponds to that depicted in **Figure 1e**, where cationic sites occupy both octahedral and tetrahedral positions. The compound selected for the functionalization study was the LHS modified with 1.0 mol% of Cu^{2+} .

3.3. Functionalization studies by electron paramagnetic resonance spectroscopy

Once the LDH and LHS are prepared with a low amount of copper cations, the EPR spectroscopy analysis can be conducted.

The most representative EPR spectra to discuss functionalization correspond to the LDH with 0.2 mol% of Cu^{2+} and the LHS with 1.0 mol% of Cu^{2+} . The spectra plotted with black lines in **Figure 4** correspond to experimental data from the LDH and LHS. The former is composed of four lines and one intense signal of axial and parallel components of Cu^{2+} ions in Oh coordination, which is confirmed with a simulated spectrum of Cu^{2+} in octahedral coordination, fitting the experimental data. With the aid of the SimFonia software, the crucial parameters to achieve the fitting were the g factor and the spin-nucleus coupling constant A , with values of $g_{xx,yy} = 2.069$ and $A_{xx,yy} = 13 \times 10^{-4} \text{ cm}^{-1}$ for two parallel components, respectively, and $g_{zz} = 2.362$ and $A_{zz} = 139 \times 10^{-4} \text{ cm}^{-1}$ for the perpendicular components, respectively [59, 61]. Once $g_{xx} = g_{yy}$ and $g_{xx,yy} > g_{zz} > 2$, the copper cations underwent a high distortion affected by the elongation of the z -axis [60, 64]; furthermore, the $g_{xx,yy}/A_{xx,yy}$ ratio ($2.069/13 \times 10^{-4} \text{ cm}^{-1} = 172 \text{ cm}$) is close to 200 cm, and this value has been associated with such tetrahedral distortion [65, 66]; therefore, the simulated spectra correspond to copper cations in octahedral sites.

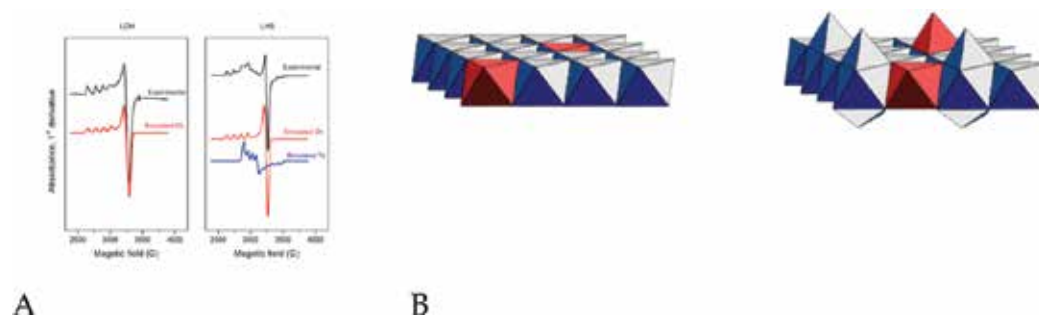


Figure 4. (A) EPR spectra of LDH modified with 0.2 mol% of Cu^{2+} and the LHS modified with 1.0 mol% of Cu^{2+} . Adapted from [62]. (B) Left: layer of LDH with octahedral units, where Cu^{2+} cations replace zinc positions (red octahedra); right: layer of LHS with octahedral and tetrahedral units, where Cu^{2+} cations replace both zinc positions (red polyhedra).

Regarding the spectra of the LHS, more absorption signals are present, and they were recomposed with the sum of two spectra: one similar to that proposed for the LDH with copper in octahedral coordination with values of $g_{xx,yy} = 2.089$, $A_{xx,yy} = 15 \times 10^{-4} \text{ cm}^{-1}$; $g_{zz} = 2.400$ and $A_{zz} = 113 \times 10^{-4} \text{ cm}^{-1}$; and a second spectrum with $g_{xx} = 2.274$, $A_{xx} = 41 \times 10^{-4} \text{ cm}^{-1}$; $g_{zz} =$

2.020 and $A_{zz} = 80 \times 10^{-4} \text{ cm}^{-1}$ associated with copper center in tetrahedral coordination [59]. These results indicate that copper cations are located in both octahedral and tetrahedral sites in the LHS as represented in **Figure 4**.

Regarding the octahedral positions, the g and A parameters, and especially the $g_{\parallel}/A_{\parallel}$ ratio, undergo a change when the crystal field of copper is modified; in other words, the substitution of hydroxyl groups from the coordination sphere by other anions corresponds to a functionalization phenomenon revealed by a change in the $g_{\parallel}/A_{\parallel}$ ratio [59, 61, 62].

The spectra in **Figure 5** belong to an LDH subjected to an exchange reaction with adipic ($\text{HOOC}-(\text{CH}_2)_4-\text{COOH}$) and azelaic ($\text{HOOC}-(\text{CH}_2)_7-\text{COOH}$) acids. Dotted lines in the spectrum indicate that the signals after intercalation of adipic acid are in the same position, indicating that the crystal field of copper cations did not change, i.e., the hydroxyl groups were not substituted since the adipic acid only replaced nitrate ions and remained hydrated and “loose” in the interlayer space as depicted in **Figure 5B**. Conversely, the spectrum of the compound treated with azelaic acid presented shifted lines and appeared closer to each other as result of a lower spin-nucleus coupling, detected through the simulated spectrum where $A_{zz} = 123 \times 10^{-4} \text{ cm}^{-1}$ [59]. Simultaneously, the g_{zz} factor increased to 2.385. Both of these changes indicate that the crystal field was modified, and therefore the functionalization of the layers was accomplished with azelaic acid. This crystal field change of the Cu^{2+} sites is represented in **Figure 5B**.

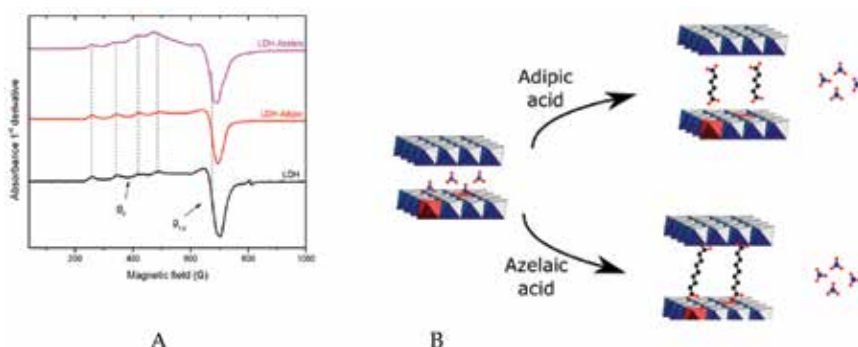


Figure 5. (A) EPR spectra of LDH modified with 0.2 mol% of Cu^{2+} and the intercalation products with adipic and azelaic acids. (B) Intercalation products of LDH with adipic acid where the exchanged anions are loosely retained between the layers and azelaic acid substituting the hydroxyl groups of the layers (functionalization).

The evidence of functionalization in the LHS was also demonstrated with the EPR spectra of the intercalation products with adipic and azelaic acids (**Figure 6A**). First, the product with adipic acid produced the same spectrum profile found in the initial LHS; in fact, similar g and A parameters were found in the simulated spectrum of copper in the octahedral and tetrahedral sites [59]. However, more information obtained from infrared and nuclear magnetic resonance indicated that the carboxylate group was probably coordinated to a metal center; in this case, only copper in octahedral position could be affected since the g and A parameters, from the octahedral simulated component, were modified slightly (**Figure 6B**).

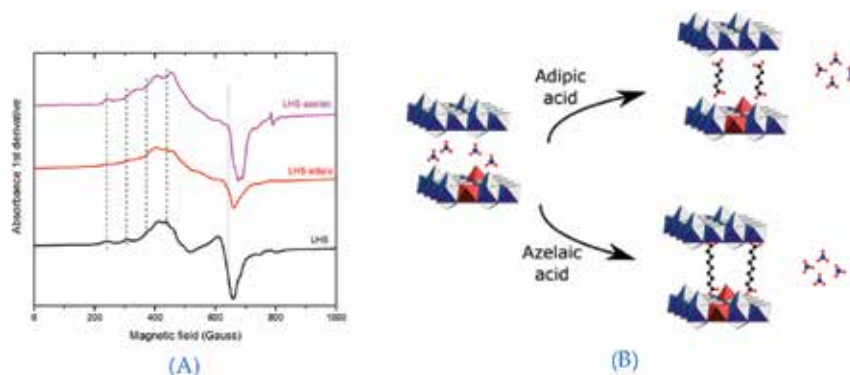


Figure 6. (A) EPR spectra of the LHS modified with 1.0 mol% of Cu²⁺ and (B) a representation of the intercalation products with adipic and azelaic acids.

The product from the reaction with azelaic acid has a clearer shift of the EPR spectrum. The simulation to fit the experimental data revealed that the coupling constant A increased for copper in the octahedral position and decreased for that in the tetrahedral position (from $A_{zz} = 80 \times 10^{-4} \text{ cm}^{-1}$ to $A_{zz} = 72 \times 10^{-4} \text{ cm}^{-1}$) [59]. This data indicates that both octahedral and tetrahedral units experience a change in the crystal field associated with functionalization of azelaic acid as presented in **Figure 6B**.

The use of EPR spectroscopy and Cu²⁺ probes demonstrated to be a useful tool to assess the functionalization of LDH and LHS layers. The information obtained is important from the point of view of basic science and can help to interpret the performance and properties of new materials based on layered hydroxide compounds.

3.4. Functionalization studies by infrared spectroscopy

Infrared spectroscopy is one of the most important techniques to analyze materials once it provides molecular information in a very short time; it is non-destructive and, in most cases, the sample does not need special treatments. Although commercial equipment is provided with detectors for the middle region of the infrared spectrum and details for the metal-oxygen bonds are not clearly observed, the information obtained from the interlayer anions, especially those related to symmetry changes, is relevant to determine if functionalization occurs, mainly in LHS.

The functionalization or effective pillaring in LDH is scarcely studied and the specific study is reported in the articles analyzed in the EPR section [59, 61, 62]. A confirmation of functionalization exclusively based on infrared spectroscopy has not been reported to the best of our knowledge. One of the deepest studies by infrared spectroscopy only determined the orientation of nitrate ions with respect to the layers [67] and the different anion-exchange ability influenced by such orientation [68]; however, the substitution of hydroxyl groups was not detected according to elemental analysis.

On the contrary, the infrared spectra on LHS, in several cases supported by X-ray diffraction, were enough techniques to determine that hydroxyl sites were substituted by other anions, resulting in the structure depicted in **Figure 1d**.

A representative example of layers exclusively formed by cations octahedrally coordinated by hydroxyl groups and functionalized with nitrate ions is found in a copper hydroxide nitrate reported by Aguirre et al. [69]. In this case, the functionalization by nitrate ions is clearly determined by infrared spectroscopy, where the nitrate ions presented two intense bands at 1426 and 1343 cm^{-1} corresponding to asymmetric and symmetric stretching, respectively, of nitrate anions coordinating some copper cations [69].

Other researchers observed the same spectral profile with two signals at 1420 and 1338 cm^{-1} for nitrate in functionalized layers, whereas free nitrate produces a single band at 1370 cm^{-1} [70]. This splitting caused by a clear functionalization phenomenon with nitrate anions is observed in **Figure 7**, where the band at 1375 cm^{-1} in nonfunctionalized layers splits and produces two signals at 1447 and 1351 cm^{-1} when nitrate is directly coordinating the metal cations in an LHS structure [62]. These examples demonstrate that infrared spectroscopy is a practical technique to determine functionalization of layers with nitrate ions.

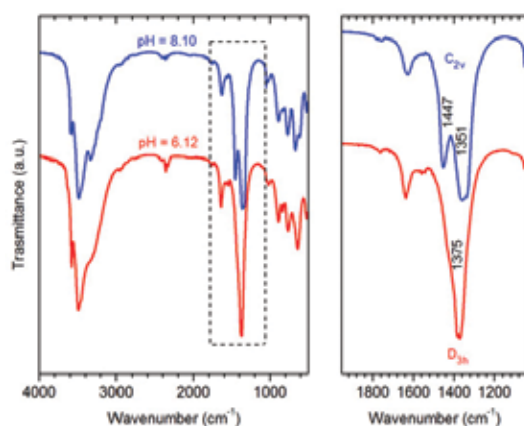


Figure 7. Infrared spectra of a zinc hydroxide nitrate salt precipitated at different pH, 6.12 and 8.10.

4. Properties of LDH and LHS dependent on functionalization

Some of the consequences of functionalization in LDH and LHS are presented in the following cases.

A physical reduction of the interlayer space is observed. Commonly, an LDH with free nitrate ions presents basal spaces between 8 and 9 Å. If nitrate ions functionalize the hydroxylated layers, the basal space decreases to 6 Å as presented in **Figure 8** [69].

The chemical reactivity clearly modified by a functionalization was observed in the LHS with composition $\text{Zn}_5(\text{OH})_8(\text{NO}_3)_2 \cdot 2\text{H}_2\text{O}$. The structure typically contains free nitrate ions in the interlayer space and therefore produces a single IR band of the symmetric stretching at 1375 cm^{-1} in **Figure 7**. This solid compound was added as heterogeneous catalyst to an esterification reaction with lauric acid and methanol and no activity was detected (**Figure 9**). On the contrary, the addition of the compound with the nitrate-functionalized layers leads to ester formation with yields higher than 95% [71].

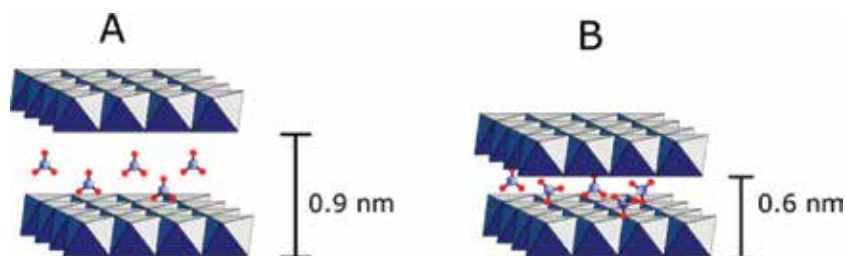


Figure 8. Basal space dependent on the interlayer anion that can be (A) “free” or (B) functionalizing the layers.

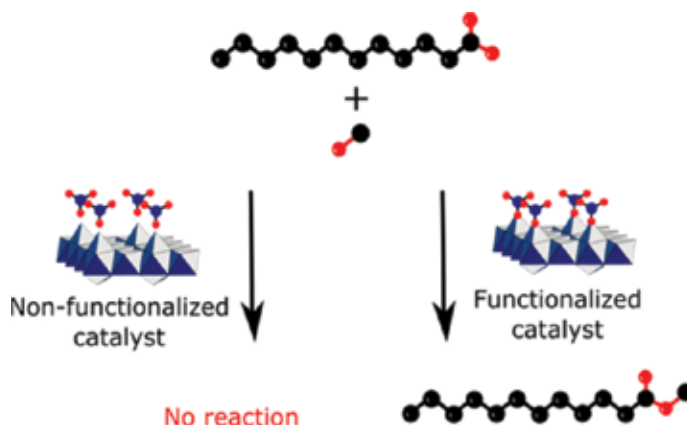


Figure 9. Methyl esterification of lauric acid is catalyzed in high yield with an LHS where nitrate ions functionalize the layers. The compound with free nitrate is not active in this reaction.

A property derived from the direct graft of nitrate anions is that nitrate functionalizing the layers in **Figure 8** has a restricted rotation degree unlike that in the LDH where nitrate is free and therefore two orientations can be adopted, one parallel and another perpendicular to the layers. Further, these two orientations influence physicochemical properties evidenced by the different anion-exchange ability [67, 68].

The functionalization of layers presented in **Figure 8B** favored a higher crystallinity degree in nickel hydroxide layers regarding better stacking. Conversely, loose intercalation of nitrate promotes rotation of layers causing a stacking disorder known as turbostraticity [31].

Another consequence observed when nitrate ions functionalize the layers is the change in thermal stability of the functionalizing anions. This effect was demonstrated with a set of LDH composed by Cu^{2+} , Mg^{2+} , Zn^{2+} , and Ni^{2+} , where the nitrate ion decomposes at a temperature dependent on the charge density of the metal cation, thus the main decomposition step occurred at 220–300, 200–320, 290–420, and 380–500°C for the LHS composed by Cu^{2+} , Zn^{2+} , Ni^{2+} , and Mg^{2+} cations, respectively [72]. This thermal stability is derived from the direct bond between the nitrate and the metal cation.

5. Conclusions

Surface functionalization of LDH and LHS can be produced by physical and chemical methods. Physical modification through anion-exchange processes is the most common phenomenon to add new properties to the layered compounds. Although this physical modification is also considered functionalization, this text discussed functionalization as a chemical reaction where hydroxyl groups were substituted by other functional groups. Based on this concept, the data demonstrated that the functionalization of hydroxylated layers in LDH or LHS is capable of modifying the physicochemical properties of those particles. Such modification of nanometric particles is relevant to adjust properties needed in specific applications.

Some of the properties modified by chemical functionalization of LDH and LHS compared to those in anion-exchanged compounds are as follows: (i) the lower interlayer space, (ii) chemical reactivity, (iii) anion-exchange capability, and (iv) thermal stability. The analyzed bibliography proves that infrared spectroscopy is a practical tool capable of confirming functionalization with nitrate ions. However, the use of EPR spectroscopy and Cu^{2+} cations as probes gives deeper information to confirm the functionalization with different anions in LDH and LHS nanoparticles. The relationship between functionalization and properties could be better understood if the functionalization phenomenon was studied in detail through these spectroscopic techniques. Therefore, a rational design of new materials with controlled properties could be achieved.

Author details

Gregorio Guadalupe Carbajal Arizaga^{1*}, Cecilia Sánchez Jiménez¹, Alexandra Viruete¹ and Jenny Arratia-Quijada²

*Address all correspondence to: gregoriocarbal@ yahoo.com.mx

¹ Chemistry Department, University of Guadalajara, Guadalajara, Jalisco, Mexico

² Health Sciences Department, University Center Tonalá, University of Guadalajara, Jalisco, Mexico

References

- [1] Carlino S. The intercalation of carboxylic acids into layered double hydroxides: a critical evaluation and review of the different methods. *Solid State Ionics*. 1997;98(1–2):73–84.
- [2] Hussein MZ bin, Yahaya AH, Shamsul M, Salleh HM, Yap T, Kiu J. Acid fuchsin-interleaved Mg–Al-layered double hydroxide for the formation of an organic–inorganic hybrid nanocomposite. *Mater Lett*. 2004;58(3–4):329–332.
- [3] Hussein MZ bin, Long CW. Synthesis of organo-mineral nanohybrid material: indole-2-carboxylate in the lamella of Zn–Al-layered double hydroxide. *Mater Chem Phys*. 2004;85(2–3):427–431.
- [4] Rives V, Arco M, Martín C. Layered double hydroxides as drug carriers and for controlled release of non-steroidal antiinflammatory drugs (NSAIDs): a review. *J Control Release*. 2013;169(1–2):28–39.
- [5] Wang Q, O'Hare D. Recent advances in the synthesis and application of layered double hydroxide (LDH) nanosheets. *Chem Rev*. 2012;112(7):4124–4155.
- [6] Riaz U, Ashraf SM. Double layered hydroxides as potential anti-cancer drug delivery agents. *Mini Rev Med Chem*. 2013;13:522–529.
- [7] Bi X, Zhang H, Dou L. Layered double hydroxide-based nanocarriers for drug delivery. *Pharmaceutics*. 2014;6:298–332.
- [8] He J, Wei M, Li B, Kang Y, Evans DG, Duan X. Preparation of layered double hydroxides. *Struct Bond*. 2006;119:89–119s.
- [9] Bullo S, Hussein MZ. Inorganic nanolayers: structure, preparation, and biomedical applications. *Int J Nanomed*. 2015;10:5609–5633.
- [10] Rives V, Arco M, Martín C. Intercalation of drugs in layered double hydroxides and their controlled release: a review. *Appl Clay Sci*. 2014;88–89:239–69.
- [11] Oh J-M, Biswick TT, Choy J-H. Layered nanomaterials for green materials. *J Mater Chem*. 2009;19(17):2553.
- [12] Oh J-M, Park C-B, Choy J-H. Intracellular drug delivery of layered double hydroxide nanoparticles. *J Nanosci Nanotechnol*. 2011;11(2):1632–1635.
- [13] Theiss FL, Ayoko GA, Frost RL. Synthesis of layered double hydroxides containing Mg^{2+} , Zn^{2+} , Ca^{2+} and Al^{3+} layer cations by co-precipitation methods: a review. *Appl Surf Sci*. 2016;383:200–213.
- [14] Mascolo G, Mascolo MC. On the synthesis of layered double hydroxides (LDHs) by reconstruction method based on the “memory effect.” *Microporous Mesoporous Mater*. 2015;214:246–248.

- [15] Nethravathi C, Rajamathi JT, George P, Rajamathi M. Synthesis and anion-exchange reactions of a new anionic clay, α -magnesium hydroxide. *J Colloid Interface Sci.* 2011;354(2):793–797.
- [16] Poul L, Jouini N, Fievet F. Layered hydroxide metal acetates (metal = zinc, cobalt, and nickel): elaboration via hydrolysis in polyol medium and comparative study. *Chem Mater.* 2000;12:3123–3132.
- [17] Ribeiro C, Arizaga GGC, Wypych F, Sierakowski M-R. Nanocomposites coated with xyloglucan for drug delivery: in vitro studies. *Int J Pharm.* 2009;367(1–2):204–210.
- [18] Kim T-H, Lee GJ, Kang J-H, Kim H-J, Kim T-I, Oh J-M. Anticancer drug-incorporated layered double hydroxide nanohybrids and their enhanced anticancer therapeutic efficacy in combination cancer treatment. *Biomed Res Int.* 2014;2014: Article ID 193401.
- [19] Xu ZP, Jin Y, Liu S, Hao ZP, Lu GQ (Max). Surface charging of layered double hydroxides during dynamic interactions of anions at the interfaces. *J Colloid Interface Sci.* 2008;326:522–529.
- [20] Deák Á, Janovák L, Tallósy SP, Bitó T, Sebok D, Buzás N, et al. Spherical LDH–Ag^o-montmorillonite heterocoagulated system with a pH-dependent sol–gel structure for controlled accessibility of AgNPs immobilized on the clay lamellae. *Langmuir.* 2015;31(6):2019–2027.
- [21] Kuthati Y, Kankala RK, Lee C. Layered double hydroxide nanoparticles for biomedical applications : current status and recent prospects. *Appl Clay Sci.* 2015;112–113:100–116.
- [22] Wei P-R, Cheng S-H, Liao W-N, Kao K-C, Weng C-F, Lee C-H. Synthesis of chitosan-coated near-infrared layered double hydroxide nanoparticles for in vivo optical imaging. *J Mater Chem.* 2012;22(12):5503.
- [23] Arratia-Quijada J, Sánchez Jiménez C, Gurinov A, Pérez Centeno A, Ceja Andrade I, Carbajal Arízaga GG. Dysprosium-containing layered double hydroxides nanoparticles intercalated with biologically active species as an approach for theranostic systems. *Mater Sci Eng B.* 2016;203:7–12.
- [24] Cursino ACT, Rives V, Carbajal Arizaga GG, Trujillano R, Wypych F. Rare earth and zinc layered hydroxide salts intercalated with the 2-aminobenzoate anion as organic luminescent sensitizer. *Mater Res Bull.* 2015;70:336–342.
- [25] Machovsky M, Kuritka I, Sedlak J, Pastorek M. Hexagonal ZnO porous plates prepared from microwave synthesized layered zinc hydroxide sulphate via thermal decomposition. *Mater Res Bull.* 2013;48(10):4002–4007.
- [26] Carbajal-Arizaga GG. Layered hydroxide salts as a base to design new materials. Structure, synthesis and applications. *Schaltungsdienst Lange o.H.G., Berlin.* 2013. 71 p.

- [27] Carbajal-Arízaga GG. Intercalation studies of zinc hydroxide chloride: ammonia and amino acids. *J Solid State Chem.* 2012;185:150–155.
- [28] Meyn M, Beneke K, Lagaly G. Anion-exchange reactions of hydroxy double salts. *Inorg Chem.* 1993;32:1209–1215.
- [29] Carbajal-Arízaga GG, Satyanarayana K, Wypych F. Layered hydroxide salts: synthesis, properties and potential applications. *Solid State Ionics.* 2007;178(15–18):1143–1162.
- [30] Majoni S, Su S, Hossenlopp JM. The effect of boron-containing layered hydroxy salt (LHS) on the thermal stability and degradation kinetics of poly(methyl methacrylate). *Polym Degrad Stab.* 2010;95(9):1593–1604.
- [31] Rajamathi M, Vishnu Kamath P. On the relationship between α -nickel hydroxide and the basic salts of nickel. *J Power Sources.* 1998;70(1):118–121.
- [32] Thomas N. Mechanochemical synthesis of layered hydroxy salts. *Mater Res Bull.* 2012;47(11):3568–3572.
- [33] Louër M, Louër D, Grandjean D. Structural study of nickel and zinc hydroxynitrates. I. Structural classification. *Acta Crystallogr Sect B Struct Crystallogr Cryst Chem.* 1973;B29:1696–1703.
- [34] Marangoni R, Mikowski A, Wypych F. Effect of adsorbed/intercalated anionic dyes into the mechanical properties of PVA: Layered zinc hydroxide nitrate nanocomposites. *J Colloid Interface Sci.* 2010;351(2):384–391.
- [35] Hongo T, Iemura T, Satokawa S, Yamazaki A. Chromate adsorption and pH buffering capacity of zinc hydroxy salts. *Appl Clay Sci.* 2010;48(3):455–459.
- [36] Halma M, Khenifi A, Sancelme M, Besse-hoggan P. Thin bacteria/layered double hydroxide films using a layer-by-layer approach. *J Colloid Interface Sci.* 2016;474:151–158.
- [37] Choy J-H, Jung J-S, Oh J-M, Park M, Jeong J, Kang Y-K, et al. Layered double hydroxide as an efficient drug reservoir for folate derivatives. *Biomaterials.* 2004;25(15):3059–3064.
- [38] Forano C, Hibino T, Leroux F. Layered double hydroxides. Chapter 13.1. In: Bergaya F, Theng B K G, Lagaly G, editors. *Developments in Clay Science*. Netherlands: Elsevier, 1021–1095.
- [39] Marangoni R, Bubniak GA, Cantão MP, Abbate M, Schreiner WH, Wypych F. Modification of the interlayer surface of layered copper(II) hydroxide acetate with benzoate groups: submicrometer fiber generation. *J Colloid Interface Sci.* 2001;240(1):245–251.
- [40] Rajamathi M, Kamath PV. Urea hydrolysis of cobalt(II) nitrate melts: synthesis of novel hydroxides and hydroxynitrates. *Int J Inorg Mater.* 2001;3(7):901–906.
- [41] Liu X, Chu PK, Ding C. Surface nano-functionalization of biomaterials. *Mater Sci Eng R.* 2010;70(3–6):275–302.

- [42] Treccani L, Yvonne Klein T, Meder F, Pardun K, Rezwan K. Functionalized ceramics for biomedical, biotechnological and environmental applications. *Acta Biomater.* 2013;9(7): 7115–7150.
- [43] Cursino ACT, Rives V, Carlos LD, Rocha J, Wypych F. Layered zinc hydroxide salts intercalated with anionic surfactants and adsorbed with UV absorbing organic molecules. *J Braz Chem Soc.* 2015;26:1769–1780.
- [44] Wypych F, Arizaga GGC. Intercalation and functionalization of brucite with carboxylic acids. *Quim Nova.* 2005;28:24–29.
- [45] Baraton M-I. Surface functionalization of semiconductor nanoparticles. In: Vaseashta A, editor. *Life Cycle Analysis of Nanoparticles: Reducing Risk and Liability.* first edit. Lancaster, Pennsylvania: DEStech Publications; 2015. pp. 404.
- [46] Ibrahim NA, Eid BM, Abdel-Aziz MS. Green synthesis of AuNPs for eco-friendly functionalization of cellulosic substrates. *Appl Surf Sci.* 2016;389:118–125.
- [47] Logith-Kumar R, Keshav-Narayan A, Dhivya S, Chawla A, Saravanan S, Selvamurugan N. A review of chitosan and its derivatives in bone tissue engineering. *Carbohydr Polym.* 2016;151:172–188.
- [48] Omar S, Dutta B, Natour S, Abu-Reziq R. Rhodium-complexed hyperbranched poly(ethyleneimine) and polyamidoamine and their non-covalent immobilization on magnetic nanoparticles. *J Organomet Chem.* 2016;818:48–57.
- [49] García-Astrain C, González K, Gurrea T, Guaresti O, Algar I, Eceiza A, et al. Maleimide-grafted cellulose nanocrystals as cross-linkers for bionanocomposite hydrogels. *Carbohydr Polym.* 2016;149:94–101.
- [50] Gomez-Gonzalez SE, Carbajal-Arizaga GG, Manriquez-Gonzalez R, Cruz-Hernandez WD La, Gomez-Salazar S. Trivalent chromium removal from aqueous solutions by a sol-gel synthesized silica adsorbent functionalized with sulphonate acid groups. *Mater Res Bull.* 2014;59:394–404.
- [51] Quirarte-Escalante CA, Soto V, de la Cruz W, Porras GR, Manríquez R, Gomez-Salazar S. Synthesis of hybrid adsorbents combining sol-gel processing and molecular imprinting applied to lead removal from aqueous streams. *Chem Mater.* 2009;21(8):1439–1450.
- [52] Carbajal-Arízaga GG, Oviedo MJ, López OEC. Electrical properties of polycrystalline GaN films functionalized with cysteine and stabilization of GaN nanoparticles in aqueous media. *Coll Surf B Biointerfaces.* 2012;98C:63–71.
- [53] Oviedo MJ, Contreras OE, Rosenstein Y, Macedo ZS, Carbajal Arízaga GG, Hirata GA. New bismuth germanate oxide nanoparticle material for biolabel applications in medicine. *J Nanomater.* 2016;2016: 9782625.
- [54] Sánchez Lafarga AK, Pacheco Moisés FP, Gurinov A, Ortiz GG, Carbajal Arízaga GG. Dual responsive dysprosium-doped hydroxyapatite particles and toxicity reduction

- after functionalization with folic and glucuronic acids. *Mater Sci Eng C*. 2015;48:541–547.
- [55] Kohno Y, Asai S, Shibata M, Fukuhara C, Maeda Y, Tomita Y, et al. Improved photostability of hydrophobic natural dye incorporated in organo-modified hydrotalcite. *J Phys Chem Solids*. 2014;75(8):945–50.
- [56] Stine R, Simpkins BS, Mulvaney SP, Whitman LJ, Tamanaha CR. Formation of amine groups on the surface of GaN: a method for direct biofunctionalization. *Appl Surf Sci*. 2010;256(13):4171–4175.
- [57] Borges RM, Arizaga GGC, Wypych F. Immobilization of enzymatic extract from *Penicillium camemberti* with lipxygenase activity onto a hybrid layered double hydroxide. *Biochem Eng J*. 2009;48(1):93–98.
- [58] Pauling L. The principles determining the structure of complex ionic crystals. *J Am Chem Soc*. 1929;51:1010–1026.
- [59] Carbajal-Arizaga GG, Mangrich AS, da Costa Gardolinski JEF, Wypych F. Chemical modification of zinc hydroxide nitrate and Zn-Al-layered double hydroxide with dicarboxylic acids. *J Colloid Interface Sci*. 2008;320(1):168–176.
- [60] Shiyamala C, Venkatesan R, Sambasiva Rao P. Single crystal EPR studies of Cu(II) doped in cadmium sodium sulphate hexahydrate: A case of low hyperfine coupling constant. *Solid State Commun*. 2003;128(4):137–142.
- [61] Carbajal-Arizaga GG, Gardolinski JEFDC, Schreiner WH, Wypych F. Intercalation of an oxalatoxonobate complex into layered double hydroxide and layered zinc hydroxide nitrate. *J Colloid Interface Sci*. 2009;330(2):352–358.
- [62] Carbajal-Arizaga GG, Mangrich AS, Wypych F. Cu²⁺ ions as a paramagnetic probe to study the surface chemical modification process of layered double hydroxides and hydroxide salts with nitrate and carboxylate anions. *J Colloid Interface Sci*. 2008;320(1):238–244.
- [63] Silva LA, Andrade JB de, Mangrich AS. Use of Cu²⁺ as a metal ion probe for the EPR study of metal complexation sites in the double sulfite Cu²SO₃.Cd^{II}SO₃.2H₂O. *J Braz Chem Soc*. 2007;18(3):607–610.
- [64] Athappan PR, Rajagopal G. Synthesis, spectroscopic and redox behaviour of copper(II), nickel(II) and cobalt(II) complexes of some macrocyclic multidentates. *Polyhedron*. 1996;15(3):527–534.
- [65] Carbajal Arizaga GG. Chemical modification of zinc hydroxynitrate and layered double hydroxides surfaces with mono and dicarboxylic acids. Federal University of Paraná; 2008.

- [66] Reddy BJ. Spectroscopic characterisation of roasite and aurichalcite. *Neues Jahrb für Mineral-Monatshefte*. Schweizerbart Science Publishers. Stuttgart, Germany. 2004;7:302–316.
- [67] Wang SL, Wang PC. In situ XRD and ATR-FTIR study on the molecular orientation of interlayer nitrate in Mg/Al-layered double hydroxides in water. *Colloids Surfaces A Physicochem Eng Asp*. 2007;292(2–3):131–138.
- [68] Chao Y-F, Lee J-J, Wang S-L. Preferential adsorption of 2,4-dichlorophenoxyacetate from associated binary-solute aqueous systems by Mg/Al-NO₃ layered double hydroxides with different nitrate orientations. *J Hazard Mater*. 2009;165(1–3):846–852.
- [69] Aguirre JM, Gutiérrez A, Giraldo O. Simple route for the synthesis of copper hydroxy salts. *J Braz Chem Soc*. 2011;22(3):546–551.
- [70] Biswick T, Jones W, Pacuła A, Serwicka E, Podobinski J. The role of anhydrous zinc nitrate in the thermal decomposition of the zinc hydroxy nitrates Zn₅(OH)₈(NO₃)₂·2H₂O and ZnOHNO₃·H₂O. *J Solid State Chem*. 2007;180(4):1171–1179.
- [71] Cordeiro C, Arizaga G, Ramos L, Wypych F. A new zinc hydroxide nitrate heterogeneous catalyst for the esterification of free fatty acids and the transesterification of vegetable oils. *Catal Commun*. 2008;9(11–12):2140–2143.
- [72] Biswick T, Jones W, Pacula A, Serwicka E. Synthesis, characterisation and anion exchange properties of copper, magnesium, zinc and nickel hydroxy nitrates. *J Solid State Chem*. 2005;178(3):3810–3816.

Carbon Compounds

Intercalation of C₆₀-Fullerol into Graphite Oxide

Raymond Arsenault and Rabin Bissessur

Additional information is available at the end of the chapter

<http://dx.doi.org/10.5772/65999>

Abstract

Herein, we report on the intercalation of C₆₀-fullerol into graphite oxide. This was achievable due to the solubility of the guest species in water and the exfoliation/reconstruction properties of the layered host. The resulting nanocomposite materials were characterized using a wide variety of techniques, including infrared spectroscopy, powder X-ray diffraction, thermogravimetric analysis, and electron microscopy.

Keywords: intercalation, fullerol, graphite oxide, exfoliation, nanocomposite

1. Introduction

C₆₀-fullerene (or buckminsterfullerene) was the first compound to be discovered in the fullerene family of carbon allotropes. It is obtained by the purification of soot derived from the pyrolysis of graphite [1]. Each carbon is covalently bonded to three other carbon atoms in the nanostructure. The remaining electrons participate in delocalized double bonds which give rise to the electrical conductivity of the material. The atoms are arranged in a cage structure that confers excellent thermal stability to the material.

Fullerenes, and many of their derivatives, are relatively nontoxic and therefore have been considered as possible replacements for harmful substances such as heavy metals in some materials applications [2]. An interesting feature of fullerenes is the region of low electron density generated in the centre of the cage structure which allows for the possibility to trap other atoms or small molecules within, resulting in binary compounds known as endohedral fullerenes [3]. Hence, these materials could serve as protecting agents, for example, in protecting the active ingredients of medications from being eliminated too quickly by the immune system. However, the use of fullerenes in biological applications has been hampered due to

their insolubility in the aqueous environment of living cells. To explore such applications, water soluble derivatives of fullerene must therefore be synthesized, for example, by multiple hydroxylation of the fullerene cage structure to obtain fullerol. This synthesis can be achieved using a solvent-free reaction as described by Sheng et al. [4].

Graphite oxide (GO) is the oxidized form of graphite, which is usually obtained through the reaction of graphite with potassium permanganate in concentrated sulfuric acid in a process known as the Hummer's method [5]. This method adds oxygen-containing functional groups along the surface of the material, such as hydroxyl and carbonyl groups, and epoxide bridges, without breaking or severely interrupting the carbon sheet structure of graphite. Because of these functional groups, the material can be exfoliated in water and subsequently restacked, allowing other molecules such as polymers to be trapped between the layers [6]. Also, because GO is relatively nontoxic, this remarkably versatile substance has found use in biological applications, for example, as a biosensor for monitoring DNA hybridization [7].

Intercalating C₆₀-fullerol into GO may lead to the discovery of a hybrid material with interesting properties, especially for applications where the protection of small molecules is important. For example, the inclusion of an endohedral fullerene derivative into a lamellar material could allow for a more controlled release of the trapped molecule in the carbon cage. In general, intercalated materials have enhanced thermal and mechanical properties [8], which may also lead to more stable protecting properties. GO is an excellent choice as a host material for fullerol as both have been shown to form strong π -electron stacking interactions [9, 10]. Experiments were performed to determine whether C₆₀-fullerol can be successfully intercalated into GO via exfoliation and restacking of the layered host, as has previously been reported with compounds containing delocalized π -electrons [9].

2. Experimental section

2.1. Materials

C₆₀-fullerene, sodium hydroxide, hydrogen peroxide, methanol and hydrochloric acid were purchased from Aldrich. Graphite oxide was prepared as described in Ref. [5].

2.2. Synthesis of C₆₀-fullerol

C₆₀-fullerol was prepared using the solvent-free method as described in Ref. [4]. C₆₀-fullerene was placed in a mortar with 60 equivalents of both solid sodium hydroxide and 30% aqueous hydrogen peroxide, forming a suspension. These were ground together for at least 15 min to ensure complete reaction. The resulting yellow-brown sludge was dissolved by stirring in deionized water and then filtered by gravity to remove impurities. The resulting solution was concentrated under high vacuum until a brown precipitate appeared. The solid was fully precipitated by adding methanol and separated from the solution by centrifuging for 30 min, followed by decanting of the excess methanol. The solid was washed with methanol and

centrifuged twice more to remove any remaining sodium hydroxide, and then freeze-dried to obtain the brown hydroxylated product.

2.3. Intercalation of C₆₀-fullerol into GO

The process for the intercalation of C₆₀-fullerol into GO was adapted from Ref. [9]. C₆₀-fullerol and GO were placed in separate round bottom flasks. Deionized water was added to the flasks, and they were then sonicated for 30 min to ensure dispersion/dissolution of the solids. The fullerol solution was then added to the flask containing GO which was again sonicated for 30 min, then stirred overnight. Five drops of concentrated hydrochloric acid were then added, followed by another night of stirring. The reaction mixture was cast on a glass substrate in order to monitor the change in structure of the material by XRD, heated to 60°C for 90 min and then allowed to cool to room temperature. A small portion of the resulting suspension was cast on another glass substrate for XRD analysis, and the rest centrifuged for 30 min. The wet solid was then collected and freeze-dried to give the final product.

3. Instrumentation

Nuclear magnetic resonance spectroscopy was performed on samples of the synthesized C₆₀-fullerol on a Bruker 300 MHz NMR spectrometer. All samples were prepared in D₂O, and a total of 6228 scans were performed for ¹³C NMR and 174 scans for ¹H NMR.

C₆₀-fullerol, GO and all intercalation products, were analyzed using a Bruker ALPHA FT-IR spectrometer equipped with an attenuated total reflectance (ATR) sampling unit. The samples were run over the range 4000–400 cm⁻¹. The resolution of the instrument was 0.9 cm⁻¹, and 17 scans were used.

Powder X-ray diffraction was performed on all materials using a Bruker AXS D8 Advance diffractometer, equipped with a graphite monochromator, variable divergence and antiscattering slits, and a scintillation detector. Cu (Kα) radiation (λ = 1.542 Å) was used for the measurements which were run in air from 2 to 60° (2θ). Intermediate samples were prepared as casts on glass substrates as mentioned in Section 2.3, while samples of the final products were pressed on double-sided scotch tape on silicon substrates.

Thermogravimetric analysis was performed on a TGA Q500 from TA instruments using a heating rate of 20°C/min.

Scanning electron microscopy (SEM) was performed using a Hitachi TM 3000 tabletop scanning electron microscope. An accelerating voltage of 15 kV was used. The samples were mounted on a carbon black tape prior to the imaging.

High resolution transmission electron microscopy (TEM) was performed on a Hitachi 7500 Bio-TEM, using an accelerating voltage of 80 KV. The powdered samples were dispersed in deionized water with the help of ultrasonication, and the dispersed samples were cast on carbon-coated copper grids.

4. Results and discussion

C₆₀-fullerol synthesized in this research was characterized using various techniques to confirm hydroxylation of the fullerene structure and the number of hydroxyl groups added, in order to determine average molar mass and product yield. The intercalated product was characterized in order to confirm insertion of fullerol and determine the material's properties such as stoichiometry, structure, thermal properties, and solubility in water.

Hydroxylation of fullerene was confirmed using IR and NMR spectroscopy. The IR data are summarized in (Table 1), and NMR data are provided in (Table 2).

Compound	Frequency (cm ⁻¹)	Intensity	Assignment
Fullerene (Aldrich)	1427	w	C=C stretch
	794.8	m	C—C stretch
Fullerol (Batch 1)	2446	w, broad	O—H stretch
	1419	s	C=C stretch
	855.7	m	C—C stretch
Fullerol (Batch 2)	2447	w, broad	O—H stretch
	1423	s	C=C stretch
	877.2	m	C—C stretch
Fullerol (Batch 3)	3323	w, broad	O—H stretch
	1419	s	C=C stretch
	877.1	m	C—C stretch

Table 1. IR signals for fullerene and derivatives.

Compound	NMR type	Shift (ppm)	Multiplicity	Assignment
Fullerol (first batch)	¹ H	3.353	s	—O—H
	¹³ C	166.0	s	—C—OH
Fullerol (third batch)	¹ H	3.349	s	—O—H

Table 2. NMR chemical shifts.

The IR spectra contain the characteristic fullerene C=C stretch peak at 1420 cm⁻¹, although the intensity differs. This is because some double bonds are lost when electrons are used

to form bonds to the hydroxyl groups. During hydroxylation, double bonds also rearrange so that only carbons with single bonds are hydroxylated, in order to maintain the integrity of the cage structure. As a result, the position of the C=C signal remains virtually unchanged, while the C—C signal is shifted to higher frequency due to the effects of the hydroxyl group. However, the hydroxyl signal in the IR spectrum is much less intense and is usually observed at around 3323 cm⁻¹ (batch 3). However, for batch 1 and batch 2, the —OH band is shifted to a lower wave number ca 2440 cm⁻¹, and this is attributed to hydrogen bonding between the fullerol molecules, via the hydroxyl groups.

¹H NMR spectroscopy was performed on the synthesized fullerol (batch 1 and batch 3), and the observed chemical shifts were compared to the literature [11]. A singlet is observed at 3.35 ppm which corresponds to the fullerol hydroxyl proton and is in good agreement with the literature. ¹H NMR spectroscopy does confirm the successful synthesis of fullerol.

¹³C NMR was also performed on fullerol (batch 1), and a single strong peak is observed at 166 ppm. This is in very good agreement with the literature and represents the fullerene carbon signal shifted upfield due to the deshielding effect of the oxygen atoms [11].

TGA was conducted on the synthesized fullerol (batch 1 and batch 3). The data show that the fullerene cage structure is more stable when hydroxylated, as it decomposes above 900°C, while fullerene itself decomposes between 500 and 600°C. Using the residue percentage at the final decomposition along with the hydroxyl decomposition observed at an early stage in the thermogram allows for calculation of the molecular formula and hence molecular weight of the fullerol. The assumption made in the calculation is that the compound fullerol consists of 60 carbon atoms similar to the starting fullerene. Knowledge of the molecular formula and molecular weight allowed for calculation of the percent yield of the synthesized fullerol. The average molecular formula, molecular weight, and percentage yield are tabulated in (Table 3).

Batch	Molecular formula	Molecular weight (g/mol)	% Yield
First	C ₆₀ (OH) _{5.897}	820.9	87.7
Second	C ₆₀ (OH) _{5.897}	820.9	100.0
Third	C ₆₀ (OH) _{10.32}	896.1	86.3

Table 3. Reaction products and yields for fullerol synthesis.

Powder X-ray diffraction shows that the synthesized fullerol is completely amorphous. The powder pattern is featureless as there are no diffraction peaks present (Figure 1).

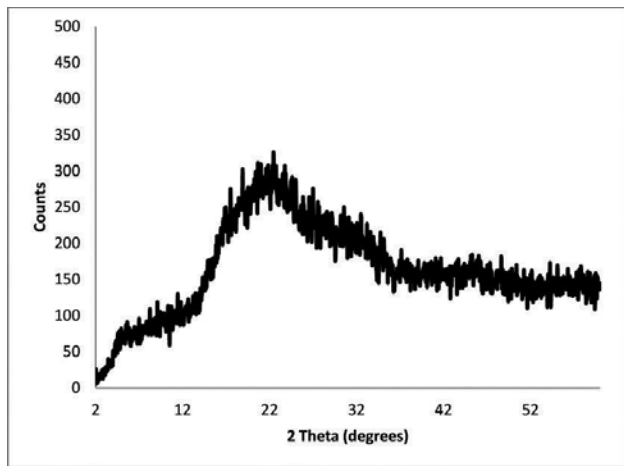


Figure 1. XRD of fullerol.

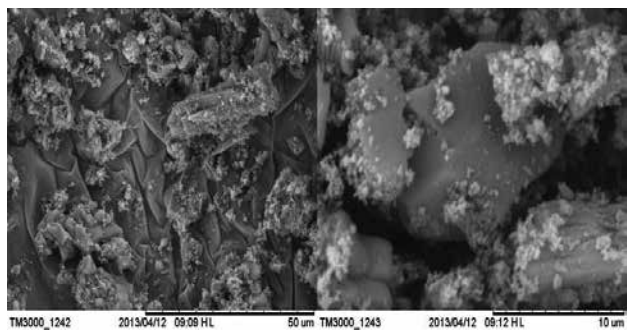


Figure 2. SEM images of fullerol.



Figure 3. TEM images of fullerol.

SEM (**Figure 2**) and TEM (**Figure 3**) provide supporting evidence that the synthesized fullerol is, in fact, amorphous. The SEM and TEM micrographs display complete lack of crystallinity, and hence the absence of long range structural order in fullerol in the solid state.

Intercalation of fullerol into GO was performed by adapting the synthetic methodology described in Ref. [9]. Using the molecular weight of fullerol as calculated from TGA, the mole ratio of fullerol to GO used in the intercalation experiments were 0.6:1, 1.2:1, and 2.4:1, and the resulting products will be referred to as the first, second, and third intercalate, respectively. Confirmation of intercalation and elucidation of the structural features of the intercalates were performed using IR, XRD, SEM, and TEM.

Compound	Frequency (cm ⁻¹)	Intensity	Assignment
GO	3201	s, broad	O—H stretch
	1717	m	C=O stretch
	1575	m	C=C stretch (GO)
	1368	m	C—C stretch
	1045	s	C—O stretch
First intercalate (fullerol:GO = 0.6:1)	3100	s, broad	O—H stretch
	1717	s	C=O stretch
	1576	m	C=C stretch (GO)
	1375	w	C—C stretch
	1223	m	C—O stretch (C ₆₀)
	1053	s	C—O stretch (GO)
Second intercalate (fullerol:GO = 1.2:1)	3210	s, broad	O—H stretch
	1714	s	C=O stretch
	1582	m	C=C stretch
	1371	w	C—C stretch
	1217	s	C—O stretch (C ₆₀)
	1036	s	C—O stretch (GO)
Third intercalate (fullerol:GO = 2.4:1)	1716	s	C=O stretch
	1565	m	C=C stretch (GO)
	1428	w	C=C stretch (C ₆₀)
	1227	s	C—O stretch (C ₆₀)
	1046	s	C—O stretch (GO)

Table 4. IR signals for GO and intercalated products.

It is worthy to note that the IR spectrum of graphite oxide contains, as expected, peaks characteristic of hydroxyl, carbonyl, and other C—O functional groups. The IR spectra of the first two intercalates closely resemble that of graphite oxide; however, they also contain two different absorptions in the region for C—O stretching. The one just above 1200 cm^{-1} may be related to the fullerol C—O bond as it is more intense for the second intercalate where a higher ratio of fullerol was used in its formation. For the third intercalate, where almost twice as much fullerol was used in comparison to the second intercalate, the intensity of the peak is reduced, and the hydroxyl peak disappeared. However, a peak at 1428 cm^{-1} characteristic of the fullerene cage structure is observed. This is a good evidence for intercalation, as it suggests that adding enough fullerol causes the hydroxyl groups in the material to react with functionalities on the GO layers in some way that prevents them from absorbing in the IR region. This could, for example, be a hydrolysis reaction of the hydroxyl groups, creating an ester linkage between the fullerene cage and graphite oxide layers. The major peaks from the IR spectra are recorded in (Table 4).

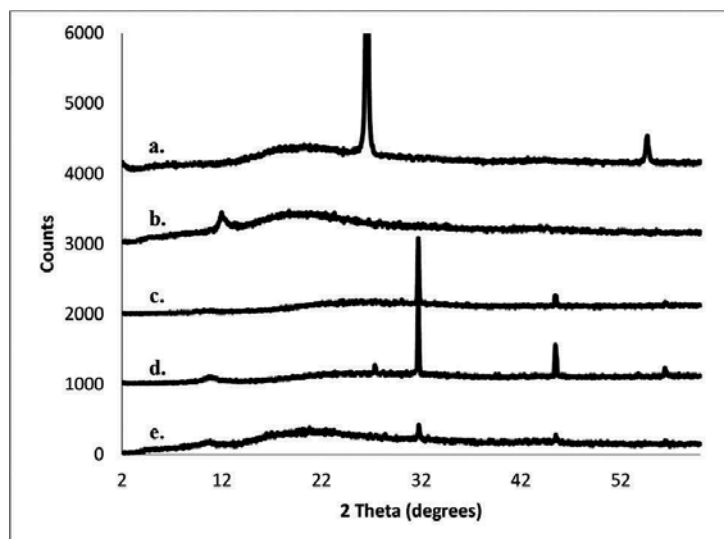


Figure 4. XRD of (a) graphite, (b) graphite oxide, (c) first intercalate after acid treatment (cast), (d) first intercalate, after acid followed by heat treatment (cast), and (e) first intercalate (final solid, freeze-dried product).

XRD was performed on the final solid products of the three intercalation reactions. In addition, XRD was run on cast samples during the formation of the first intercalate, after acid and heat treatments (**Figure 4**). For comparison, the XRD scans of graphite and GO are also included in **Figure 4**. The X-ray diffractograms show that addition of acid and heat treatment during the intercalation process leads to the formation of a more ordered intercalated material. Acid and heat treatments cause the appearance of a peak with a d-spacing value of 2.8 Å ($2\theta = 32$) which is not seen in the diffractograms of the starting materials. This is actually supporting evidence for the hydrolysis mechanism proposed from the IR data, a likely mechanism for the intercalation of fullerol into GO. The appearance of a peak with a d-spacing of 8 Å (higher than that

of GO) is also good evidence for intercalation, and this peak is much more intense in the product with higher fullerol content. However, it is interesting to note that the final freeze-dried product does contain an amorphous character, and this could be due to the fact that the XRD was run on the solid sample adhered to double-sided scotch tape on silicon substrate.

Although the above experiments offer excellent evidence for intercalation, full intercalation would, however, result in a d-spacing value higher than 8 Å, as the diameter of the fullerene cage is over 1 nm. Therefore, the most likely explanation is partial intercalation of fullerol into the graphite oxide layers. Hence, the best evidence for determining the detailed structure of these materials is by SEM (**Figure 5**) and TEM (**Figure 6**). With these techniques, one can directly observe the surface of the materials and between the layers, as well. In some of the images shown in **Figures 5** and **6**, amorphous clumps resembling those of fullerol can be seen packed between the layers, as well as attached to the surface of the layers. This is the clearest evidence that at least partial intercalation did occur.

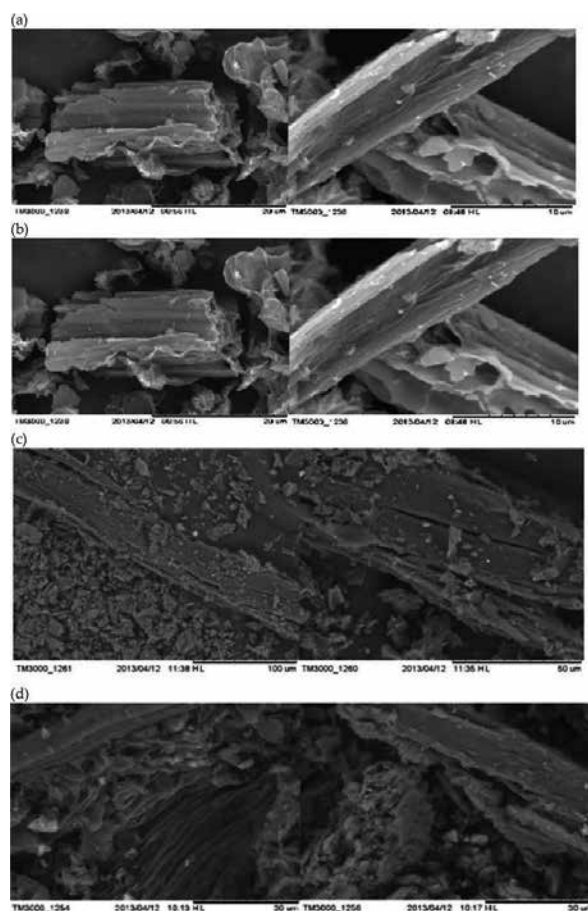


Figure 5. SEM micrographs of (a) graphite oxide, (b) first intercalate, (c) second intercalate, and (d) third intercalate.

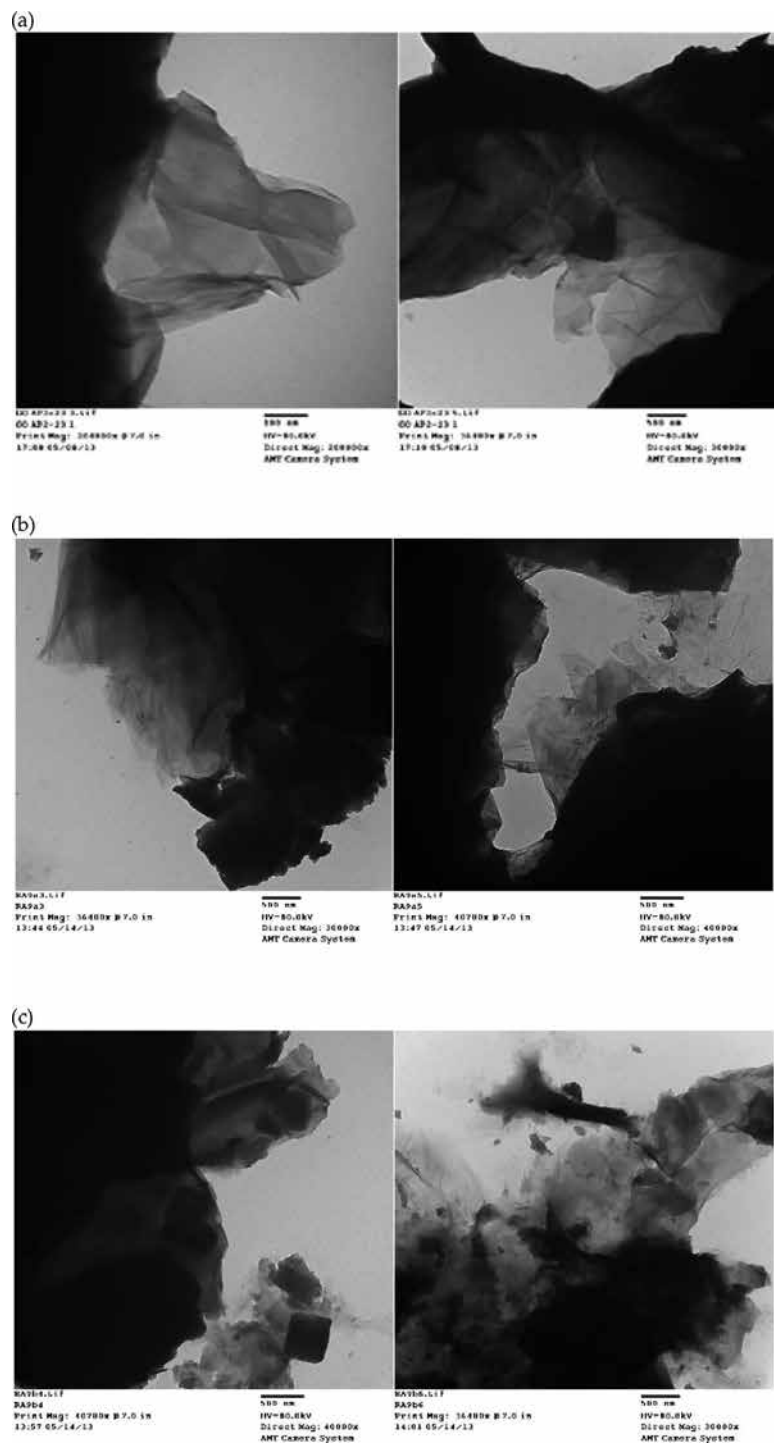


Figure 6. TEM micrographs of (a) graphite oxide, (b) second intercalate, and (c) third intercalate.

TGA studies were used to determine the stoichiometry of the intercalated materials by making use of the observed mass losses, molecular weight of fullerol, and that of GO as reported in Ref. [9]. As an illustration, the thermogram of the second intercalate (fullerol:GO = 1.2:1) is depicted in **Figure 7**; the other two intercalates show similar decomposition patterns. The mass loss seen at around 400°C is due to the release of the fullerene cage structure from the intercalated material, and the loss at around 800°C is attributed to be oxidation of carbon residues remaining from graphite oxide (**Figure 7**). Using this information, the stoichiometries of the intercalated materials were calculated and are shown in (**Table 5**). The evidence suggests that increasing the fullerol ratio increases the amount of fullerol contained in the final product, but not all of the fullerol ends up in the gallery space of the GO, especially at higher molar ratios where any excess fullerol will end up on the surface and edge of the layered structure as evidenced by SEM.

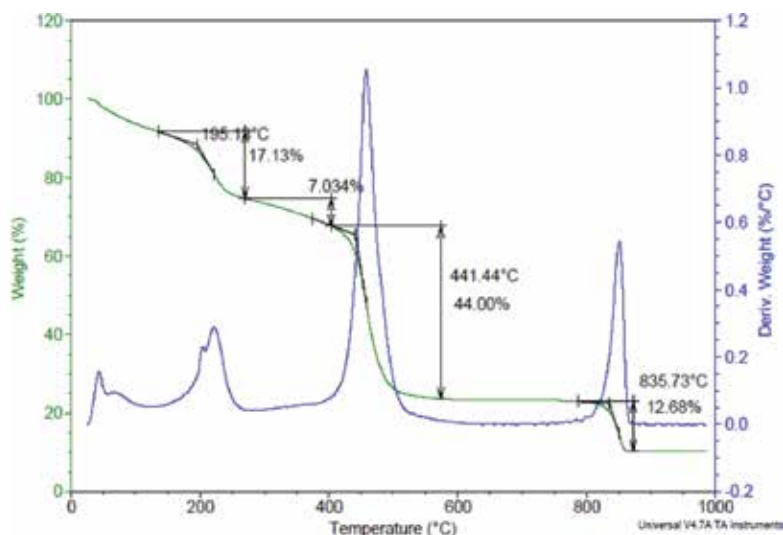


Figure 7. TGA of second intercalate.

Experiment	Fullerol:GO ratio	Calculated stoichiometry
1	0.60:1	(C ₆₀ (OH) _{5.897}) _{0.67} GO
2	1.2:1	(C ₆₀ (OH) _{10.32}) _{0.80} GO
3	2.4:1	(C ₆₀ (OH) _{10.32}) _{1.7} GO

Table 5. Stoichiometries of intercalated products.

The intercalation compounds were tested for their solubility in water. The third intercalate dissolved readily, while the first and second intercalates could only be dispersed in water, with observed pieces of solids settling down over time. This suggests a clear trend that having more

fullerol in the composite material increases its polarity and thus its solubility in a polar solvent such as water.

5. Potential applications of materials

The intercalated materials synthesized in this research could potentially be used as drug delivery systems. Graphite oxide (GO) and fullerol are both nontoxic materials which can be dispersed or solubilized in an aqueous environment. Our research shows that fullerol can be partially intercalated into GO. Hence, drug molecules entrapped within the cage structure of fullerol can potentially be inserted into layered GO, and the resulting intercalated systems would allow for the slow and controlled release of these drugs in humans and animals.

6. Conclusion

C₆₀-fullerol was successfully synthesized and partially intercalated between the layers of graphite oxide. The stoichiometry of these nanocomposite materials was determined via TGA, and their structure elucidated using a variety of techniques. Solubility tests showed that the intercalate with highest fullerol content was more soluble in water, and IR analysis suggests that the mechanism of intercalation is the hydrolytic formation of bonds between the fullerene cage structure and functionalities on the GO layers. The lower than expected d-spacing value of the intercalates as observed by XRD suggests partial intercalation of the fullerol into the GO layers. SEM and TEM proved to be valuable characterization techniques for this research, as they allowed for direct observation of the fact that fullerol was, indeed, partially intercalated into the layered structure.

In perspective, if endohedral fullerenes can be successfully intercalated into GO, the chemical and thermal stability of the resulting intercalated nanocomposites materials could make them useful in applications that require protection for sensitive or reactive molecules. In addition, their water solubility could make them useful materials as drug delivery systems, since fullerene and GO are both nontoxic allotropes of carbon. Further research is required in order to determine the types of fullerenes that can be intercalated into GO, as well as the properties of the resulting nanocomposite materials.

Acknowledgements

Financial support from the Natural Sciences and Engineering Research Council of Canada (NSERC) and the University of Prince Edward Island is gratefully acknowledged.

Author details

Raymond Arsenault and Rabin Bissessur*

*Address all correspondence to: rabisessur@upei.ca

Department of Chemistry, University of Prince Edward Island, Charlottetown, Prince Edward Island, Canada

References

- [1] Kroto HW et al. Fullerenes studies at sussex. In *Buckminsterfullerenes*; VCH: New York, 1993.
- [2] Prato M. [60] Fullerene chemistry for materials science applications. *Journal of Materials Chemistry*. 1997; 7: 1097–1109.
- [3] Chai Y et al. Fullerenes with metals inside. *Journal of Physical Chemistry*. 1991; 95(20): 7564–7568.
- [4] Sheng W et al. Novel and efficient synthesis of water-soluble [60] fulleranol by solvent-free reaction. *Synthetic Communication*. 2005; 35(13): 1803–1808.
- [5] Hummers WS Jr., Offeman RE. Preparation of graphitic oxide. *Journal of American Chemical Society*. 1958; 80: 1339.
- [6] Bissessur R, Scully SF. Intercalation of solid polymer electrolytes into graphite oxide. *Solid State Ionics*. 2007; 178: 877–882.
- [7] Wu J et al. A biosensor monitoring DNA hybridization based on polyaniline intercalated graphite oxide nanocomposite. *Sensors Actuators B*. 2004; 104: 43–49.
- [8] Ray SS, Okamoto M. Polymer/layered silicate nanocomposites: a review from preparation to processing. *Progress in Polymer Science*. 2003; 28: 1539–1641.
- [9] Bissessur R et al. Encapsulation of polyanilines into graphite oxide. *Langmuir*. 2006; 22: 1729–1734.
- [10] Sygula A et al. A double concave hydrocarbon buckycatcher. *Journal of American Chemical Society*. 2007; 129(13): 3842–3843.
- [11] Alves GC et al. Synthesis of C₆₀(OH) 18–20 in aqueous alkaline solution under O₂-atmosphere. *Journal of the Brazilian Chemical Society*. 2006; 17(6): 1186–1190.

Covalently Functionalized Nano-Graphene Oxide for Fine Chemical Synthesis

Surjyakanta Rana and Sreekantha B. Jonnalagadda

Additional information is available at the end of the chapter

<http://dx.doi.org/10.5772/65941>

Abstract

Nano-graphene, which is entirely composed of aromatic carbon atoms is relatively a new material, with two dimensional periodic structures and possess amazingly interesting chemical and mechanical properties. Graphene and graphene oxide (GO) materials have been explored widely as supports due to their tunable electrical properties and high surface area as well as different functional groups. The covalent modification of surface oxygen of carbon based materials, like graphene oxide and nano graphene oxide (NGO) with organo amine and other functional groups is very opt for various applications. Covalent immobilization of various organic functional moieties and metal modified organo functionalized species on nano-graphene oxide surface enables a robust immobilization of the reactive catalytic sites through strong binding on the support surfaces. Such materials prevent the leaching of active metals and improve their recyclability, when used as catalysts in solution phase. As the stability of metal depends also on the functionalization of the NGO support, metal modified/ covalently functionalized nano-graphene oxide materials are widely used in fine chemical synthesis. The functional group of NGO also prevents the aggregation of the catalytically active metal species during the reaction time. Both amine functionalized and metal (Pd) modified amine functionalized nano graphene oxide exhibit excellent activity towards fine chemical synthesis, such as with multicomponent reactions, oxidation reactions and C-C coupling reactions.

Keywords: graphene oxide, different amine functionalized, metal nanoparticles, oxidation reaction, one-pot reaction multicomponent reaction, coupling reactions

1. Introduction

High surface-to-volume ratio as well as distinctive thermal, electrical, mechanical, as well as optical characteristic can be named as the main advantages of the nano materials. Generally, carbon-based nanomaterials, with at least 1D in nanometer size, possess exceptional and innovative properties in their specific structure. Carbon allotropes, fullerene, carbon nano-tube (CNT), graphene, graphite etc. exist in different forms in zero, one, two, or three dimensions. Some of the carbon based nanomaterials are preferred as a support for active materials in catalysis. Among these materials, nano-graphene oxide is preferred to be an ideal 2D catalytic support, because of its outstanding electrical and thermal conductivity as well as mechanical strength with high surface area [1–15]. The characteristics of graphene nanomaterials enable them to interact with organic molecules through both covalent and non-covalent bonds. H-bonding, π - π stacking, π -cation interaction, π -anion interaction, hydrophobic interaction, and van-der Waals bonding etc. are examples of such non-covalent interactions. Covalent bonds happen between organic molecules and graphene based carbon nanomaterials with certain functional groups, such as carboxyl, hydroxyl, and epoxy group, facilitating the functionalization of graphene based nano materials. Pristine forms of these graphene based nanomaterials are water insoluble and in most of the organic solvents. Exploiting the exceptional property, a variety of plans have been established to obtain stable and uniform dispersions of active materials [16–18]. Chemical modification is an outstanding, alternative for the connection of organic group on the graphitic surface of these nanomaterials [4, 6, 19]. Metal modified functionalized graphene based nano materials prevent the leaching of the nano metals.

Many researchers contributed to the improvement in the activity and selectivity of functionalized graphene based nanomaterials in different applications, relative to the pristine material. This chapter provides an insight into the covalently functionalized nano-graphene oxide and metal modified covalently functionalized nano-graphene oxide materials and their versatile applications in the field of catalysis plus their applicability in fine chemical synthesis.

2. Carbon nanomaterials and their allotropes

Carbon receives its designation from the Latin word ‘carbo’ meaning charcoal, and forms the more well-known stable allotropes compared to other elements. While, the basic carbon atom builds up with tetrahedral lattice of sp^3 hybridization in diamond, the sp^2 hybridized extended networks are responsible for the formation of graphite. In past three decades, different allotropes of carbon have been discovered with periodic binding networks of alternate $-sp^3$, $-sp^2$ and sp hybridized carbon atoms. Among the allotropes, buckminsterfullerene (C₆₀), carbon nanotubes (CNTs) and graphene are most famous. These carbon allotropes appear in zero, one, two, or three dimensions and in different forms (**Figure 1**). While many allotropes of carbon like carbon nanofibers, amorphous carbon etc. exist, depending on the type of hybridization and shape of the materials, these allotropes exhibit varied exciting properties. The reporting of first stable two dimensional graphene material with extraordinary properties in 2007 may be considered as a breakthrough in the Nano carbon chemistry arena [2].

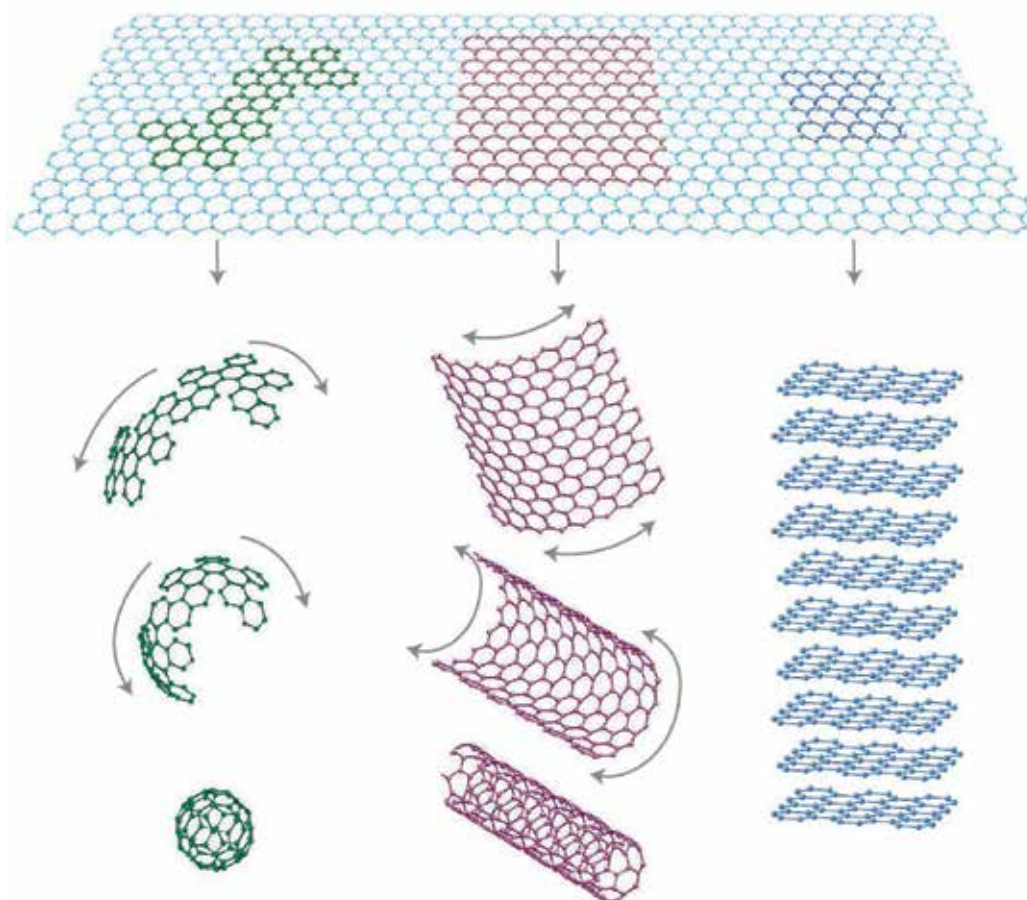


Figure 1. Mother of all graphitic forms. Graphene is a 2D building material for carbon materials of all other dimensionalities. It can be wrapped up into 0D Bucky balls, rolled into 1D nanotubes or stacked into 3D graphite [reproduced with permission from Ref. [2]].

3. Graphene

Graphene is a tightly packed monolayer of sp^2 -bonded carbon atoms into honeycomb two dimensional (2-D) crystal lattice. Graphene has fascinated both physicists and chemists due to its extraordinary properties such as thermal conductivity, an excellent electronic properties, high specific area etc. Graphene can be prepared by various methods and each process enjoys diverse advantages and limitations.

4. Synthesis of graphene

Literature survey reveals that graphene can be synthesized by using different techniques and starting materials. Quality of graphene synthesis can be achieved either by top-down or bottom-up approaches as summarized in the **Figure 2**.

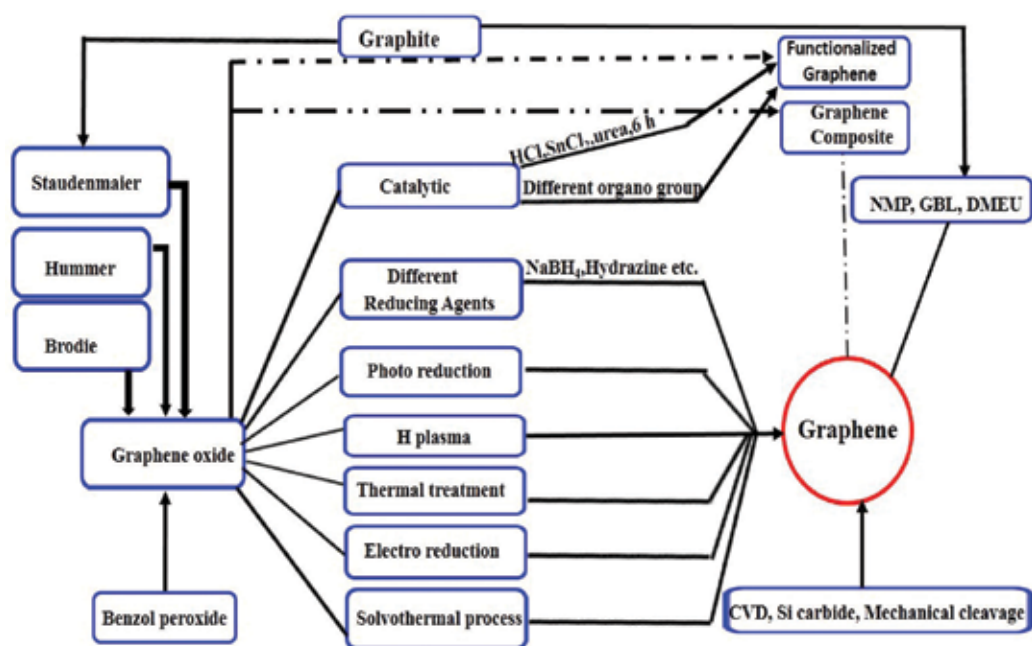


Figure 2. Road map to high quality graphene.

4.1. Top-down Synthesis

In top-down method, the graphene oxide and reduced graphene oxide are produced from the graphite powder. Generally using a large quantities of graphite, graphene oxide (GO) was obtained through oxidation process, while graphene was generated by reduction or exfoliation process of GO. Although reduced graphene oxide and graphene have similar properties, the surface of reduced graphene oxide possess some functional groups and carbon vacancies. Due to the similarity in properties, many researchers have used reduced graphene oxide in place of graphene. The different methods were developed by Brodie (1860) [20], Staudenmaier (1898) [21], and Hummers and Hoffman (1958) [22] for the preparation of graphene. Out of these Hummers and Hoffman Method gained more popularity and this method involves stoichiometry amounts of numerous strong acids and oxidizing agents such as con. nitric acid, con. sulfuric acid, sodium nitrite, and KMnO_4 for oxidation. The synthesis of graphene oxide (GO), followed by modified Hummers method with sonication method for exfoliation of few-layer stacked graphite oxide to graphene oxide. Successful exfoliation totally depends on the sonication time, energy and solvents used. The advantages of this process are easy preparation in short reaction times and lower generation of toxic gases.

4.2. Bottom-Up process

In bottom up process for synthesis of graphene sheets by pyrolyzation is called as solvothermal method. In this method sodium and ethanol are used for sodium ethoxide, and sodium ethoxide was pyrolyzed into stacked layers of graphene. The stacked layered graphene is

converted into single layered graphene sheet by sonication. This method is highly cost-effective, but provides defective graphene. Another approach for synthesis of graphene is by unzipping or unwrapping of CNTs. Chemical vapor deposition (CVD) is also an alternate method for synthesis of graphene [23–27]. The main advantages of CVD are the quality parameters, such as size, shape, and morphology of anticipated material which can be tuned by controlling the conditions of chemical vapor decomposition.

5. Functionalized Graphene Oxide

Surface functionalization is fundamental technique in material science, in which new functional groups are added onto the surface of the materials by chemical methods. Modification and functionalization of graphene oxide surface is possible only due to presence of different oxygen containing functional groups. Covalent and non-covalent methods are the two ways for functionalization of carbon based graphene oxide materials with different advantages and drawbacks. The final characteristics of the materials will be dependent on the nature of functionalization.

5.1. Non covalent Functionalization

In noncovalent modification can be achieved through van-der Waals force between planer groups and the carbon atom. Noncovalent modification avoids disrupting the construction of the carbon materials, allowing their original characteristics to be reserved. Non covalent functionalization is a type of physical adsorption, just likes the weak interactions, which does not affect the basal plan structure of carbon based graphene sheets. Sometime metal modified carbon based materials and also some heteroatoms such as N, O, and S doped on to the carbon based materials have also been used to support metal nano particles to enhance the reactivity as well as stability through the interactions of active metal clusters and carbon vacancies. The main approaches for the non-covalent modification/functionalization of carbon based materials to form metal nano particles are wet impregnation and dry synthesis [28].

Many researchers have proposed non covalent functionalization of metal nano particles over carbon based materials by wet synthesis method. Wet synthesis procedure often undergoes from several drawbacks, such as non-homogeneous distribution and adhesion and many sources such as the type of organic solvents, reducing agents, metal precursors concentration and temperature also influence the quality of the product. Thus, this method is less used.

The dry synthesis method has been receiving vital consideration due to its simplicity and advantage of controlling parameters plus enhanced adhesion. Generally, carbon based materials are of hydrophobic nature, which can be lessened through decoration with metal nano particles via dry synthesis method. In this method to creates bridging of functional groups of support materials with nano metals [29, 30]. Thus the problems associated with wet synthesis procedure have been resolved by dry synthesis approach for preparation of carbon based materials loaded with metal Nano particles.

5.2. Covalent Functionalization

Covalent modification/functionalization makes covalent linkage of chemical bonds or functional groups onto the surface. The chemical bond is formed between different chosen functional groups such as carboxylic, hydroxyl and epoxy groups with oxides of the graphene oxide. The covalent modification of carbon based materials mainly changes the hybridization of carbons in sp^2 to sp^3 . Not only functionalization with mono-, di- or tri- amine groups [4, 31], different hetero atoms such as P, B, and O also can be introduced to the carbon network of graphene oxide. The inorganic complexes/nano composites have also been introduced on to the carbon based graphene through covalent modification. The covalent modification enhances both physical and chemical properties of nano graphene such as solubility, catalytic activity, electron mobility and introduces hydrophilicity to the materials. Co-precipitation method is one of the techniques to achieve covalent functionalization of carbon based materials which enhances activity, selectivity and stability of materials. Hydrothermal method is the other method for covalent functionalization of Nano graphene oxide, which not only improves the activity, selectivity and stability of materials, but also affords good morphology. In hydrothermal method, Specific temperature and pressure with constant rate are maintained to facilitate the morphology of the materials. Thus, hydrothermal method is considered the ideal technique for preparation of covalent functionalization of carbon based Nano graphene oxide.

6. Catalytic Applications

Catalyzed organic transformation reactions display an important role in industries for the synthesis of natural products, pharmaceuticals product, and agricultural derivatives [32, 33]. Carbon based materials such as graphitic carbon and their functionalization and metal modified functionalized graphitic carbon based compounds have been used as catalysts for fine chemical synthesis. Functionalized carbons based materials are often more active and/or more selective catalysts than the un-functionalized carbon based materials. Nitrogen insertion into the graphene materials is one of the interesting modifications, which includes the pyrrolic N, pyridinic N, graphitic N, or different of amino groups in to graphene structures. Functionalized carbon based graphene materials are active for a different reactions including selective oxidative oxidation of aromatic compounds [34], dehydrogenation of hydrocarbons [35, 36], decarboxylation of fatty acids [37], base catalyzed reactions and one-pot multicomponent reactions [12].

6.1. Catalysis by GO based materials

Graphene oxide (GO) based materials have been festooned with different oxygen functional groups, including carbonyl, epoxy, hydroxyl, and carboxylic acids. These functional groups impart graphene oxide inherent acidity, and oxidative properties, chemical and catalytic activity. Due to the oxygen containing groups, GO based materials have been successfully explored as catalysts for a variety of fine chemical syntheses reactions involving oxidation, epoxidation, oxidative coupling, dehydrative polymerization, Claisen–Schmidt coupling and

hydrogenation. Bielawski and coworkers have reported [38] the oxidation reaction of alcohols to ketones and aldehydes, as well as alkenes to diketones using graphene oxide catalyst at 150 °C. GO itself a solid acid catalyst, so it has been employed for the synthesis of dipyrromethane and calix-4-pyrroles [39]. GO was found to be good to catalyze the Aza-Michael additions [40], Claisen–Schmidt coupling reactions [41], ring opening polymerization [42] and Friedel-Crafts reactions [43]. Some fine chemical syntheses using graphene oxide based catalysts are summarized in **Table 1**.

6.2. Catalysis by Functionalized nano GO Catalysts

Although graphene oxide is a solid acid catalyst, researchers have modified its surface characteristics through functionalization according to their requirements. Modifying the GO by covalent modification of its surface silanol groups with different nitrogen containing organo amines increase the basicity of this materials making them suitable for base catalyzed reactions such as Knoevenagel condensation and MCRs. Rana et al have reported a method for covalent modification of organo-functionalized graphene oxide which showed excellent activity towards one-pot synthesis of pyrazolo-pyranopyrimidine derivatives [12]. Graphene-based solid acid materials anchored with both amine and sulfonic acid containing groups proved good for both acid and base catalyzed reactions, such as decarboxylation of nitro aldol reactions [44]. The graphene-based solid acid catalyst prepared by anchoring with sulfonic acid-containing group to a graphene oxide/reduced graphene oxide surface reportedly exhibited excellent activity towards acid catalyzed reactions of esterification of acetic acid with cyclohexanol gave 58.9% yields [47]. Details of various reactions catalyzed by functionalized GO based materials are shown in **Table 2**.

6.3. Catalysis by metal modified amine functionalized nano carbon based catalysts

Hybrid materials involving inorganic graphene oxide and organo amine groups have an extra advantage in binding the metal atom strongly as compared to un-functionalized GO. The amine functionalized graphene oxide as support material has high surface area to enhance catalytic activity as well as dispersion capacity. The metal remains strongly covalently bounded to the support of graphene oxide and also it does not leach in the reaction medium. Hence it will be reusable for several cycles. Furthermore, the functionalized amine possess external binding capacity, which will readily provide more number of active sites. Generally, metal modified amine functionalized graphene oxide (GO)/reduced graphene oxide/ graphene based materials are also decorated with selective oxygen functional groups, including carbonyl, epoxy, carboxylic acids and nitrogen containing group as well as metal particles. These groups impart graphene oxide their inherent acidity, basicity and oxidative properties and their chemical and catalytic activity.

The activity of the metal modified amine functionalized carbon based graphene materials depends on type of metal and also on the oxidation state of the metal particles. Among the noble metals particles, generally, palladium metal particles have been more promising in nanotechnology and catalysis. Palladium having zero oxidation state will be more active towards coupling reactions, while the bivalent palladium metal particles will be active for oxidative

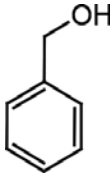
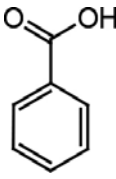
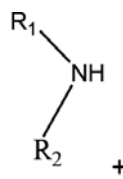

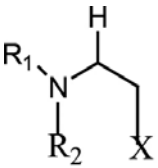
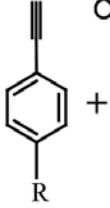
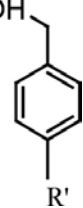
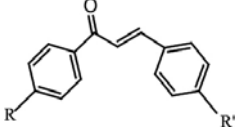
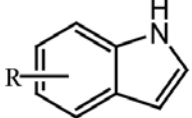

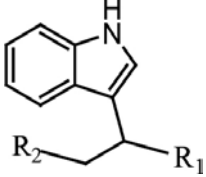
Starting Material	Product	Conditions	Catalyst (wt% GO)	Yield (%)	Ref.
		24 h, 100 °C	200	92	[38]
 + 	 R=H, CH ₃ R ₁ =Et, n-Pr, n-Bu, Bz R ₂ =Et, n-Pr, n-Bu, Bz X=CN, CONH ₂ , COOC	RT	-	≥85	[39, 40, 42]
 + 		80–100 °C, 14–24 h	200	R or R': Electron donating group >50 R or R': Electron withdrawing group <30	[41]
 +  R ₁ =COCH ₃ , NO ₂ R ₂ =CH ₃ , Aryl		1–6 h, RT	10–50	52–94	[43]

Table 1. Some reactions catalyzed by graphene oxide (GO).

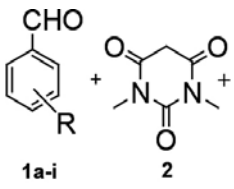
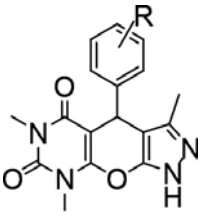
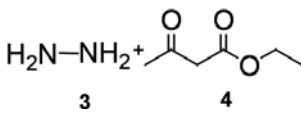
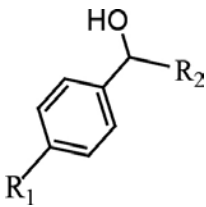
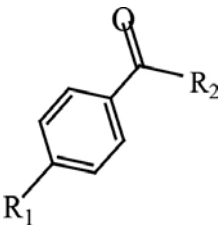
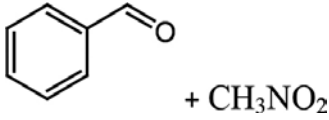
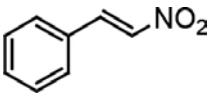
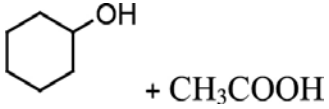
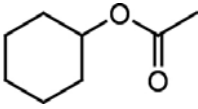
Starting Materials	Product	Conditions	Catalyst	Yield (%)	Ref.
 1a-i 2	 5a-i	45–60 min,	Diamine functionalized GO	<93	[12]
 3 4					
 R₁ R₂		10 h 1atm O ₂ 40–70 °C	N-doped graphene		[45]
 + CH₃NO₂		10 h 100 °C	1° and 3° amine functionalized graphene oxide	100	[46]
 + CH₃COOH		100 °C	Sulfated graphene	58.9	[47]

Table 2. Reaction catalyzed by functionalized GO and hetero atom doped.

reactions. Researchers have described the C-C coupling reactions with inert conditions and various type of organic solvents by different catalysts loaded on acidic supports. For example, the palladium modified montmorillonite as catalyst for C-C coupling reaction with 92% yield was reported at 150 °C and reaction time of 2–3 h [48]. A 35 % conversion towards C-C coupling reaction with organic solvent at 3 h reported by Corral et al., [49]. Melania et al. have published the C-C coupling reaction with Pd@GO/Pd@RGO catalysts and using organic solvents at 80 °C >90% yield after 20 h [50]. Rumi et al. presented that, GO-PdNPs gave C-C coupling products (85% yield) with toluene at 110 °C in 24 h [51]. Xiang et al. reported that, Pd²⁺/GO gave C-C coupling products (85.5% yield) with DMA/H₂O at 80 °C in 24 h [52]. Li et al. have employed Pd–Ni/RGO catalyst with ethanol and water solvent at 300 °C for 5 h and reported 98.6% yield towards C-C coupling products [53].

Siamaki et al. have reported the C-C coupling by Pd/G catalyst gave excellent yields with Turnover frequency (TOF) = 108,000 h⁻¹ [54]. Nie et al., have reported that C-C reaction with Pd-Ni/RGO catalyst gave TOF = 38,750 h⁻¹ [55]. Turnover frequency (TOF) provides the clear information about the efficiency of catalyst, which will be necessary for any applications. The TOF totally depends on the metal concentration of the materials. Mulhaupt et al. have reported a coupling reaction over Pd²⁺ exchanged graphite oxide with turnover frequency of TOF = 39000 h⁻¹ [56].

Earlier, we have reported the design and fabrication of hybrid materials such as amine functionalized nano graphene oxide materials and metal modification with Pd(II)/Pd(0) [1–3]. We have also studied the C-C Suzuki reaction with Pd(0)-AAPTMS@G catalyst and observed an impressive TOF = 185 078 h⁻¹ with recyclability of catalyst up to 6th run using eco-friendly water as solvent [4] In this review, we include our latest results on the scope of GO and amine functionalized GO-based materials/ metal modified amine functionalized GO based materials in selective coupling reactions. We evaluated the activity of different graphene based materials catalysts in C-C coupling of idobenzene with phenylboronic acid and different

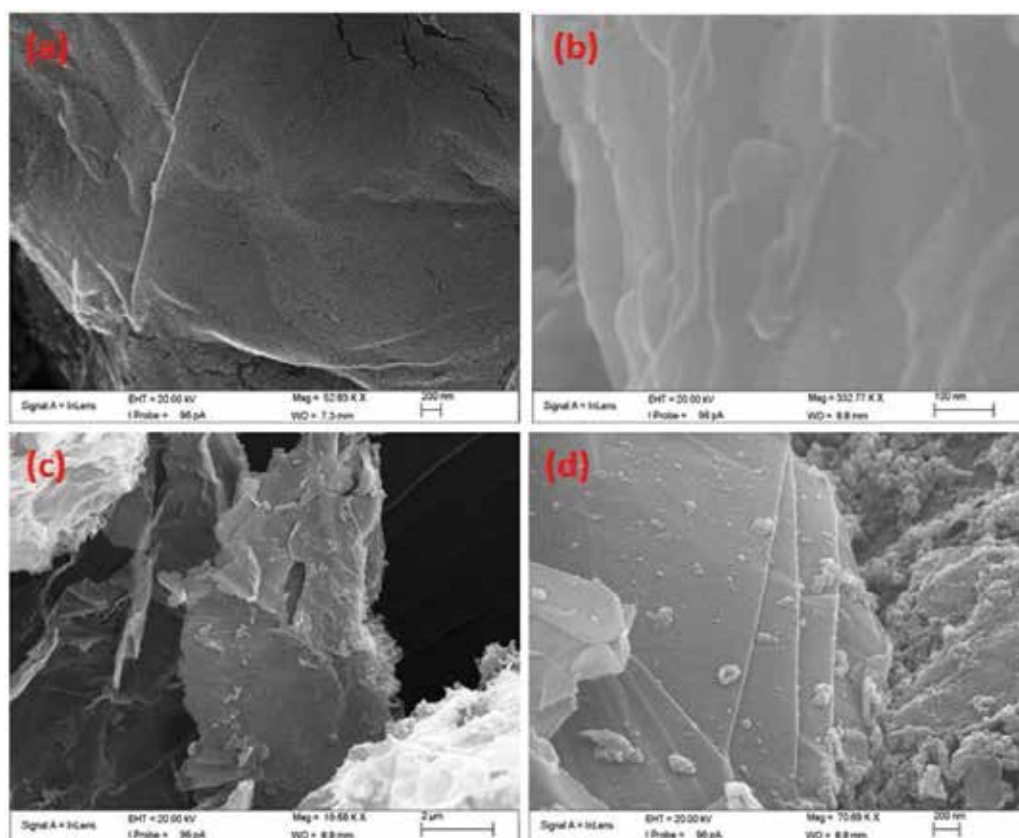


Figure 3. SEM Image of (a) graphene oxide, Scale bar = 200 nm (b) amine functionalized graphene oxide, Scale bar = 100 nm, (c) Pd(0) modified amine functionalized graphene, Scale bar = 2 μm and (d) Higher magnification of Pd(0) modified amine functionalized graphene, Scale bar = 200 nm [reproduced with permission from Ref. [4]].

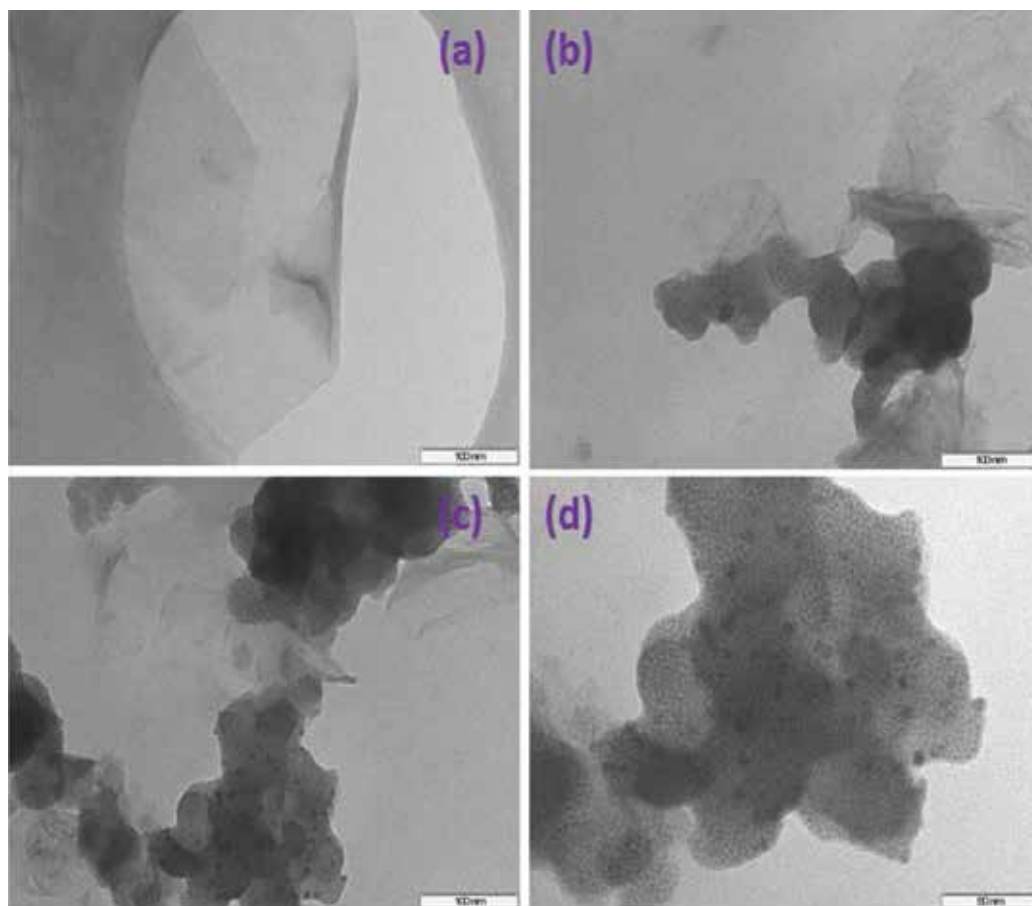


Figure 4. TEM Image of (a) graphene oxide, scale bar = 100 nm (b) amine functionalized graphene oxide, scale bar = 100 nm (c) Pd(0) modified amine functionalized graphene, scale bar = 100 nm and (d) Higher magnification of Pd(0) modified amine functionalized graphene, scale bar = 50 nm. [reproduced with permission from Ref. [4]].

halo benzenes with varied halo pyridines. Considering the bond energies of C-I, C-Br and C-Cl, bonds are 222.6, 281.4 and 340.2 kJmol⁻¹ respectively, the C-I bond breaks easily to form C-C coupling product then others. Thus, iodobenzene benzene gave excellent yields (98%) in short reaction time (25 min) with Pd (0)-AAPTMS@G material. The organo amine modified GO sheets serve to stabilize the Pd metal nanoparticles as well as to supply suitable electron density to the metal species. The catalyst is stable in aqueous medium due to strong interaction of amino group and metal particles. Up to the 6th cycle the recycled catalyst showed full efficacy with minimal loss of activity and 7th onwards some reduction in its efficiency was observed.

Al-Marri et al reported that, Pd@graphene nanocomposite gives 100% conversion towards oxidation of benzyl alcohol with toluene solvent at 100 °C [57]. MnO₂/graphene oxide at 80 °C and in 3 h gave 91 % yield towards conversion of benzyl alcohol to benzaldehyde reported by Kadam et al. [58].

Earlier we reported the controlled oxidation of benzyl alcohol to benzaldehyde with Pd(II)-AAPtMS@GO as the catalyst, which showed excellent (95%) conversion and 99% selectivity in 1 h under eco-friendly room temperature and solvent free conditions [6]. It is also observed that metal modified amine functionalized nano graphene oxide materials showed excellent activity and stability then metal modified graphene materials. Scanning/ Transmitted electron microscopy gave the clear evidence about the nano graphene sheet and metal nano particles. SEM/ TEM Image of graphene oxide (a) amine functionalized graphene oxide (b) Pd(0) modified amine functionalized graphene (c) and Higher magnification of Pd(0) modified amine functionalized graphene (d) are illustrated in **Figures 3** and **4**. In these figures, the net-like structure performed after functionalization over the graphene oxide surface and graphene oxide sheets get converted to Nano graphene sheets. A perusal of the **Figure 4** confirms the uniform distribution of metal Nano particles on the surface. Solvents used and sonication process play important role in the changes in building blocks and stacking modes between graphene oxides based composites and covalent functionalization of different nano structures of final materials obtained.

7. Conclusions

Although metal deficient, GO is used in many catalytic reactions due to its surface oxy groups. To overcome the deficiency, covalently functionalized nano-graphene oxide/ metal modified functionalized nano-graphene oxides of metal have been developed, which are ideal to catalyze the C-C coupling and oxidation reactions. The surface functionalized/ metal modified surface functionalized materials proved superb with increased stability, reusability as well as activity towards fine chemical synthesis. With various potential applications, these surface functionalized materials have opened new opportunities in the fields of nanotechnology and catalysis. In this book chapter, we have summarized the recent advances in covalent functionalization of Nano graphene oxides, plus the stability and activity relationship in the field towards fine chemical synthesis.

Acknowledgements

The authors acknowledge the support received from the School of Chemistry & Physics and College of Agriculture, Engineering & Science, University of KwaZulu-Natal, Durban, South Africa in the form of research facilities and financial support.

Author details

Surjyakanta Rana and Sreekantha B. Jonnalagadda*

*Address all correspondence to: jonnalagaddas@ukzn.ac.za

School of Chemistry and Physics, College of Agriculture, Engineering and Science, University of KwaZulu-Natal, Durban, South Africa

References

- [1] Allen M J, Tung V C, Kaner R B. Honeycomb Carbon: A Review of Graphene. *Chem. Rev.* 2010, **110**, 132–145. DOI: 10.1021/cr900070d
- [2] Geim AK, Novoselov KS. The rise of graphene. *Nat. Mater.* 2007, **6**, 183–191. DOI: 10.1038/nmat1849
- [3] Yu D, Dai L. Self-Assembled Graphene/Carbon Nanotube Hybrid Films for Super capacitors. *J. Phys. Chem. Lett.* 2010, **1**, 467–470. DOI: 10.1021/jz9003137
- [4] Rana S, Maddila S, Yalagala K, Jonnalagadda SB. Organo functionalized graphene with Pd nanoparticles and its excellent catalytic activity for Suzuki coupling reaction. *Applied Catalysis A: General.* 2015, **505**, 539–547. DOI:10.1016/j.apcata.2015.07.018
- [5] Liu Y, Yu D, Zeng C, Miao ZC, Dai L. Biocompatible Graphene Oxide-Based Glucose Biosensors. *Langmuir.* 2010, **26**, 6158–6160. DOI: 10.1021/la100886x
- [6] Rana S, Maddila S, Jonnalagadda SB. Synthesis and characterization of Pd(II) dispersed over diamine functionalized graphene oxide and its scope as a catalyst for selective oxidation. *Catalysis Science & Technology.* 2015, **5**, 3235–3241. DOI: 10.1039/C5CY00192G
- [7] Geim AK. Graphene: Status and prospects. *Science.* 2009, **324**, 1530–1534. DOI: 10.1126/science.1158877
- [8] Nair R R, Blake P, Grigorenko AN, Novoselov K S, Booth TJ, Stauber T, Peres NMR, Geim A K. Fine Structure Constant Defines Visual Transparency of Graphene. *Science*, 2008, **320**, 1308–1308. DOI: 10.1126/science.1156965
- [9] Varadwaj GBB, Nyamori VO. Layered double hydroxides and graphene based hierarchical nanocomposites: A study on their synthetic strategies and promising applications in energy conversion and conservation. *Nano Research.* DOI 10.1007/s12274-016-1250-3
- [10] Zhu Y, Murali S, Cai W, Li X, Suk J W, Potts JR, Ruoff R S. Graphene and Graphene Oxide: Synthesis, Properties, and Applications. *Adv. Mater.* 2010, **22**, 3906–3924. DOI: 10.1002/adma.201001068
- [11] Park S, Ruoff R S. Chemical methods for the production of graphenes. *Nat. Nanotechnol.* 2009, **4**, 217–224. DOI: 10.1038/nnano.2009.58
- [12] Rana S, Maddila S, Maddila S, Yalagala K, Jonnalagadda SB. Covalent Modification of Organo-Functionalized Graphene Oxide and its Scope as Catalyst for One-Pot Pyrazolo-Pyranopyrimidine Derivatives. *Chemistry Open.* 2015, **4**, 703–707. DOI: 10.1002/open.201500121
- [13] Qu LT, Liu Y, Baek JB, Dai L. Nitrogen-Doped Graphene as Efficient Metal-Free Electrocatalyst for Oxygen Reduction in Fuel Cells. *ACS Nano.* 2010, **4**, 1321–1326. DOI: 10.1021/nr901850u
- [14] Dreyer DR, Park S, Bielawski CW, Ruoff RS. The chemistry of graphene oxide. *Chem. Soc. Rev.* 2010, **39**, 228–240. DOI: 10.1039/B917103G

- [15] Huang X, Yin Z, Wu S, Qi X, He Q, Zhang Q, Yan Q, Boey F, Zhang H. Graphene-based materials: synthesis, characterization, properties, and applications. *Small*. 2011, **7**, 1876–1902. DOI: 10.1002/sml.201002009
- [16] Bose S, Khare RA, Moldenaers P. Assessing the strengths and weaknesses of various types of pre-treatments of carbon nanotubes on the properties of polymer/carbon nanotubes composites: A critical review. *Polymer*. 2010, **51**(5), 975–993. DOI: 10.1016/j.polymer.2010.01.044
- [17] Huang YY, Terentjev EM. Dispersion of carbon nanotubes: Mixing, sonication, stabilization, and composite properties. *Polymers*. 2012, **4**(1), 275–295. DOI: 10.3390/polym4010275
- [18] Ma PC, Siddiqui NA, Marom G. Dispersion and functionalization of carbon nanotubes for polymer-based nanocomposites: A review. *Composites Part A: Applied Science and Manufacturing*, 2010, **41**(10), 1345–1367. DOI: 10.1016/j.compositesa.2010.07.003
- [19] Navarro-Pardo F, Martínez-Barrera G, Martínez-Hernández AL. Influence of 1D and 2D carbon fillers and their functionalisation on crystallization and thermo-mechanical properties of injection moulded nylon 6,6 nanocomposites. *Journal of Nanomaterials*. 2014. Article ID: 670261. DOI: 10.1155/2014/670261
- [20] Brodie BC. On the atomic weight of graphite. *Ann. Chim. Phys.* 1860, **59**, 466–472.
- [21] Staudenmaier L. Method for the preparation of graphitic acid. *Euro. J. Inorg. Chem.* 1898. **31**: 1481–1499.
- [22] Hummers WS, Hoffman RE. Preparation of graphite oxide. *Journal of American Chemical Society*. 1958, **80** (6), 1339–1339. DOI: 10.1021/ja01539a017
- [23] Obraztsov AN. Chemical vapor deposition: Making graphene on a large scale. *Nature Nanotechnology*. 2009, **4** (4), 212–213. DOI: 10.1038/nnano.2009.67
- [24] Obraztsov AN, Obraztsova E A, Tyurnina AV, Zolotukhin AA. Chemical vapor deposition of thin graphite films of nanometer thickness. *Carbon*, 2007, **45** (10), 2017–2021. DOI: 10.1016/j.carbon.2007.05.028
- [25] Yu QK, Lian J, Siriponglert S, Li H, Chen YP, Pei SS. Graphene segregated on Ni surfaces and transferred to insulators. *Applied Physics Letters*. 2008, **93** (11), 113103-3. DOI: 10.1063/1.2982585
- [26] Verma VP, Das S, Lahiri I, Choi W. Large-area graphene on polymer film for flexible and transparent anode in field emission device. *Applied Physics Letters*. 2010, **96** (20), 203108. DOI: 10.1063/1.3431630
- [27] Kim KS, Zhao Y, Jang H, Lee SY, Kim JM, Kim KS, Ahn JH, Kim P, Choi JY, Hong BH. Large-scale pattern growth of graphene films for stretchable transparent electrodes. *Nature*. 2009, **457** (7230), 706–710. DOI: 10.1038/nature07719

- [28] Jinbin L, Yulin L, Yueming L, Jinghong L, Zhaoxiang D. Noncovalent DNA decorations of graphene oxide and reduced graphene oxide toward water-soluble metal-carbon hybrid nanostructures *via* self-assembly. *J. Mater. Chem.* 2010, **20**, 900–906. DOI: 10.1039/B917752C
- [29] Fan X, Peng W, Li J, Li X, Wang S, Zhang, G., Zhang, F. 2008. Deoxygenation of exfoliated graphite oxide under alkaline conditions: A green route to graphene preparation. *Adv. Mater.* 2008, **20**, 4490–4493. DOI: 10.1002/adma.200801306
- [30] Kuila T, Bhadra S, Yao D, Kim NH, Bose S, Lee JH. 2010. Recent advances in graphene based polymer composites. *Prog. Polym. Sci.* 2010, **35**, 1350–1375. DOI: 10.1016/j.progpolymsci.2010.07.005
- [31] Yao H, Jin L, Sue HJ, Sumi Y, Nishimura R. Facile decoration of Au nanoparticles on reduced graphene oxide surfaces via a one-step chemical functionalization approach, *J. Mater. Chem. A*, 2013, **1**, 10783–10789. DOI: 10.1039/c3ta11901g.
- [32] Diederich F, Stang PJ. *Metal-Catalyzed Cross-Coupling Reactions*. Wiley-VCH, Weinheim, Germany, 1998.
- [33] Baur JA, Sinclair DA. Therapeutic potential of resveratrol: The in vivo evidence. *Nat. Rev. Drug Discov.* 2006, **5**, 493–506. DOI: 10.1038/nrd2060
- [34] Hayashi M. Oxidation using activated carbon and molecular oxygen system. *Chem Rec.* 2008, **8**, 252–267. DOI: 10.1002/tcr.20152
- [35] Su DS, Maksimova N, Delgado JJ, Keller N, Mestl G, Ledoux MJ, Schlögl R Nanocarbons in selective oxidative dehydrogenation reaction. *Catal. Today.* 2005, **102–103**, 110–114. DOI: 10.1016/j.cattod.2005.02.012
- [36] Pereira MFR, Orfao JJM, Figueiredo JL. Oxidative dehydrogenation of ethylbenzene on activated carbon catalysts. I. Influence of surface chemical groups. *Appl Catal A.* 1999, **184**, 153–160. DOI: 10.1016/S0926-860X(99)00124-6
- [37] Fu J, Shi F, Thompson LT, Lu X, Savage PE. Activated carbons for hydrothermal decarboxylation of fatty acids. *ACS Catal.* 2011, **1**, 227–231. DOI: 10.1021/cs1001306
- [38] Dreyer DR, Jia HP, Bielawski CW. Graphene oxide: a convenient carbocatalyst for facilitating oxidation and hydration reactions. *Angew Chem Int Ed.* 2010, **49**, 6813–6816. DOI: 10.1002/anie.201002160
- [39] Chauhan SMS, Mishra S. Use of graphite oxide and graphene oxide as catalysts in the synthesis of dipyrromethane and calix pyrrole. *Molecules.* 2011, **16**, 7256–7266. DOI: 10.3390/molecules16097256
- [40] Verma S, Mungse HP, Kumar N, Choudhary S, Jain SL, Sain B, Khatri OP. Graphene oxide: an efficient and reusable carbocatalyst for aza-Michael addition of amines to activated alkenes. *Chem Commun.* 2011, **47**, 12673–12675. DOI: 10.1039/C1CC15230K

- [41] Jia HP, Dreyer DR, Bielawski CW. Graphite oxide as an auto-tandem oxidation-hydration-aldol coupling catalyst. *Adv. Synth Catal.* 2011, **353**, 528–532. DOI: 10.1002/adsc.201000748
- [42] Dreyer DR, Jarvis KA, Ferreira PJ, Bielawski CW. Graphite oxide as a carbocatalyst for the preparation of fullerene reinforced polyester and polyamide nanocomposites. *Polym Chem.* 2012, **3**, 757. DOI: 10.1039/C2PY00545J
- [43] Kumar VA, Rao RK. Recyclable graphite oxide catalyzed Friedel–Crafts addition of indoles to α , β -unsaturated ketones. *Tetrahedron Lett*, 2011, **52**, 5188–5191. DOI: 10.1016/j.tetlet.2011.08.002
- [44] Li Y, Zhao Q, Ji J, Zhang G, Zhang F, Fan X. Cooperative catalysis by acid–base bifunctional graphene. *RSC Adv.*, 2013, **3**, 13655–13658. DOI: 10.1039/c3ra41970c
- [45] Long J, Xie X, Xu J, Gu Q, Chen L, Wang X. Nitrogen doped graphene nanosheets as metal-free catalysts for aerobic selective oxidation of benzylic alcohols. *ACS Catal*, 2012, **2**, 622–631. DOI: 10.1021/cs3000396
- [46] Zhang W, Wang S, Ji J, Li Y, Zhang G, Zhang F, Fan X. Primary and tertiary amines bifunctional graphene oxide for cooperative catalysis. *Nanoscale*, 2013, **5**, 6030–6033. DOI: 10.1039/c3nr01323e
- [47] Liu F, Sun J, Zhu L, Meng X, Qi C, Xiao F-S. Sulfated graphene as an efficient solid catalyst for acid-catalyzed liquid reactions. *J Mater Chem*, 2012, **22**, 5495. DOI: 10.1039/c2jm16608a
- [48] Molnár Á, Papp A. Efficient heterogeneous palladium-montmorillonite catalysts for Heck coupling of aryl bromides and chlorides. *Synlett* 2006, **18**, 3130–3134. DOI: 10.1055/s-2006-951493
- [49] Corral JA, López MI, Esquivel D, Mora M, Jiménez-Sanchidrián S, Romero-Salguero FJ. Preparation of palladium-supported periodic mesoporous organosilicas and their use as catalysts in the Suzuki cross-coupling reaction. *Materials* 2013, **6**, 1554–1565. DOI: 10.3390/ma6041554
- [50] Gómez-Martínez M, Buxaderas E, Pastor IM, Alonso DA. Palladium nanoparticles supported on graphene and reduced graphene oxide as efficient recyclable catalyst for the Suzuki-Miyaura reaction of potassium aryltrifluoroborates. *J. Mol. Catal. A: Chem.* 2015, **404–405**, 1–7. DOI: 10.1016/j.molcata.2015.03.022
- [51] Rumi L, Scheuermann GM, Mlhaupt R, Bannwarth W. Palladium Nanoparticles on Graphite Oxide as Catalyst for SuzukiMiyaura, MizorokiHeck, and Sonogashira Reactions. *Helv. Chim. Acta* 2011, **94**, 966–973. DOI: 10.1002/hlca.201000412
- [52] Xiang G, He J, Li T, Zhuang J, Wang X. Rapid preparation of noble metal nanocrystals via facile coreduction with graphene oxide and their enhanced catalytic properties. *Nanoscale* 2011, **3**, 3737–3742. DOI: 10.1039/C1NR10439J

- [53] Li Y, Fan X, Qi J, Ji J, Wang S, Zhang G, Zhang F. Palladium nanoparticle-graphene hybrids as active catalysts for the Suzuki reaction. *Nano Res.* 2010, **3**, 429–437. DOI: 10.1007/s12274-010-0002-z
- [54] Siamaki AR, Khder AERS, Abdelsayed V, El-Shall MS, Gupton BF. Microwave-assisted synthesis of palladium nanoparticles supported on graphene: A highly active and recyclable catalyst for carbon-carbon cross-coupling reactions. *J. Catal.* 2011, **279**, 1–11. DOI: 10.1016/j.jcat.2010.12.003
- [55] Nie R, Shi J, Du W, Hou Z. Ni₂O₃-around-Pd hybrid on graphene oxide: An efficient catalyst for ligand-free Suzuki-Miyaura coupling reaction. *Appl. Catal. A Gen.* 2014, **473**, 1–6. DOI: 10.1016/j.apcata.2013.12.029
- [56] Scheuermann GM, Rumi L, Steurer P, Bannwarth W, Mulhaupt R. Palladium nanoparticles on graphite oxide and its functionalized graphene derivatives as highly active catalysts for the Suzuki-Miyaura coupling reaction. *J. Am. Chem. Soc.* 2009, **131**, 8262–8270. DOI: 10.1021/ja901105a
- [57] Al-Marri AH, Khan M, Shaik MR, Mohri N, Adil SF, Kuniyil M, Alkathlan HZ, Al-Warthan A, Tremel W, Tahir MN, Khan M, Siddiqui MRH. Green synthesis of Pd@graphene nanocomposite: Catalyst for the selective oxidation of alcohols. *Arabian J. Chem.* 2015, DOI: 10.1016/j.arabjc.2015.12.007
- [58] Kadam MM, Dhopte KB, Jha N, Gaikar VG, Nemade PR. Synthesis, characterization and application of γ -MnO₂/graphene oxide for the selective aerobic oxidation of benzyl alcohols to corresponding carbonyl compounds. *New J. Chem.* 2016, **40**, 1436–1442. DOI: 10.1039/C5NJ03140K

Multifunctional Polymer Nanocomposites Based on Thermoplastic Polyesters

Sandra Paszkiewicz

Additional information is available at the end of the chapter

<http://dx.doi.org/10.5772/66121>

Abstract

Polymer nanocomposites containing carbon nanoparticles have exhibited remarkable thermal, mechanical and electrical properties. This review is concerned with a narrow sector of polymer nanocomposites, namely those based on engineering polyesters, which are of great industrial interest. The various functionalization methods of modifying carbon nanotubes and graphene derivative forms to allow interacting with polymer matrices will be summarized. Moreover, the review on the processing techniques of obtaining polymer nanocomposites with the emphasis of their effect on the final properties of the obtained material will be highlighted. The light will be also shed on the nanofiller dispersion in the polymer matrix. Finally, the opportunities and challenges in the high-performance polymer nanocomposites will be presented.

Keywords: polymer nanocomposites, thermoplastic polyesters, carbon nanoparticles

1. Introduction

Engineering polyesters, such as poly (ethylene terephthalate) (PET) and poly (butylene terephthalate) (PBT), constitute a group of engineering thermoplastics. However, this group is now expanded by new members of the polyester family, that is, poly (trimethylene terephthalate) (PTT) and poly (ethylene-2, 6-naphthalate) (PEN). They combine excellent mechanical, electrical and thermal properties with very good chemical resistance and dimensional stability. Moreover, with excellent processing characteristics and high strength and rigidity, they are widely used in industrial applications. However, still at a commercial level the aforesaid properties, one can further improve through an addition of suitable modifying agents such as nanofillers. There is a wide array of organic and inorganic nanofillers

some of which have been studied more thoroughly than others. An addition of carbon nanofillers (CNF) such as carbon nanotubes (CNT) and graphene derivative forms (GDF) may seem particularly interesting from the point of view of their influence on the enhancement of a wide array of material characteristics.

The properties of polymer nanocomposites that can be improved due to the presence of carbon nanoparticles (CNP), such as carbon nanotubes (single- and multi-walled carbon nanotubes) and graphene derivatives (graphene, expanded graphite, graphene oxide, etc.), include tensile strength, tensile modulus, toughness, thermal properties, electrical and thermal conductivity, optical and barrier properties. However, the aforementioned properties one can obtain only when the nanofillers are uniformly dispersed and aligned in the polymer matrix. However, since carbon nanoparticles usually tend to form aggregates/agglomerates due to the van der Waals interactions, obtaining proper dispersion is a critical issue. The functionalization of CNP is an effective way to prevent their aggregation, which helps for a better disperse within the polymer matrix. The second approach is the preparation method such as solution mixing, melt blending and in situ polymerization. Herein, the study on the functionalization of carbon nanoparticles and preparation of polymer nanocomposites will be emphasized.

There are several approaches for developing multifunctional polymer nanocomposites utilizing unique properties of carbon nanotubes and graphene derivatives. The key issue is the development of methods that improve the dispersion of carbon nanoparticles in the polymer matrix since the proper dispersion enhanced the properties in the strongest manner. Additionally, the light will be shed on the influence of CNP on the crystallization behavior of the selected engineering polyesters, especially on PET and PTT. Despite various methods of obtaining polymer nanocomposites, such as melt blending or in situ polymerization, there are still challenges and opportunities that need to be found in order to improve the dispersion and thus modify the interfacial interactions. Therefore, the greatest emphasis will be placed on the in situ polymerization method, which in our opinion seems to have the greatest opportunity to transfer into an industrial scale.

2. Functionalization of carbon nanoparticles (CNP)

2.1. Functionalization of CNT

Because CNT usually tend to agglomerate due to van der Waals forces, one can find dispersing and aligning CNT in the polymer matrix extremely difficult. Therefore, a valid approach toward developing high-performance polymer/CNT nanocomposites is to implement individual CNT into the polymer matrix in order to achieve better alignment and dispersion, strong interfacial interactions and improvement in the load transfer across the CNT-polymer matrix interface [1]. One can find functionalization of CNT as an effective way to prevent nanotube aggregation, which allows for a better dispersion and stabilization of the CNT within a polymer matrix. There are many approaches for functionalization of CNT, and however, defect functionalization, covalent functionalization and non-covalent functionalization [2] will be the main ones described herein.

In the methods of defect functionalization, defects are preferentially observed at the open ends of CNT [1]. CNT are purified by oxidative methods in order to remove amorphous carbon or metal particles from the raw materials [3, 4]. The purified single-walled carbon nanotubes (SWCNT) comprise oxidized carbon atoms in the form of $-\text{COOH}$ group [5, 6]. In these oxidizing methods, SWCNT are fractured to very short tubes with lengths of 100–300 nm [7]. The functionalized CNT are more soluble in organic solvents than raw CNT [1].

The non-covalent functionalization of nanotubes is of particular interest because without affecting the physical properties of CNT it improves solubility and processability. This type of functionalization mostly engages surfactants, bio-macromolecules or polymers' wrapping. In one of the nondestructive purification methods, nanotubes can be transferred to the aqueous phase in the presence of surfactants [8, 9], where the nanotubes are surrounded by the hydrophobic components of the corresponding micelles. The interactions become stronger when the hydrophobic part of the amphiphilic contains aromatic group. CNT can be well dispersed in water using anionic, cationic and nonionic surfactants [10–13]. The interactions between CNT and the surfactants depend on the nature of the surfactants (its alkyl chain length, headgroup size and charge). Moreover, the dispersion of CNT in both water [14, 15] and organic solvents [16] may be further improved by the physical coupling of polymers with CNT, which can be explained by the 'wrapping' mechanism [15] attributed to the specific interactions between the polymer matrix and CNT. The supramolecular complexes can be formed when the polymers wrap around CNT [17, 18], where the π -stacking interactions between the polymer and the nanotube surface are responsible for the close coupling of the structures [1]. Moreover, the non-wrapping approaches have also been used for the dispersion and solubility of CNT in different media [19, 20]. In both cases, copolymers efficiently act as stabilizers and may be tailored so as to disperse the tubes in a variety of solvents.

In the case of covalent functionalization, the translational symmetry of CNT is decomposed by changing sp^2 to sp^3 carbon atoms, and thus their properties, such as electronic and transport, are affected [21]. However, this type of CNT functionalization can improve both solubility and dispersion in solvents and polymers. Moreover, such improvement can be achieved by modification of surface-bound carboxylic acid groups on the nanotubes or direct reagents to the side walls of nanotubes [1]. In general, functional groups such as carboxyl or hydroxyl groups are initiated on the CNT during the oxidation process using various oxidizing agents, among others oxygen, air, concentrated sulfuric acid, nitric acid, aqueous hydrogen peroxide and mixture of acids [7, 22]. The presence of such groups on the nanotube surface allows attaching organic [23, 24] or inorganic materials, which is important from the solubilizing point of view. However, the presence of $-\text{COOH}$ groups on the nanotube surface is more suitable than the others groups due to a variety of chemical reactions that can be conducted with this group. In order to enhance CNT' dispersion and solubilization in solvents and in polymer matrices, CNT can be either functionalized at end caps or at the sidewall [25, 26]. Functionalization with polymer molecules (polymer grafting) [27, 28] is of particular interest from processing of polymer/CNT nanocomposites' standpoint. Two main categories, that is, "grafting to" and "grafting from" approaches, have been reported for the covalent grafting of polymers to nanotubes [1]. The "grafting to" approach consists in attaching as-prepared or

commercially available polymer molecules on CNT surface via chemical reactions, such as esterification, amidation, radical coupling, etc. [1]. In this approach, the polymer has to possess suitable reactive functional groups for preparation of composites, whereas, in the “grafting from” approach, the polymer is combined with CNT surface through polymerization of monomers in the presence of reactive CNT or CNT supported initiators. The greatest advantage of this approach is that the polymer/CNT composites can be prepared with high grafting density [1].

The last method of functionalization of CNT raised herein is the “click” chemistry that is an ideal reaction for material synthesis and modification and for self-assembly of nanomaterials. It also provides an unexpected advantage of introducing azide and alkyne groups into organic and polymer molecules, the stabilization of these groups in many reaction conditions, etc. [1]. The click chemistry benefits its toleration of other functional groups, a short reaction time, high yield, high purity and regiospecificity, as well as its suitability for the use under aqueous conditions [29]. The wide range of examples of applying the click chemistry has been presented by Sahoo et al. [1]. By using this approach, CNT can be easily functionalized with desired molecules, which enhance their importance from nanoelectronics to nanobiotechnology. The breadth of attached molecules can enhance the validity of click chemistry and opens the new prospect of CNT-based nanomaterials.

2.2. Functionalization of graphene sheets

By the reason of great interest of using graphene as a reinforcing filler of polymer matrices in order to obtain multifunctional materials, a variety of methods for the graphene surface modification has been developed [30]. Among many other factors, the nature of the interfacial interactions between the filler and the matrix has a significant impact on the final properties of the composite material. At the same time, most dispersion methods allow to obtain composites where polymer matrix and the filler interact through relatively weak dispersive forces. Thus, there is a growing research interest on introducing covalent bonding between GDF and the polymer matrix, since the chemically functionalized graphene can be processed further by solvent-assisted techniques [31]. Moreover, the proper functionalization of graphene sheet staves off further agglomeration of single-layer graphene (SLG) during reduction in solvent phase and supports the maintenance of the inherent properties of graphene. Graphene oxide (GO) has been widely employed as a starting material for the synthesis of GDF. There are several methods for producing GO from natural graphite, and however, the modified Hummers method is the most fruitful nowadays [32]. The surface of GO sheet, which is highly oxygenated, can significantly alter the van der Waals interactions and lead to a range of solubility in water and organic solvents [31], while, in order to prepare graphene, the chemical, thermal or photochemical reduction in GO needs to be carried out. Nonetheless, the GO reduction without suitable stabilizers leads to precipitation of graphite particles restacking due to the rapid and irreversible aggregation of graphene sheets. Therefore, prior to the reduction process, surface modification of GO sheets is usually carried out by covalent modifications or non-covalent functionalization, followed by reduction. The covalent modification of graphene can be achieved in four different ways: nucleophilic

substitution, electrophilic addition, condensation and addition [31]. The first method takes place very facilely, both at room temperature and in an aqueous medium. Thus, the nucleophilic substitution is handled to be a promising method for a large-scale production of functionalized graphene. Additionally, all types of aliphatic and aromatic amines, amino acids, amine terminated biomolecules, ionic liquids, small molecular weight polymers, etc. have been successfully applied in the preparation of functionalized graphene [31]. Electrophilic substitution reaction with graphene involves the displacement of the hydrogen atom by an electrophile. An example of such reaction can be the spontaneous grafting of aryl diazonium salt to the surface of graphene [33]. In turn, a condensation reaction is a chemical reaction in which two molecules (functional groups) combine with another in order to form one single molecule with a loss of entropy. In this case, condensation occurs with isocyanate, diisocyanate and amine compounds through the formation of amides and carbamate ester linkages [31], while, in the last method, in organic addition reactions, two or more molecules combine to form a larger molecule. Many examples of the above-mentioned method provide Kuila et al [31] in the review study on the chemical functionalization of graphene.

Similarly as in the case of CNT, the non-covalent interactions primarily involve van der Waals, hydrophobic and electrostatic forces and require the physical adsorption of suitable molecules on the surface of graphene. Non-covalent functionalization is achieved by polymer wrapping, adsorption of surfactants or small aromatic molecules, etc. [32]. Furthermore, one can utilize GDF as a support to disperse and stabilize nanoparticles [30]. Particularly interesting tend to be metallic nanoparticles that can play an important role in wide number of applications such as display devices, microelectronics, photovoltaic cells, but also in medical or biological applications. The majority of the papers concerning the preparation and applications of the new class of graphene-based materials utilize precious metals like gold [34, 35], platinum [36], palladium [37] and silver [38]. However, there is also a growing interest in the use of other metals like, iron, copper, tin and cobalt [32]. Muszynski et al. [39] presented the preparation of graphene/metal material using organic spacers, like octadecylamine, to anchor the metallic nanoparticles to the graphene surface or organic solvents such as tetrahydrofuran, methanol and ethylene glycol. Nevertheless, the in situ synthesis of the metal nanoparticles in the presence of GO has received particular interest, as it enables control over the growth of the nanoparticles on the surface of graphene through the utilization of the precursors of the metallic particles, which are then subjected to reduction by the addition of reducing agents and reducing GO at the same time. Inasmuch as the functionalization of graphene via different chemical, electrochemical and other methods has been discussed above, and since the reduction is an essential step to obtain functionalized graphene from functionalized GO, few words will be given below. The most commonly used reducing agents that can be applied in the reduction in pure GO or functionalized GO are hydrazine monohydrate, sodium borohydride (NaBH_4), p-phenylene diamine, hydroquinone and sodium hydrosulfite [40, 41]. However, these chemicals are hazardous to human health and the environment. Therefore, some alternative methods have been recently proposed [42, 43].

3. Preparation of polymer/CNP nanocomposites

To enlarge the benefits of CNP as effective reinforcement for high strength polymer nanocomposites with at the same time improved electrical, thermal and/or barrier properties, etc., the CNP should not form aggregates/agglomerates and must be well dispersed to enhance the interfacial interactions with polymer matrix. In past review paper, several processing methods available for fabricating CNP/polymer composites based on either thermoplastic or thermosetting matrices have been described [30, 44, 45]. They mainly include melt blending, in situ polymerization and solution mixing.

3.1. Melt mixing

Melt mixing is a typical and simple method, particularly useful for thermoplastic polymer nanocomposites. It is an eco-friendly, cheap and suitable method for mass production in industrial applications. The compounding is generally achieved in a single- or twin-screw extruder where the polymer and the nanoparticles mixture are heated to form a melt [46]. CNP are mechanically dispersed in a polymer matrix using a high temperature and high shear force mixer. The shear forces help to break apart the nanofiller aggregates/agglomerates or prevent their formation. Better dispersion is achieved with MWCNT than SWCNT [47]. Moreover, by changing the process conditions, that is, screw configuration, one can better control shear and mixing. Another advantage of melt mixing is the lack of necessity of using organic solvents during the process. The prepared CNP/polymer nanocomposite (usually in the form wire) one can further processed using the typical processing techniques such as injection molding, profile extrusion, blow molding, etc. However, the large number of variables referring to the process (temperature, screw-speed and shear stress) but also to the characteristics of the nanofillers (agglomerate structure, packing density, length to diameter ratio and purity) requires proper optimization of process parameters. Additionally, the polymer matrix (mainly its viscosity) can affect the quality of the dispersion. Thus, the amount of CNT introduced in melt mixing process must be lower due to high viscosities of the composites at higher loading of CNT [48]. Most of the studies reported CNT-based nanocomposites involved polymer matrices such as polyolefins, polystyrene (PS), polycarbonate (PC) but most of all polyesters [44, 45, 49]. However, no significant improvement in mechanical properties was observed in the melt blended nanocomposites. Only in case of functionalized nanotubes that interacted with polymers containing functional groups, one can observe the enhancement in the degree of dispersion along with the enhancement in selected physical properties [50]. On the other hand, in the case of GDF/polymer nanocomposites, there are a limited number of studies. Probably, low thermal stability of most chemically modified graphene derivatives and the low bulk density of graphene makes the use of melt processing difficult. Despite the fact that high shear melt mixing has been used to fabricate GDF-based nanocomposites with polylactid (PLA) [51], PET [52], etc., high shear forces can cause buckling, rolling or shortening of graphene sheets [53], thus reducing its aspect ratio.

3.2. Solution mixing

Solution mixing is another approach of producing polymer nanocomposites containing CNT and GDF. This is a widely used method due to the facile nature of the process consisting of the dispersion of nanoparticles in a polymer that is dissolved in a solvent before casting in a mold and evaporating the solvent. The difficulties with obtaining proper dispersion of CNP in the solvent by simple stirring are well known. Therefore, a high power ultrasonication process, which found to be more effective, is applied more and more often. The aggregates/agglomerates of CNP can be effectively crumbled utilizing the multitasking of ultrasonication. However, the crucial challenges in solution mixing are to minimize the residual solvents [54] and obtain proper dispersion of the fillers in viscous polymeric solutions [55]. Therefore, in the case of thermoplastic polyesters, which have excellent resistance to most substances, such as acids, oxidizers (ex. hydrogen peroxide), hydrocarbon fuels, oils, and lubricants, this method does not find a wider use. Despite the fact that the solution mixing generally leads to better particle dispersion than melt mixing process, slow solvent evaporation often induces particle re-aggregation, especially since the complete drying to eliminate residual solvents is needed. The aggregated graphene or GO nanoplatelets, due to the poor solubility or gravimetric precipitation by unexfoliated graphene or GO nanosheets, are a critical problem often occurring in nanocomposites obtained via solution mixing. Therefore, in the case of GO, its thermal reduction should be carefully considered because GO can easily decompose, even at low temperatures (below 150°C). This can often lead to the local structural deformations in the polymer matrix that cause a significant loss of the physical properties in the obtained polymer nanocomposites. However, the solution mixing approach is a convenient method when residual solvents can be eliminated completely and an excellent dispersion can be achieved.

3.3. In situ polymerization

In situ polymerization method is another way for preparing homogeneously distributed CNT and GDF in the polymer matrix, where nanoparticles are dispersed in monomer followed by polymerization. A higher percentage of CNP may be easily dispersed in this method, and however, the viscosity generally increases, which may cause deterioration in processability of nanocomposites [55]. In comparison with melt and solvent mixing methods, in situ polymerization may amend the dispersion state and cause better compatibility between CNP and the polymer through the introduction of additional functional (active) groups on the nanoparticles surfaces but also due to the additional step of dispersing process (mechanical stirring and ultrasonication) that can be added in advance [55–58]. Besides, this method requires monomer units and a lot of reagent for the polymerization procedure, and thus, it might be less applicable in the case of naturally existing polymers [59]. Moreover, in situ polymerization should also be performed in the solution state. Therefore, the elimination of residual solvents should be addressed when one uses the solution mixing method [55].

4. Functional properties of polymer/CNP nanocomposites

4.1. Morphology and crystallization behavior

Since properties enhancement strongly correlates with nanocomposite microstructure, proper characterization of morphology is important to establish structure-property relations for these materials. Lots of research efforts have been directed toward manufacturing polymer nanocomposites containing CNP for functional and structural applications [60, 61]. However, it is worth mentioning that the nature of the dispersion problem for CNT differs from other conventional fillers, such as spherical particles and carbon fibers, due to the small diameter in nanometer scale with high aspect ratio (>1000) and thus extremely large surface area of CNT [62]. Ma et al. [62] compared the dimensions of commonly used fillers, including carbon fibers, Al_2O_3 particles, graphite nanoplatelets (GNP) and CNT and the number of particles corresponding to a uniform filler volume fraction of 0.1% in a composite of 1.0 mm^3 cube. They found that in the composite, only two pieces of Al_2O_3 particles can be found, and this number increases to 65 thousands when GNP are added and further increases to ca. 442 million pieces when CNT are introduced, all with the same filler volume fraction. Therefore, aforementioned observation clearly displays that simply due to the sheer order of magnitude a uniform dispersion of CNT in a polymer matrix is more difficult than the other fillers. However, as mentioned above the yield of CNP/polymer nanocomposite depends on the dispersion of CNP in the matrix and interfacial interactions between the CNP and the polymer. For instance, Yoo et al. [63] prepared PET nanocomposites by melt extruding mixtures of PET and benzyl isocyanate and phenyl isocyanate functionalized MWCNT. Nanocomposites with functionalized MWCNT showed better dispersion of nanotubes in the PET matrix due to enhanced interactions between PET chains and nanotubes in comparison with pristine MWCNT/PET and MWCNT-COOH/PET nanocomposites. In turn, Jin et al. [64] used the surface-modified MWCNT having acid groups (acid-MWCNT) and diamine groups (diamine-MWCNT) in order to improve the dispersion of MWCNTs in PET matrix. Due to van der Waals interactions, pristine MWCNT exhibited high degree of aggregation, whereas, the acid-MWCNT, which has been treated with sulfuric and nitric acids, showed a lower degree of entanglement due to shortened nanotube lengths. Moreover, the diamine-MWCNT was also characterized by a lower degree of aggregation as compared to pristine MWCNT which was attributed not only to the functional groups, such as carboxyl and diamine, but also to their shorter lengths. The increased interfacial interaction was also evident in PET/diamine-MWCNT nanocomposites, resulting from good wetting of the diamine-MWCNTs in the PET matrix. This was explained by the fact that the acid and diamine groups on the surface of acid-MWCNT and diamine-MWCNT, respectively, may have reacted with PET during in situ polymerization, resulting in good dispersion of acid-MWCNT and diamine-MWCNT. Additionally, Lee et al. [65] prepared via in situ polymerization PET-based nanocomposites with two types of functionalized MWCNT: methoxybenzoyl-functionalized (MeO-MWCNT) and ethoxybenzoyl-functionalized (EtO-MWCNT) nanotubes. It was found that the PET/MWCNT system has poor MWCNT dispersion in comparison with the PET/MeO-MWCNT system. However, EtO-MWCNT in PET matrix was most homogeneously dispersed, and the

interfacial boundary between EtO-MWCNT and PET matrix was practically indiscernible. In our previous study [58], nanocomposites based on poly (ethylene terephthalate) prepared by in situ polymerization with expanded graphite (EG) were compared to those with functionalized graphite sheets (GO). It was found that no big difference in the level of filler dispersion/exfoliation was observed (SEM) between GO and EG-filled composites at the same loading of 0.4 wt.%, suggesting that at low loadings the presence of functional groups on the surface of GO does not lead to significant improvement in GO exfoliation in PET matrix. However, GO seemed to be covered with polymer matrix in the stronger manner, which might suggest that some interactions between functional groups of GO and PET matrix occurred. The presence of functional groups such as carboxylic groups on the surface of GO can improve interfacial adhesion between graphene sheets and polymer matrix mainly due to the possible interaction of hydrogen bonding between the COOH groups of GO and the ester groups in polymer matrix, as it was described above for functionalized carbon nanotubes. However, in this case, same was not observed.

In the case of research on other thermoplastic polyesters, similar remarks were made. For instance, Szymczyk et al. [66] in the in situ prepared PTT/MWCNT-COOH nanocomposites observed homogenous distribution of carbon nanotubes in the PTT matrix. Individual nanotubes, some entanglements or bundles of CNT, apparently pulled out from the matrix during fracturing are observed on the surface. Moreover, most of the nanotubes showed pulling out and sliding at the surface of nanocomposite, suggesting a limitation of load transfer. Similar observations were seen for PTT-based nanocomposites with pure (non-functionalized) MWCNT [67]. Despite the fact that control over the dispersion degree of nanotubes in a polymer matrix is difficult due to strong intermolecular forces that exist between nanoparticles, and lack of functional groups on the surface of CNT, we were able to obtain well-dispersed MWCNT in the whole volume of polymer matrix. As can be seen, the high shear forces along with alternately applied ultrasounds introduced by high-speed mechanical stirring and sonication, followed by in situ polymerization, were sufficient to disperse the MWCNT in PTT matrix. However, the residual functional groups on the surface of GNS improved both the interfacial interaction with PTT chain and stabilize the dispersion of MWCNT-COOH, thus affecting electrical conductivity [68]. Several studies on the influence of the functionalization of CNT on PBT-based nanocomposites were also published by the group of prof. Z. Roslaniec [69, 70]. In both cases, it was confirmed that functionalization of nanotubes allows for the better distribution of nanotubes in the whole volume of polymer matrix. Nanotubes seem to be wrapped with PBT matrix suggesting that a strong interaction exists between the PBT matrix and functionalized MWCNT. Moreover, the presence of a modified epoxy resin seems to stabilize the MWCNT dispersion by interaction with the PBT matrix [71]. However, there is still no study on how the influence of the modification of graphene surface affects the dispersion properties in PBT matrix. However, Fabbri et al. [72] demonstrated that all prepared PBT/graphene composites showed a good dispersion of graphene into the polymer matrix. Moreover, they proved that interfacial adhesion between polymer and graphene nanoplatelets appeared thanks to the applied in situ polymerization of the ultra-low viscosity CBT oligomers. It is also worth mentioning that Kim et al. [73] compared nanocomposites reinforced with graphite platelets to those with functionalized

graphite sheets (FGS) prepared by partial pyrolysis of graphite oxide. FGS, a thermally exfoliated graphite oxide and graphite were melt blended into PEN using a small scale, twin-screw extruder. It was found that in the case of PEN/graphite nanocomposites no delamination of graphene layers was observed, since each stack was composed of ~100 single graphene layers. This was probably due to strong van der Waals binding between the closely spaced graphene layers. As compared to PEN/graphite composites, high aspect ratio FGS exhibit better dispersion state in the whole volume of PEN matrix. The statistical analysis conducted for 88 FGS particles yielded a thickness and mean diameter of 2.9 and 222 nm (~8 single graphene layer—the interlamellar spacing equals 0.34 nm), respectively, which is far much lower than in the case of PEN/graphite nanocomposites.

In the case of semicrystalline polymers, incorporation of nanofiller (depending on its type, aspect ratio, etc.) can affect degree of crystallinity, crystallite size and spherulite structure and can even cause crystallization of otherwise amorphous polymers [73, 74]. Depending on the type of the polymer, incorporation of CNT and GDF has been reported to cause an increase [57, 63, 66, 75–77], decrease [78] or no change [79] in the degree of crystallinity of a semicrystalline polymer matrix. Changes in the polymer melting and crystallization temperature have also been reported [57, 66, 69]. Yoo et al. [63] observed that the crystallinity of the PET/functionalized MWCNT nanocomposites was significantly higher than that of the pristine and acid-treated MWCNT. Nanotubes accelerated PET crystallization via change in conformation in the ethylene glycol residue from gauche to trans conformation. In turn, graphene oxide nanosheets displayed a nucleating effect on the PET crystallization due to the increase in the onset and peak crystallization temperature of nanocomposites compared to neat PET [57]. The degree of crystallinity of the nanocomposites containing of 0.3 and 0.5 wt.% of GO was higher than for the neat PET. Analysis of nanostructure parameters for PET/0.5GO composite and neat PET has shown that non-isothermally crystallized composite and neat PET have comparable values of long period. Moreover, the study on the isothermal cold crystallization of amorphous PTT and its nanocomposites [66] revealed that the presence of MWCNT-COOH affected the crystallization rate, especially at higher concentration (0.3 wt.%) of CNT. The melting and glass transition temperatures of nanocomposites obtained by non-isothermal crystallization were not significantly affected by the presence of CNT. Moreover, nanocomposites exhibited slightly higher degree of crystallinity than neat PTT. Similarly, in PBT-based nanocomposites [69], carbon nanotubes accelerated crystallization during cooling and in consequence, the crystallization peaks of the DSC curves shifted toward higher temperatures. With increasing CNT concentration (to 0.1 wt.% oxidized SWCNT), the crystallization temperature also increased, suggesting that interactions between the CNT and the matrix occurred.

4.2. Mechanical properties

The extraordinary mechanical properties, low density and large aspect ratio [44, 45] make CNT particularly attractive as candidates for the development of CNT-reinforced polymer nanocomposites. However, the in-plane elastic modulus of pristine, defect-free graphene is approximately 1.1 TPa and is the strongest material that has ever been measured on a micron length scale [80]. In both cases, processing and dispersion of CNT and GDF including GO in

the polymeric hosts constitutes the main challenge before implementation of high-performance CNP-based nanocomposites. So as mentioned before, the chemical functionalization of the nanofillers has been found to be a feasible and effective way for improving the dispersion of CNP and interfacial bonding between the CNP and the matrix. Indeed, a wide range of polymer matrixes has been used for the development of such nanocomposites. The PET-based composites containing functionalized MWCNT showed a large increase in the tensile strength and modulus [64]. The PET-based composites containing diamine-MWCNT exhibit maximum tensile strength and modulus increases by 350 and 290% at 0.5 and 2.0 wt.%, respectively, as compared to neat PET. In turn, Yoo et al. [63] observed that the addition of MWCNT-benzyl and MWCNT-phenyl at the same loading of 3 wt.% improved the tensile strength and modulus of the PET matrix. The MWCNT-phenyl nanocomposite provided the most enhanced tensile strength. The highest modulus was obtained in the PET/MWCNT-phenyl composite. Consistently, it was concluded that the incorporation of functionalized MWCNT can make a great input to the polymer reinforcement due to the enhancement of the dispersion of MWCNT in the whole volume of polymer matrix and consequent stress transfer between MWCNT and the matrix. In addition, Szymczyk et al. [66] demonstrated that along with the increasing content of MWCNT-COOH (to 0.3 wt.%) the tensile strength and Young's modulus also increased. However, further addition of MWCNT (0.4–0.5 wt.%) lowered tensile strength and Young's modulus, but their values were still comparable or higher (modulus) to neat PTT. The values of elongation at break are higher or comparable to the neat PTT. Additionally, in PBT-based nanocomposites [69], it was observed that with an increase from 0.01 to 0.1 wt.% of oxidized SWCNT, the Young's modulus, tensile strength and strain to failure increased. This was probably due to better performance of the carbon nanotubes when incorporated in the PBT. However, in the case of GDF-based nanocomposites, not so many reports were published on the improvement in thermoplastic polyester matrices. Several different types of GDF as reinforcing agent in PET and PTT matrices were described in details in Ref. [81]. It was found that the presence of the nanoparticles resulted only in a moderate (compared to the neat polymer) increase in the mechanical properties, including tensile strength.

4.3. Thermal properties (thermal stability and dimensional stability)

The exceptional thermal properties of CNT and GDF and CNP-based materials have been harnessed as fillers to improve the thermal stability and dimensional stability of polymers.

A significant number of reports have reported increased thermal stability (typically defined by the maximum mass loss rate measured by thermogravimetric methods) of polymers using CNT and GDF as nanofiller, but herein only those referring to thermoplastic polyesters will be mentioned. For instance, Yoo et al. [63] reported that the chemical modification of MWNT-COOH resulted in a higher degree of thermal degradation due to the COOH group. However, the MWCNT-benzyl and MWCNT-phenyl showed higher thermal stability than pristine MWCNT. On the other hand, Szymczyk et al. [66] showed that the thermal and oxidative stability of PTT is independent of the COOH functionalized MWCNT content. Moreover, the incorporation of expanded graphite and graphene nanoplatelets into PET and PTT matrices [81] did not affect the thermal stability of the obtained via in situ polymerization nanocom-

posites at inert atmosphere. However, the addition of CNT and GDF individually and in the mixture of both caused an enhancement of thermo-oxidative stability (shifting the beginning of the chemical decomposition temperature of up to 20–25°C).

4.4. Electrical conductivity

CNP exhibit high aspect ratio and high electrical conductivity, which makes them excellent candidates for conducting composites. Percolation theory predicts that there is a critical concentration at which composites containing conducting fillers in the insulating polymer matrices become electrically conductive. The electrical percolation threshold in polymer/CNT nanocomposites depends on the dispersion [82], alignment [82, 83], aspect ratio [82], degree of surface modification [84] of CNT, polymer types [44, 45] and composite processing methods [82]. However, in the case of GDF, although GO can be readily dispersed in many solvents (even in water) and provides functional groups that allow for better interactions with polymer chains, it is electrically insulating and thermally unstable [85]. Therefore, at least partial reduction in graphene oxide is necessary to restore electrical conductivity. Bauhofer and Kovacs [86] reviewed experimental and theoretical work on electrical percolation of carbon nanotubes (CNT) in polymer composites. They gave a comprehensive survey of published data together with an attempt of systematization. Therefore, only some newer papers on the polymer/CNT nanocomposites will be mentioned along with review on the GDF-based nanocomposites. Zhang et al. [52] presented that the electrical conductivity of PET/graphene composites increased rapidly from 2.0×10^{-13} S/m to 7.4×10^{-2} S/m with only small addition of graphene (from 0.47 to 1.2 vol.%). On the other hand, the percolation threshold of PET/graphite composites equals to 2.4 vol.%. The incorporation of EG to the PET resulted in a sharp insulator-to-conductor transition with a percolation threshold (σ_c) as low as 0.05 wt.% [87]. Additionally, the influence of the degree of crystallinity on the conductivity was studied. Amorphous films found to be exhibited higher conductivity than semicrystalline films. In turn, Hernandez et al. [88] compared how the preparation method affects the percolation threshold. Nanocomposites prepared by direct mixing showed a low electrical percolation threshold ($\phi = 0.024$ wt.% of SWCNT) and were more transparent to light than samples prepared by in situ polymerization. However the electrical percolation threshold of 0.9 wt.% has been found for PET/MWCNT, nanocomposites prepared by coagulation method [89]. It was noticed that at 1 wt.% of MWCNT loading, the conductivity level exceeded the antistatic criterion of thin films (1×10^{-8} S/cm). By the addition of MWCNT into PTT matrix, the conductivity of nanocomposites increases by 10 orders of magnitude, approaching a value of 10^{-3} S/cm for PTT/0.3 MWCNT. The percolation threshold was below 0.1 wt.% of nanotubes' concentration. In turn, the PTT/MWCNT-COOH nanocomposites [66] at concentration below 0.2 vol.% (0.4 wt.%) exhibited strong frequency dependence of the conductivity. In addition, in PTT-based nanocomposites prepared via in situ polymerization, the effect of the EG flake size on the electrical conductivity was measured [90]. It was clearly found that smaller platelets (50 μm) enabled to obtain conductive thin polymer films with a nanoplatelet content of 0.3–0.5 wt.%. At the same time, nanocomposite based on PTT with 0.5 wt.% of EG with the flake size of 500 μm proved to be nonconductive. Moreover, Li et al. [91] demonstrated that the electrical volume resistivities decreased dramatically at the exfoliated graphite (E \times G) content between 3.0 and 5.0 wt.% for nanocompo-

sites based on PTT prepared via melt compounding. Additionally, the conductivity percolation for PEN/FGS nanocomposites was obtained with as little as 0.3 vol.% FGS, whereas 3 vol.% was required for graphite [77].

4.5. Gas barrier properties

There is a strong demand for improving the gas barrier properties of existing polymers used in food packaging applications, which require the near-perfect exclusion of gas molecules. The high aspect ratio of GDF insinuates their potential use for reducing gas permeability of polymer foils/films. Gas permeability through a polymer nanocomposite containing high aspect ratio impermeable flakes can be significantly lowered via both reduced crosssection for gas diffusion and a tortuous path mechanism [77]. Study of the oxygen transmission rate through nanocomposite and neat PET films has shown that the exfoliated structure of GO in PET matrix improved their oxygen barrier properties. The improvement in oxygen permeability for PET nanocomposite films at 0.3–0.5 wt.% loading of GO over the neat PET was approximately factors of 2–3.3. These improvements in oxygen barrier properties of PET are important from the application point of view in packing industry. Moreover, two series of PTT nanocomposites with EG with the flake size of 50 and 500 μm [91] demonstrated a significant enhancement in impermeability to CO_2 and O_2 . The PTT/0.3EG50 μm and PTT/0.5EG50 μm nanocomposites showed over 10-fold improvement in barrier properties with respect to carbon dioxide. However, the hydrogen permeability of PEN with 4 wt.% FGS [77] was decreased by 60%, while the same amount of graphite reduced permeability only 25%. Gas barrier performance of composites reinforced with FGS was superior to that of graphite composites, and this was attributed to its higher aspect ratio.

5. Concluding remarks

There are number of approaches for developing high-performance CNP/polymer nanocomposites taking advantage of the unique properties of CNP. Thermoplastic polyesters were chosen as polymer matrices, due to their great importance in industrial applications. However, the crucial challenge is to develop the methods of nanofillers' dispersion improvement in the polymer matrix since it greatly affects the mechanical, electrical and thermal properties of nanocomposites. Despite diverse methods, such as melt mixing, solution processing and in situ polymerization along with chemical functionalization, challenging is to enhance the dispersion and modify interfacial interactions. One of the issues that need to be resolved is to obtain the optimal functionalization of CNT that can maximize interfacial adhesion between nanofillers and the polymer matrix. A proper functionalization of both CNT and GDF allows for strong interfacial interactions between CNP and polymer matrix, which may at the same time improve the dispersion of CNT in the whole volume of polymer matrix. Moreover, in the case of semicrystalline polymers (especially PET and PBT), by incorporating the nanofiller, one can affect the crystallization behavior and thus the morphology of the samples. Since the degree of crystallinity can indirectly affect mechanical and electrical properties of polymer nanocomposites, one should particularly pay attention to this factor. The enhancement in mechanical

properties of CNP/polymer nanocomposites may represent a compromise between carbon-carbon bond damage and increased CNP-polymer interaction due to CNP functionalization. Moreover, the incorporation of nanofillers like nanotubes or graphene reduces the thermal expansion of polymers by constraining the movement of a significant volume of polymer chains because of their interaction with the filler. Additionally, the electrical conductivity of a CNP/polymer nanocomposite is determined by the negative effect of carbon-carbon bond damage and the positive effect of improved CNP dispersion due to the chemical functionalization. However, in the case of oxidized graphene nanosheets, the partial reduction has to be employed in order to restore its conducting behavior. However, in each case, the choice and control over chemical modification of CNP are necessary. Moreover, composites containing fillers with large aspect ratio (like GDF) can impede and affect the diffusion path of penetrating molecules. Well-dispersed fillers create a tortuous path for gases. To achieve the best performance of CNP/polymer composites, it is important to choose the functionalization method, a suitable polymer matrix for CNT dispersion as well as polymer composite processing conditions. To conclude, the CNP functionalization and polymer matrix design for the dispersion of CNP and interfacial interactions between nanofiller and a polymer matrix are the key issues for the development of high-performance CNP composites.

Acknowledgements

This work is the result of the research project GEKON2/O5/266860/24/2016 funded by the National Centre for Research and Development, Poland.

Author details

Sandra Paszkiewicz

Address all correspondence to: sandra.paszkiewicz@zut.edu.pl

West Pomeranian University of Technology, Institute of Material Science and Engineering, Szczecin, Poland

References

- [1] Sahoo NG, Rana S, Cho JW, Li L, Chan SH. Polymer nanocomposites based on functionalized carbon nanotubes. *Progress in Polymer Science*. 2013;35:837–867. doi:10.1016/j.progpolymsci.2010.03.002
- [2] Hirsch A. Functionalization of single-walled carbon nanotubes. *Angewandte Chemie International Edition*. 2002;41(11):1853–1859. doi:10.1002/1521-3773

- [3] Ebbesen TW, Ajayan PM, Hiura H, Tanigaki K. Purification of nanotubes. *Nature*. 1994;367:519. doi:10.1038/367519a0
- [4] Nalwa HS, editor. *Handbook of Nanostructured Materials and Nanotechnology*. 5th ed. New York: Academic Press; 2000. 778 p.
- [5] Hiura H, Ebbesen TW, Tanigaki K. Opening and purification of carbon nanotubes in high yield. *Advanced Materials*. 1995;7:275–276. doi:10.1002/adma.19950070304
- [6] Kuznetsova A, Mawhinney DB, Naumenko V, Yates JT, Liu J, Smalley RE. Enhancement of adsorption inside of single-walled nanotubes: opening the entry ports. *Chemical Physics Letters*. 2000;321:292–296. doi:10.1016/S0009-2614(00)00341-9
- [7] Liu J, Rinzler AG, Dai H, Hafner JH, Bradley RK, Boul PJ, Lu A, Iverson T, Shelimov K, Huffman CB, Rodriguez-Macias F, Shon Y-S, Lee TR, Colbert DT, Smalley RE. Fullerene pipes. *Science*. 1998;280:1253–1256. doi:10.1126/science.280.5367.1253
- [8] Bandow S, Rao AM, Williams KA, Thess A, Smalley RE, Eklund PC. Purification of single-wall carbon nanotubes by microfiltration. *The Journal of Physical Chemistry B*. 1997;101:8839–8842. doi:10.1021/jp972026r
- [9] Duesberg GS, Burghard M, Muster J, Philipp GS. Separation of carbon nanotubes by size exclusion chromatography. *Chemical Communication*. 1998;3:435–436. doi:10.1039/A707465D
- [10] Paredes JI, Burghard M. Dispersions of individual single-walled carbon nanotubes of high length. *Langmuir*. 2004;20:5149–5152. doi:10.1021/la049831z
- [11] Duesberg GS, Muster J, Krstic V, Burghard M, Roth S. Chromatographic size separation of single-wall carbon nanotubes. *Applied Physics A*. 1998;67:117–119. doi:10.1007/s003390050747
- [12] Moore VC, Strano MS, Haroz EH, Hauge RH, Smalley RE, Schmidt J, Talmon Y. Individually suspended single-walled carbon nanotubes in various surfactants. *Nano Letters*. 2003;3:1379–1382. doi:10.1021/nl034524j
- [13] Islam MF, Rojas E, Bergey DM, Johnson AT, Yodh AG. High weight fraction surfactant solubilization of single-wall carbon nanotubes in water. *Nano Letters*. 2003;3:269–273. doi:10.1021/nl025924u
- [14] Bandyopadhyaya R, Nativ-Roth E, Regev O, Yerushalmi-Rozen R. Stabilization of individual carbon nanotubes in aqueous solutions. *Nano Letters*. 2002;2:25–28. doi:10.1021/nl010065f
- [15] Pei X, Hu L, Liu W, Hao J. Synthesis of water-soluble carbon nanotubes via surface initiated redox polymerization and their tribological properties as water-based lubricant additive. *European Polymer Journal*. 2008;44:2458–2464. doi:10.1016/j.eurpolymj.2008.06.016
- [16] Wu HX, Qiu XQ, Cao WM, Lin YH, Cai RF, Qian SX. Polymer-wrapped multiwalled carbon nanotubes synthesized via microwave-assisted *in situ* emulsion polymerization

- and their optical limiting process. *Carbon*. 2007;45:2866–2872. doi:10.1016/j.carbon.2007.10.009
- [17] Cheng F, Imin P, Maunders C, Botton G, Adronov A. Soluble, discrete supramolecular complexes of single-walled carbon nanotubes with fluorene-based conjugated polymers. *Macromolecules*. 2008;41:2304–2308. doi:10.1021/ma702567y
- [18] Yang L, Zhang B, Liang Y, Yang B, Kong T, Zhang LM. *In situ* synthesis of amylose/single-walled carbon nanotubes supramolecular assembly. *Carbohydrate Research*. 2008;343:2463–2467. doi:10.1016/j.carres.2008.06.031
- [19] Shvartzman-Cohen R, Nativ-Roth E, Baskaran E, Levi-Kalisman Y, Szleifer I, Yerushalmi-Rozen R. Selective dispersion of single-walled carbon nanotubes in the presence of polymers: the role of molecular and colloidal length scales. *Journal of American Chemical Society*. 2004;126:14850–14857. doi:10.1021/ja046377c
- [20] Shvartzman-Cohen R, Kalisman YL, Navi-Roth E, Yerushalmi-Rozen R. Generic approach for dispersing single-walled carbon nanotubes: the strength of a weak interaction. *Langmuir*. 2004;20:6085–6088. doi:10.1021/la049344j
- [21] Park H, Zhao J, Lu JP. Effects of sidewall functionalization on conducting properties of single wall carbon nanotubes. *Nano Letters*. 2006;6:916–919. doi:10.1021/nl052488d
- [22] Zhang X, Sreekumar TV, Liu T, Kumar S. Properties and structure of nitric acid oxidized single wall carbon nanotube films. *Journal of Physical Chemistry B*. 2004;108:16435–16440. doi:10.1021/jp0475988
- [23] Chen J, Rao AM, Lyuksyutov S, Itkis ME, Hamon MA, Hu H, Cohn RW, Eklund PC, Colbert DT, Smalley RE, Haddon RC. Dissolution of full-length single-walled carbon nanotubes. *Journal of Physical Chemistry B*. 2001;105:2525–2528. doi:10.1021/jp002596i
- [24] Hamon MA, Chen J, Hui H, Chen Y, Itkis ME, Rao AM, Eklund PC, Haddon RC. Dissolution of single-walled carbon nanotubes. *Advanced Materials*. 1999;11:834–840. doi:10.1002/(SICI)1521-4095(199907)11:10<834:AID-ADMA834>3.0.CO;2-R
- [25] Niyogi S, Hamon MA, Hu H, Zhao B, Bhowmik P, Sen R, Itkis ME, Haddon RC. Chemistry of single-walled carbon nanotubes. *Account of Chemical Research*. 2002;35:1105–1113. doi:10.1021/ar010155r
- [26] Zhou O, Fleming RM, Murphy DW, Chen CH, Haddon RC, Ramirez AP, Glarum SH. Defects in carbon nanostructures. *Science*. 1994;263:1744–1747. doi:10.1126/science.263.5154.1744
- [27] Baek JB, Lyons CB, Tan LS. Grafting of vapor-grown carbon nanofibers via *in situ* polycondensation of 3-phenoxybenzoic acid in poly(phosphoric acid). *Macromolecules*. 2004;37:8278–8285. doi:10.1021/ma048964o

- [28] Jin Z, Sun X, Xu G, Goh SH, Ji W. Nonlinear optical properties of some polymer/multi-walled carbon nanotube composites. *Chemical Physics Letters*. 2000;218:505–510. doi: 10.1016/S0009-2614(00)00091-9
- [29] Kumar I, Rode CV. Efficient synthesis of fused 1,2,3-triazolo-delta lactams using huisgen [3+2] dipolar cycloaddition click-chemistry in water. *Chemistry Letters*. 2007;36:592–593. doi:10.1246/cl.2007.592
- [30] Marques PAAP, Gonçalves G, Cruz S, Almeida N, Singh MK, Gracio J, Sousa ACM. Functionalized graphene nanocomposites. In: Hashim A, editor. *Advances in Nanocomposite Technology*. Sheffield Hallam University, UK. InTech Open Access Publisher 2011. p. 247–272.
- [31] Kuila T, Bose S, Mishra AK, Khanra P, Kim NH, Lee JH. Chemical functionalization of graphene and its applications. *Progress in Polymer Science*. 2012;57:1061–1105. doi: 10.1016/j.pmatsci.2012.03.002
- [32] Park S, Ruoff RS. Chemical methods for the production of graphenes. *Nature Nanotechnology*. 2009;4:217–224. doi:10.1038/nnano.2009.58
- [33] Bekyarova E, Itkis ME, Ramesh P, Berger C, Sprinkle M, Herr WA, et al. Chemical modification of epitaxial graphene: spontaneous grafting of aryl groups. *Journal of American Chemical Society*. 2009;131:1336–1337. doi:10.1021/ja8057327
- [34] Goncalves G, Marques P, Granadeiro CM, Nogueira HIS, Singh MK, Gracio J. Surface modification of graphene nanosheets with gold nanoparticles: the role of oxygen moieties at graphene surface on gold nucleation and growth. *Chemistry of Materials*. 2009;21:4796–4802. doi:10.1021/cm901052s
- [35] Hong W, Bai H, Xu Y, Yao Z, Gu Z, Shi G. Preparation of gold nanoparticle/graphene composites with controlled weight contents and their application in biosensors. *The Journal of Physical Chemistry C*. 2010;114:1822–1826. doi:10.1021/jp9101724
- [36] Si Y, Samulski ET. Exfoliated graphene separated by platinum nanoparticles. *Chemistry of Materials*. 2008;20:6792–6797. doi:10.1021/cm801356a
- [37] Scheuermann GM, Rumi L, Steurer P, Bannwarth W, Mülhaupt R. Palladium nanoparticles on graphite oxide and its functionalized graphene derivatives as highly active catalysts for the Suzuki-Miyaura coupling reaction. *Journal of the American Chemical Society*. 2009;131:1344–1354. doi:10.1021/ja901105a
- [38] Shen J, Shi M, Li N, Yan B, Ma H, Hu Y, Ye M. Facile synthesis and application of Ag-chemically converted graphene nanocomposite. *Nano Research*. 2010;3:339–349. doi: 10.1007/s12274-010-1037-x
- [39] Muszynski R, Seger B, Kamat PV. Decorating graphene sheets with gold nanoparticles. *The Journal of Physical Chemistry C*. 2008;112:5263–5266. doi:10.1021/jp800977b

- [40] Stankovich S, Dikin DA, Piner RD, Kohlhaas KA, Kleinhammes A, Jia Y, Wu Y, Nguyen ST, Ruoff RS. Synthesis of graphene-based nanosheets via chemical reduction of exfoliated graphite oxide. *Carbon*. 2007;45:1558–1565. doi:10.1016/j.carbon.2007.02.034
- [41] Shin HJ, Kim KK, Benayad A, Yoon SM, Park HK, Jung IS, Jin MH, Jeong HK, Kim JM, Choi JY, Lee YH. Efficient reduction of graphite oxide by sodium borohydride and its effect on electrical conductance. *Advanced Functional Materials*. 2009;19:1987–1992. doi:10.1002/adfm.200900167
- [42] Fan X, Peng W, Li Y, Wang S, Zhang G, Zhang F. Deoxygenation of exfoliated graphite oxide under alkaline conditions: a green route to graphene preparation. *Advanced Materials*. 2008;20:4490–4493. doi:10.1002/adma.200801306
- [43] Amarnath CA, Hong CE, Kim NH, Ku BC, Kuila T, Lee JH. Efficient synthesis of graphene sheets using pyrrole as a reducing agent. *Carbon*. 2011;49:3497–3502. doi:10.1016/j.carbon.2011.04.048
- [44] Coleman JN, Khan U, Blau WJ, Gun'ko YK. Small but strong: a review of the mechanical properties of carbon nanotube polymer composites. *Carbon*. 2006;44:1624–1652. doi:10.1016/j.carbon.2006.02.038
- [45] Moniruzzaman M, Winey KI. Polymer nanocomposites containing carbon nanotubes. *Macromolecules*. 2006;39:5194–5205. doi:10.1021/ma060733p
- [46] Bhattacharya M. Polymer nanocomposites—a comparison between carbon nanotubes, graphene, and clay as nanofillers. *Materials*. 2016;9:262–297. doi:10.3390/ma9040262
- [47] Grady BP. *Carbon Nanotube-Polymer Composites Manufacture, Properties, and Applications*. New York: John Wiley and Sons; 2011. p. 145.
- [48] Guo Q. *Polymer Morphology: Principles, Characterization, and Processing*. New York: Wiley and Sons; 2016. p. 464.
- [49] McClory C, Chin SJ, McNally T. Polymer/carbon nanotube composites. *Australian Journal of Chemistry*. 2009;62:762–785. doi:10.1071/CH09131
- [50] Wu D, Sun Y, Zhang M. Kinetics study on melt compounding of carbon nanotube/polypropylene nanocomposites. *Journal of Polymer Science Part B Polymer Physics*. 2009;47:608–618. doi:10.1002/polb.21668
- [51] Kim IH, Jeong YG. Polylactide/exfoliated graphite nanocomposites with enhanced thermal stability, mechanical modulus, and electrical conductivity. *Journal of Polymer Science Part B Polymer Physics*. 2010;48:850–858. doi:10.1002/polb.21956
- [52] Zhang HB, Zheng WG, Yan Q, Yang Y, Wang JW, Lu ZH, Ji GY, Yu ZZ. Electrically conductive polyethylene terephthalate/graphene nanocomposites prepared by melt compounding. *Polymer*. 2010;51:1191–1196. doi:10.1016/j.polymer.2010.01.027
- [53] An X, Simmons T, Shah R, Wolfe C, Lewis KM, Washington M, Nayak SK, Talapatra S, Kar S. Stable aqueous dispersions of noncovalently functionalized graphene from

- graphite and their multifunctional high-performance applications. *Nano Letters*. 2010;10:4295–4301. doi:10.1021/nl903557p
- [54] Verdejo R, Bernal MM, Romasanta LJ, Lopez J. Graphene filled polymer nanocomposites. *Journal of Materials Chemistry*. 2011;21:3301–3310. doi:10.1039/C0JM02708A
- [55] Yoo BM, Shin HJ, Yoon HW, Park HB. Graphene and graphene oxide and their uses in barrier polymers. *Journal of Applied Polymer Science*. 2014;131:39628.
- [56] Paszkiewicz S, Kwiatkowska M, Roslaniec Z, Szymczyk A, Jotko M, Lisiecki S. The influence of different shaped nanofillers (1D, 2D) on barrier and mechanical properties of polymer hybrid nanocomposites based on PET prepared by *in situ* polymerization. *Polymer Composites*. 2016;37:1949–1959. doi:10.1002/pc.23373
- [57] Szymczyk A, Paszkiewicz S, Pawelec I, Lisiecki S, Jotko M, Spitalsky Z, Mosnacek J, Roslaniec Z. Oxygen barrier properties and melt crystallization behavior of poly(ethylene terephthalate)/graphene oxide nanocomposites. *Journal of Nanomaterials*. 2015;382610:10. doi:10.1155/2015/382610
- [58] Paszkiewicz S, Nachman M, Szymczyk A, Spitalsky Z, Mosnacek J, Roslaniec Z. Influence of expanded graphite (EG) and graphene oxide (GO) on physical properties of PET based nanocomposites. *Polish Journal of Chemical Technology*. 2014;16:45–50. doi:10.2478/pjct-2014-0068
- [59] Sadasivuni KK, Ponnammma D, Thomas S, Grohens Y. Evolution from graphite to graphene elastomer composites. *Progress in Polymer Science*. 2014;39:749–780. doi:10.1016/j.progpolymsci.2013.08.003
- [60] Thostenson ET, Ren ZF, Chou TW. Advances in the science and technology of CNTs and their composites: a review. *Composites Science and Technology*. 2001;61:1899–1912. doi:10.1016/S0266-3538(01)00094-X
- [61] Ajayan PM, Schadler LS, Braun PV. *Nanocomposite Science and Technology*. Weinheim: Wiley-VCH; 2003. pp. 77–80.
- [62] Ma PC, Siddiqui NA, Marom G, Kim J-K. Dispersion and functionalization of carbon nanotubes for polymer-based nanocomposites: a review. *Composites Part A: Applied Science and Manufacturing*. 2010;41:1345–1367. doi:10.1016/j.compositesa.2010.07.003
- [63] Yoo HJ, Jung YC, Cho JW. Effect of interaction between poly(ethylene terephthalate) and carbon nanotubes on the morphology and properties of their nanocomposites. *Journal of Polymer Science: Part B: Polymer Physics*. 2008;46:900–910. doi:10.1002/polb.21424
- [64] Jin SH, Park Y-B, Yoon KH. Rheological and mechanical properties of surface modified multi-walled carbon nanotube-filled PET composite. *Composites Science and Technology*. 2007;67:3434–3441. doi:10.1016/j.compscitech.2007.03.013
- [65] Lee HJ, Oh SJ, Choi JY, Kim JW, Han J, Tan LS, Baek JB. *In situ* synthesis of poly(ethylene terephthalate) (PET) in ethylene glycol containing terephthalic acid and functionalized

- multiwalled carbon nanotubes (MWNTs) as an approach to MWNT/PET nanocomposites. *Chemistry of Materials*. 2005;17:5057–5064. doi:10.1021/cm051218t
- [66] Szymczyk A, Roslaniec Z, Zenker M, Garcia-Gutierrez M-C, Hernandez JJ, Rueada DR, Nogales A, Ezquerro TA. Preparation and characterization of nanocomposites based on COOH functionalized multi-walled carbon nanotubes and on poly(trimethylene terephthalate). *Express Polymer Letters*. 2011;5:977–995. doi:0.3144/expresspolymlett.2011.96
- [67] Paszkiewicz S, Szymczyk A, Janowska I, Jedrzejewski R, Linares A, Ezquerro TA, Wagner TA, Roslaniec Z. Comparative study on the properties of poly(trimethylene terephthalate) based nanocomposites containing multi-walled carbon (MWCNT) and tungsten disulfide (INT-WS₂) nanotubes. *Polymers for Advanced Technologies*. (Forthcoming).
- [68] Paszkiewicz S, Szymczyk A, Kasproviak I, Zenker M, Pilawka R, Linares A, Ezquerro TA, Roslaniec Z. Electrical and rheological characterization of poly(trimethylene terephthalate) hybrid nanocomposites filled with COOH functionalized MWCNT and graphene nanosheets. *Polymer Composites*. (Forthcoming).
- [69] Kwiatkowska M, Broza G, Schulte K, Roslaniec Z. The *in-situ* synthesis of polybutylene terephthalate/carbon nanotubes composites. *Reviews on Advanced Materials Science*. 2006;12:154–159.
- [70] Piesowicz E, Irska I, Bryll K, Gawdzinska K, Bratychak M. Poly(butylene terephthalate/carbon nanotubes nanocomposites. Part II. Structure and properties. *Polimery*. 2016;61:18–24. doi:10.14314/polimery.2016.024
- [71] Fabbri P, Bassoli E, Bon SB, Valentini S. Preparation and characterization of poly(butylene terephthalate)/graphene composites by *in-situ* polymerization of cyclic butylene terephthalate. *Polymer*. 2010;53:897–902. doi:10.1016/j.polymer.2012.01.015
- [72] Kim H, Macosko CW. Morphology and properties of polyester/exfoliated graphite nanocomposites. *Macromolecules*. 2008;41:3317–3327. doi:10.1021/ma702385h
- [73] Schadler LS, Brinson LC, Sawyer WG. Polymer nanocomposites: a small part of the story. *The Journal of the Minerals, Metals and Materials Society*. 2007;59:53–60. doi:10.1007/s11837-007-0040-5
- [74] Xu JZ, Chen T, Yang CL, Li ZM, Mao YM, Zeng BQ, Hsiao BS. Isothermal crystallization of poly(l-lactide) induced by graphene nanosheets and carbon nanotubes: a comparative study. *Macromolecules*. 2010;43:5000–5008. doi:10.1021/ma100304n
- [75] Liang JJ, Huang Y, Zhang L, Wang Y, Ma YF, Guo TY, Chen Y. Molecular-level dispersion of graphene into poly(vinyl alcohol) and effective reinforcement of their nanocomposites. *Advanced Functional Materials*. 2009;19:2297–2302. doi:10.1002/adfm.200801776
- [76] Yang X, Li L, Shang S, Tao X. Synthesis and characterization of layer-aligned poly(vinyl alcohol)/graphene composites. *Polymer*. 2010;51:3431–3435.

- [77] Ansari S, Kalarakis A, Estevez L, Giannelis EP. Oriented arrays of graphene in a polymer matrix by *in situ* reduction of graphite oxide nanosheets. *Small*. 2010;6:205–209. doi:10.1002/sml.200900765
- [78] Cai D, Song M. A simple route to enhance the interface between graphite oxide nanoplatelets and asemi-crystalline polymer for stress transfer. *Nanotechnology*. 2009;20:315708. doi:10.1088/0957-4484/20/31/315708
- [79] Du N, Zhao CY, Chen Q, Wu G, Lu R. Preparation and characterization of nylon 6/graphite composite. *Material Chemistry and Physics*. 2010;120:167–171. doi:10.1016/j.matchemphys.2009.10.041
- [80] Lee C, Wei X, Kysar JW, Hone J. Measurement of the elastic properties and intrinsic strength of monolayer graphene. *Science*. 2008;321:385–388. doi:0.1126/science.1157996
- [81] Paszkiewicz S. Polymer hybrid nanocomposites containing carbon nanoparticles. *In situ* synthesis and physical properties. Szczecin: West Pomeranian University of Technology. 2014. p. 190. Available from: <http://zbc.ksiaznica.szczecin.pl/dlibra/docmetadata?id=30212&from=publication>
- [82] Li J, Ma PC, Chow WS, To CK, Tang BZ, Kim JK. Correlations between percolation threshold, dispersion state, and aspect ratio of carbon. *Advanced Functional Materials*. 2007;17:3207–3215. doi:10.1002/adfm.200700065
- [83] Choi ES, Brooks JS, Eaton DL, Al Haik MS, Hussaini MY, Garmestani H, Li D, Dahmen K. Enhancement of thermal and electrical properties of carbon nanotube polymer composites by magnetic field processing. *Journal of Applied Polymer Science*. 2003;94:6034. doi:10.1063/1.1616638
- [84] Georgakilas V, Kordatos K, Prato M, Guldi DM, Holzinger M, Hirsch A. Organic functionalization of carbon nanotubes. *Journal of the American Chemical Society*. 2002;124:760–761. doi:10.1021/ja016954m
- [85] Kim H, Abdala AA, Macosko CW. Graphene/polymer nanocomposites. *Macromolecules*. 2010;43:6515–6530. doi:10.1021/ma100572e
- [86] Bauhofer W, Kovacs JZ. A review and analysis of electrical percolation in carbon nanotube polymer nanocomposites. *Composites Science and Technology*. 2009;69:1486–1498. doi:10.1016/j.compscitech.2008.06.018
- [87] Paszkiewicz S, Szymczyk A, Spitalsky Z, Soccio M, Mosnacek J, Ezquerro TA, Roslaniec Z. Electrical conductivity of poly(ethylene terephthalate)/expanded graphite nanocomposites prepared by *in situ* polymerization. *Journal of Polymer Science Part B: Polymer Physics*. 2012;50:1645–1652. doi:10.1002/polb.23176
- [88] Hernandez JJ, Garcia-Gutierrez MC, Nogales A, Rueda DR, Kwiatkowska M, Szymczyk A, Roslaniec Z, Concheso A, Guinea I, Ezquerro TA. Influence of preparation procedure on the conductivity and transparency of SWCNT-polymer nanocomposites.

- Composites Science and Technology. 2009;69:1867–1872. doi:10.1016/j.compscitech.2009.04.002
- [89] Hu G, Zhao C, Zhang S, Yang M, Wang Z. Low percolation thresholds of electrical conductivity and rheology in poly(ethylene terephthalate) through the networks of multi-walled carbon nanotubes. *Polymer*. 2006;47:480–488. doi:10.1016/j.polymer.2005.11.028
- [90] Paszkiewicz S, Pawelec I, Szymczyk A, Spitalsky Z, Mosnacek Z, Kochmanska A, Roslaniec Z. Effect of exfoliated graphite nanoplatelets' size on the phase structure, electrical and barrier properties of poly(trimethylene terephthalate) (PTT) based nanocomposites. *Polymer Engineering and Science*. 2015;55:2222–2230. doi:10.1002/pen.24107
- [91] Li M, Jeong YG. Preparation and characterization of high-performance poly(trimethylene terephthalate) nanocomposites reinforced with exfoliated graphite. *Macromolecular Materials and Engineering*. 2011;296:159–167. doi:10.1002/mame.201000295

Nanocomposites of Carbon Nanotubes and Semiconductor Nanocrystals as Advanced Functional Material with Novel Optoelectronic Properties

Rima Paul and Apurba Krishna Mitra

Additional information is available at the end of the chapter

<http://dx.doi.org/10.5772/66218>

Abstract

Semiconductor nanoparticles of very small size, or quantum dots, exhibit fascinating physical properties, completely different from their bulk varieties, mostly because of the quantum confinement effect. Due to their modified band structure, they particularly show attractive optoelectronic characteristics. Carbon nanotubes are a class of nanomaterials, which also possess wonderful optoelectronic properties and can revolutionize modern semiconductor technology to a great extent. Carbon nanotube field-effect transistors (CNTFETs) can replace standard MOSFETs in an array of devices and can function in a more effective way. When these two optoelectronic components combine together in nanocomposites, one may get advanced optoelectronic devices for widespread application in sensors, solar cells, energy storage devices, light-emitting diodes, electrocatalysts, etc.

Keywords: nanocomposites, nanohybrids, quantum dots, carbon nanotubes, optoelectronics

1. Introduction

Advanced research in Materials Science introduced a new direction to control the properties of materials with grain size at nanometer level (1–100 nm). At such reduced scale, materials exhibit fascinating physical properties completely different from their bulk counterparts. The properties of this new class of materials, called nanomaterials, can be tuned by changing their grain size and hence find a wide range of applications. Semiconductor nanoparticles are useful ingredients for the development of optoelectronic devices. This is due to their striking optical and optoelectronic properties, which strongly differ from those of the corresponding bulk

materials. In principle, this is related to the existence of quantum confinement effects of excitons in the nanoparticles. Bandgaps are significantly changed with the size of the nanoparticles, thus modifying the mechanism of radiative recombination of the electrons and holes, which lead to large changes in the emission wavelengths of the excited nanocrystals. Thus, even Si-based nanoelectronic structures may become luminescent with visible light emission, leading to the vast possibilities of optoelectronics [1].

Due to quantum confinement effect, the continuous energy states split into discrete states, with effective blue-shift in the bandgap of the nanomaterials relative to that of bulk materials. Presence of defects such as vacancies, interstitial atoms, surface and grain boundaries in the semiconductor nanocrystals and also doping with appropriate dopants introduce discrete energy levels, which alter the luminescence property of such nanomaterials. An increase in energy bandgap with decrease in particle size leads to a blue-shift in the absorption spectrum. The influence of particle size is found not only in the absorption spectrum but also in the wavelength of the emitted photons. Carbon nanostructures and carbon nanotubes (CNTs), in particular, have such remarkable electronic and structural properties that they are used as active building blocks for a large variety of nanoscale devices. Precisely, the use of carbon nanotubes as active components in electronic and optoelectronic nanodevices has great potential. When nanostructures are synthesized with the hybridization of the above two promising optoelectronic components, a new set of functional nanocomposites appear with fascinating optoelectronic characteristics that may lead to the fabrication of advanced optoelectronic devices for a great variety of potential applications.

2. Quantum confinement in semiconductor nanoparticles

If the size of a nanoparticle becomes comparable to or smaller than the radius of the orbit of the electron-hole pair, then we have a quantum dot (QD) and the case of quantum confinement arises. Quantum confinement can be well explained by applying the laws of quantum mechanics. Quantum confinement is observed in the case of interaction of very small nanocrystals with radiation, when free electrons and holes are created. The hole and the electron form a hydrogen-like system called an 'exciton.' The radius of the exciton, called the 'excitonic Bohr radius,' may range from a fraction of a nanometer to a few nanometers. Quantum confinement occurs when at least one dimension of a nanocrystal is smaller than the diameter of the exciton. In this case, the absorption and emission of light are strongly particle size-dependent and the phenomenon can be explained by the mechanism of quantum confinement. The behavior of subatomic particles is understood by using Schrödinger equation. In a bulk semiconductor, the electrons of the conduction band and the holes of the valence band are free to move throughout the crystal and their motion can be described by the linear combination of plane waves with wavelength of the order of nanometers. Whenever the size of a semiconducting solid becomes comparable to these wavelengths, a free charge carrier confined in this structure will behave as a particle in a potential box. In such a case, the solutions of the Schrödinger equation are standing waves confined within the potential well, and the energies associated with two distinct wave functions are in general different and discontinuous. Thus, the energy of the

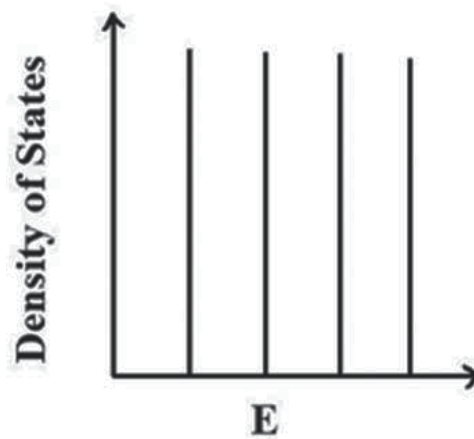


Figure 1. Density of states for a particle in a zero-dimensional nanostructure.

particle exhibits a discrete energy level spectrum. Brus [2] modelled in a simple way the excited electronic states of semiconductor crystallites of sufficiently small size. He expressed the energy of the lowest excited state as:

$$E = \hbar^2 \pi^2 / 2R^2 (1/m_e + 1/m_h) - 1.8e^2 / \epsilon_2 R + e^2 / R f(\epsilon_1, \epsilon_2) \quad (1)$$

where, R is the radius of the spherical particle with dielectric coefficient, ϵ_2 , which is surrounded by a medium of coefficient, ϵ_1 ; E is the shift with respect to the bulk bandgap; m_e and m_h , the effective mass of electron and hole, respectively, and e is the charge of the electron.

In Eq. (1), the second term describes the increase in energy due to confinement effects, while the third term describes the decrease in energy due to Coulomb interaction between electrons and holes.

For a zero-dimensional nanostructure, such as a quantum dot, the density of states is given by:

$$\rho(E)_{0D} = \sum_i 2\delta(E - E_i) \quad (2)$$

where, $\delta(E - E_i)$ is the Dirac δ -function. The density of states for 0D nanostructure is shown in **Figure 1**.

2.1. Optoelectronic properties of QDs

In this section, some significant recent research investigations on the striking optoelectronic properties of semiconductor nanocrystals will be discussed. Liu et al. [3] reported a facile chemical synthesis of SnSe nanocrystals with tunable sizes, by using common alkylphosphine-Se precursors in combination with SnCl_2 . The optoelectronic properties of colloidal SnSe NCs were studied by fabricating a SnSe NC thin film between interdigitated gold electrodes (**Figure 2(A)**). The current-voltage (I-V) curves were measured in the dark and

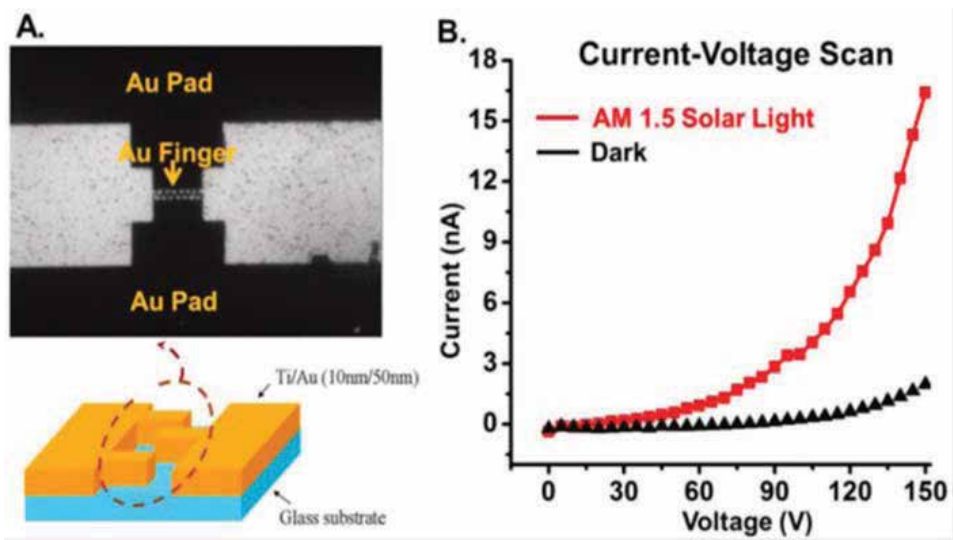


Figure 2. (A) Interdigitated microstructure of metal – semiconductor – metal (MSM) device. (B) Photoresponse of SnSe NC thin-film to AM 1.5 illumination. Reprinted with permission from Liu et al. [3].

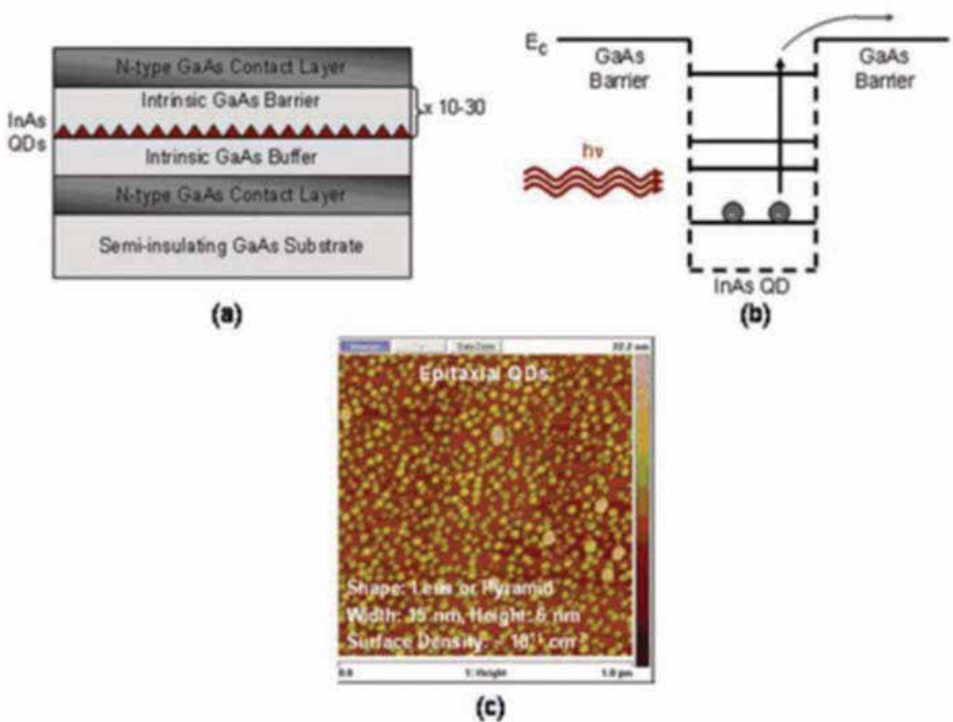


Figure 3. Schematic diagrams of (a) device heterostructure and (b) energy vs. position of intraband transitions demonstrating photocurrent generation in epitaxial InAs/GaAs quantum dot infrared photodetectors. (c) Atomic force microscopy image of epitaxial InAs/GaAs QDs demonstrating important structural characteristics. Reproduced with permission from Stokes et al. [4].

under AM 1.5 simulated solar illumination. The film showed a significant photoresponse (**Figure 2(B)**). The photoresponse of the SnSe nanocrystal thin-film to simulated solar light indicates that the materials have potential for use in solution-processed photovoltaic and optoelectronic devices.

Stokes et al. [4] reported a wet chemical synthesis of semiconductor quantum dots (SQDs), such as cadmium sulphide (CdS) or cadmium selenide (CdSe), etc. They stabilized nanocrystals and controlled their size for specific optical and electronic properties, by chemical capping using some organic capping agent, such as tri-n-octylphosphine oxide (TOPO). They further manipulated their properties by using a core-shell structure of SQDs. Core-shell structures are made by covering the surface of a SQD with a shell of another SQD, which has a greater bandgap than the core (e.g., ZnS over CdS or CdSe). Also as discussed by them, epitaxial quantum dot films (EQDs) of III-V compound semiconductors (InAs/GaAs) have been widely used in infrared photodetectors. **Figure 3** shows the schematics of a typical epitaxial InAs/GaAs infrared photodetector.

3. Carbon nanotubes

The atomic structure of carbon nanotubes depends on tube chirality, which is characterized by the chiral vector C_h and the chiral angle θ . The chiral vector, is defined as a line connecting two crystallographically equivalent sites on a two-dimensional graphene layer, and can be represented in terms of lattice translation indices (n , m) and the basis vectors a_1 and a_2 as follows:

$$C_h = n a_1 + m a_2 \quad (3)$$

where, $n \geq m$ (**Figure 4**).

CNT is constructed by rolling up the graphene sheet such that the two end-points of the vector C_h are superimposed. This CNT is denoted as (n , m) tube with diameter as:

$$D = |C_h|/\pi = a (n^2 + nm + m^2)^{1/2}/\pi. \quad (4)$$

where $a = |a_1| = |a_2|$ is the lattice constant of the graphene sheet. The tubes with $m = n$ are commonly referred to as armchair tubes, while $m = 0$ as zigzag tube and others having $m \neq n$ are called as chiral tubes. A chiral angle is represented as:

$$\theta = \tan^{-1} [3^{1/2} m / (m + 2n)] \quad (5)$$

For an armchair tube, $\theta = 30^\circ$. In the case of a zigzag tube, $\theta = 0^\circ$ and all tubes having chiral angle, $0^\circ < \theta < 30^\circ$, are called chiral tubes. A tube made of a single graphitic layer is called a single-walled carbon nanotube (SWCNT), a tube formed by two coaxial graphitic layers is called a double-walled carbon nanotube (DWCNT), and a tube comprising of several coaxial graphitic cylinders is referred to as a multiwalled carbon nanotube (MWCNT). Through

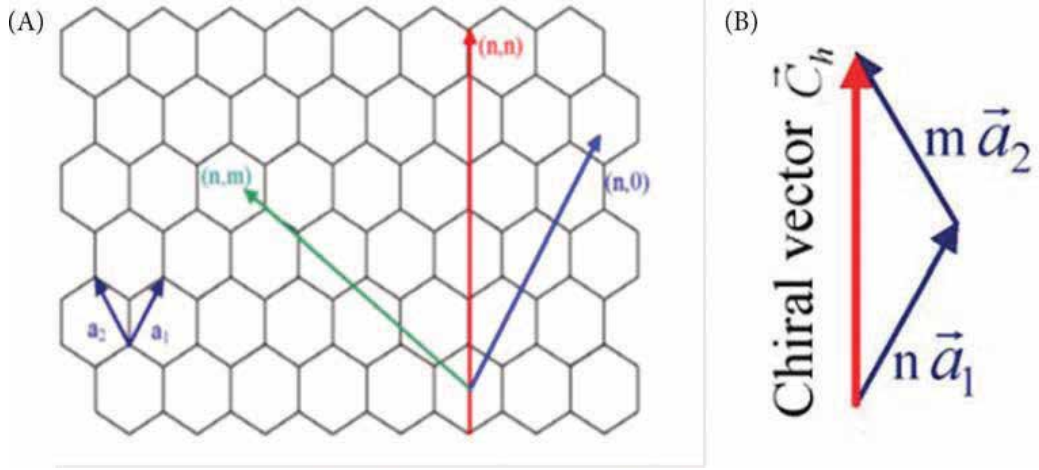


Figure 4. Geometrical structure of carbon nanotubes (CNTs): (A) honeycomb structure and basis vectors, (B) the chiral vector.

theoretical calculations and experimental observations, it has been found that C-C bond length $d_{cc} = 0.142$ nm or $a = |\vec{a}_1| = |\vec{a}_2| = 0.246$ nm, while the intertube spacing $d_{tt} = 0.34$ nm in a MWCNT. A carbon nanotube can be semiconducting or metallic depending upon its band structure, which in turn depends on the chirality and diameter of the tube. The electronic structure of the SWCNTs is related to a 2D graphene sheet, but, because of the radial confinement of the wave function, DOS in graphite divides into a series of spikes in SWCNTs (shown in **Figures 5A** and **5B**), which are referred to as van Hove singularities [6]. Density of states gives the number of available energy states and electrons in a given energy interval. For all metallic nanotubes, the density of states per unit length along the tube axis is constant and is given by:

$$N(E_F) = 8/\sqrt{3\pi a \gamma_o} \quad (6)$$

where a is the lattice constant of the graphene sheet and γ_o is the nearest neighbour C-C tight binding overlap energy. The density of states near the Fermi level E_F located at $E = 0$ for semiconducting nanotubes is zero (**Figure 5A**), but is non-zero and small in the case of metallic nanotubes (**Figure 5B**). Semiconducting nanotubes show that their energy gap depends upon the reciprocal of the nanotube diameter D and is independent of the chiral angle. Thus,

$$E_g = \gamma_o a / \sqrt{3D} \quad (7)$$

Electronic transitions between the energy bands of carbon nanotubes and their standard designations are illustrated in the diagram below for single-walled carbon nanotubes (SWNTs), synthesized in three different techniques, namely hi-pressure carbon monoxide-chemical vapour deposition (HiPCO-CVD), laser ablation, and arc discharge method. Their absorbance characteristics are shown along with following Niyogi et al. [6] (**Figure 5C**).

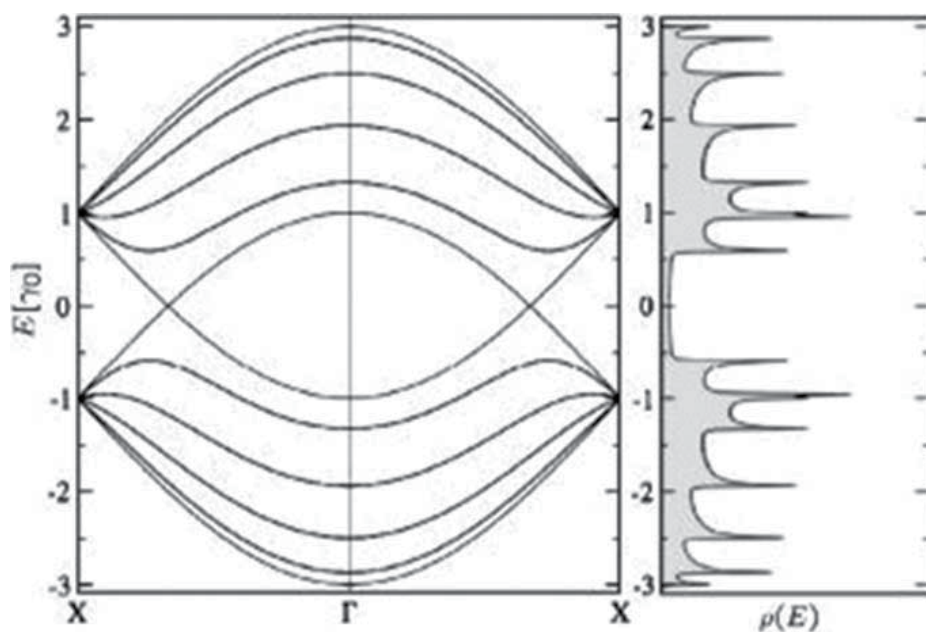


Figure 5A. Band structure and density of states for a (5, 5) armchair nanotube within the zone-folding model. Adapted with permission from Ref. [5].

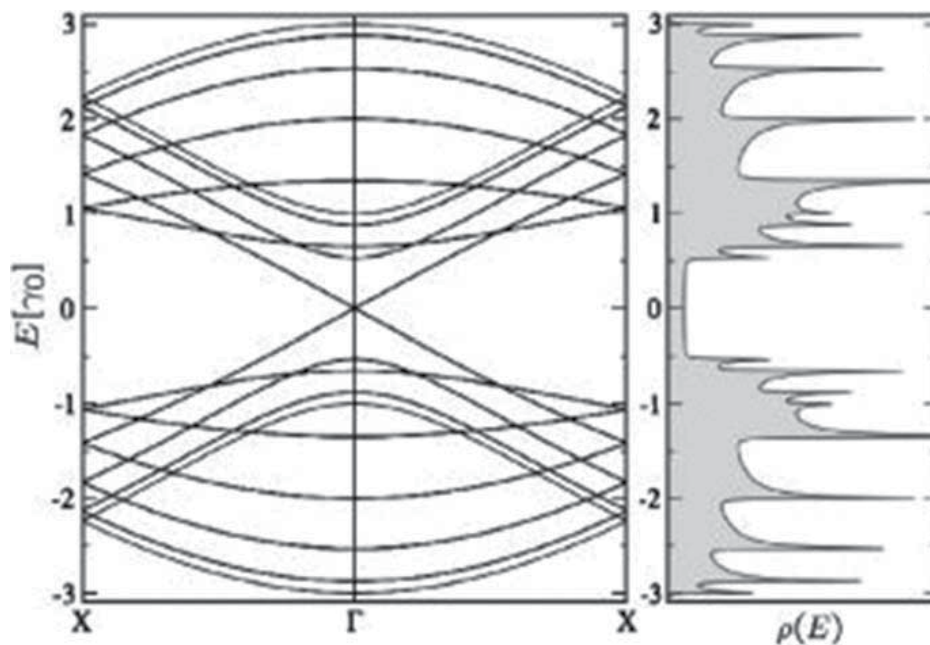


Figure 5B. Band structure and density of states for a (9,0) zigzag nanotube within the zone-folding model. Adapted with permission from Ref. [5].

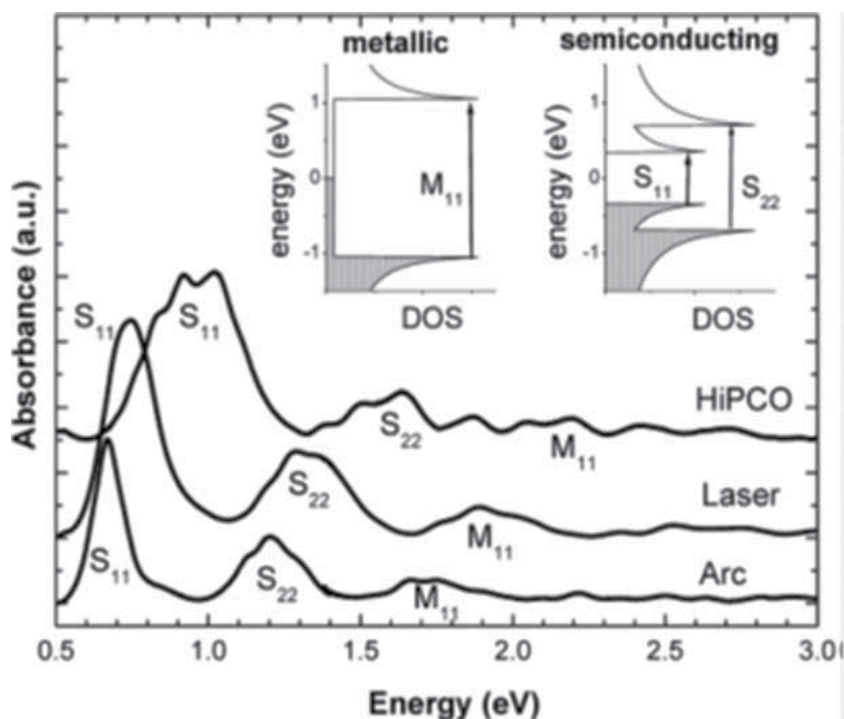


Figure 5C. Electronic transitions between the energy bands of SWNTs, observed by transmission spectroscopy of films, together with a schematic of the nomenclature used to designate the intraband transitions. Reprinted with permission from Ref. [6].

3.1. Optoelectronic properties of carbon nanotubes

A great characteristic of carbon nanotubes is their ability to withstand a very high current density, exceeding 10^9 A/cm² [7–9]. For metallic nanotubes, the current-carrying capability may even rise up to a value of 25 μ A, limited by Joule self-heating, and by the scattering of optical phonons. The saturation current limit for semiconducting nanotubes is controlled by the Schottky barrier electrical resistance at the nanotube-metal contact, which in turn depends on the diameter of the tube and the work function of the contact metal.

A promising material for fabricating cold cathodes for the next-generation high-performance flat-panel devices is carbon nanotubes (CNTs). Sridhar et al. [10] synthesized a forest of vertically aligned MWCNTs on Inconel 718 substrate and studied its field emission properties. Compared to similar CNT structures grown on silicon, the ones on Inconel substrate were found to possess lower switching fields (~ 1.5 V/ μ m), higher operating current (~ 100 mA/cm²), and higher amplification factor (~ 7300), and thus promised enormous potential for use as cold cathodes in microwave vacuum devices, etc. (**Figure 6**).

As explained by Kinoshita [11], a carbon nanotube field-effect transistor (CNTFET) may be designed in a simple way, with the carbon nanotube providing the transport channel when

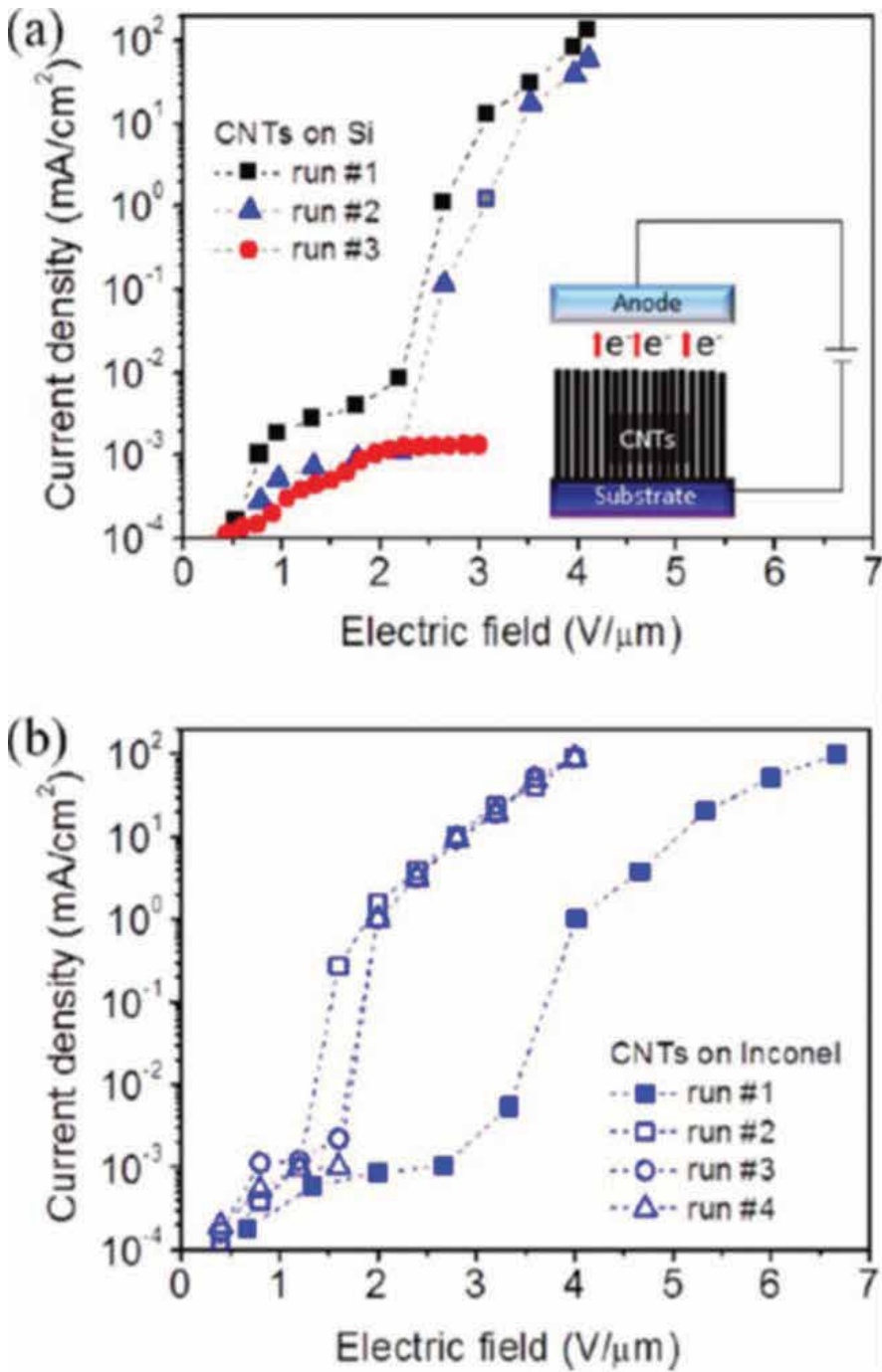


Figure 6. Plots of emission current density as a function of applied electric field in repeated experiments for CNTs grown on (a) Si and (b) Inconel. Reprinted with permission from Ref. [10].

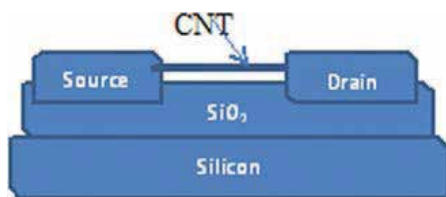


Figure 7. Schematic diagram of a carbon nanotube field-effect transistor (CNTFET).

contacted on each end by bulk metal, and a heavily doped Si substrate acts as the back gate, with SiO_2 performing the function of the gate dielectric. Unlike a conventional MOSFET, a CNTFET operates as a Schottky barrier transistor where the gate controls the Schottky barrier and the injection of carriers. In a CNTFET, one can obtain an $I_{\text{on}}/I_{\text{off}}$ ratio of 10^5 – 10^7 and an on-current of $\sim 1 \mu\text{A}$ at the operating drain-source voltage V_{DS} of 1 V, as observed by Kinoshita [11]. The details of the conduction characteristics depend on the tube diameter, the choice of the contact metal, etc. (**Figure 7**).

Topinka et al. [12] studied carbon nanotube network field-effect transistors (CNTN-FETs). They investigated the microscopic transport mechanism of such devices and observed that in CNTN-FETs the voltage dropped abruptly at a point in the channel where the current was constricted to just one tube. They varied the semiconducting/metallic tube ratio and studied the effect of Schottky barriers on conductance of the channel.

4. Nanoparticle-carbon nanotube composites

When the external surfaces of carbon nanotubes are decorated with semiconductor nanoparticles or quantum dots (NPs/QDs), a new class of functional materials is produced with remarkable properties, which combine the unique characteristics of the individual components. Such nanostructures are known as CNT-NP (or CNT-QD) hybrids, or nanocomposites. These nanocomposite materials are potentially useful in a wide range of advanced applications, in the field of chemical sensors [13], biosensors [14], electrocatalysis [15], fuel cells [16], and nanoelectronics [17]. Semiconductor NPs of very small size are known as quantum dots (QDs), as they exhibit interesting size-dependent optical and electronic properties, due to quantum confinement effect. As observed by Georgakilas et al. [18] CNTs hybridized with QDs of II–VI or III–V semiconductors are ideal optoelectronic materials and can be used in solar cells, light-emitting diodes, etc.

Therefore, varieties of semiconductor NPs, such as CdSe, CdS, CdTe, PbSe, ZnS, ZnO, SiO_2 , TiO_2 , and In_2S_3 , have been bound to CNT surfaces and properties studied by several researchers.

The electronic interaction between CNTs and the externally attached nanocrystals (NCs) plays a crucial role in constructing optoelectronic devices [19, 20]. Hybridizing semiconductor NPs on CNT surfaces can modify their optical characteristics and luminescent property significantly and hence can find application in assembling photoelectrochemical cells [21], in tailoring

light-emitting diodes [22], in organizing sensor systems, and in fabricating electrochromic devices [23].

4.1. Synthesis and characterization of the CNT-QD composites

There are several methods to decorate carbon nanotubes with nanoparticles. Chen and Lu [24] proposed an efficient gas-phase route of the electrostatic force directed assembly (ESFDA) process. The locally enhanced electric field near CNTs results in directed assembly of charged aerosol nanoparticles onto CNTs. They coated MWCNTs with a mixture of SnO_2 and Ag nanocrystals by using this method.

However, the most widely exploited route for synthesis of semiconductor nanoparticle-coated carbon nanotubes is the wet chemical process. In this method, the size of the QDs can be tuned and the proportions of the two components of the composite can be adjusted to obtain the desired properties. Carboxyl groups on the surface of acid-treated CNTs are often used to attach amine-terminated or mercapto-terminated inorganic nanoparticles through amide bonds.

Banerjee and Wong [25] used a multistep procedure to attach modified CdSe QDs to carboxyl-group functionalized CNTs (**Figure 8**).

Li et al. [26] used polyamine- and amino-functionalized MWCNTs (MWCNT-NH_2) templates to load CdTe quantum dots (QDs) and Fe_3O_4 magnetic nanoparticles by the electrostatic self-assembly approach, synthesizing MWCNT/CdTe and $\text{MWCNT/Fe}_3\text{O}_4$ nanohybrids (**Figure 9**).

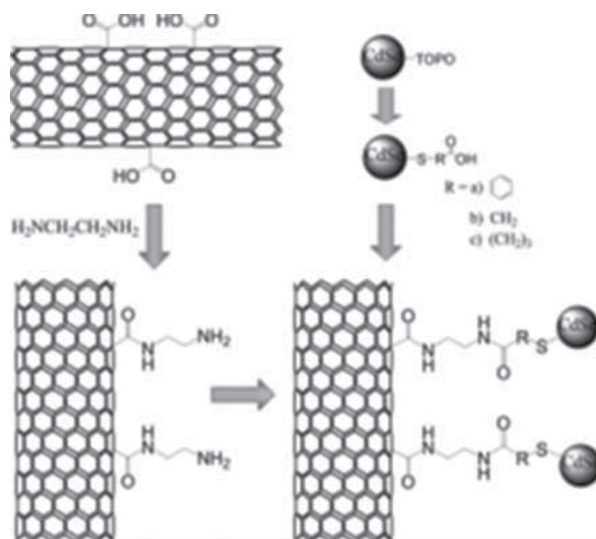


Figure 8. Multistep process for linking modified CdSe QDs to CNTs via amide bonds, involving (1) the oxidation of CNTs in KMnO_4 and functionalization with ethylenediamine and (2) the thiolization of CdSe and termination with acid groups. Reprinted with permission from Ref. [25].

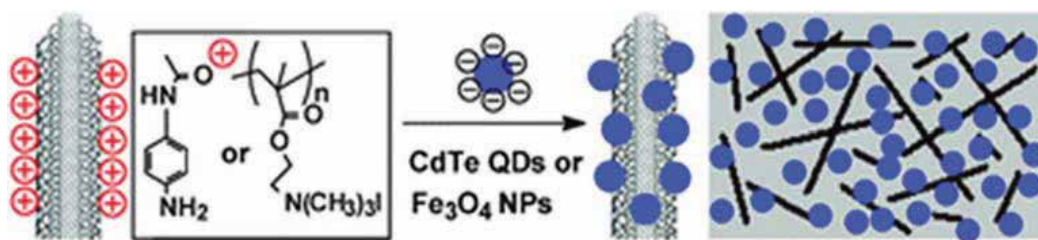


Figure 9. Synthesis procedure for preparation of MWCNT/nanoparticle hybrids from multiamino-functionalized MWCNTs by the electrostatic self-assembly approach. Reprinted with permission from Ref. [26].

Robel et al. [27] investigated the single-walled carbon nanotube-CdS nanocomposites as light-harvesting assemblies and studied their photoinduced charge-transfer interactions, undertaking a simple solution-mixing synthesis of the samples as shown in **Figure 10**.

Paul et al. [28] reported a simple chemical precipitation technique for the synthesis of a hybrid nanostructure of single-wall carbon nanotubes (SWCNT) and titania (TiO_2) nanocrystals of average size 5 nm (**Figure 11**). They prepared SWCNT/ TiO_2 nanohybrid structures by mixing purified SWCNT in TiCl_3 solution and stirring the mixture in a magnetic stirrer. NH_4OH solution was added in drops to attain pH neutrality and the mixture was further stirred for a few hours. Then, they centrifuged the colloidal solution at 9°C , washed it with deionized water and 2-propanol, and dried up at room temperature. They did structural and morphological characterization of the samples, and studied their optical and electrical properties.

In the absorbance spectra of the nanohybrid material, a blue-shift was observed by them, confirming the charge transfer between SWCNTs and titania nanoparticles. There was a

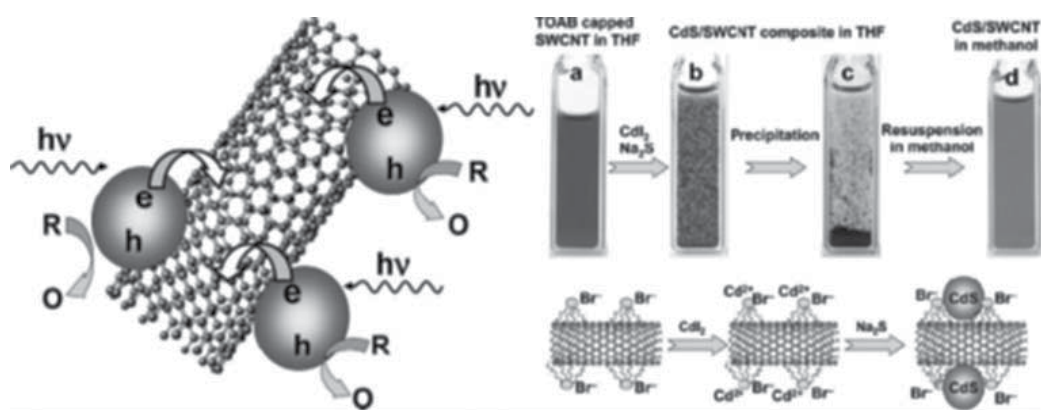


Figure 10. Chemical synthesis of SWCNT/CdS hybrid structure in THF solution is shown on the right part of the figure. The different stages of formation of the nanocomposite are shown in a labelled flowchart. The left part shows the charge transfer mechanism between excited CdS nanoparticles and SWCNTs. Reproduced with permission from Ref. [27].

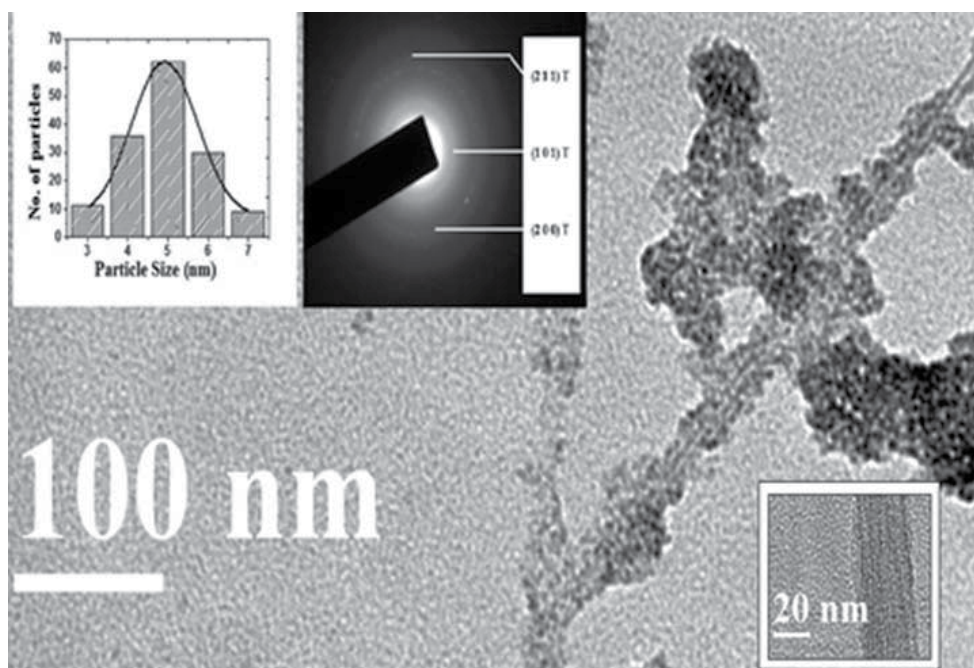


Figure 11. HRTEM micrograph of SWCNT/TiO₂ hybrid; insets showing the HRTEM micrograph of pristine SWCNT, SAED pattern of the composite material and the particle size distribution of TiO₂ NCs. Copyright © 2013 Techno-Press, Ltd.

considerable visible emission in the photoluminescence spectrum with the peak emission at 400 nm.

Figure 12 shows the Raman spectrum of pristine SWCNT and that of SWCNT/TiO₂ hybrid. The peaks at 150, 408, and 650 cm⁻¹ of the hybrid sample correspond to the photoelectronically active TiO₂ anatase phase. There is an upshift by 12 cm⁻¹ in the position of G-band indicating charge transfer to SWCNTs from TiO₂ NCs. I_D/I_G for pristine SWCNT was 0.546, while that for SWCNT/TiO₂ hybrid was found to be 0.939.

Study of DC conductivity of pristine SWCNT showed a crossover from a semiconductor-like temperature dependence of conductivity to a metal-like one with the increase of temperature, transition temperature being 180 K (**Figure 13**). When coated with TiO₂ NPs, the whole material behaves as a semiconducting material and its conductivity decreases by several orders of magnitude. A broad luminescence in the visible region in the range of 325–500 nm was observed, which could be attributed to the charge transfer from the titania NCs to the SWCNTs. Thus, the hybridization of TiO₂ nanoparticles with SWCNTs rendered an advanced functional material with improved photocatalytic response due to reduced recombination of photoelectrons. Also, this nanocomposite could find application as a useful optical material for sensor devices.

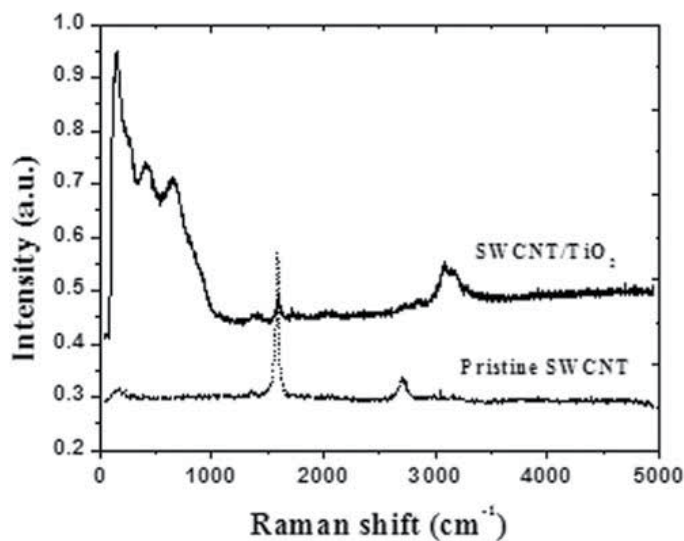


Figure 12. Raman spectrum of pristine SWCNT and SWCNT/TiO₂ composite. Copyright © 2013 Techno-Press, Ltd.

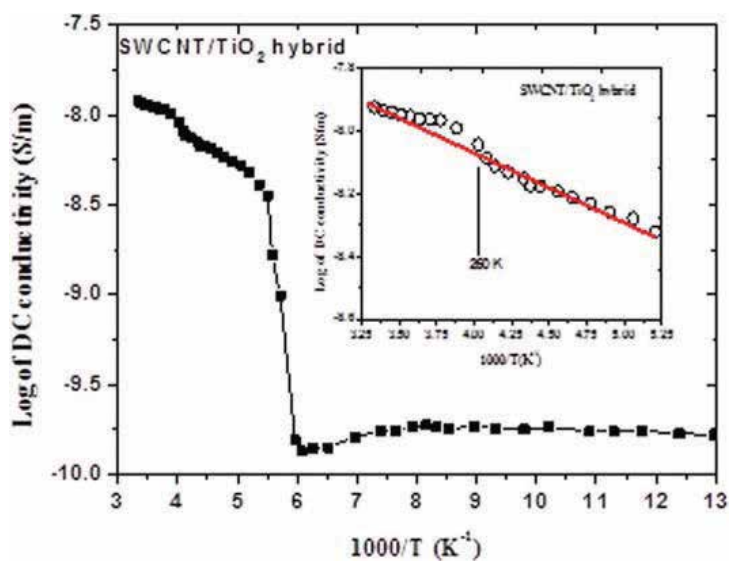


Figure 13. Variation of log of DC conductivity of SWCNT/TiO₂ hybrid with $1000/T$ (K^{-1}); inset shows the higher temperature plot of DC conductivity of the hybrid. Copyright © 2013 Techno-Press, Ltd.

4.2. Optoelectronic applications of CNT-QD composites

Yang et al. [29] synthesized In₂S₃-carbon nanotube nanocomposites through a facile refluxing wet chemistry process, as shown in the micrograph (Figure 14). The as-synthesized In₂S₃-CNT nanocomposites were used as selective and active visible-light driven photocatalysts toward

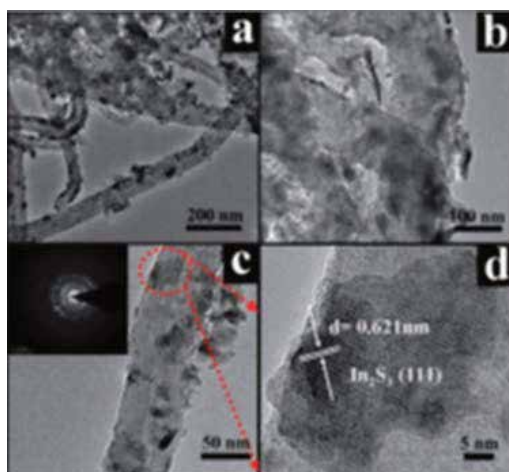


Figure 14. Typical TEM images (a-c) and high-resolution TEM (HR-TEM) image (d) of the sample of In_2S_3 -3% CNT; the inset of panel (c) is the corresponding SAED pattern. Reprinted with permission from Ref. [29].

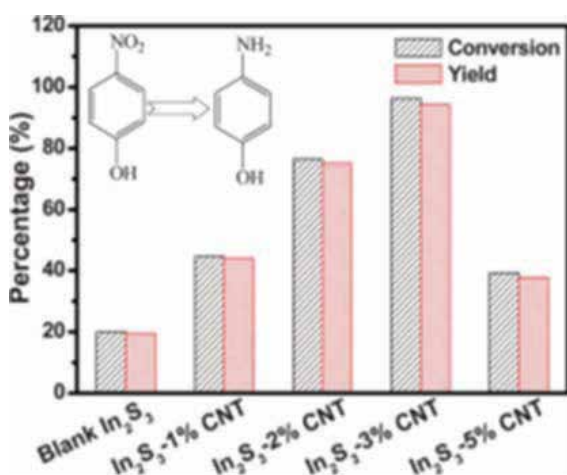


Figure 15. Photocatalytic selective hydrogenation of 4-NP over blank In_2S_3 and In_2S_3 -CNT nanocomposites under visible light irradiation for 1 h in water with the addition of ammonium formate as a hole scavenger and N_2 purge at room temperature. Reprinted with permission from Ref. [29].

hydrogenation of nitroaromatics to amines in water, with enhanced photocatalytic performance (**Figure 15**).

Shi et al. [30] reported a simple process for the synthesis of a sandwich structure of SWCNT-CdSe hybrid film (thickness ~ 200 nm), in between two SWCNT films (each thickness ~ 36 nm). They tested it as an optoelectronic conversion device under the illumination of simulated solar

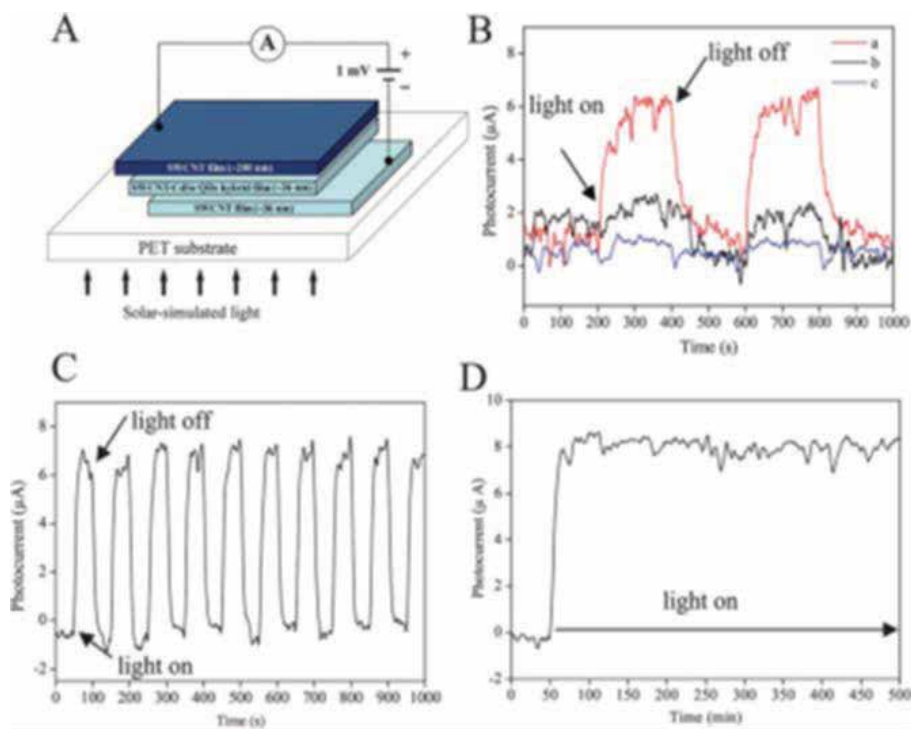


Figure 16. (A) Schematic diagram of an optoelectronic device using SWCNT-CdSe hybrid film. (B) Photocurrent vs. time under alternating light on and light off condition (a) for the device using calcined SWCNT-CdSe film as the middle layer. Curve (b) is for the device using SWCNT-CdSe film without calcination. Curve (c) is for the device using pure SWCNT film. (C) On/off light cycles of photocurrent and (D) photocurrent for a long-time illumination with light of 100 mW cm^{-2} . Reproduced with permission from Shi et al. [30].

light. They found that the device could generate photocurrent with high sensitivity and their observations are illustrated in **Figure 16**.

5. Conclusion

Attachment of semiconductor nanoparticles or quantum dots on the surfaces of carbon nanotubes has opened up innumerable possibilities of their applications in a variety of advanced nanodevices in various areas of nanotechnology. Combining the remarkable optoelectronic properties of the two outstanding nanoscale components, a vast array of fascinating optoelectronic devices is being proposed by researchers every day all over the world. In our brief review, we have touched upon a few of such applications.

Acknowledgment

One of the authors (Rima Paul) is indebted to Dr. D. S. Kothari Foundation for supporting her through Dr. D. S. Kothari Post Doctoral Fellowship at Indian Institute of Science, Bangalore, India.

Author details

Rima Paul¹ and Apurba Krishna Mitra^{2,3*}

*Address all correspondence to: akmrecdgp@yahoo.com

1 Materials Engineering Department, Indian Institute of Science, Bangalore, India

2 Department of Physics, National Institute of Technology, Durgapur, India

3 Presently retired

References

- [1] Gonzalez-Varona O, Perez-Rodríguez A, Garrido B, Bonafos C, Lopez M, Morante JR, Montserrat J, Rodríguez R. Ion beam synthesis of semiconductor nanoparticles for Si-based optoelectronic devices. *Nuclear Instruments and Methods in Physics Research B*. 2000; 161–163: 904–908.
- [2] Brus LE. Electron-electron and electron-hole interactions in small semiconductor crystallites: The size dependence of the lowest excited electronic state. *The Journal of Chemical Physics*. 1984; 80: 4403–4409. DOI: 10.1063/1.447218
- [3] Liu X, Li Y, Zhou B, Wang X, Cartwright AN, Swihart MT. Shape-controlled synthesis of SnE (E = S, Se) semiconductor nanocrystals for optoelectronics. *Chemistry of Materials*. 2014; 26: 3515–3521. DOI: 10.1021/cm501023w
- [4] Stokes EB, Stiff-Roberts AD, Dameron, CT. Quantum dots in semiconductor optoelectronic devices. *The Electrochemical Society Interface Winter*. 2006; 15(4).
- [5] Charlier JC, Blase X, Roche S. Electronic and transport properties of nanotubes. *Reviews of Modern Physics*. 2007; 79: 677–732. DOI: 10.1103/RevModPhys.79.677
- [6] Niyogi S, Hamon MA, Hu H, Zhao B, Bhowmik P, Sen R, Itkis ME, Haddon RC. Chemistry of single-walled carbon nanotubes. *Accounts of Chemical Research*. 2002; 35: 1105–1113. DOI: 10.1021/ar010155r
- [7] Collins PG, Arnold MS, Avouris P. Engineering carbon nanotubes and nanotube circuits using electrical breakdown. *Science*. 2001; 292(5517): 706–709. DOI: 10.1126/science.1058782
- [8] Wei Y, Xie C, Dean KA, Coll BF. Stability of carbon nanotubes under electric field studied by scanning electron microscopy. *Applied Physics Letters*. 2001; 79(27): 4527–4529. DOI: 10.1063/1.1429300
- [9] Yao Z, Kane CL, Dekker C. High-field electrical transport in single-wall carbon nanotubes. *Physical Review Letters*. 2000; 84(13): 2941–2944. DOI: 10.1103/PhysRevLett.84.2941

- [10] Sridhar S, Ge L, Tiwary CS, Hart AC, Ozden S, Kalaga K, Lei S, Sridhar SV, Sinha RK, Harsh H, Kordas K, Ajayan PM, Vajtai R. Enhanced field emission properties from CNT arrays synthesized on inconel superalloy. *ACS Applied Materials & Interfaces*. 2014; 6: 1986–1991. DOI: 10.1021/am405026y
- [11] Kinoshita M. *Optoelectronics with Carbon Nanotubes*, Ph.D. Dissertation, State University of New York at Stony Brook: 2011; pp. 15–17.
- [12] Topinka MA, Rowell MW, Goldhaber-Gordon D, McGehee MD, Hecht DS, Gruner G. Charge transport in interpenetrating networks of semiconducting and metallic carbon nanotubes. *Nano Letters*. 2009; 9(5): 1866–1871. DOI: 10.1021/nl803849e
- [13] Kong J, Chapline MG, Dai HJ. Functionalized carbon nanotubes for molecular hydrogen sensors. *Advanced Materials*. 2001; 13: 1384–1386. DOI: 10.1002/1521-4095(200109)13
- [14] Chen RJ, Bangsaruntip S, Drouvalakis KA, Kam NWS, Shim M, Li YM, Kim W, Utz PJ, Dai HJ. Noncovalent functionalization of carbon nanotubes for highly specific electronic biosensors. *Proceedings of the National Academy of Sciences*, 2003 USA. 2003; 100: 4984–4989. DOI: 10.1073/pnas.0837064100
- [15] Luo J, Jones VW, Maye MM, Han L, Kariuki NN, Zhong CJ. Thermal activation of molecularly-wired gold nanoparticles on a substrate as catalyst. *Journal of the American Chemical Society*. 2002; 124: 13988–13989. DOI: 10.1021/ja028285y
- [16] Che GL, Lakshmi BB, Fisher ER, Martin CR. Carbon nanotubule membranes for electrochemical energy storage and production. *Nature*. 1998; 393: 346–349. DOI: 10.1038/30694
- [17] Hu JT, Min OY, Yang PD, Lieber CM. Controlled growth and electrical properties of heterojunctions of carbon nanotubes and silicon nanowires. *Nature*. 1999; 399: 48–51. DOI: 10.1038/19941
- [18] Georgakilas V, Gournis D, Tzitzios V, Pasquato L, Guldi DM, Prato M. Decorating carbon nanotubes with metal or semiconductor nanoparticles. *Journal of Materials Chemistry*. 2007; 17: 2679–2694. DOI: 10.1039/B700857K
- [19] Strano MS, Dyke CA, Usrey ML, Barone PW, Allen MJ, Shan HW, Kittrell C., Hauge RH, Tour JM, Smalley RE. Electronic structure control of single-walled carbon nanotube functionalization. *Science*. 2003; 301(5639): 1519–1522. DOI: 10.1126/science.1087691
- [20] Cao J, Sun JZ, Heng H, Li HY, Chen HZ, Wang M. Carbon nanotube/CdS core-shell nanowires prepared by a simple room-temperature chemical reduction method. *Advanced Materials*. 2004; 16(1): 84–87. DOI: 10.1002/adma.200306100
- [21] Hickey SG, Riley DJ, Tull EJ. Photoelectrochemical studies of CdS nanoparticle modified electrodes: Absorption and photocurrent investigations. *Journal of Physical Chemistry B*. 2000; 104: 7623–7326. DOI: 10.1021/jp993858n
- [22] Tessler N, Medvedev V, Kazes M, Kan SH, Banin U. Efficient near-infrared polymer nanocrystal light-emitting diodes. *Science*. 2002; 295(5559): 1506–1508. DOI: 10.1126/science.1068153

- [23] Bechinger C, Ferrer S, Zaban A, Sprague J, Gregg BA. Photoelectrochromic windows and displays. *Nature*. 1996; 383: 608–610. DOI: 10.1038/383608a0
- [24] Chen J, Lu G. Controlled decoration of carbon nanotubes with nanoparticles. *Nanotechnology*. 2006; 17: 2891–2894. DOI: 10.1088/0957-4484/17/12/011
- [25] Banerjee S, Wong SS. Synthesis and characterization of carbon nanotube – nanocrystal heterostructures, *Nano Letters*. 2002; 2: 195–200. DOI: 10.1021/nl015651n
- [26] Li W, Gao C, Qian H, Ren J, Yan D. Multiamino-functionalized carbon nanotubes and their applications in loading quantum dots and magnetic nanoparticles. *Journal of Materials Chemistry*. 2006; 16: 1852–1859. DOI: 10.1039/B600190D
- [27] Robel I, Bunker BA, Kamat PV. Single-walled carbon nanotube–CdS nanocomposites as light-harvesting assemblies: photoinduced charge-transfer interactions. *Advanced Materials*. 2005; 17: 2458–2463. DOI: 10.1002/adma.200500418
- [28] Paul R, Kumbhakar P, Mitra AK. A facile chemical synthesis of a novel photo catalyst: SWCNT/titania nanocomposite. *Advances in Nano Research*. 2013; 1(2): 71–82. DOI: 10.12989/anr.2013.1.2.071
- [29] Yang MQ, Weng B, Xu Y-J. Synthesis of In_2S_3 –CNT nanocomposites for selective reduction under visible light. *Journal of Materials Chemistry A*. 2014; 2: 1710–1720. DOI: 10.1039/C3TA14370H
- [30] Shi Z, Liu C, Shen Lv W, Shen H, Wang D, Chen L, Li LS, Jin J. Free-standing single-walled carbon nanotube–CdSe quantum dots hybrid ultrathin films for flexible optoelectronic conversion devices. *Nanoscale*. 2012; 4: 4515–4521. DOI: 10.1039/C2NR30920C



Edited by Muhammad Akhyar Farrukh

Generally the nanometer scale covers from 1 to 100 nm while discussing the nanomaterials. Nanomaterials have very high potency and emerge with large applications piercing through all the discipline of knowledge, leading to industrial and technological growth. Nanotechnology is a multidisciplinary science that has its roots in fields such as colloidal science, device physics, and biomedical and supramolecular chemistry. The main objective of the book is to cover maximum areas focusing on synthesis, characterization with various microscopic techniques, and multiple applications. This book is divided into two sections with Non-carbon Compounds and Carbon Compounds. The synthesis, characterization, and applications of metal, metal oxides, and metal hydroxide nanoparticles are covered in the section Non-carbon Compounds, while the section Carbon Compounds focuses on the carbon nanotubes, graphite oxide, graphene oxide, etc.

Photo by Rost-9D / iStock

IntechOpen

